



*energies*

# New Perspectives on Geothermal Energy Exploration and Evaluation of Geothermal Potential

---

Edited by

Renato Somma and Daniela Blessent

Printed Edition of the Special Issue Published in *Energies*

# **New Perspectives on Geothermal Energy Exploration and Evaluation of Geothermal Potential**



# **New Perspectives on Geothermal Energy Exploration and Evaluation of Geothermal Potential**

Editors

**Renato Somma**

**Daniela Blessent**

MDPI • Basel • Beijing • Wuhan • Barcelona • Belgrade • Manchester • Tokyo • Cluj • Tianjin



*Editors*

Renato Somma  
Istituto Nazionale Di  
Geofisica e Vulcanologia  
Sezione Di Napoli  
Osservatorio Vesuviano  
Italy

Daniela Blessent  
Universidad de Medellín  
Colombia

*Editorial Office*

MDPI  
St. Alban-Anlage 66  
4052 Basel, Switzerland

This is a reprint of articles from the Special Issue published online in the open access journal *Energies* (ISSN 1996-1073) (available at: [https://www.mdpi.com/journal/energies/special\\_issues/geothermal\\_energy\\_exploration\\_and\\_evaluation](https://www.mdpi.com/journal/energies/special_issues/geothermal_energy_exploration_and_evaluation)).

For citation purposes, cite each article independently as indicated on the article page online and as indicated below:

LastName, A.A.; LastName, B.B.; LastName, C.C. Article Title. <i>Journal Name</i> <b>Year</b> , <i>Volume Number</i> , Page Range.
--

**ISBN 978-3-0365-5243-9 (Hbk)**

**ISBN 978-3-0365-5244-6 (PDF)**

Cover image courtesy of Renato Somma

© 2022 by the authors. Articles in this book are Open Access and distributed under the Creative Commons Attribution (CC BY) license, which allows users to download, copy and build upon published articles, as long as the author and publisher are properly credited, which ensures maximum dissemination and a wider impact of our publications.

The book as a whole is distributed by MDPI under the terms and conditions of the Creative Commons license CC BY-NC-ND.

# Contents

About the Editors . . . . .	vii
Preface to “New Perspectives on Geothermal Energy Exploration and Evaluation of Geothermal Potential” . . . . .	ix
<b>Mafalda M. Miranda, Jasmin Raymond and Chrystel Dezayes</b> Uncertainty and Risk Evaluation of Deep Geothermal Energy Source for Heat Production and Electricity Generation in Remote Northern Regions Reprinted from: <i>Energies</i> 2020, 13, 4221, doi:10.3390/en13164221 . . . . .	1
<b>Abdek Hassan Aden, Jasmin Raymond, Bernard Giroux and Bernard Sanjuan</b> New Insights into Hydrothermal Fluid Circulation Affected by Regional Groundwater Flow in the Asal Rift, Republic of Djibouti Reprinted from: <i>Energies</i> 2021, 14, 1166, doi:10.3390/en14041166 . . . . .	37
<b>Jian Kuang, Shihua Qi and Xiangyun Hu</b> New Insights into Crust and upper Mantle Structure in Guangdong Province, China and Its Geothermal Implications Reprinted from: <i>Energies</i> 2021, 14, 2236, doi:10.3390/en14082236 . . . . .	61
<b>Renato Somma, Daniela Blessent, Jasmin Raymond, Madeline Constance, Lucy Cotton, Giuseppe De Natale, Alessandro Fedele, Maria Jose Jurado, Kirsten Marcia, Mafalda Miranda, Claudia Troise and Thomas Wiersberg</b> Review of Recent Drilling Projects in Unconventional Geothermal Resources at Campi Flegrei Caldera, Cornubian Batholith, and Williston Sedimentary Basin Reprinted from: <i>Energies</i> 2021, 14, 3306, doi:10.3390/en14113306 . . . . .	79
<b>Tomislav Malvić, Uroš Barudžija, Borivoje Pašić and Josip Ivšinić</b> Small Unconventional Hydrocarbon Gas Reservoirs as Challenging Energy Sources, Case Study from Northern Croatia Reprinted from: <i>Energies</i> 2021, 14, 3503, doi:10.3390/en14123503 . . . . .	103
<b>Max Hesselbrandt, Mikael Erlström, Daniel Sopher and Jose Acuna</b> Multidisciplinary Approaches for Assessing a High Temperature Borehole Thermal Energy Storage Facility at Linköping, Sweden Reprinted from: <i>Energies</i> 2021, 14, 4379, doi:10.3390/en14144379 . . . . .	119
<b>Alberto Carotenuto, Francesca Ceglia, Elisa Marrasso, Maurizio Sasso and Laura Vanoli</b> Exergoeconomic Optimization of Polymeric Heat Exchangers for Geothermal Direct Applications Reprinted from: <i>Energies</i> 2021, 14, 6994, doi:10.3390/en14216994 . . . . .	149
<b>Guillem Piris, Ignasi Herms, Albert Griera, Montse Colomer, Georgina Arnó and Enrique Gomez-Rivas</b> 3DHIP-Calculator—A New Tool to Stochastically Assess Deep Geothermal Potential Using the Heat-In-Place Method from Voxel-Based 3D Geological Models Reprinted from: <i>Energies</i> 2021, 14, 7338, doi:10.3390/en14217338 . . . . .	169



# About the Editors

## **Renato Somma**

Renato Somma is a Geologist and has a PhD in Geophysics and Volcanology from the University of Naples Italy. A researcher at the Italian National Institute of Geophysics and Volcanology, he has extensive experience in the development of original interpretative geochemical models for several Italian volcanic districts, modelling of geothermal reservoirs, development of new concepts for the interpretation of ground deformation and seismicity at collapse calderas, stress–strain modelling and studies of fault interaction and volcano-tectonic, geo-mechanics and induced seismicity by fluid injection, medical geology and environmental pollution. He is currently involved in researches related to resilience and volcanic risk mitigation and innovation of insurance services in catastrophe risk management as associate researcher at CNR-IRISS and research for the localization and characterization of submarine fumarolic and hydrothermal emissions as associate researcher at CNR-ISMAR. He is principal investigator of relevant national and international projects, he has coordinated wide high-quality research groups. He is Associate Editor for *Energies*, *Challenges*, *Sensors* by MDPI and *Frontiers for Young Minds*. By *Frontiers*. He is the author of more than 60 publications ISI and 150 presentations at meetings.

## **Daniela Blesent**

Daniela Blesent is an Environmental Engineer from the Politecnico di Torino (Italy). She obtained a PhD in Earth Sciences at Laval University (Quebec, Canada) in numerical modeling in Hydrogeology. She worked as a lecturer at Ecole Polytechnique de Montréal between 2010 and 2012. Since 2013, she has been working as professor at the University of Medellin, in the Environmental Engineering program and was associate editor of the *Hydrogeology Journal* between 2016 and 2018. She received the “Geothermal Special Achievement Award” from Geothermal Rising (United States Geothermal Association) in 2020, which recognizes special or outstanding achievements in any aspect of the development of geothermal energy and related areas. She is the leader of the project “Geothermal Resources for Energy Transition” supported by the international geosciences program, IGCP, of UNESCO, with 18 participating countries, and since January 2020, she has been the president of the Colombian Geothermal Association.



# Preface to “New Perspectives on Geothermal Energy Exploration and Evaluation of Geothermal Potential”

Due to the increasing need for energy in emerging countries, as well as energy transition requirements, geothermal resources’ characterization and use is generating more and more interest, in both low/intermediate and high temperature fields. However, their characterization and use can be challenging. Deep geothermal resources can be hosted in highly heterogeneous volcanic complexes, sedimentary basins, or old basement rocks. Reservoir permeability can be enhanced through different engineering techniques (hydraulic, chemical, and thermal stimulation), although their application may raise problems of social acceptability. Development of interdisciplinary methodologies to characterize geothermal systems from a volcanological, geophysical, geochemical, and geo(hydro)thermal point of view is fundamental. Moreover, improvement of assessment methods is a key aspect to unlock the use of geothermal resources, including high temperature borehole thermal energy storage (HT-BTES) and direct use of thermal waters for building heating systems.

This book came up as the result of a Special Issue in the *Energies* Journal with 8 papers published during 2021. Its idea arose in the context of the IGCP636 project “Geothermal resources for energy transition”, approved in 2020 by the International Geoscience Programme of the UNESCO. The main objectives of IGP636 are promoting the use of geothermal resources as a clean, baseload, and renewable energy by: (1) increasing knowledge about deep geothermal reservoirs, (2) conducting outreach activities with focus groups and community, and (3) promoting the installation of low-enthalpy geothermal systems. This book includes topics related with these three items, although only five papers are co-authored by researchers that are members of the IGCP636 group, since the Special Issue was open to contributions from any author.

**Renato Somma and Daniela Blessent**

*Editors*



Article

# Uncertainty and Risk Evaluation of Deep Geothermal Energy Source for Heat Production and Electricity Generation in Remote Northern Regions

Mafalda M. Miranda <sup>1,\*</sup>, Jasmin Raymond <sup>1</sup> and Chrystel Dezayes <sup>2</sup>

<sup>1</sup> INRS—Institut National de la Recherche Scientifique, 490 Rue de la Couronne, Québec, QC G1K 9A9, Canada; jasmin.raymond@inrs.ca

<sup>2</sup> BRGM, F-45060 Orléans, France; c.dezayes@brgm.fr

\* Correspondence: mafalda\_alexandra.miranda@ete.inrs.ca

Received: 13 July 2020; Accepted: 11 August 2020; Published: 14 August 2020

**Abstract:** The Canadian off-grid communities heavily rely on fossil fuels. This unsustainable energetic framework needs to change, and deep geothermal energy can play an important role. However, limited data availability is one of the challenges to face when evaluating such resources in remote areas. Thus, a first-order assessment of the geothermal energy source is, therefore, needed to trigger interest for further development in northern communities. This is the scope of the present work. Shallow subsurface data and outcrop samples treated as subsurface analogs were used to infer the deep geothermal potential beneath the community of Kuujuaq (Nunavik, Canada). 2D heat conduction models with time-varying upper boundary condition reproducing climate events were used to simulate the subsurface temperature distribution. The available thermal energy was inferred with the volume method. Monte Carlo-based sensitivity analyses were carried out to determine the main geological and technical uncertainties on the deep geothermal potential and risk analysis to forecast future energy production. The results obtained, although speculative, suggest that the old Canadian Shield beneath Kuujuaq host potential to fulfill the community's annual average heating demand of 37 GWh. Hence, deep geothermal energy can be a promising solution to support the energy transition of remote northern communities.

**Keywords:** geothermal energy; geothermal gradient; paleoclimate; numerical model; Monte Carlo method; heat-in-place; theoretical potential; technical potential; petrothermal system; Nunavik

## 1. Introduction

The access to electricity is still a global challenge nowadays. In 2016, there were about 1 billion people off-grid worldwide [1]. In Canada, 239 communities rely solely on fossil fuels for electricity, space heating, and domestic hot water [2,3]. In most of these communities, the fuel is shipped only once a year with long-term storage period in sometimes old facilities having a risk of spill [3]. Moreover, the electricity cost is volatile and more than 50% higher than in southern Canada [3,4]. Therefore, the volatility and high cost of the diesel price, the will for higher energy security, and the severe environmental consequences brought interest to develop local, sustainable, and carbon-free energy resources, not only in the Canadian remote communities but also in other off-grid areas worldwide (e.g., [1,5–19]). Geothermal energy can be one of such renewable options to replace diesel consumption and provide electricity and heating/cooling for both Arctic/subarctic (e.g., [20–24]) and non-Arctic (e.g., [25–28]) remote and off-grid regions. Compared with other sources of renewable energy, geothermal has a high capacity factor and is available indefinitely regardless of weather conditions [29]. Ground-coupled heat pumps are believed to be an interesting heating alternative for the residential dwellings [30,31] and to support greenhouses food production [32] in

such arctic and subarctic climate. Borehole thermal energy storage has also been studied and can be a promising technology to help improve energy and food security in the arctic/subarctic environment [33]. Furthermore, geothermal systems of all kinds can be integrated with other renewable sources and technologies, enhancing their individual efficiency in cold climates [34]. Technological advances in the geothermal energy sector now allow to envision the exploitation of deep geothermal energy source in geological environments other than hydrothermal systems. For example, the engineered geothermal systems (EGS) concept (e.g., [35]), together with binary cycle geothermal power plants (GPP), can generate electricity from low-temperature resources (e.g., [36]).

Unfortunately, an important data gap exists in northern territories to accurately assess the local and deep geothermal energy source potential (cf. [2,37,38]). For this reason, efforts have been made to adapt methodologies and draw guidelines using outcrops as subsurface analogs to provide initial data for preliminary geothermal energy source assessment associated with petrothermal systems. Thus, an evaluation of the geothermal energy source and potential heat and power output is presented in this work to forecast future energy production. It is convenient to highlight that the term geothermal energy source was utilized in this work to follow the United Nations Framework Classification on fossil energy and mineral reserves and resources 2009 to geothermal energy resources [39].

Guidelines to carry out geothermal energy source and potential power output assessment associated with petrothermal systems have been proposed in the literature (e.g., [35,40,41]) and were adopted in this work to account for heat production and cogeneration. These previous studies differ in terminology and somewhat calculation methods. Tester et al. [35] followed the resources terminology of Muffler and Cataldi [42], while Beardsmore et al. [40] and Limberger et al. [41] followed the geothermal potential classification of Rybach [43]. Moreover, Limberger et al. [41] extended Beardsmore et al. [40] protocol and evaluated the leveled cost of energy and the economic potential. Regardless of the protocol followed, the basic element of the geothermal energy source and potential heat and power output assessment is the estimation of the available thermal energy, or “heat-in-place”. The volume method introduced by USGS (United States Geological Survey) researchers (e.g., [42,44,45]) is the most widely used evaluation technique to infer the available thermal energy (e.g., [35,37,40,41,46–51]). This method is based on the evaluation of the heat stored in a certain volume of rock at specified depths in relation to the mean annual surface temperature [42]. However, many authors argued that, for a more realistic assessment, the reference temperature should be equivalent to the reservoir abandonment temperature. This is dependent on the intended application (space heating and/or electricity generation) and on the type of GPP to be installed (e.g., [40,49,52]). The second key element is the recoverable fraction. This concept was introduced since only a fraction of the available thermal energy can be harvested. This is mostly due to technical and economic constraints, such as drilling depth and cost, the active stimulated volume, the allowed reservoir thermal drawdown, and the surface land area available [35,40,47]. Finally, the conversion of thermal energy to power output takes into account the project lifetime, the availability of the GPP throughout the year, and the cycle thermal efficiency [35,40,49].

An evaluation of the subsurface temperature distribution is imperative to calculate the available thermal energy accordingly with the volume method. Thus, 2D transient heat conduction models were solved numerically with finite element method (FEM). Several climate episodes have occurred throughout Earth’s history (e.g., [53]) that propagates downwards by thermal diffusion influencing the subsurface temperature (e.g., [54,55]) and these shall not be ignored. Additionally, the effect of temperature and pressure on thermal conductivity was considered and implemented in the numerical models used to simulate the subsurface temperature. The variability of the rock thermal conductivity has been shown to influence these predictions (e.g., [56–58]).

Then, the assessment of the available thermal energy was constrained by the envisioned applications: heat production and electricity generation. The minimum temperature for space heating is about 30–50 °C [49,59] and for electricity generation using a binary cycle GPP designed for an Arctic climate is about 120–140 °C [60]. Thus, these were used as reservoir abandonment temperatures.

Nevertheless, Organic Rankine Cycle with an optimized working fluid may generate electricity from geothermal energy source lower than 120 °C (e.g., [61–64]). The thermal energy was assessed every 1 km in depth for a total depth of 10 km, for the land surface area occupied by the community of Kuujuaq (ca. 4 km<sup>2</sup>). Finally, a range of theoretical recovery factors was investigated. The planar fracture method developed by Bodvarsson [65] and Bodvarsson and Tsang [66], later modified by Williams [67], has been widely used to predict theoretical recovery factors values for fracture-dominated systems (8 to 20%; [68]). Sanyal and Butler [69], however, simulated recovery factors of about 40% for a stimulated rock volume higher than 0.1 km<sup>3</sup>. In this work, a conservative range between 2% and 20% was preferred following the recommendations of Tester et al. [35,47] and Beardsmore et al. [40].

Afterward, thermal energy was converted to heat and power output. For the latter, a cycle net thermal efficiency correlation equation has been proposed by Tester et al. [35] and was used in this study. This equation estimates quantitatively the percentage of heat that can be converted to electricity by binary GPP, thus allowing for a first-order evaluation of the potential power output. The project lifetime is constrained by several economic and technical factors, such as the minimum economic limit, design life, reservoir sustainable management, maintenance, contract, and entitlement periods [39,49]. Often, a 30-year life cycle is assumed for the evaluation of the geothermal potential [35,40]. However, technical aspects may dictate a longer or shorter lifetime, and this needs to be considered to evaluate the potential heat and power output and plan future energy production. Therefore, project lifetimes of 20 to 50 years were examined in this study. The GPP factor usually varies between 90% and 97% [49] and this range was considered in this study.

Lastly, global sensitivity analysis with Monte Carlo simulations was undertaken in this study for uncertainty and risk evaluation [68,70]. The global sampling and probabilistic approach were preferred to account for the current geological and technical uncertainties considered in this study. Detailed explanations of the Monte Carlo method and global sensitivity analysis can be found in, for example, Rubinstein and Kroese [71], Graham and Talay [72], Thomopoulos [73], and Scheidt et al. [74]. Broadly, global sensitivity analysis based on Monte Carlo simulates the possible scenarios by random sampling the input variables jointly, within the defined span of the probability distribution functions. The use of these methods enabled to infer the most influential uncertainties and assess the probability of the deep geothermal energy source to meet the community's heat and power demand.

The influence of the statistical distribution of the bedrock thermophysical properties cannot be neglected [75] when doing such geothermal energy source assessment and this uncertainty was considered throughout this study. Moreover, the effect of water saturation on the thermophysical properties was considered as well. Although the water saturation cannot be readily observed at depth, its effect may lead to significant miscalculations and shall not be ignored (e.g., [76]).

Thus, this study is the first of its kind undertaken in the Canadian Shield and represents an initial step to assess if deep geothermal energy source can be a viable alternative for remote northern communities settled in that physiographic region. Nevertheless, the approach followed in this study can be extended to other remote areas facing the same off-grid challenges (e.g., Svalbard, Faeroe Islands, Greenland, and other Arctic and non-Arctic communities). The thermal energy and potential output for heat production and electricity and cogeneration were examined and the main current geological (both epistemic and aleatory variability) and technical uncertainties were determined by the sensitivity analysis carried out. The statistical distribution of the thermophysical properties due to their intrinsic heterogeneous character is an aleatory variability type. The subsurface temperature, the conditions of the thermophysical properties (dry and water saturation), and the climate signal during a glacial period are epistemic uncertainties that can be decreased with further geothermal exploration development. Reservoir abandonment temperature, recovery factor, project lifetime, and GPP factor are technical uncertainties that can be optimized to maximize the energy production. The outcomes of this first-order assessment are useful to plan further geothermal developments and forecast future energy production, hence, helping remote northern communities to move toward a more sustainable energetic framework.

## 2. Geographic and Geological Setting

Nunavik is home to 14 communities that are independent of the southern provincial electrical grid and rely exclusively on diesel for electricity, space heating, and domestic hot water, like the majority of communities in northern Canada [2,3]. In this region, the price of fuel oil per liter amounted to \$2.03 in 2018, which was subsidized to \$1.63 by the local government [4]. Therefore, geothermal energy sources may be a solution for this unfavorable energetic framework. However, in Nunavik, a territory of about 507,000 km<sup>2</sup>, only three deep boreholes exist to evaluate heat flux. Those are Raglan mine, Asbestos Hill mine, and camp Coulon, which are located away from the Inuit communities (Figure 1; [38] and references therein). This highlights the need of adapting geothermal exploration methodologies to use outcrops treated as subsurface analogs to obtain a first estimate of the geothermal potential.

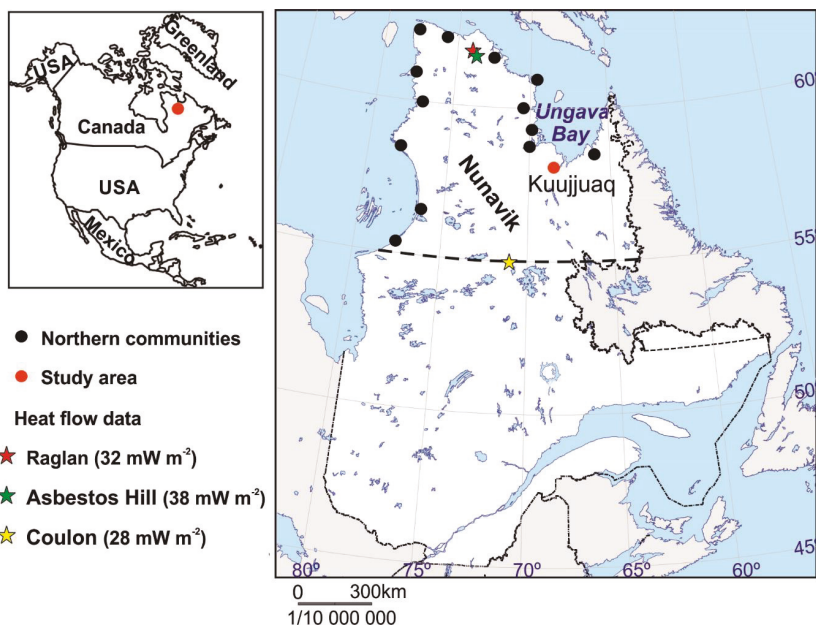


**Figure 1.** Geographical location of Kuujuaq and the remaining Nunavik communities (Canada) along the shore of a vast territory with few heat flow assessments: camp Coulon, Raglan, and Asbestos Hill mining sites [38] and references therein (adapted from Miranda et al. [75]).

Nunavik is a vast territory, with the communities dispersed along the shore (Figure 1), and for that reason, a community-focused assessment was preferred to foster local deep geothermal development. Thus, avoiding to (1) extrapolate sparse data over such a large region and (2) blind the local potential by regional anomalies far away from the communities and useless for their energy transition. Kuujuaq (Figure 1) is used as a case study and an example for the remaining communities. This village is the administrative capital of Nunavik and the largest within that territory, enclosing about 2750 inhabitants and 518 private dwellings [77] in a surface land area of approximately 4 km<sup>2</sup> [78]. In 2000, the annual electricity demand in Kuujuaq was about 12,000 MWh [79], increasing to 15,100 MWh in 2011 [80]. The daily electricity consumption amounts typically to 15 to 22 kWh per dwelling, depending on the season, and is used exclusively for lighting and electrical household appliances [81]. Gunawan et al. [31] simulated the heating load of a typical 5-occupants residential dwelling in Kuujuaq. Their results reveal an annual heating energy demand of about 71 MWh per residence. These values provide a gross, first-order perspective of Kuujuaq heat and power demand.

The main lithologic units outcropping near Kuujuaq are paragneiss and diorite that were sampled in the framework of this study (Figure 2). These rocks belong to the Canadian Shield and are Neoproterozoic in age [82]. A detailed description of these units and the samples collected can be found in Miranda et al. [75] and references therein. The two main structures present in the study area are Lac Pingiajjulik and Lac Gabriel faults (Figure 2). Both are described as regional thrust faults with dextral movement [82].

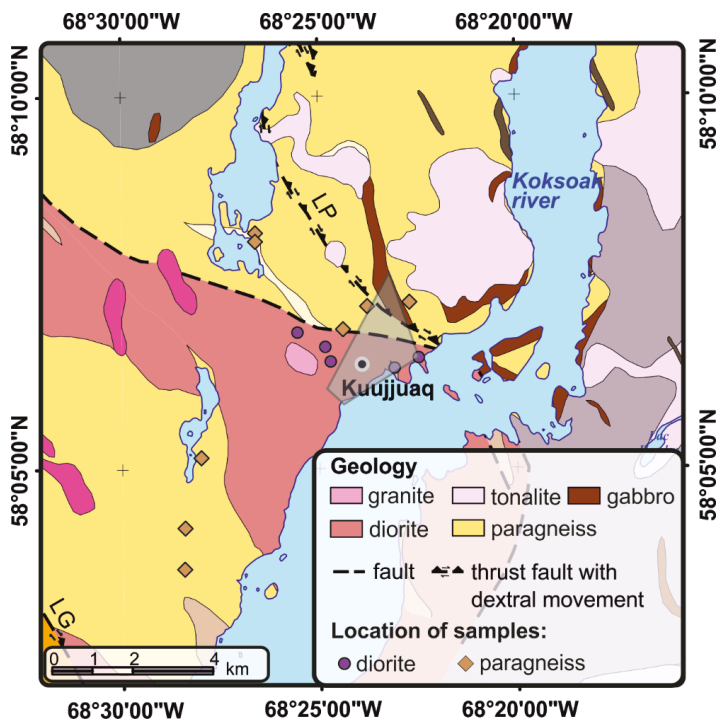


**Figure 2.** Geological map of the study area (adapted from SIGÉOM [82] and Miranda et al. [75]). LP—Lac Pingiajjulik fault, LG—Lac Gabriel fault. The grey polygon represents the surface land area occupied by Kuujuaq’s community [78].

### 3. Materials and Methods

#### 3.1. Thermophysical Properties

A total of 13 rock samples were collected in the study area (Figure 2) and prepared for the laboratory analyses. Core plugs with 20-mm-radius and 20 to 30-mm-thickness were drilled from the hand samples. Then, the core plugs were analyzed for thermal conductivity and volumetric heat capacity at dry conditions with a guarded heat flow meter. In a second time, the plugs were placed in a vacuum chamber and immersed in water for 24 h to reach the water saturation state. Thermal conductivity and volumetric heat capacity were re-evaluated considering water-saturation. Porosity was additionally evaluated as a function of pressure to indirectly infer the effect of pressure on thermal conductivity. The concentration in uranium (U), thorium (Th), and potassium (K) was determined by gamma-ray spectrometry and inductively coupled plasma—mass spectrometry (ICP-MS).

Thermal conductivity and volumetric heat capacity were evaluated at both dry and water-saturated conditions in the laboratory using a FOX50 device from TA Instruments that has an accuracy of 3%. The device consists of two plates, two heat flow meters, and two insulating casings to prevent heat

losses. The method follows the ASTM (American Society for Testing and Materials) standard C1784-13 (2013). The sample is placed between the plates and the temperature is allowed to reach equilibrium. A temperature difference of 10 °C is imposed on each plate for thermal conductivity assessment. The temperature of the plates is changed instantaneously for volumetric heat capacity evaluation and the time to reach equilibrium is needed to evaluate this property based on the energy conservation equation [83]. For both properties, successive data acquisition cycles grouped in blocks are run until all the necessary equilibrium criteria are reached and the sample is considered in thermal equilibrium (see Miranda et al. [75] for further details). Thermal conductivity was additionally evaluated within the temperature range of 20–160 °C to define an experimental relationship that describes the effect of temperature on thermal conductivity (e.g., [84]):

$$\frac{1}{\lambda(T)} = \frac{1}{\lambda_{20}} + b(T - 20) \Leftrightarrow \lambda(T) = \frac{1}{(\lambda_{20})^{-1} + b(T - 20)} \quad (1)$$

where  $\lambda$  ( $\text{W m}^{-1} \text{K}^{-1}$ ) is thermal conductivity,  $T$  (°C) is temperature, and  $b$  is an experimental coefficient that controls temperature dependence of the thermal conductivity. The subscript 20 stands for room temperature. The effect of pressure on thermal conductivity was assessed indirectly from the pressure dependence on porosity. The combined gas permeameter-porosimeter AP-608 was used to evaluate porosity at different confining pressures from 2.8 to 69 MPa. The evaluation of porosity follows Boyle's law, which states that the pressure exerted by a given mass of an ideal gas is inversely proportional to the volume it occupies (e.g., [85] and references therein).

The results from this analysis were used to indirectly infer the effect of pressure on thermal conductivity, which is described by the following function:

$$\lambda(P) = d \ln(P) + \lambda_{20} \quad (2)$$

where  $P$  (Pa) is pressure and  $d$  is an experimental coefficient that controls the pressure dependence of thermal conductivity. The following relationship was then obtained when combining Equation (2) with Equation (1) to describe the effect of both temperature and confining pressure on thermal conductivity:

$$\lambda(T) = \frac{1}{(d \ln(P) + \lambda_{20})^{-1} + b(T - 20)} \quad (3)$$

The concentration in U, Th, and K was evaluated by both gamma-ray spectrometry and ICP-MS to avoid biased results (cf. [75]). The Ortec gamma-ray spectrometer detector used for this purpose is NaI(Tl) with  $7.62 \times 7.62$  cm, surrounded by a 5-cm-thick lead shield. The concentrations of the radioisotopes were measured using the three-window method taking into account the emitted gamma radiation. The system is calibrated with standard solutions certified by the International Atomic Energy Agency (IAEA). The ICP-MS method, where the chemical elements passed through decomposition into their atomic constituents, was also used. The positively charged ions are extracted and separated, being finally measured by an ion detector. A quality control protocol was followed and certified reference materials used to guarantee the reliability of the analyses (see Miranda et al. [75] for further details).

Radiogenic heat production was then calculated by applying Rybach's empirical function [86]:

$$A = 10^{-5} \rho (9.51C_U + 2.56C_{Th} + 3.50C_K) \quad (4)$$

where  $A$  ( $\text{W m}^{-3}$ ) is the radiogenic heat production,  $\rho$  ( $\text{kg m}^{-3}$ ) is the density, and  $C$  ( $\text{mg kg}^{-1}$ ; %) is the concentration of each radioisotope. The subscripts U, Th, and K stand for uranium, thorium, and potassium, respectively.

### 3.2. 2D Subsurface Temperature Distribution

The temperature-at-depth was solved numerically by FEM in COMSOL Multiphysics® with the 2D transient heat conduction equation:

$$\frac{\partial}{\partial x} \left( \lambda \frac{\partial T}{\partial x} \right) + \frac{\partial}{\partial z} \left( \lambda \frac{\partial T}{\partial z} \right) + A = \rho c \frac{\partial T}{\partial t} \quad (5)$$

where  $x$  (m) and  $z$  (m) are spatial variables,  $\rho c$  ( $\text{J m}^{-3} \text{K}^{-1}$ ) is the volumetric heat capacity, and  $t$  (s) is time. The geometry of the model is rectangular with width of 32 km and depth of 10 km (Figure 3) and takes into account the regional geological cross-section of Simard et al. [87].

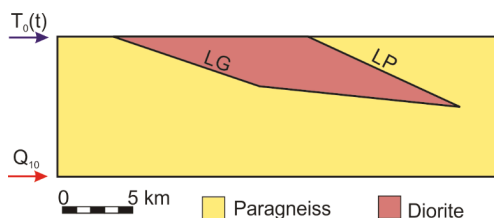


**Figure 3.** Simplified geological cross-section and model's geometry (based on Simard et al. [87]). LP—Lac Pingiajjulik fault, LG—Lac Gabriel fault;  $T_0(t)$ —time-varying upper boundary condition,  $Q_{10}$ —basal heat flux.

The initial temperature condition to run the transient simulations was calculated using the 1D analytical solution of Equation (5) in steady-state:

$$T(z) = T_0 + \frac{Q}{\lambda} z - \frac{A}{2\lambda} z^2 \quad (6)$$

The lateral boundary conditions were assumed adiabatic. The lower boundary condition is the basal heat flux. A numerical approach has been developed by Marquez et al. [88] and improved by Miranda et al. [89] to simulate climate events and find the basal heat flux that best matches a measured temperature log. The results of the latter were used in this work. The temperature profile was measured in an 80-m-deep groundwater monitoring well drilled prior to any of these studies. Considering the thermophysical properties at dry conditions, Miranda et al. [89] estimated the basal heat flux to range between 31.8 to 52.3  $\text{mW m}^{-2}$ , with an average value of 41.6  $\text{mW m}^{-2}$ . In turn, the thermophysical properties evaluated at water saturation conditions led to an increase of the heat flux: 34.1 to 69.4  $\text{mW m}^{-2}$ , with an average value of 49.7  $\text{mW m}^{-2}$  [89]. The heat flux estimates of Miranda et al. [89] were used as the lower boundary condition in the present work.

A time-varying upper boundary condition was imposed to represent the ground surface temperature history (GSTH). COMSOL Multiphysics® piecewise function was used to implement the climate events (Table 1). The fourfold stratigraphic framework proposed by Flint [90] and Emiliani [91] to characterize the late Pleistocene (300–11.6 ka before present (B.P.)) climate events were considered in this study. The temperature at the base of the Laurentide Ice Sheet is still debatable. GSTH inversion from deep temperature profiles in Canada points toward an average temperature of  $-5$  °C during the last glacial maximum, though lower temperatures were simulated in eastern Canada than in central Canada [92–96]. During the last glacial maximum, the Laurentide Ice Sheet reached a maximum thickness higher than 3 km [97], highlighting that under such thick ice the temperature was close to the freezing point ( $-1$  to  $-2$  °C; [54,98]). A sensitivity study was undertaken to deal with the uncertainty of the Laurentide Ice Sheet basal temperature and its influence on the subsurface temperature (Table 1).

**Table 1.** Time and temperature steps of the major Pleistocene and Holocene climate events considered for ground surface temperature history (GSTH) in this work.

Event	Time Step (Years B.P.)	Temperature Step (°C)	
		Cold Scenario	Warm Scenario
Nebraskan (MIS 14 *)	300,000–265,000	−10	−1
Aftonian (MIS 13–11 *)	265,000–200,000	0	0
Kansan (MIS 10 *)	200,000–175,000	−10	−1
Yarmouth (MIS 9–7 *)	175,000–125,000	0	0
Illinoian (MIS 6 *)	125,000–100,000	−10	−1
Sangamonian (MIS 5 *)	100,000–75,000	0	0
Wisconsinan (MIS 4–2 *)	75,000–11,600	−10	−1
Holocene (MIS 1)	11,600–present		
Holocene thermal maximum	7000–5800		+2
Roman and Medieval warm periods	3200–1000		+1
Little Ice Age	500–270		−1
Pre-industrial and Industrial Revolution	270–80		+1.4
Present-day global warming	30–present		+2

\* Based on Emiliani [91], MIS—Marine Isotope Stage, B.P.—before present.

The interglacial Holocene thermal maximum occurred ca. 7–5.8 ka B.P. ([99–101] and references therein) and is referred to have been 1–2 °C warmer than the present-day temperature [99,100,102,103]. The temperature during the interstadial Roman and Medieval warm periods (ca. 3.2–1 ka B.P.; [101] and references therein) were estimated to have been 1–1.5 °C warmer than at present [102]. During the stadial Little Ice Age (ca. 500–270 years B.P.; [101] and references therein), the temperature is estimated to have been 1 °C lower than today [102]. Majorowicz et al. [104] and Chouinard et al. [105] identified warming of about 1.4–2 °C during the pre-industrial and Industrial Revolution (ca. 270–80 years B.P.). This episode was followed by a short cooling episode (80–30 years B.P.), where temperature decreased around 0.4 °C [105]. Nowadays, meteorological data [106] can be converted empirically to undisturbed ground temperature with [107]:

$$T_g = 17.898 + 0.951T_{amb} \quad (7)$$

where the subscripts *g* and *amb* are used for ground and ambient (air), respectively. This was done with Kuujuaq historic weather data and revealed a sharp increase in the temperature of about 2 °C for the last 30 years.

The thermal properties of the geological materials were assumed at both dry and water-saturated state and the effect of temperature and pressure on thermal conductivity (Equation (3)) was implemented in the model. The statistical distribution of the thermophysical properties was also taken into account. The transient simulations were carried out for 300 ka with yearly time step to ensure a smooth solution for the effect of the more recent and short episodes of surface temperature changes. The backward differentiation formula was chosen for the time step method (e.g., [108]). The steps taken by the solver were set as free after a step-independency study have been undertaken.

### 3.3. Geothermal Energy Source and Potential Heat and Power Output

#### 3.3.1. Volume Method

The available thermal energy content was assessed within the limits of Kuujuaq land surface area covering 4 km<sup>2</sup> (Figure 2) down to 10 km. Volumetric heat capacity at both dry and water-saturated state was used in the calculations and its statistical distribution was considered as well. The available thermal energy was inferred with (e.g., [42]):

$$H = V\rho c(T_{res} - T_{ref})R \quad (8)$$

where *H* (J) is the thermal energy, *V* (m<sup>3</sup>) is the volume, and *R* (%) is the recovery factor. The subscripts *res* and *ref* stand for reservoir and reference temperature, respectively. The former was obtained through

the 2D temperature simulations previously described and for the latter, the following hypotheses were assumed:

1. The reservoir abandonment temperature for space heating is about 30–50 °C [49,59]
2. The minimum temperature to generate electricity by a binary GPP considering an Arctic design is around 120–140 °C [60]

The recovery factor is not yet well constrained at this early stage of the geothermal exploration and, therefore, a theoretical range of 2–20% was used [35,40,47]. The conversion of the thermal energy to potential heat and power output ( $PO$ ;  $W_{th,e}$ ) was calculated with [35,40,49]:

$$PO = \frac{H\eta_{th}}{F_{GPP}t} \quad (9)$$

where  $\eta$  (%) is the cycle efficiency and  $F_{GPP}$  (%) is the GPP factor related with its availability throughout the year. The subscript  $th$  stands for thermal. The cycle net thermal efficiency was calculated as indicated by Tester et al. [35]:

$$\eta_{th} = 0.0935T_{res} - 2.3266 \quad (10)$$

The cycle thermal efficiency was only used to estimate the theoretical potential for electricity generation. The heat production evaluation did not consider this parameter since the heat energy is used directly (e.g., [109]). A range between 20 to 50 years of project lifetime was assumed. The GPP factor was varied between 90% and 97% [49]. It is important to highlight that no temperature loss was considered in this study [40].

### 3.3.2. Global Sensitivity Analysis with Monte Carlo Method

A global sensitivity analysis was undertaken to assess the joint effect of each parameter (and respective uncertainty; Table 2) on the potential heat and power output based on Monte Carlo method [74]. The simulations were carried out with @Risk [110] using Latin Hypercube sampling [111] and the pseudorandom number generator Marsenne Twister [112]. The Latin Hypercube sampling was chosen since it is referred to be more reliable and efficient than Monte Carlo sampling [113]. A total of 10,000 iterations (i.e., possible scenarios) were run per simulation to assure output stability. Moreover, the initial random number seed was fixed to 1 in all the simulations carried out. A total of 3 simulations without changing any of the inputs were run to confirm the solidity of the randomness of the sampling [113]. This approach was followed after carrying out an analysis of the stochasticity component of the response [74]. Five simulations were run and the difference in the output was less than 10%, indicating that the spatial uncertainty of the input parameters will have a minor impact on the deep geothermal energy source and potential heat and power output, and therefore can be neglected.

The existent GSTH and conditions of the thermophysical properties (dry or water-saturated) are unknown at this early stage of the geothermal development. Therefore, three hypotheses for the reservoir temperature were analyzed separately:

1. Thermophysical properties at dry conditions and warm GSTH
2. Thermophysical properties at dry conditions and cold GSTH
3. Thermophysical properties at water saturation conditions and warm GSTH

The outcomes from the uncertainty analysis can be translated to risk, enabling to forecast the probability of the deep geothermal energy source to meet the community's heat and power demand [114].

**Table 2.** Monte Carlo method input parameters and their uncertainty.

Parameter Code	Parameter Description	Variable Type	Distribution
Geological uncertainties			
$V$	Reservoir volume		Single value
$T_{res}$	Reservoir temperature	Continuous	Triang(min,median,max)
$\rho c$	Volumetric heat capacity	Continuous	Normal( $\mu,\sigma$ )
Technical uncertainties			
$T_{ref}$	Reservoir abandonment temperature	Continuous	Uniform(min,max)
$R$	Recovery factor	Continuous	Uniform(min,max)
$\eta_{th}$	Cycle thermal efficiency		$f(T)$
$F_{GPP}$	GPP factor	Continuous	Uniform(min,max)
$t$	Project lifetime	Continuous	Triang(min,most,max)

Triang—Triangular probability distribution, min and max—minimum and maximum values, respectively,  $\mu$ —arithmetic mean,  $\sigma$ —population standard deviation,  $f$ —function, most—most likely value.

## 4. Results

### 4.1. Thermophysical Properties

At dry conditions and room temperature, the paragneiss samples are characterized by lower thermal conductivity than the diorite samples. The former has an average value of  $2.26 \text{ W m}^{-1} \text{ K}^{-1}$ , while the latter is characterized by an average thermal conductivity of  $2.78 \text{ W m}^{-1} \text{ K}^{-1}$  (Table 3). Per contra, the volumetric heat capacity is higher for the paragneiss samples than for the diorite (Table 3). An average value of  $2.32 \text{ MJ m}^{-3} \text{ K}^{-1}$  was inferred for the diorite while a value of  $2.36 \text{ MJ m}^{-3} \text{ K}^{-1}$  was evaluated for the paragneiss. At water saturation conditions, the same trend is observed. The paragneiss samples have lower thermal conductivity but higher volumetric heat capacity than the diorite (Table 3). Likewise, higher concentration of radiogenic elements (U, Th, K) was evaluated for the paragneiss samples than for the diorite. This consequently influenced the inferred internal heat generation (Table 3). An average value of  $1.08 \text{ } \mu\text{W m}^{-3}$  was inferred for the paragneiss while an average value of  $0.53 \text{ } \mu\text{W m}^{-3}$  was evaluated for the diorite. These are average values from the two methods used in this work to evaluate the radiogenic element concentrations (gamma-ray spectrometry and ICP-MS).

**Table 3.** Results of the thermophysical properties analyses.

	Paragneiss		Diorite	
	Dry	Wet	Dry	Wet
$\lambda \text{ (W m}^{-1} \text{ K}^{-1}\text{)}$				
$\mu$	2.26	2.67	2.78	3.08
$\alpha$	0.55	0.64	0.65	0.82
$\chi$	2.10	2.84	2.60	2.82
[min–max]	1.62–3.15	1.95–3.95	2.12–3.98	2.08–4.54
$\rho c \text{ (MJ m}^{-3} \text{ K}^{-1}\text{)}$				
$\mu$	2.36	2.44	2.32	2.36
$\alpha$	0.10	0.18	0.14	0.12
$\chi$	2.37	2.34	2.31	2.33
[min–max]	2.20–2.47	2.27–2.71	2.16–2.53	2.22–2.59
$A \text{ (}\mu\text{W m}^{-3}\text{)}$				
$\mu$	1.08		0.53	
$\alpha$	0.59		0.41	
$\chi$	1.16		0.44	
[min–max]	0.21–1.99		0.16–1.14	

$\lambda$ —thermal conductivity,  $\rho c$ —volumetric heat capacity,  $A$ —radiogenic heat production,  $\mu$ —arithmetic mean,  $\sigma$ —population standard deviation,  $\chi$ —median, min and max—minimum and maximum values, respectively.

The thermal conductivity analysis of both paragneiss and diorite samples evaluated at dry conditions within the temperature range of 20 to 160 °C reveal a decrease between 18% to 40% as a function of temperature for the paragneiss samples (Table 4), while for the diorite samples the decrease is 34% to 52% (Table 5). The effect of pressure on thermal conductivity indirectly inferred (Equation (2)) reveal an increase of 3% to 15% for the paragneiss samples (Table 4) and 2% to 5% for the diorite samples (Table 5). The experimental coefficient  $b$  (Equation (1)) is found to range between 0.0003 and 0.002 for the paragneiss samples and between 0.0011 and 0.0051 for the diorite. The coefficient  $d$  (Equation (2)) varies within 0.02 and 0.20 and between 0.02 and 0.09 for the paragneiss and diorite samples, respectively.

**Table 4.** Thermal conductivity of the paragneiss samples as a function of temperature and pressure.

Paragneiss								
$\lambda(\text{W m}^{-1} \text{K}^{-1})$								
$T$ (°C)	20	40	60	80	100	120	140	160
$\mu$	2.32	2.28	2.22	2.11	2.05	1.95	1.88	1.63
$\alpha$	0.63	0.63	0.66	0.66	0.76	0.72	0.71	0.63
$\chi$	2.20	2.12	2.00	1.84	1.70	1.59	1.49	1.32
[min-max]	1.69–3.21	1.67–3.20	1.66–3.22	1.58–3.13	1.49–3.30	1.40–3.13	1.33–3.05	1.10–2.63
$\lambda(\text{W m}^{-1} \text{K}^{-1})$								
$P$ (MPa)	2.8	4.8	6.2	10.3	20.7	34.5	48.3	
$\mu$	2.32	2.32	2.33	2.34	2.40	2.43	2.44	
$\chi$	2.15	2.16	2.17	2.19	2.22	2.25	2.26	
[min-max]	1.64–3.32	1.64–3.43	1.65–3.53	1.66–3.67	1.67–3.79	1.70–3.86	1.68–3.92	

$\lambda$ —thermal conductivity,  $T$ —temperature,  $P$ —pressure,  $\mu$ —arithmetic mean,  $\sigma$ —population standard deviation,  $\chi$ —median, min and max—minimum and maximum values, respectively.

**Table 5.** Thermal conductivity of the diorite samples as a function of temperature and pressure.

Paragneiss								
$\lambda(\text{W m}^{-1} \text{K}^{-1})$								
$T$ (°C)	20	40	60	80	100	120	140	160
$\mu$	2.39	2.33	2.25	2.10	1.96	1.86	1.78	1.49
$\alpha$	0.87	0.83	0.81	0.78	0.80	0.77	0.76	0.68
$\chi$	2.58	2.57	2.53	2.36	2.24	2.12	2.02	1.70
[min-max]	1.41–3.73	1.39–3.60	1.30–3.42	1.18–3.16	1.01–2.91	0.94–2.75	0.87–2.67	0.68–2.33
$\lambda(\text{W m}^{-1} \text{K}^{-1})$								
$P$ (MPa)	2.8	4.8	6.2	10.3	20.7	34.5	48.3	
$\mu$	2.83	2.86	2.87	2.90	2.94	2.96	2.98	
$\chi$	2.65	2.67	2.68	2.71	2.75	2.76	2.78	
[min-max]	2.13–4.10	2.14–4.11	2.15–4.12	2.16–4.16	2.17–4.23	2.17–4.29	2.18–4.33	

$\lambda$ —thermal conductivity,  $T$ —temperature,  $P$ —pressure,  $\mu$ —arithmetic mean,  $\sigma$ —population standard deviation,  $\chi$ —median, min and max—minimum and maximum values, respectively.

#### 4.2. 2D Subsurface Temperature Distribution

Sensitivity analyses were carried out to assess the influence of GSTH and conditions of the thermophysical properties (dry and water-saturated state) on the subsurface temperature distribution. The statistical distribution of the thermophysical properties was taken into account to run these simulations. Moreover, the effect of pressure and temperature on thermal conductivity was implemented in the models. A deterministic approach was followed, and the minimum subsurface temperature was obtained by combining the maximum value evaluated for thermal conductivity with the maximum value of volumetric heat capacity and radiogenic heat production. The maximum temperature was obtained by using the inverse combination.

#### 4.2.1. Influence of Model Mesh

A mesh-dependency study was carried out to guarantee the reliability of the results. The free-triangular mesh was gradually refined until a constant temperature at a given point ( $x, z$ ) in the model was obtained. This study started with an extremely coarse mesh (22 elements) until a constant temperature at (17,999, −4999.5) was reached for an extremely fine mesh with 8544 elements. However, a mesh with 13,725 elements was used instead to guarantee the correct distribution of the elements throughout the geometry (Table 6). The maximum and minimum element size was set as 250 and 0.5 m, respectively, with a maximum element growth of 1.1 and resolution of 1 in narrow regions.

**Table 6.** Verification of the mesh independence.

Number of Elements	$T$ (17,999, −4999.5) (°C)	Relative Difference (%)
22	98.71	-
289	98.56	−0.15
758	98.52	−0.04
2223	98.53	0.01
8544	98.55	0.02
9750	98.55	0
13,725	98.55	0

#### 4.2.2. Influence of GSTH

The following temperature simulations were run considering the samples at dry state. The comparison between dry and water saturation conditions is discussed in the next section. The different scenarios for the Laurentide Ice Sheet basal temperature (Table 1) reveal a minimal influence on the subsurface temperature distribution at the base of the model. The difference between the warm and the cold scenarios is up to 1% (Figure 4; Table 7). In the first kilometers, however, the difference is about 80% for the minimum temperature simulated and 14% for the maximum (Figure 4, Table 7). The climate scenarios reveal no influence on the median temperature simulated (Figure 4, Table 7). The uncertainty of the subsurface temperature due to the heterogeneous character of the lithological units is 78% (Figure 4, Table 7). This corresponds to the difference between the maximum and minimum simulated temperatures.

**Table 7.** Subsurface temperature distribution as a function of the GSTH. The reader is referred to Table 1 for further information on the climate scenarios.

Depth (km)	$T_{\min}$ (°C)		$T_{\text{median}}$ (°C)		$T_{\max}$ (°C)	
	Cold	Warm	Cold	Warm	Cold	Warm
0–1	1	5	13	13	19	22
1–2	10	15	38	38	62	65
2–3	20	24	63	63	105	107
3–4	30	33	88	88	148	150
4–5	39	42	113	113	191	193
5–6	49	52	137	137	234	235
6–7	59	61	162	162	277	278
7–8	68	70	187	187	320	321
8–9	78	79	212	212	363	363
9–10	88	89	237	237	406	406

$T$ —temperature, min—minimum, max—maximum. Minimum, median, and maximum refer to the values evaluated for the temperature considering varying thermophysical properties in each climate scenario.

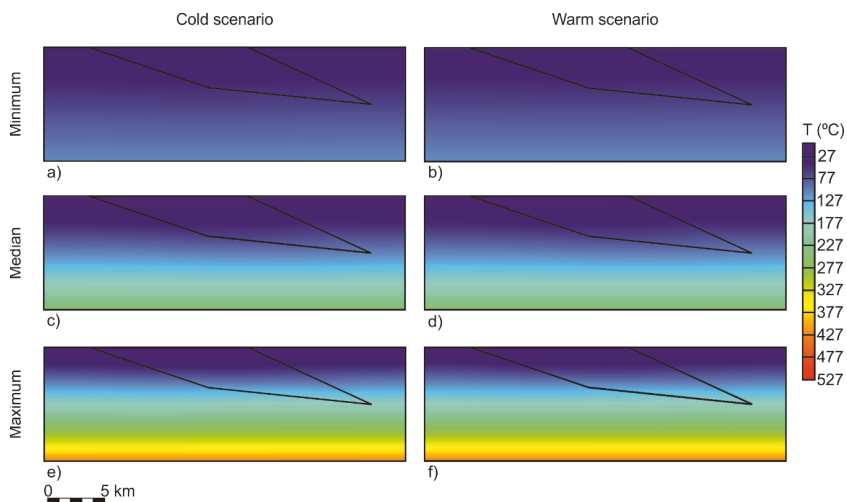


**Figure 4.** 2D subsurface temperature distribution: (a) minimum temperature considering the cold scenario; (b) minimum temperature considering the warm scenario; (c) median temperature considering the cold scenario; (d) median temperature considering the warm scenario; (e) maximum temperature considering the cold scenario; (f) maximum temperature considering the warm scenario. The reader is referred to Table 1 for further information on the climate scenarios. Minimum, median, and maximum refer to the values evaluated for the temperature considering varying thermophysical properties in each climate scenario.

### 4.2.3. Influence of Thermophysical Properties Conditions

The warm climate scenario was chosen to run the following temperature simulations since it revealed the best match between measured and simulated temperature profiles when evaluating the basal heat flux [74]. The water saturation of the thermophysical properties leads to a decrease of the simulated temperature in the minimum and median scenarios (on average, 17–10%, respectively; Figure 5, Table 8). Per contra, the maximum temperature scenario reveals an average increase of 10% (Figure 5, Table 8). The difference between the maximum and minimum temperature is, on average, 78% for the simulations at dry conditions. This difference increases to 84% in the simulations considering water saturation.

**Table 8.** Subsurface temperature distribution as a function of the thermophysical properties conditions.

Depth (km)	$T_{min}$ (°C)		$T_{median}$ (°C)		$T_{max}$ (°C)	
	Dry	Wet	Dry	Wet	Dry	Wet
0–1	5	5	13	12	22	25
1–2	15	12	38	34	65	72
2–3	24	20	63	57	107	120
3–4	33	28	88	79	150	167
4–5	42	36	113	102	193	215
5–6	52	43	137	124	235	262
6–7	61	51	162	147	278	310
7–8	70	59	187	169	321	358
8–9	79	67	212	191	363	405
9–10	89	74	237	214	406	453

T—temperature, min—minimum, max—maximum. Dry and wet conditions refer to the state at which the thermophysical properties were evaluated. Minimum, median, and maximum refer to the values evaluated for the temperature considering varying thermophysical properties.

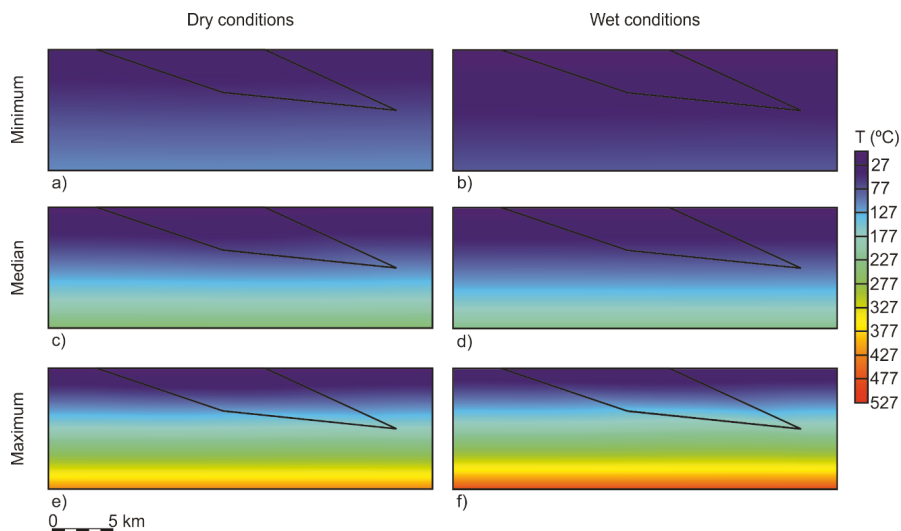


**Figure 5.** 2D subsurface temperature distribution: (a) minimum temperature considering the thermophysical properties at dry conditions; (b) minimum temperature considering the thermophysical properties at water saturation conditions; (c) median temperature considering the thermophysical properties at dry conditions; (d) median temperature considering the thermophysical properties at water saturation conditions; (e) maximum temperature considering the thermophysical properties at dry conditions; (f) maximum temperature considering the thermophysical properties at water saturation conditions. Dry and wet conditions refer to the state at which the thermophysical properties were evaluated. Minimum, median, and maximum refer to the values evaluated for the temperature considering varying thermophysical properties.

#### 4.3. Geothermal Energy Source and Potential Heat and Power Output

The geothermal energy source and potential output are examined in two different sections considering the envisioned applications. Results obtained for heat production are first described, followed by electricity generation. Two key questions are answered in both sections:

1. Which geological and technical uncertainties are the most influential input parameters?
2. Can the deep geothermal energy source meet the heat/power demand in Kuujuaq?

##### 4.3.1. Heat Production

The depth of 1 km was excluded from the following analyses since the 2D subsurface temperature models revealed lower reservoir temperature than the defined reservoir abandonment temperature (30–50 °C; Tables 7 and 8).

Sensitivity analyses were carried out to infer the consistency of the input-output relationship and to compare the relative importance of the input parameters, and thus answering the first aforementioned key question. The Spearman correlation coefficient was evaluated to obtain a qualitative measure of the effect of the uncertain parameters in the potential heat output. A strong positive or negative correlation (i.e., high correlation coefficient) indicates high influence of the input parameter in the output. Per contra, a weak correlation (i.e., low correlation coefficient) suggests a minor influence. The results reveal that volumetric heat capacity and GPP factor have a very weak correlation with the potential heat output, regardless the depth, GSTH, and conditions of the thermophysical properties. The obtained Spearman coefficients range between −5% and 1% for the GPP factor and −1% and 11% for the volumetric heat capacity. The project lifetime and reservoir abandonment temperature are

weakly to moderately correlated with the potential heat output. The former has correlation coefficients ranging between  $-1\%$  at 2 km depth and  $-27\%$  at 10 km depth. The correlation coefficients of the latter vary from  $-44\%$  at 2 km depth to  $-4\%$  at 10 km depth. The recovery factor and reservoir temperature reveal a moderate to very strong correlation with the potential heat output. The reservoir temperature has correlation coefficients varying between 82% and 48% as a function of depth, while for the recovery factor the coefficients increase with depth from 42% to 80%.

Therefore, due to their low correlation coefficients, any change in the GPP factor and volumetric heat capacity will have a minimal influence on the potential heat output (Figure 6). At 2 km depth, the potential heat output is sensitive to the reservoir abandonment temperature, but this variable loses importance as a function of depth (Figure 6). The significance of the project lifetime increases with depth (Figure 6). Nonetheless, reservoir temperature and recovery factor are clearly the most influential input parameters, regardless of the depth, GSTH, and conditions of the thermophysical properties (Figure 6). The results indicate a switch of rank between reservoir temperature and recovery factor (Figure 6) with the increase of the minimum reservoir temperature when reaching values above the minimum reservoir abandonment temperature ( $30\text{ }^{\circ}\text{C}$ ).

Moreover, the results highlight that decreasing the reservoir abandonment temperature and the project lifetime and increasing the recovery factor lead to an increase in the potential heat output.

The probabilistic approach together with the following assumptions helps to answer the second key question: “Can the deep geothermal energy source meet the heating demand in Kuujuaq?”:

- The average annual heating need is approximately 71 MWh per residential dwelling in Kuujuaq [31]
- The total number of dwellings is 518 [77]

Thus, this corresponds to an average annual heat consumption of about 37,000 MWh (or, 37 GWh). This value was used as the threshold to assess the probability of the geothermal energy source to meet the community’s estimated heating demand (Figure 7). It is convenient to highlight, however, that this approach neglected peak loads as an auxiliary system is more likely to be used to supply heat during peak conditions.

The probability of meeting the estimated heating demand is higher than 98% at a depth of 4 km and below, considering the current geological and technical uncertain parameters along with their distribution span and regardless of the GSTH and conditions of the thermophysical properties (Figure 7d–i). At 2 km depth, the probability of meeting the heating demand ranges from 24.8%, for the cold GSTH, to 33.0%, for the water saturation scenario (Figure 7a). The geothermal energy source at 2 km depth will fulfill the community’s needs only if the reservoir temperature is above its 65th–70th percentile and the reservoir abandonment temperature is decreased to values below its 15th–30th percentile (Figure 8). Although the probability of meeting the heating demand at 3 km depth is 80.5% to 83.7% (Figure 7b), the reservoir temperature is required to be higher than its 15th percentile and the recovery factor cannot be lower than the minimum value defined (2%; Figure 8). At 4 km and below, the heating needs are met if the uncertain parameters (mainly reservoir temperature and recovery factor) are within the defined distribution spans (Figure 8).

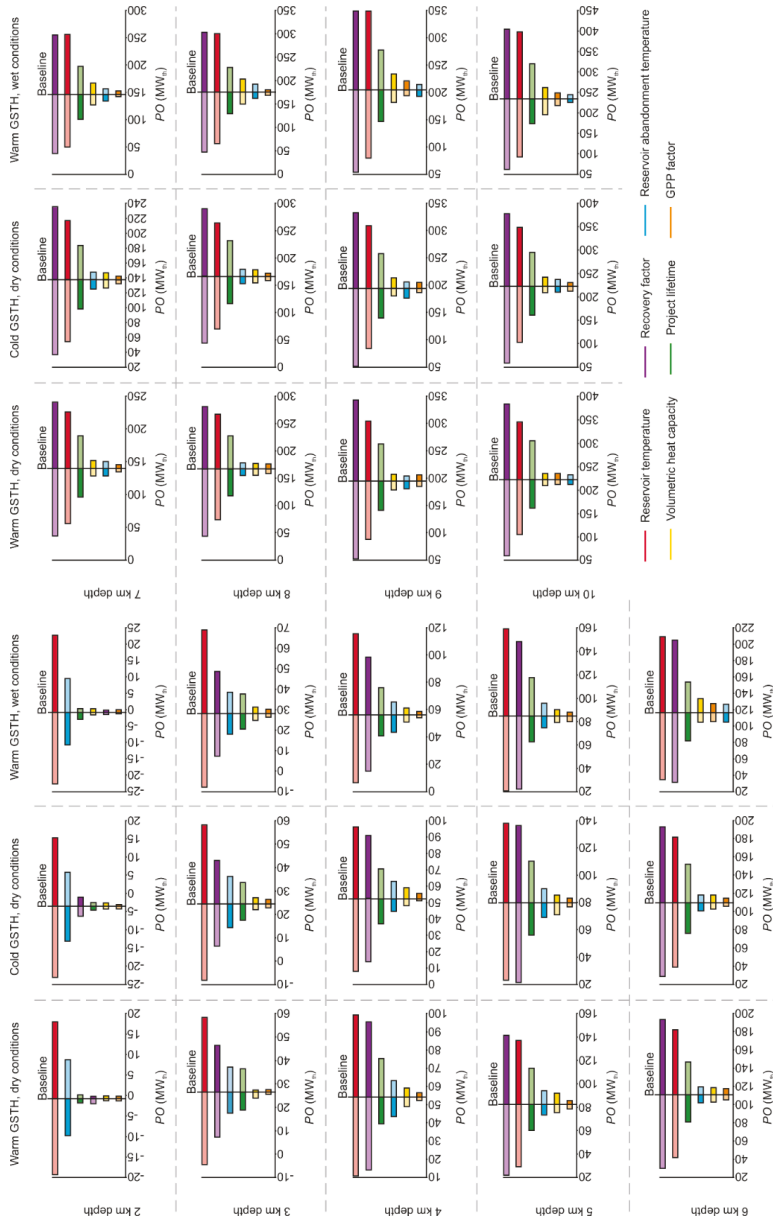


**Figure 6.** Input parameters ranked according to their influence on the geothermal energy source and potential heat output. The reader is referred to Table 1 for further information on the climate scenarios. Dry and wet conditions refer to the state at which the thermophysical properties were evaluated. Baseline—overall simulated mean value; solid color—positive impact on the output; transparency—negative impact on the output. The reader is referred to the online version of the manuscript for further information on the colors.

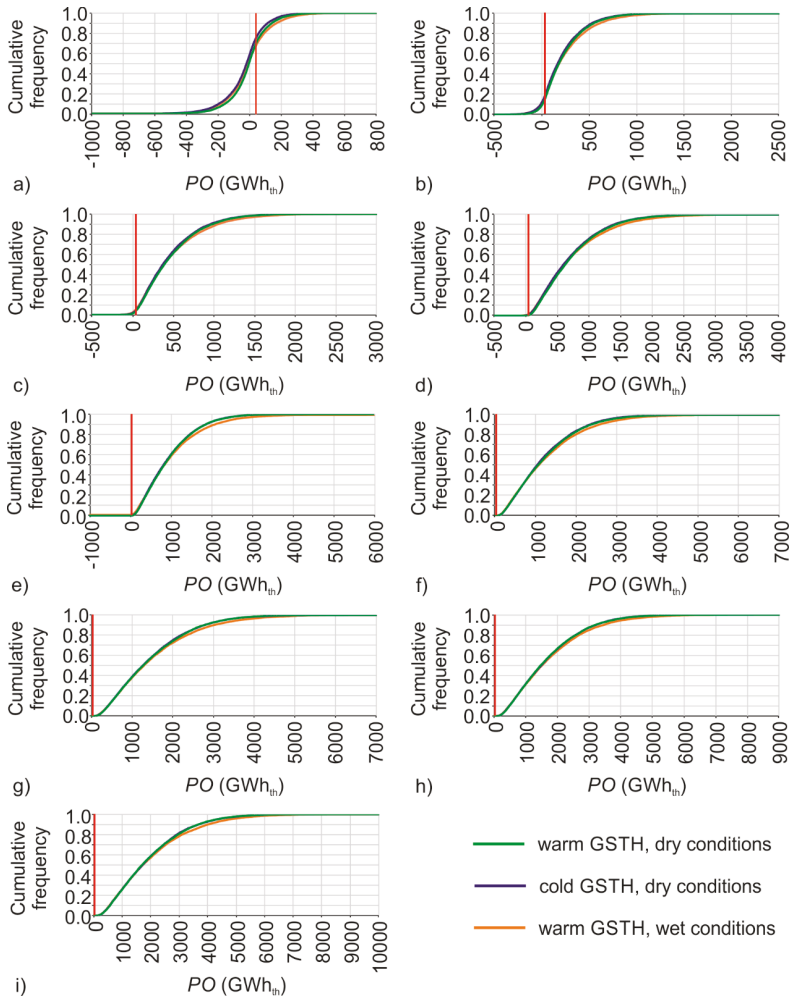


**Figure 7.** Annual geothermal heat output potential and probability of meeting the community’s annual average heating demand: (a) 2 km depth; (b) 3 km depth; (c) 4 km depth; (d) 5 km depth; (e) 6 km depth; (f) 7 km depth; (g) 8 km depth; (h) 9 km depth and (i) 10 km depth. Red line—community’s estimated heating demand (see text for further details). The reader is referred to Table 1 for further information on the climate scenarios. Dry and wet conditions refer to the state at which the thermophysical properties were evaluated. The reader is referred to the online version of the manuscript for further information on the colors.

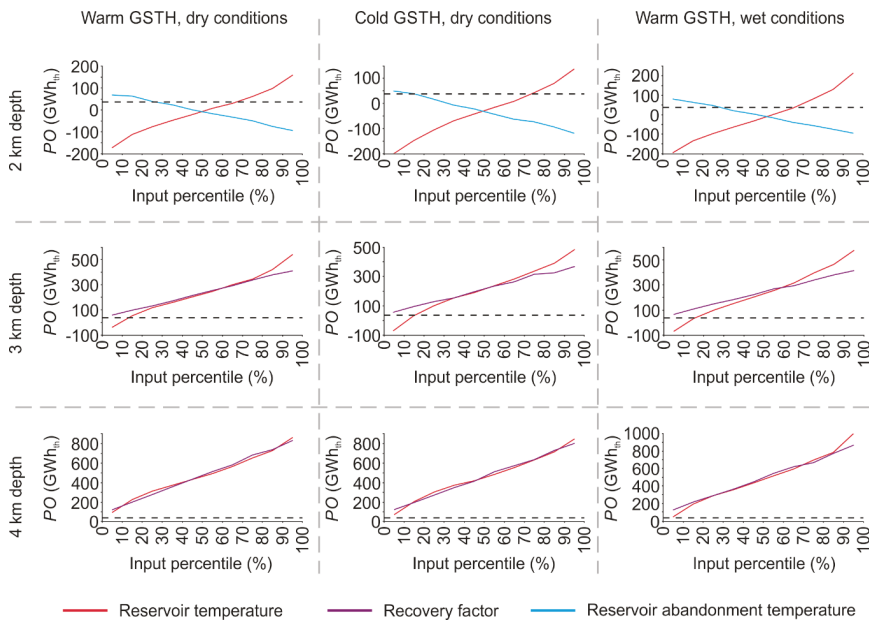


**Figure 8.** Annual geothermal heat output potential as a function of the uncertain parameters’ percentile. Dashed line—community’s estimated heating demand (see text for further details). The reader is referred to Table 1 for further information on the climate scenarios. Dry and wet conditions refer to the state at which the thermophysical properties were evaluated. The reader is referred to the online version of the manuscript for further information on the colors.

#### 4.3.2. Electricity Generation

The following analysis was made at a depth of 5 km and below since the 2D subsurface temperature models revealed lower reservoir temperature than the reservoir abandonment temperature defined for electricity generation (120–140 °C; Tables 7 and 8). Moreover, although the maximum temperature simulated at 4 km is higher than 120 °C (Tables 7 and 8), the potential power output predominantly falls within the negative values leading to biased results.

Similarly to heat production, the Spearman correlation coefficient was also inferred in this section to qualitatively evaluate the input-output relationship. Higher positive/negative correlation coefficient implies more consistency in the relationship than lower coefficient. The relative importance of the input parameters was likewise illustrated with tornado charts.

The results reveal that volumetric heat capacity and GPP factor have a very weak correlation, with the potential power output, regardless the depth, GSTH, and conditions of the thermophysical properties. The correlation coefficients vary within −2% and 2% for the GPP factor and −2% and 5% for the volumetric heat capacity. Hence, the influence of these uncertainties is minimal (Figure 9). The project lifetime has a weak negative correlation with the potential power output ranging between 8% and −16%. The significance of this parameter increases as a function of depth (Figure 9). The reservoir abandonment temperature is negatively weakly correlated to the potential power output, with coefficients varying between −20% and −5%, losing importance as a function of depth (Figure 9). The recovery factor is moderately correlated with the potential power output. The Spearman coefficient ranges between −26% and 48%. This uncertain parameter becomes more influential as a function of depth (Figure 9). Lastly, the reservoir temperature has a moderate to very strong correlation with the potential power output, with coefficients ranging within 37% and 94% and is clearly the most influential parameter for the electricity generation potential (Figure 9).

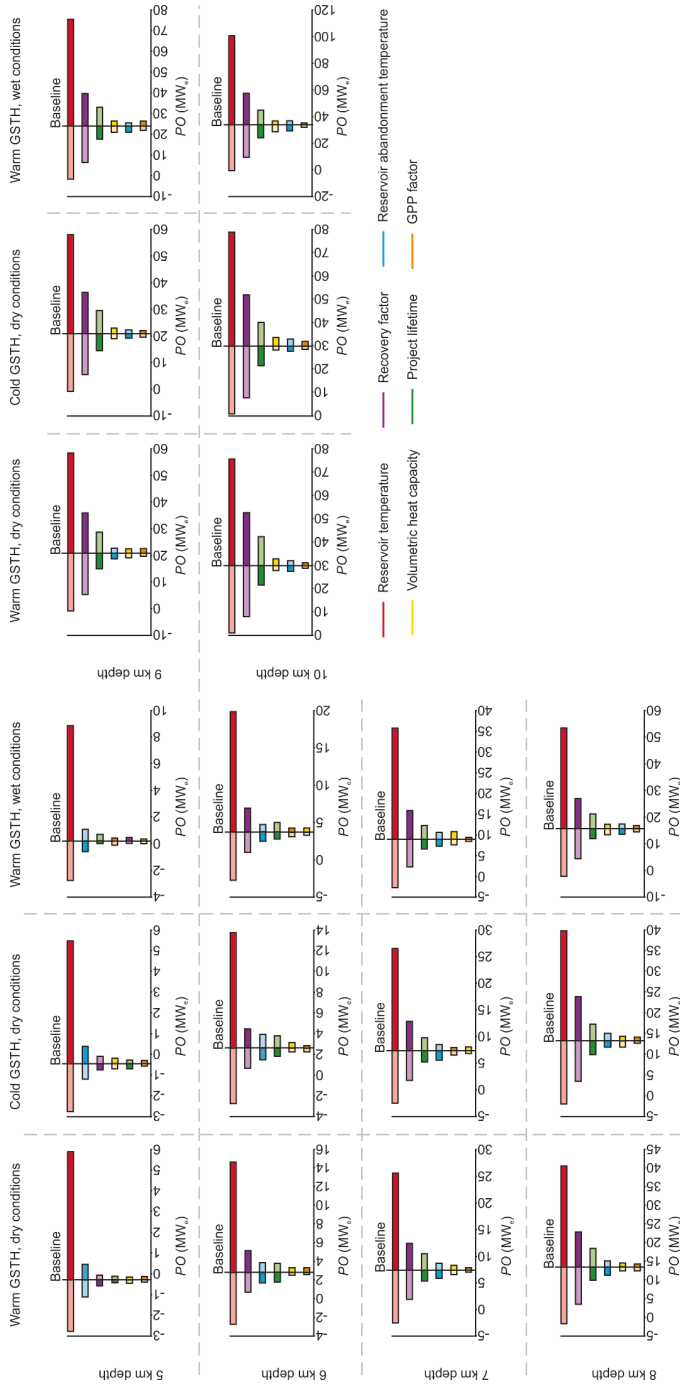


**Figure 9.** Input parameters ranked according to their influence on the geothermal energy source and potential power output. The reader is referred to Table 1 for further information on the climate scenarios. Dry and wet conditions refer to the state at which the thermophysical properties were evaluated. Baseline—overall simulated mean value; solid color—positive impact on the output; transparency—negative impact on the output. The reader is referred to the online version of the manuscript for further information on the colors.

Moreover, the results highlight that decreasing the reservoir abandonment temperature and the project lifetime and increasing the recovery factor leads to an increase in the potential power output.

Combining the probabilistic approach with the following assumptions enables to answer the question: “Can the deep geothermal energy source meet the power demand in Kuujuaq?”:

- In 2011, the electricity consumption in Kuujuaq was 15,100 MWh [80]
- The population in the community of Kuujuaq increased about 14% from 2011 to 2016 [77]

Hence, assuming the same growth rate in terms of electricity needs, this corresponds to the current annual consumption of approximately 18,900 MWh (or, 18.9 GWh). This value was used as the threshold to assess the probability of the geothermal energy source to meet the community’s estimated power needs (Figure 10). It is important to highlight that the electricity produced and consumed in the community of Kuujuaq is only for lighting, electrical household appliances, and other electrical devices in service buildings [81]. The space heating and domestic hot water are provided by oil furnaces [81].

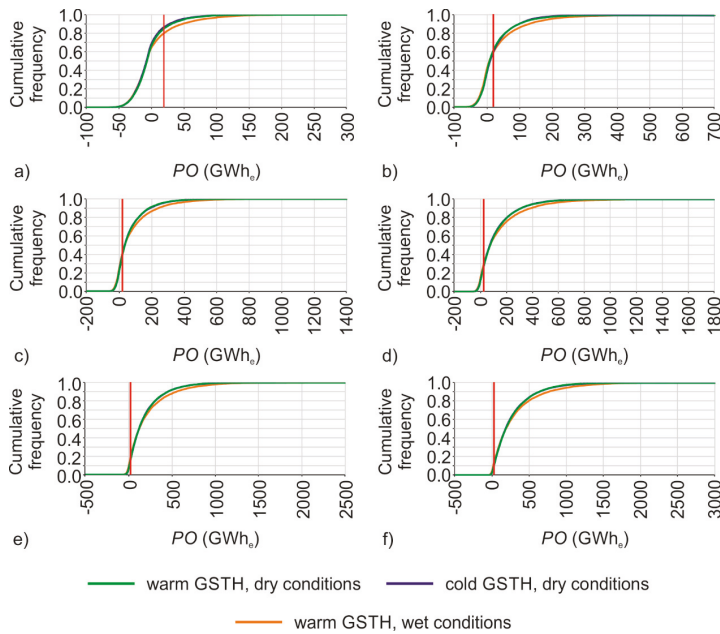


**Figure 10.** Annual geothermal power output potential and probability of meeting the community’s electricity demand: (a) 5 km depth; (b) 6 km depth; (c) 7 km depth; (d) 8 km depth; (e) 9 km depth and (f) 10 km depth. Red line—community’s estimated electricity demand (see text for further details). The reader is referred to Table 1 for further information on climate scenarios. Dry and wet conditions refer to the state at which the thermophysical properties were evaluated. The reader is referred to the online version of the manuscript for further information on the colors.

The probability of meeting the power demand ranges from 13.6% to 20.2% at 5 km depth (Figure 10) and is between 38.4% and 40.8% at 6 km (Figure 10), considering the current geological and technical uncertain parameters and their distribution span. The highest percentage was obtained for the water saturation conditions while the lowest percentage is associated to the cold GSTH. At depths of 7 km and below, the probability of meeting the power demand is higher than 50% but lower than 100% (Figure 10). The probability is 88% to 91.2% at 10 km, depending on the GSTH and the conditions of the thermophysical properties (Figure 10). The lowest value was obtained for the water saturation state while the highest value for the dry conditions.

Moreover, a detailed analysis was carried out indicating that at 5 km depth, the power demand will be met if the reservoir temperature is higher than its 80th percentile, regardless of the GSTH and the conditions of the thermophysical properties (Figure 11). At 6 km, the reservoir temperature must be higher than its 55th percentile, the recovery factor higher than its 40th percentile, and the reservoir abandonment temperature and the project lifetime lower than their 80th percentile (Figure 11). At 7 km, the demand is met if the reservoir temperature is above its 35th percentile (Figure 11). At 8 km, the reservoir temperature needs to be higher than its 20th percentile and at 9 and 10 km, above its 10th percentile (Figure 11). At 7 km and below, the recovery factor is required to be higher than the minimum defined value (2%; Figure 11).

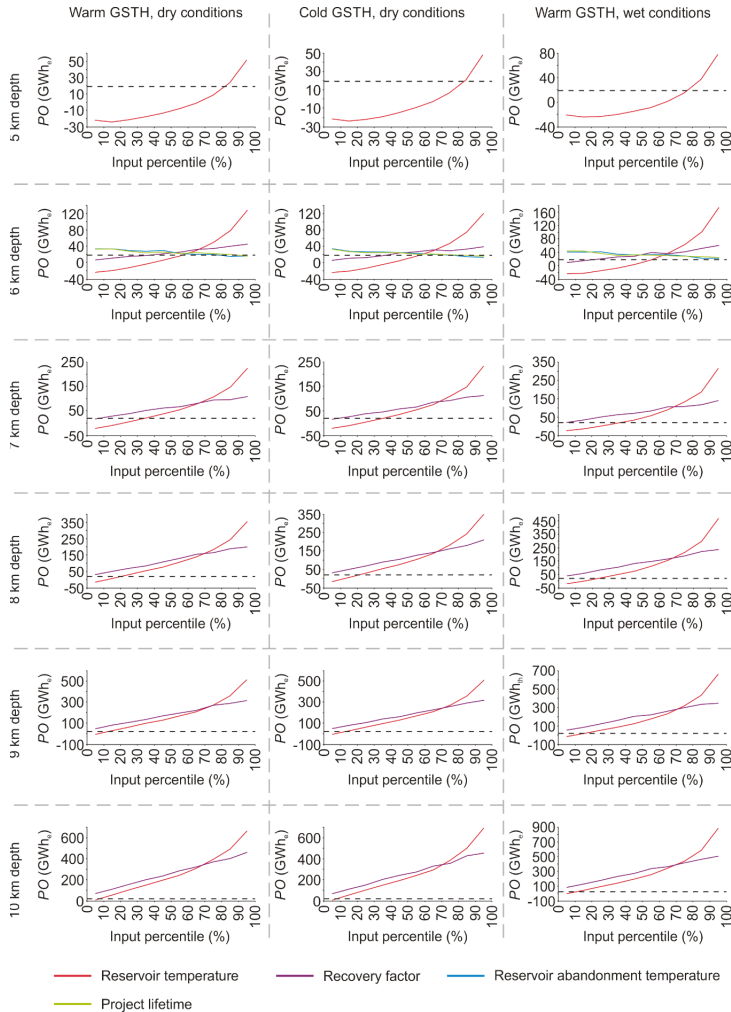


**Figure 11.** Annual geothermal power output potential as a function of the uncertain parameters' percentile. Dashed line—community's estimated power demand (see text for further details). The reader is referred to Table 1 for further information on the climate scenarios. Dry and wet conditions refer to the state at which the thermophysical properties were evaluated. The reader is referred to the online version of the manuscript for further information on the colors.

Cogeneration of heat and electricity, or combined heat and power (CHP), can potentially improve the efficiency of the geothermal energy source. The waste heat from the conversion process can be used for heat supply instead of being discharged to the environment [115–118]. Thus, an analysis was carried out for a depth of 5 km and below to assess if CHP can be an alternative to supply both heat and power.

The results reveal that about 5 to 14 MW<sub>th</sub> are rejected per each MW<sub>e</sub> produced when considering geothermal energy sources in Kuujuaq (Table 9). The waste heat decreases as a function of depth as the cycle thermal efficiency increases as a function of the reservoir temperature. Although 50% to 60% of this waste heat can only be used for other applications [118] as the remaining is utilized by parasitic equipment requirements [116], the annual heat output potential associated to CHP is significant (Table 9). However, the probability of fulfilling the community's annual heating demand is lower than 90% at 5 km depth, decreasing to less than 12% at 10 km depth (Figure 12).

**Table 9.** Waste heat produced per unit electric capacity (MW<sub>th</sub>/MW<sub>e</sub>) and combined heat and power (CHP) heat output potential considering 50% of the waste heat is recovered.

Depth (km)		Waste Heat (MW <sub>th</sub> )			CHP (GWh <sub>th</sub> )		
		Warm GSTH, Dry	Cold GSTH, Dry	Warm GSTH, Wet	Warm GSTH, Dry	Cold GSTH, Dry	Warm GSTH, Wet
5	$\mu$	13	14	14	58	62	62
	$\sigma$	6	7	8	26	32	37
	[min–max]	6–51	6–72	6–93	28–222	28–317	25–406
6	$\mu$	10	11	11	46	47	48
	$\sigma$	4	5	6	19	21	25
	[min–max]	5–39	5–42	5–58	22–169	23–185	20–254
7	$\mu$	8	9	9	37	38	38
	$\sigma$	3	4	4	15	16	19
	[min–max]	4–29	4–31	4–39	19–126	19–134	17–172
8	$\mu$	7	7	7	31	32	32
	$\sigma$	3	3	3	12	13	15
	[min–max]	4–23	4–24	3–30	16–102	16–106	14–132
9	$\mu$	6	6	6	27	27	28
	$\sigma$	2	2	3	10	10	13
	[min–max]	3–19	3–20	3–25	14–85	14–87	12–108
10	$\mu$	5	5	6	24	24	24
	$\sigma$	2	2	2	9	9	11
	[min–max]	3–17	3–16	3–21	12–72	12–72	11–91

$\mu$ —arithmetic mean,  $\sigma$ —standard deviation, min—minimum, max—maximum. The reader is referred to Table 1 for further information on the climate scenarios. Dry and wet conditions refer to the state at which the thermophysical properties were evaluated.

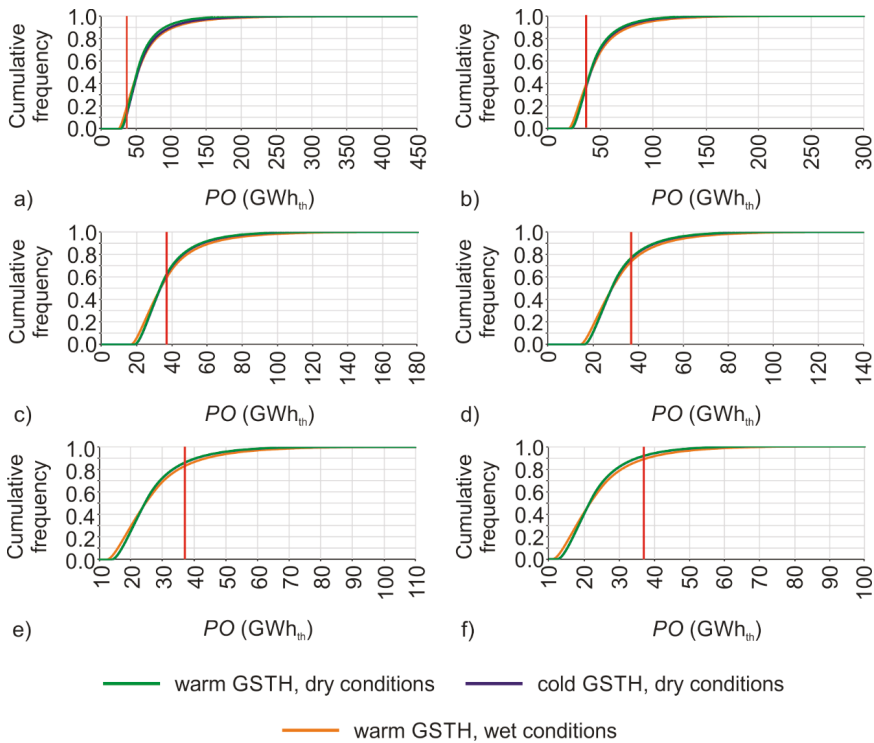


**Figure 12.** Annual CHP heat output potential and probability of meeting the community’s heating demand: (a) 5 km depth; (b) 6 km depth; (c) 7 km depth; (d) 8 km depth; (e) 9 km depth; and (f) 10 km depth. Red line—community’s estimated heating demand (see text for further details). The reader is referred to Table 1 for further information on the climate scenarios. Dry and wet conditions refer to the state at which the thermophysical properties were evaluated. The reader is referred to the online version of the manuscript for further information on the colors.

**5. Discussion**

The exclusive reliance on diesel for electricity, space heating, and domestic hot water is a reality in Canada, not only in Nunavik but also in the remaining 225 communities spread over Northwest Territories, Nunavut, Yukon, and in the northern part of the provinces of British Columbia, Manitoba, Ontario, and Newfoundland and Labrador [3]. These Arctic and subarctic communities are at the front line of climate change and can play a leading role in providing energy solutions to this national and global challenge. The investment in the geothermal energy sector, for instance, can support local and sustainable economic development by creating business opportunities, improve energy security, ensure price stability, and help reducing greenhouse gas emissions [119]. However, there are still significant challenges in remote northern regions that need to be overcome, for example, at the level of the early stage of geothermal research and development. As mentioned in this study, important data gaps exist in remote areas. Deep boreholes suitable for geothermal energy source assessment are limited to areas of interest for oil and gas and mining exploration [2,38], and thus often located away from the communities where the targeted energy customers are. Therefore, there is a growing need to adapt methodologies and define guidelines in the remote northern regions using outcrops treated as subsurface analogs and shallow data for a first-order assessment of the deep geothermal energy source. This is paramount to stimulate interest to finance further developments and help to advance the

stage of exploration, mainly in the Canadian Shield. This geological province has been assumed less favorable for geothermal development when compared to the western sedimentary basins [2,120–122]. However, these previous geothermal energy source assessments have been based on the extrapolation of limited and uneven distributed heat flux data. Thus, this first-order community-scale research targeting deep geothermal energy source based on surface geological information is an important contribution to help advance the stage of geothermal research and development in remote northern regions. The work has been undertaken in the community of Kuujuaq (Nunavik, Canada) as a case study to define guidelines that can be further used in the remaining Canadian remote northern communities.

In the following subsections are discussed the weaknesses and strengths of this work, highlighting not only additional envisioned work and future directions but also data limitations that require further geothermal exploration developments for a more accurate evaluation of the deep geothermal energy source. Moreover, the contribution of this work is discussed in the context of the energy transition of remote northern communities located in unconventional geological settings with respect to geothermal energy, and the advantages of deep geothermal energy are compared with other renewable energy sources.

### 5.1. Thermophysical Properties

In the lack of borehole cores, the thermophysical properties of surficial rocks treated as subsurface analogs are essential for a first-order characterization of the deep geothermal energy source [75] and references therein. Therefore, these properties were evaluated, and the results obtained are in the range of values mentioned in literature for similar lithologies of Canadian Shield rocks (e.g., [38,123–125]). Moreover, the values are in accordance with the mineralogical composition and geochemistry of the rock samples (see Miranda et al. [75] for further details). The obtained decrease of thermal conductivity as a function of temperature (Tables 4 and 5) and its increase as a function of pressure (Tables 4 and 5) and water saturation (Table 3) also agree with other experimental studies (e.g., [126–128]).

### 5.2. 2D Subsurface Temperature Distribution

The subsurface temperature distribution was simulated numerically in COMSOL Multiphysics® with the FEM solving the 2D transient heat conduction equation. The geometry of the conceptual model (Figure 3) is based on a schematic regional cross-section of the Ungava Bay area proposed by Simard et al. [87] and thus simplified. Further geothermal exploration developments, such as drilling of exploratory wells and geophysical campaigns (e.g., borehole logging, magnetotellurics; [129]) will be needed to obtain a more complex subsurface geological model.

Nevertheless, this simplified geological conceptual model is helpful for this first-order assessment of the deep geothermal energy source. Moreover, by imposing a time-varying upper boundary condition, the model is capable to reproduce the variations in the surface temperature caused by the several climate events that have been occurring since late Pleistocene (Table 1; [90–106]). These climate disturbances propagate downwards by thermal diffusion, disrupting the steady-state geothermal gradient and affecting not only the present-day heat flux [89] and references therein but the subsurface temperature as well (as supported by this work; Table 7). The amplitude of the climate events exponentially decay with depth and their signal attenuates [55]. Therefore, at a depth below 5 km, the disturbance caused by the paleoclimate is expected to be in phase with the subsurface temperature, as demonstrated by the analytical solution to correct temperature profiles for the paleoclimate effects [130]. The two GSTH scenarios simulated to address the uncertainty associated with the Laurentide Ice Sheet basal temperature (cold and warm; Table 1) revealed a difference between scenarios up to 80% at the surface, progressively decreasing to 1% at the base of the model (Figure 4, Table 7). Therefore, agreeing with the climate signal attenuation with depth. Moreover, the model also reveals that the effects of the climate events are stronger than the lateral variation of the thermophysical properties. The temperature distribution is laterally uniform throughout the model.

The existent subsurface conditions (dry or water saturation) is an unknown that cannot be readily observed at depth. Therefore, two possible scenarios were simulated and compared to deal with this uncertainty. The difference between them is  $-20$  to  $10\%$  (Figure 5, Table 8), agreeing with Harlé et al. [76] and highlighting that both scenarios shall be considered when evaluating the deep geothermal energy source.

Beyond the uncertainty imposed by the GSTH and subsurface conditions, the aleatory variability associated with the statistical distribution of the bedrock thermophysical properties was also considered. The three-point estimation technique was used to infer the variability of both the heat flux [89] and the thermophysical properties and, therefore, to presume a minimum, median, and maximum scenarios for the subsurface temperature. The associated uncertainty ranges from  $78\%$  to  $84\%$ . Deep temperature profiles will enable to ascertain more accurately the heat flux and, subsequently, the subsurface temperature and more complex geostatistical tools can then be applied for the uncertainty quantification [74,131,132]. Nevertheless, the adopted methodology developed by Marquez et al. [88] and improved by Miranda et al. [89] to infer heat flux from shallow temperature logs (80 m), together with the thermophysical properties of the surficial rock samples, is a valuable tool to carry out a first-order assessment of the deep geothermal potential in remote northern communities.

Finally, the effect of both pressure and temperature on thermal conductivity was implemented in the numerical models. The volumetric heat capacity, however, was assumed independent of temperature and a uniform distribution of the radiogenic heat production as a function of depth was considered. Nevertheless, further developments can be envisioned to account for the effect of temperature on the volumetric heat capacity (e.g., [126]) and the possible exponential decay of heat production with depth [133].

### 5.3. Geothermal Energy Source and Potential Heat and Power Output

In this study, the volume method together with a Monte Carlo-based sensitivity analysis was used to evaluate the deep geothermal energy source. The approach followed considered both current geological and technical uncertainties and evaluated the deep geothermal potential in terms of heat production and electricity and cogeneration at each 1 km depth. Three different scenarios were assumed separately to deal with the uncertainty imposed by the GSTH and the conditions of the thermophysical properties (dry vs. water saturation) on the subsurface temperature. The recovery factor is considered a technical uncertainty in this work rather than a geological one [114] since reservoir active volume and flow rate can be optimized by engineering interventions [35].

A key point in the Monte Carlo method is the correct specification of the distribution functions of the input parameters [74,113], as these determine the output response. A single value was defined for the reservoir volume as the goal of this work was to evaluate the deep geothermal energy source at each 1 km depth and within the land surface area occupied by the community (Figure 2). Reservoir simulation and optimization can help to infer the potential microseismic cloud and thus provide a better constraint for the reservoir volume. The triangular distribution function was chosen for the reservoir temperature in the three studied scenarios since the three-point estimation technique was used to define the worst-case, most likely, and best-case subsurface temperature estimations [113]. The Gaussian (normal) distribution was specified for the volumetric heat capacity based on the results from the laboratory analyses. However, the triangular distribution has been commonly assigned for this thermophysical property (e.g., [70]). Further work can be envisioned to compare the outcomes from both distribution functions and evaluate the associated variability. The technical uncertainties related to reservoir abandonment temperature, recovery factor, and GPP factor were assumed to follow a uniform distribution bounded by common minimum and maximum values mentioned in literature. This choice was based on the assumption that, within the defined limit, each outcome of the random variable has equal probability of occurring. The triangular distribution, however, was specified for the project lifetime, assuming 30 years as the most likely value [35,40,41,49].

The sensitivity of the input parameters in this work was determined through a linear regression-based global sensitivity method, using the Spearman correlation coefficient. Moreover, the input parameters were compared and ranked according to their relative importance. This provides a gross, first-order qualitative assessment of the most influential parameters on the deep geothermal energy source and potential heat and power output. Future directions of this work can be envisioned to quantitatively measure the sensitivity through other linear methods, such as the standardized regression coefficients, or through variance-based methods or regionalized sensitivity analysis [74]. Nevertheless, the qualitative results reveal that reservoir temperature and recovery factor are clearly the most influential parameters, and further geothermal exploration should be focused on decreasing their uncertainty (Figures 6 and 9).

#### 5.4. Deep Geothermal Energy as a Viable Solution to Reduce Fossil Fuels Dependency of Remote Communities

The following criteria, based on Glassley [109], can be used to evaluate if geothermal energy is a viable alternative solution to fossil fuels in remote northern communities:

1. Is the deep geothermal energy source sufficiently abundant to meet the local heat and power demand?
2. Is the deep geothermal energy source cost-competitive compared to fossil fuels?
3. Will the deep geothermal energy source help to reduce or eliminate greenhouse gas emissions?

The ultimate goal of this work is obviously related to the first fundamental question. A probabilistic approach, accounting for the current geological and technical uncertainties, was used for this purpose and the results revealed deep geothermal energy as a promising solution for the community of Kuujuaq, especially for heat production. Moreover, the estimated annual average potential power output at 6 km depth (11 GWh<sub>e</sub>; Figure 10b) is within the range of values inferred by Majorowicz and Grasby [21] for the northwestern sedimentary basins (10–15 GWh).

In the present work, the threshold value used as the community's heating demand did not consider the heat consumed by service buildings (health clinic, shops, hotels, etc.). Only the total residential dwellings (518; [77]) were accounted. Moreover, these were considered as typical 5-occupant household with an annual average heating need of approximately 71 MWh per dwelling [31]. However, 157 of those are single-family houses with an annual average heating demand of about 22 MWh per dwelling [134]. This reduces the estimated annual average consumption from 37 to 29 GWh. In any case, service buildings were left outside from the estimate such that the threshold value represent a fair starting point to evaluate the risk of meeting the heating demand. Thus, the results reveal that, at 4 km depth and below, heat production from deep geothermal energy source is a low-risk application with more than 98% probability of fulfilling the community's heating demand (Figure 7). Moreover, the results show that heat production can be possible at shallower depths of 2 and 3 km if the reservoir temperature is above its 65th–70th percentile and its 15th percentile, respectively (Figure 8). This can help to narrow estimates of a project's capital costs, mainly associated with well drilling. In Nunavut (Canada), a 4 km deep full-size production well can cost approximately \$12 million USD (US dollars), increasing up to \$30 million USD for an 8 km deep well [37].

A reservoir abandonment temperature of 120–140 °C was selected for the electricity generation analysis based on the operational binary cycle GPP of Kamchatka Peninsula (Russia; [60]). However, Organic Rankine Cycle using an optimized working fluid has helped to achieve favorable electricity generation from lower geothermal energy source of about 80 °C [61–64,135]. Although the efficiency of the GPP with such low heat source is lower than 10% [35], this can be advantageous for remote northern regions where deep drilling cost is high (\$12 million USD for a 4-km-well; [37]). Moreover, decreasing the reservoir abandonment temperature leads to an increase in the potential power output. Furthermore, Organic Rankine Cycle has been capable of generating electricity from even lower temperature sources. For example, power generation from waste energy during the process of liquified natural gas regasification was achieved with a source temperature of 100 to 30 °C

(e.g., [136,137]). Thus, Organic Rankine Cycle can be a promising technology for northern regions. However, compared to heat production, electricity generation produced by deep geothermal energy source is a high to medium risk application. The probability of meeting the power needs is low (0.1% at 3 km depth and 94% at 10 km depth), even if the reservoir abandonment temperature is reduced to 80 °C.

Considering the reservoir abandonment temperature threshold of 120–140 °C, the probability of meeting the community's annual power demand is lower than 95% at 10 km depth, with reservoir temperature and recovery factor playing the major roles in constraining the feasibility of such application (Figure 11). A first-order assessment of CHP viability was also undertaken. The waste heat from the power conversion process has low probability to fulfill the community's total heating demand assuming the 37 GWh threshold (Figure 12). However, if this waste heat is only used to provide space heating to half of the residential dwellings, for instance, then the probabilities increase substantially. For example, at 10 km depth, it increases from less than 12% to more than 67%.

Beyond geothermal energy, other alternative solutions to supplant the northern communities' reliance on fossil fuels have been studied. Yan et al. [134] carried out a multi-criteria decision analysis based on the preference ranking organization method for enrichment evaluation method to evaluate the possibility of replacing the traditional heating oil-based systems in Kuujuaq by either natural gas, biomass, or gasification of domestic waste. Their analysis took into account environmental considerations, social improvements, and economic feasibility and concluded that biomass (using wood pellets) is the favored solution. Thompson and Duggirala [138] compared the economic and environmental costs of electricity generation by biomass CHP, wind, and solar with the traditional diesel engine for off-grid Canadian communities. Their results revealed biomass CHP as the most competitive renewable energy technology. However, in both studies, geothermal energy (shallow or deep systems) was not considered. Often, biomass resources need to be transported and stored similarly to fossil fuels, which is a disadvantage compared to local geothermal energy exploitation [134]. Moreover, wind and solar are highly dependent on weather conditions [139]. Ground-coupled heat pumps and underground thermal energy storage can be viable alternative heating solutions [30,31,33]. However, the energy taken from the subsurface with such shallow systems is generally no more than 50% of the heat needed by a building, requiring an auxiliary system to cover the remaining load [31,33]. Deep geothermal energy sources are the only local alternatives to provide base load heat and electricity, as indicated by this study. Nevertheless, it can be more economic to use an auxiliary system in conjunction with a GPP to supply heat during peak conditions. Future activities can be planned to follow Yan et al. [134] or Thompson and Duggirala [138] methodology comparing biomass resources with deep geothermal energy sources to evaluate which renewable technology is economically, socially, and environmentally best suited for the Canadian remote northern communities.

## 6. Conclusions

Geothermal energy source assessment is an iterative process and imperative to forecast future energy production. In this work, a first-order evaluation of the geothermal energy source and potential heat and power output in a remote northern community of Canada was undertaken based on shallow data and outcrops treated as subsurface analogs. Monte Carlo-based sensitivity analyses were carried out to deal with the current geological (both epistemic and aleatory variability) and technical uncertainties. The statistical distribution of the thermophysical properties due to their intrinsic heterogeneous character is an aleatory variability type. The subsurface temperature, the conditions of the thermophysical properties (dry and water saturation), and the climate signal during a glacial period are epistemic uncertainties. The reservoir abandonment temperature, recovery factor, project lifetime, and GPP factor are technical uncertainties. The study was focused on the community of Kuujuaq (Nunavik) to provide an example for the remaining off-grid northern communities relying on an unsustainable energetic framework, where fossil fuels are their main source of energy for electricity and space heating.

Thus, a new and alternative approach to conduct geothermal energy source assessment at the community scale based on surface geological information was presented. The knowledge gained can advance the stage of geothermal exploration to take decision on deep drilling. The uncertainty analysis revealed the parameters that have a major impact on the potential heat and power output and the risk analysis highlighted promising geothermal development despite the outcoming uncertainties. Reservoir temperature and recovery factor are the most influential geological and technical uncertainties on the potential heat and power output. Thus, these parameters need to be accurately assessed. Given the current state of knowledge and the high uncertainty, electricity generation, and hence CHP, is high to medium risk applications with less than 92% probability of fulfilling this community with 2750 inhabitants' needs. Heat production, per contra, is a low-risk application at depths of 4 km and below. The probability of meeting the estimated annual average heating demand of the community of Kuujuaq is higher than 98%, regardless of the GSTH and the conditions of the thermophysical properties.

The results obtained with this study indicate that, although found at a significant depth of at least more than 4 km, the old Canadian Shield beneath the community of Kuujuaq can host significant geothermal energy source for space heating applications. This is especially important for remote northern communities like Kuujuaq since this source of energy appears as the only local alternative that can fulfill their heating needs.

To conclude, it is important to highlight that this analysis was based on shallow data and surficial rock samples treated as subsurface analogs. These are low-cost geothermal exploration tools useful for a first-order assessment of the deep geothermal energy source, as indicated by this study. Nonetheless, the stage of geothermal exploration in remote northern regions needs to advance. Deep exploratory wells are essential and the step missing to accurately infer the deep geothermal energy source and potential heat and power output. Thus, helping remote northern communities to move toward a more sustainable and green energetic future.

**Author Contributions:** Conceptualization, M.M.M., J.R., and C.D.; methodology, M.M.M.; validation, M.M.M.; formal analysis, M.M.M.; investigation, M.M.M.; resources, M.M.M., J.R., and C.D.; data curation, M.M.M.; writing—original draft preparation, M.M.M., J.R., and C.D.; writing—review and editing, M.M.M., J.R., and C.D.; visualization, M.M.M.; supervision, J.R. and C.D.; project administration, J.R.; funding acquisition, J.R. All authors have read and agreed to the published version of the manuscript.

**Funding:** This study was funded by the Institut Nordique du Québec (INQ) through the Chaire de recherche sur le potentiel géothermique du Nord awarded to Jasmin Raymond. The Centre d'études Nordiques (CEN), supported by the Fonds de recherche du Québec—nature et technologies (FRQNT), and the Observatoire Homme Milieu Nunavik (OHMI) are further acknowledged for helping with field campaigns cost and logistics.

**Acknowledgments:** The authors would like to acknowledge Félix-Antoine Comeau, Inès Kanzari, Jean-François Dutil, Sérgio Seco, and Stefane Premont for the support during the analyses of the thermophysical properties. Acknowledges are extended to Erwan Gloaguen for the discussions on global sensitivity analysis and Monte Carlo simulation. The authors are also thankful to the two anonymous reviewers whose recommendations helped to improve the manuscript.

**Conflicts of Interest:** The authors declare no conflict of interest. The funders had no role in the design of the study; in the collection, analyses, or interpretation of data; in the writing of the manuscript; or in the decision to publish the results.

**Notation**

<i>A</i>	Radiogenic heat production	$W m^{-3}$
<i>b, d</i>	Experimental constants	
<i>C</i>	Radioelements concentration	$mg kg^{-1}, \%$
<i>F</i>	Factor	$\%$
<i>f</i>	Function	
<i>H</i>	Thermal energy	J
<i>P</i>	Pressure	Pa
<i>PO</i>	Power output	W
<i>Q</i>	Heat flux	$W m^{-2}$
<i>R</i>	Recovery factor	$\%$
<i>T</i>	Temperature	$^{\circ}C$
<i>t</i>	Time	s
<i>V</i>	Volume	$m^3$
<i>x, z</i>	Spatial variables	m

**Greek letters**

$\eta$	Thermal efficiency	$\%$
$\lambda$	Thermal conductivity	$W m^{-1} K^{-1}$
$\mu$	Arithmetic mean	
$\rho$	Density	$kg m^{-3}$
$\rho c$	Volumetric heat capacity	$J m^{-3} K^{-1}$
$\sigma$	Population standard deviation	

**Subscript**

0	Surface
10	10-km-depth
20	Room temperature
amb	Ambient
dry	Dry conditions
e	Electrical
g	Ground
GPP	Geothermal power plant
K	Potassium
max	Maximum
min	Minimum
res	Reservoir
ref	Reference
Th	Thorium
th	Thermal
U	Uranium
Wet	Water-saturation conditions

**Abbreviations**

ASTM	American Society for Testing and Materials
B.P.	Before present
CHP	Combined heat and power
EGS	Engineered geothermal systems
FEM	Finite element method
GPP	Geothermal power plant
GSTH	Ground surface temperature history
IAEA	International Atomic Energy Agency
ICP-MS	Inductively coupled plasma-mass spectrometry
MIS	Marine Isotope Stage
USD	US dollars
USGS	United States Geological Survey

## References

- IRENA—International Renewable Energy Agency. *Off-Grid Renewable Energy Solutions to Expand Electricity Access: An Opportunity Not to Be Missed*; IRENA: Abu Dhabi, UAE, 2019; 28p.
- Grasby, S.E.; Majorowicz, J.; McCune, G. *Geothermal Energy Potential for Northern Communities*; Open File 7350; Geological Survey of Canada: Calgary, AB, Canada, 2013; 50p. [CrossRef]
- Arriaga, M.; Brooks, M.; Moore, N. Energy access—The Canadian context. In *Waterloo Global Science Initiative's OpenAccess Energy Blueprint*; Rutherford, H., Wright, J., Eds.; WGS: Waterloo, ON, Canada, 2017; pp. 1–6.
- Rise in the Cost of Gasoline. Available online: <https://www.makivik.org/rise-in-the-cost-of-gasoline/> (accessed on 6 July 2020).
- Schallenberg, J. Renewable energies in the Canary Islands: Actual situation and perspectives. In *New and Renewable Technologies for Sustainable Development*; Afgan, N.H., da Graça Carvalho, M., Eds.; Springer: Boston, MA, USA, 2002; pp. 233–246. [CrossRef]
- Kanase-Patil, A.B.; Saini, R.; Sharma, M. Integrated renewable energy systems for off grid rural electrification of remote area. *Renew. Energy* **2010**, *35*, 1342–1349. [CrossRef]
- Palit, D.; Chaurey, A. Off-grid rural electrification experiences from South Asia: Status and best practices. *Energy Sustain. Dev.* **2011**, *15*, 266–276. [CrossRef]
- Chmiel, Z.; Bhattacharyya, S.C. Analysis of off-grid electricity system at Isle of Eigg (Scotland): Lessons for developing countries. *Renew. Energy* **2015**, *81*, 578–588. [CrossRef]
- Bhattacharyya, S.C.; Palit, D. Mini-grid based off-grid electrification to enhance electricity access in developing countries: What policies may be required? *Energy Policy* **2016**, *94*, 166–178. [CrossRef]
- Görgen, M.A. Feasibility Study of Renewable Energy Systems for Off-Grid Islands: A Case Study Concerning Cuttyhunk Island. Master's Thesis, University of Rhode Island, Kingston, RI, USA, 2016. [CrossRef]
- Off-Grid Renewable Energy in Africa. Available online: <https://www.irena.org/-/media/Files/IRENA/Agency/Data-Statistics/Off-grid-renewable-energy-in-Africa.pdf?la=en&hash=0FEC28407B13C1A7AAD58F5AC28E295A4541EEA4> (accessed on 12 August 2020).
- International Bank for Reconstruction and Development/The World Bank. *Reliable and Affordable Off-Grid Electricity Services for the Poor: Lessons from the World Bank Group Experience*; The World Bank: Washington, DC, USA, 2016; 100p.
- Islam, F.M.R.; Mamun, K.A.; Amanullah, M.T.O. (Eds.) *Smart Energy Grid Design for Island Countries: Challenges and Opportunities*; Springer: Cham, Switzerland, 2017; 468p. [CrossRef]
- Wu, Q.; Larsen, E.; Heussen, K.; Binder, H.; Douglass, P. Remote Off-Grid Solutions for Greenland and Denmark: Using smart-grid technologies to ensure secure, reliable energy for island power systems. *IEEE Electr. Mag.* **2017**, *5*, 64–73. [CrossRef]
- Rud, J.N.; Hørmann, M.; Hammervold, V.; Ásmundsson, R.; Georgiev, I.; Dyer, G.; Andersen, S.B.; Jessen, J.E.; Kvorning, P.; Brødsted, M.R. *Energy in the West Nordics and the Arctic: Cases Studies*; TemaNord 2018:539; Nordic Council of Ministers: Copenhagen, Denmark, 2018; 82p.
- Selosse, S.; Garabedian, S.; Ricci, O.; Maizi, N. The renewable energy revolution of reunion island. *Renew. Sustain. Energy Rev.* **2018**, *89*, 99–105. [CrossRef]
- Viteri, J.P.; Henao, F.; Cherni, J.; Dyner, I. Optimizing the insertion of renewable energy in the off-grid regions of Colombia. *J. Clean. Prod.* **2019**, *235*, 535–548. [CrossRef]
- Off-Grid Innovation Improves Thousands of Lives in Rural Peru. Available online: <http://documents1.worldbank.org/curated/en/541211565721769744/pdf/Off-Grid-Innovation-Improves-Thousands-of-Lives-in-Rural-Peru.pdf> (accessed on 29 July 2020).
- Ringkjøb, H.-K.; Haugan, P.M.; Nybø, A. Transitioning remote Arctic settlements to renewable energy systems—A modelling study of Longyearbyen, Svalbard. *Appl. Energy* **2020**, *258*, 114079. [CrossRef]
- Hjartarson, A.; Armannsson, H. Geothermal Research in Greenland. In Proceedings of the World Geothermal Congress, Bali, Indonesia, 25–29 April 2010.
- Majorowicz, J.A.; Grasby, S.E. Geothermal Energy for Northern Canada: Is it Economical? *Nat. Resour. Res.* **2013**, *23*, 159–173. [CrossRef]
- Midttome, K.; Jochmann, M.; Henne, I.; Wangen, M.; Thomas, P.J. Is geothermal energy an alternative for Svalbard? In Proceedings of the 3rd Sustainable Earth Sciences Conference & Exhibition, Celle, Germany, 13–15 October 2015; pp. 1–5. [CrossRef]

23. Eidesgaard, Ó.R.; Schovsbo, N.H.; Boldreel, L.; Ólavsdóttir, J. Shallow geothermal energy system in fractured basalt: A case study from Kollafjørður, Faroe Islands, NE-Atlantic Ocean. *Geothermics* **2019**, *82*, 296–314. [CrossRef]
24. Gascuel, V.; Bédard, K.; Comeau, F.-A.; Raymond, J.; Malo, M. Geothermal resource assessment of remote sedimentary basins with sparse data: Lessons learned from Anticosti Island, Canada. *Geotherm. Energy* **2020**, *8*, 1–32. [CrossRef]
25. Franco, A.; Ponte, C. The role of geothermal in the energy transition in the Azores, Portugal. *Eur. Geol. J.* **2019**, *47*, 21–27.
26. Geothermal Country Overview: The Canary Islands. Available online: <https://www.geoenergymarketing.com/energy-blog/geothermal-country-overview-the-canary-islands/> (accessed on 12 August 2020).
27. Koon, R.K.; Marshall, S.; Morna, D.; McCallum, R.; Ashtine, M. A review of Caribbean geothermal energy resource potential. *West Indian J. Eng.* **2020**, *42*, 37–43.
28. Rajaobelison, M.; Raymond, J.; Malo, M.; Dezayes, C. Classification of geothermal systems in Madagascar. *Geotherm. Energy* **2020**, *8*, 1–26. [CrossRef]
29. Kagel, A.; Bates, D.; Gawell, K. *A Guide to Geothermal Energy and the Environment*; Geothermal Energy Association: Washington, DC, USA, 2005; 88p.
30. Kanzari, I. Évaluation du Potentiel des Pompes à Chaleur Géothermique Pour la Communauté Nordique de Kuujuaq. Master's Thesis, Institut National de la Recherche Scientifique, Quebec, QC, Canada, 2019.
31. Gunawan, E.; Giordano, N.; Jensson, P.; Newson, J.; Raymond, J. Alternative heating systems for northern remote communities: Techno-economic analysis of ground-coupled heat pumps in Kuujuaq, Nunavik, Canada. *Renew. Energy* **2020**, *147*, 1540–1553. [CrossRef]
32. Kinney, C.; Dehghani-Sanij, A.; Mahbaz, S.; Dusseault, M.B.; Nathwani, J.; Fraser, R.A.; Sanij, D. Geothermal Energy for Sustainable Food Production in Canada's Remote Northern Communities. *Energies* **2019**, *12*, 4058. [CrossRef]
33. Giordano, N.; Raymond, J. Alternative and sustainable heat production for drinking water needs in a subarctic climate (Nunavik, Canada): Borehole thermal energy storage to reduce fossil fuel dependency in off-grid communities. *Appl. Energy* **2019**, *252*, 113463. [CrossRef]
34. Mahbaz, S.; Dehghani-Sanij, A.; Dusseault, M.; Nathwani, J. Enhanced and integrated geothermal systems for sustainable development of Canada's northern communities. *Sustain. Energy Technol. Assess.* **2020**, *37*, 100565. [CrossRef]
35. Tester, J.W.; Anderson, B.J.; Batchelor, A.S.; Blackwell, D.D.; DiPippo, R.; Drake, E.M.; Garnish, J.; Livesay, B.; Moore, M.C.; Nichols, K.; et al. *The Future of Geothermal Energy: Impact of Enhanced Geothermal Systems (EGS) on the United States in the 21st Century*; MIT: Idaho Falls, ID, USA, 2006; 372p.
36. DiPippo, R. (Ed.) *Geothermal Power Generation: Developments and Innovation*; Woodhead Publishing: Duxford, UK, 2016; 818p.
37. Minnick, M.; Shewfelt, D.; Hickson, C.; Majorowicz, J.; Rowe, T. *Nunavut Geothermal Feasibility Study*; Topical Report RSI-2828; Qulliq Energy Corporation: Iqaluit, NU, Canada, 2018; 42p.
38. Comeau, F.-A.; Raymond, J.; Malo, M.; Dezayes, C.; Carreau, M. Geothermal potential of Northern Québec: A regional assessment. *GRC Trans.* **2017**, *41*, 1076–1094.
39. UNECE—United Nations Economic Commission for Europe. *Specifications for the Application of the United Nations Framework Classification for Fossil Energy and Mineral Reserves and Resources 2009 (UNFC—2009) to Geothermal Energy Resources*; UNECE: Geneva, Switzerland, 2016; 28p.
40. Beardsmore, G.R.; Rybach, L.; Blackwell, D.; Baron, C. A protocol for estimating and mapping global EGS potential. *GRC Trans.* **2010**, *34*, 301–312.
41. Limberger, J.; Calcagno, P.; Manzella, A.; Trumpy, E.; Boxem, T.; Pluymaekers, M.P.D.; Van Wees, J.-D. Assessing the prospective resource base for enhanced geothermal systems in Europe. *Geotherm. Energy Sci.* **2014**, *2*, 55–71. [CrossRef]
42. Muffler, P.; Cataldi, R. Methods for regional assessment of geothermal resources. *Geothermics* **1978**, *7*, 53–89. [CrossRef]
43. Rybach, L. Classification of geothermal resources by potential. *Geotherm. Energy Sci.* **2015**, *3*, 13–17. [CrossRef]
44. Bolton, R.S. Management of a geothermal field. In *Geothermal Energy—Review and Research and Development*; Armstead, H.C.H., Ed.; UNESCO: Paris, France, 1973; pp. 175–184.

45. White, D.E.; Williams, D.L. *Assessment of Geothermal Resources of the United States—1975*; Circular 726; USGS: Arlington, VA, USA, 1975; 155p.
46. Blackwell, D.D.; Negraru, P.T.; Richards, M.C. Assessment of the Enhanced Geothermal System Resource Base of the United States. *Nat. Resour. Res.* **2007**, *15*, 283–308. [[CrossRef](#)]
47. Tester, J.W.; Anderson, B.J.; Batchelor, A.S.; Blackwell, D.D.; DiPippo, R.; Drake, E.M.; Garnish, J.; Livesay, B.; Moore, M.C.; Nichols, K.; et al. Impact of enhanced geothermal systems on US energy supply in the twenty-first century. *Philos. Trans. R. Soc. A Math. Phys. Eng. Sci.* **2007**, *365*, 1057–1094. [[CrossRef](#)]
48. Williams, C.F.; Reed, M.J.; Mariner, R.H. *A Review of Methods Applied by the U.S. Geological Survey in the Assessment of Identified Geothermal Resources*; Open-File Report 2008–1296; USGS: Reston, VA, USA, 2008; 30p.
49. Sarmiento, Z.F.; Steingrímsson, B.; Axelsson, G. Volumetric Resource Assessment. In Proceedings of the Short Course V on Conceptual Modelling of Geothermal Systems, Santa Tecla, El Salvador, 2 February–2 March 2013.
50. Busby, J.; Terrington, R. Assessment of the resource base for engineered geothermal systems in Great Britain. *Geotherm. Energy* **2017**, *5*, 7. [[CrossRef](#)]
51. Agemar, T.; Weber, J.; Moeck, I.S. Assessment and Public Reporting of Geothermal Resources in Germany: Review and Outlook. *Energies* **2018**, *11*, 332. [[CrossRef](#)]
52. Garg, S.K.; Combs, J. A reformulation of USGS volumetric “heat in place” resource estimation method. *Geothermics* **2015**, *55*, 150–158. [[CrossRef](#)]
53. Crowell, J.C. Continental glaciation through geologic times. In *Climate in Earth History: Studies in Geophysics*; National Research Council, Ed.; The National Academies Press: Washington, DC, USA, 1982; pp. 77–82. [[CrossRef](#)]
54. Jessop, A.M. *Thermal Geophysics*; Elsevier: Amsterdam, The Netherlands, 1990; 304p.
55. Beardsmore, G.R.; Cull, J.P. *Crustal Heat Flow: A Guide to Measurement and Modelling*; Cambridge University Press: Cambridge, UK, 2001; 334p.
56. LeMenager, A.; O’Neill, C.; Zhang, S.; Evans, M. The effect of temperature-dependent thermal conductivity on the geothermal structure of the Sydney Basin. *Geotherm. Energy* **2018**, *6*, 6. [[CrossRef](#)]
57. Vélez, M.I.; Blessent, D.; Córdoba, S.; López-Sánchez, J.; Raymond, J.; Parra-Palacio, E. Geothermal potential assessment of the Nevado del Ruiz volcano based on rock thermal conductivity measurements and numerical modeling of heat transfer. *J. South Am. Earth Sci.* **2018**, *81*, 153–164. [[CrossRef](#)]
58. Norden, B.; Förster, A.; Förster, H.-J.; Fuchs, S. Temperature and pressure corrections applied to rock thermal conductivity: Impact on subsurface temperature prognosis and heat-flow determination in geothermal exploration. *Geotherm. Energy* **2020**, *8*, 1–19. [[CrossRef](#)]
59. Lindal, B. Industrial and other application of geothermal energy. In *Geothermal Energy*; Armstead, H.C.H., Ed.; UNESCO: Paris, France, 1973; pp. 135–148.
60. Tomarov, G.V.; Shipkov, A.A. Modern geothermal power: Binary cycle geothermal power plants. *Therm. Eng.* **2017**, *64*, 243–250. [[CrossRef](#)]
61. Liu, X.; Wei, M.; Yang, L.; Wang, X. Thermo-economic analysis and optimization selection of ORC system configurations for low temperature binary-cycle geothermal plant. *Appl. Therm. Eng.* **2017**, *125*, 153–164. [[CrossRef](#)]
62. Tillmanns, D.; Gertig, C.; Schilling, J.; Gibelhaus, A.; Bau, U.; Lanzerath, F.; Bardow, A. Integrated design of ORC process and working fluid using PC-SAFT and Modelica. *Energy Procedia* **2017**, *129*, 97–104. [[CrossRef](#)]
63. Shi, W.; Pan, L. Optimization Study on Fluids for the Gravity-Driven Organic Power Cycle. *Energies* **2019**, *12*, 732. [[CrossRef](#)]
64. Chagnon-Lessard, N.; Mathieu-Potvin, F.; Gosselin, L. Optimal design of geothermal power plants: A comparison of single-pressure and dual-pressure organic Rankine cycles. *Geothermics* **2020**, *86*, 101787. [[CrossRef](#)]
65. Bodvarsson, G. Report on the Hengil geothermal area. *J. Engrs. Assn. Icel.* **1951**, *36*, 1.
66. Bodvarsson, G.S.; Tsang, C.F. Injection and Thermal Breakthrough in Fractured Geothermal Reservoirs. *J. Geophys. Res. Space Phys.* **1982**, *87*, 1031–1048. [[CrossRef](#)]
67. Williams, C.F. Updated Methods for Estimating Recovery Factors for Geothermal Resources. In Proceedings of the 32nd Workshop on Geothermal Reservoir Engineering, Stanford, CA, USA, 22–24 January 2007.
68. Williams, C.F. Evaluating the volume method in the assessment of identified geothermal resources. *GRC Trans.* **2014**, *38*, 967–974.

69. Sanyal, S.K.; Butler, S.J. An Analysis of Power Generation Prospects from Enhanced Geothermal Systems. In Proceedings of the World Geothermal Congress 2005, Antalya, Turkey, 24–29 April 2005.
70. Sarmineto, Z.F.; Steingrímsson, B. Computer Programme for Resource Assessment and Risk Evaluation Using Monte Carlo Simulation. In Proceedings of the Short Course on Geothermal Project Management and Development, Entebbe, Uganda, 20–22 November 2008.
71. Rubinstein, R.Y.; Kroese, D.P. *Simulation and the Monte Carlo Method*; John Wiley & Sons, Inc.: Hoboken, NJ, USA, 2008; 377p.
72. Graham, C.; Talay, D. *Stochastic Simulation and Monte Carlo Methods: Mathematical Foundations of Stochastic Simulation*; Springer: Berlin, Germany, 2013; 264p.
73. Thomopoulos, N.T. *Essentials of Monte Carlo Simulation: Statistical Methods for Building Simulation Models*; Springer: New York, NY, USA, 2013; 183p.
74. Scheidt, C.; Li, L.; Caers, J. (Eds.) *Quantifying Uncertainty in Subsurface Systems*; AGU and Wiley: Washington, DC, USA; Hoboken, NJ, USA, 2018; 281p.
75. Miranda, M.M.; Giordano, N.; Raymond, J.; Pereira, A.; Dezayes, C. Thermophysical properties of surficial rocks: A tool to characterize geothermal resources of remote northern regions. *Geotherm. Energy* **2020**, *8*, 1–27. [CrossRef]
76. Harlé, P.; Kushnir, A.R.L.; Aichholzer, C.; Heap, M.J.; Hehn, R.; Maurer, V.; Baud, P.; Richard, A.; Genter, A.; Düringer, P. Heat flow density estimates in the Upper Rhine Graben using laboratory measurements of thermal conductivity on sedimentary rocks. *Geotherm. Energy* **2019**, *7*, 1–36. [CrossRef]
77. Data products, 2016 Census. Available online: [www12.statcan.gc.ca/census-recensement/2016/dp-pd/index-eng.cfm](http://www12.statcan.gc.ca/census-recensement/2016/dp-pd/index-eng.cfm) (accessed on 11 May 2020).
78. Community Maps. Available online: <https://www.krg.ca/en-CA/map/community-maps> (accessed on 11 May 2020).
79. Quebec, H. *Particularités des Réseaux Autonomes*; Hydro-Quebec Distribution; Hydro Quebec: Quebec City, QC, Canada, 2002; 17p.
80. AANDC—Aboriginal Affairs and Northern Development Canada; NRCAN—Natural Resources Canada. *Status of Remote/Off-Grid Communities in Canada*; M154-71/2013E; Government of Canada: Quebec City, QC, Canada, 2011; 44p.
81. Rate DN. Available online: <http://www.hydroquebec.com/residential/customer-space/rates/rate-dn.html> (accessed on 11 May 2020).
82. SIGÉOM—Système D’information Géominière du Québec. Available online: [http://sigeom.mines.gouv.qc.ca/signet/classes/I1108\\_afchCarteIntr](http://sigeom.mines.gouv.qc.ca/signet/classes/I1108_afchCarteIntr) (accessed on 11 May 2020).
83. Ruuska, T.; Vinha, J.; Kivioja, H. Measuring thermal conductivity and specific heat capacity values of inhomogeneous materials with a heat flow meter apparatus. *J. Build. Eng.* **2017**, *9*, 135–141. [CrossRef]
84. Schatz, J.F.; Simmons, G. Thermal conductivity of Earth materials at high temperatures. *J. Geophys. Res. Space Phys.* **1972**, *77*, 6966–6983. [CrossRef]
85. Raymond, J.; Comeau, F.-A.; Malo, M.; Blessent, D.; Sánchez, I.J.L. The Geothermal Open Laboratory: A Free Space to Measure Thermal and Hydraulic Properties of Geological Materials. In Proceedings of the IGCP636 Annual Meeting; Available online: <http://pubs.geothermal-library.org/lib/grc/1032270.pdf> (accessed on 12 August 2020).
86. Rybach, L. Determination of heat production rate. In *Handbook of Terrestrial Heat-Flow Density Determination*; Hänel, R., Rybach, L., Stegena, L., Eds.; Kluwer Academic Publishers: Dordrecht, The Netherlands, 1988; pp. 125–142.
87. Simard, M.; Lafrance, I.; Hammouche, H.; Legoux, C. *Géologie de la Région de Kuujuaq et de la Baie d’Ungava (SRNC 24J, 24K)*; Report No. RG 2013-04; Gouvernement du Québec: Québec City, QC, Canada, 2013; 62p.
88. Márquez, M.I.V.; Raymond, J.; Blessent, D.; Philippe, M.; Velez, M.I. Terrestrial heat flow evaluation from thermal response tests combined with temperature profiling. *Phys. Chem. Earth, Parts A/B/C* **2019**, *113*, 22–30. [CrossRef]
89. Miranda, M.M.; Márquez, M.I.V.; Raymond, J.; Dezayes, C. A numerical approach to infer terrestrial heat flux from shallow temperature profiles in remote northern regions. *Geothermics*. under review.
90. Flint, R.F. *Glacial Geology and the Pleistocene Epoch*; John Wiley & Sons, Inc.: New York, NY, USA, 1947; 616p.
91. Emiliani, C. Pleistocene Temperatures. *J. Geol.* **1955**, *63*, 538–578. [CrossRef]

92. Sass, J.H.; Lachenbruch, A.H.; Jessop, A.M. Uniform heat flow in a deep hole in the Canadian Shield and its paleoclimatic implications. *J. Geophys. Res. Space Phys.* **1971**, *76*, 8586–8596. [CrossRef]
93. Mareschal, J.-C.; Rolandone, F.; Bienfait, G. Heat flow variations in a deep borehole near Sept-Îles, Québec, Canada: Paleoclimatic interpretation and implications for regional heat flow estimates. *Geophys. Res. Lett.* **1999**, *26*, 2049–2052. [CrossRef]
94. Rolandone, F. Temperatures at the base of the Laurentide Ice Sheet inferred from borehole temperature data. *Geophys. Res. Lett.* **2003**, *30*. [CrossRef]
95. Majorowicz, J.A.; Safanda, J. Effect of postglacial warming seen in high precision temperature log deep into the granites in NE Alberta. *Acta Diabetol.* **2014**, *104*, 1563–1571. [CrossRef]
96. Pickler, C.; Beltrami, H.; Mareschal, J.-C. Laurentide Ice Sheet basal temperatures during last glacial cycle as inferred from borehole data. *Clim. Past* **2016**, *12*, 1–13. [CrossRef]
97. Mareschal, J.-C.; Jaupart, C. *Heat Generation and Transport in the Earth*; Cambridge University Press: Cambridge, UK, 2011; 490p.
98. Jessop, A.M. The Distribution of Glacial Perturbation of Heat Flow in Canada. *Can. J. Earth Sci.* **1971**, *8*, 162–166. [CrossRef]
99. Renssen, H.; Seppä, H.; Crosta, X.; Goosse, H.; Roche, D.M. Global characterization of the Holocene Thermal Maximum. *Quat. Sci. Rev.* **2012**, *48*, 7–19. [CrossRef]
100. Gajewski, K. Quantitative reconstruction of Holocene temperatures across the Canadian Arctic and Greenland. *Glob. Planet. Chang.* **2015**, *128*, 14–23. [CrossRef]
101. Richerol, T.; Fréchet, B.; Rochon, A.; Pienitz, R. Holocene climate history of the Nunatsiavut (northern Labrador, Canada) established from pollen and dinoflagellate cyst assemblages covering the past 7000 years. *Holocene* **2015**, *26*, 44–60. [CrossRef]
102. Dahl-Jensen, D.; Mosegaard, K.; Gundestrup, N.; Clow, G.D.; Johnsen, S.J.; Hansen, A.W.; Balling, N. Past Temperatures Directly from the Greenland Ice Sheet. *Science* **1998**, *282*, 268–271. [CrossRef]
103. Kaufman, D.S.; Ager, T.A.; Anderson, N.J.; Anderson, P.M.; Andrews, J.T.; Bartlein, P.J.; Brubaker, L.B.; Coats, L.L.; Cwynar, L.C.; Duvall, M.L.; et al. Holocene thermal maximum in the western Arctic (0–180°W). *Quat. Sci. Rev.* **2004**, *23*, 529–560. [CrossRef]
104. Majorowicz, J.A.; Skinner, W.R.; Safanda, J. Ground Surface Warming History in Northern Canada Inferred from Inversions of Temperature Logs and Comparison with Other Proxy Climate Reconstructions. *Pure Appl. Geophys. PAGEOPH* **2005**, *162*, 109–128. [CrossRef]
105. Chouinard, C.; Fortier, R.; Mareschal, J.-C. Recent climate variations in the subarctic inferred from three borehole temperature profiles in northern Quebec, Canada. *Earth Planet. Sci. Lett.* **2007**, *263*, 355–369. [CrossRef]
106. Historical Climate Data. Available online: <https://climate.weather.gc.ca/> (accessed on 11 May 2020).
107. Ouzzane, M.; Eslami-Nejad, P.; Badache, M.; Aidoun, Z. New correlations for the prediction of the undisturbed ground temperature. *Geothermics* **2015**, *53*, 379–384. [CrossRef]
108. Beck, J.V.; Wolf, H. The nonlinear inverse heat conduction problem. *ASME* **1965**, *65-HT*, 40.
109. Glassley, W.E. *Geothermal Energy: Renewable Energy and the Environment*; CRC Press: Boca Raton, FL, USA, 2010; 410p.
110. @RISK. Available online: <https://www.palisade.com/risk/default.asp> (accessed on 18 June 2020).
111. Mackay, D.J.C. Introduction to Monte Carlo methods. In *Learning in Graphical Models*; Jordan, M.I., Ed.; Kluwer Academic Press: Dordrecht, The Netherlands, 1998; pp. 175–204.
112. Matsumoto, M.; Nishimura, T. Mersenne twister: A 623-dimensionally equidistributed uniform pseudo-random number generator. *ACM Trans. Model. Comput. Simul.* **1998**, *8*, 3–30. [CrossRef]
113. Vose, D. *Risk Analysis: A Quantitative Guide*; John Wiley & Sons, Ltd.: Chichester, UK, 2008; 729p.
114. Witter, J.B.; Trainor-Guitton, W.; Siler, D.L. Uncertainty and risk evaluation during the exploration stage of geothermal development: A review. *Geothermics* **2019**, *78*, 233–242. [CrossRef]
115. Rybach, L.; Kohl, T. Waste heat problems and solutions in geothermal energy. *Geol. Soc. Lond. Spec. Publ.* **2004**, *236*, 369–380. [CrossRef]
116. Lund, J.W.; Chiasson, A. Examples of combined heat and power plants using geothermal energy. In Proceedings of the European Geothermal Congress 2007, Unterhaching, Germany, 30 May–1 June 2007.
117. Saadat, A.; Frick, S.; Kranz, S.; Regenspurg, S. Energetic use of EGS reservoirs. In *Geothermal Energy Systems: Exploration, Development, and Utilization*; Huenges, E., Ed.; Wiley: Potsdam, Germany, 2010; pp. 303–372.

118. Gehringer, M. Use of waste heat from geothermal power plants focusing on improving agriculture in developing countries. *GRC Trans.* **2015**, *39*, 125–132.
119. Geothermal Investment Guide. Available online: <http://www.geoelec.eu/wp-content/uploads/2011/09/D3.4.pdf> (accessed on 12 August 2020).
120. Majorowicz, J.; Grasby, S.E. Heat flow, depth–temperature variations and stored thermal energy for enhanced geothermal systems in Canada. *J. Geophys. Eng.* **2010**, *7*, 232–241. [[CrossRef](#)]
121. Majorowicz, J.A.; Grasby, S.E. High Potential Regions for Enhanced Geothermal Systems in Canada. *Nat. Resour. Res.* **2010**, *19*, 177–188. [[CrossRef](#)]
122. Grasby, S.E.; Allen, D.M.; Bell, S.; Chen, Z.; Ferguson, G.; Jessop, A.; Kelman, M.; Ko, M.; Majorowicz, J.; Moore, M.; et al. *Geothermal Energy Resource Potential of Canada*; Open File 6914; Geological Survey of Canada: Calgary, AB, Canada, 2012; 322p.
123. Rolandone, F.; Jaupart, C.; Mareschal, J.C.; Gariépy, C.; Bienfait, G.; Carbonne, C.; Lapointe, R. Surface heat flow, crustal temperatures and mantle heat flow in the Proterozoic Trans-Hudson Orogen, Canadian Shield. *J. Geophys. Res. Space Phys.* **2002**, *107*, ETG 7-1–ETG 7-19. [[CrossRef](#)]
124. Perry, H.; Jaupart, C.; Mareschal, J.-C.; Bienfait, G. Crustal heat production in the Superior Province, Canadian Shield, and in North America inferred from heat flow data. *J. Geophys. Res. Space Phys.* **2006**, *111*, 1–20. [[CrossRef](#)]
125. Phaneuf, C.; Mareschal, J.-C. Estimating concentrations of heat producing elements in the crust near the Sudbury Neutrino Observatory, Ontario, Canada. *Tectonophysics* **2014**, *622*, 135–144. [[CrossRef](#)]
126. Vosteen, H.-D.; Schellschmidt, R. Influence of temperature on thermal conductivity, thermal capacity and thermal diffusivity for different types of rock. *Phys. Chem. Earth, Parts A/B/C* **2003**, *28*, 499–509. [[CrossRef](#)]
127. Abdulagatov, I.M.; Emirov, S.N.; Abdulagatova, Z.Z.; Askerov, S.Y. Effect of Pressure and Temperature on the Thermal Conductivity of Rocks. *J. Chem. Eng. Data* **2006**, *51*, 22–33. [[CrossRef](#)]
128. Nagaraju, P.; Roy, S. Effect of water saturation on rock thermal conductivity measurements. *Tectonophysics* **2014**, *626*, 137–143. [[CrossRef](#)]
129. Kana, J.D.; Djongyang, N.; Raidandi, D.; Nouck, P.N.; Dadjé, A. A review of geophysical methods for geothermal exploration. *Renew. Sustain. Energy Rev.* **2015**, *44*, 87–95. [[CrossRef](#)]
130. Birch, A.F. The effects of Pleistocene climatic variations upon geothermal gradients. *Am. J. Sci.* **1948**, *246*, 729–760. [[CrossRef](#)]
131. Caers, J. *Modeling Uncertainty in the Earth Sciences*; Wiley-Blackwell: Chichester, UK, 2011; 249p.
132. Athens, N.D.; Caers, J.K. A Monte Carlo-based framework for assessing the value of information and development risk in geothermal exploration. *Appl. Energy* **2019**, *256*, 113932. [[CrossRef](#)]
133. Lachenbruch, A.H. Crustal temperature and heat production: Implications of the linear heat-flow relation. *J. Geophys. Res. Space Phys.* **1970**, *75*, 3291–3300. [[CrossRef](#)]
134. Yan, C.; Rousse, D.; Glaus, M. Multi-criteria decision analysis ranking alternative heating systems for remote communities in Nunavik. *J. Clean. Prod.* **2019**, *208*, 1488–1497. [[CrossRef](#)]
135. Imre, A.; Kustán, R.; Groniewsky, A. Mapping of the Temperature–Entropy Diagrams of van der Waals Fluids. *Energies* **2020**, *13*, 1519. [[CrossRef](#)]
136. Dutta, A.; Karimi, I.A.; Farooq, S. Economic Feasibility of Power Generation by Recovering Cold Energy during LNG (Liquefied Natural Gas) Regasification. *ACS Sustain. Chem. Eng.* **2018**, *6*, 10687–10695. [[CrossRef](#)]
137. Yu, H.; Kim, D.; Gundersen, T. A study of working fluids for Organic Rankine Cycles (ORCs) operating across and below ambient temperature to utilize Liquefied Natural Gas (LNG) cold energy. *Energy* **2019**, *167*, 730–739. [[CrossRef](#)]
138. Thompson, S.; Duggirala, B. The feasibility of renewable energies at an off-grid community in Canada. *Renew. Sustain. Energy Rev.* **2009**, *13*, 2740–2745. [[CrossRef](#)]
139. Bremen, L.V. Large-scale variability of weather dependent renewable energy sources. In *Management of Weather and Climate Risk in the Energy Industry*; Troccoli, A., Ed.; Springer: Dordrecht, The Netherlands, 2010; pp. 189–206.





Article

# New Insights into Hydrothermal Fluid Circulation Affected by Regional Groundwater Flow in the Asal Rift, Republic of Djibouti

Abdek Hassan Aden <sup>1,\*</sup>, Jasmin Raymond <sup>1</sup>, Bernard Giroux <sup>1</sup> and Bernard Sanjuan <sup>2</sup>

<sup>1</sup> INRS-Institut National de la Recherche Scientifique, 490, Rue de la Couronne, Québec, QC G1K 9A9, Canada; jasmin.raymond@inrs.ca (J.R.); bernard.giroux@ete.inrs.ca (B.G.)

<sup>2</sup> BRGM, 3, Avenue Claude Guillemin, la CEDEX 02, 45062 Orléans, France; b.sanjuan@brgm.fr

\* Correspondence: Abdek.Hassan\_Aden@ete.inrs.ca

**Abstract:** The Asal Rift hosts a lake located in a depression at 150 m below sea level, where recharge is influenced by regional groundwater flow interacting with the Ghoubbet Sea along the coast of Djibouti. This regional groundwater flow is believed to influence hydrothermal fluid circulation, which we aim to better understand in this study, having the objective of developing concepts for geothermal exploration in the area. To this end, magnetotelluric data acquired in the Asal Rift were processed and analyzed. 1D inversion models of electrical conductivity were interpolated for interpretation. These data were then used to build a 2D hydrogeological model, allowing multiphase flow and heat transfer simulations to be performed, considering the regional groundwater flow near the surface and the site topography, in order to confirm the preferred path of fluid flow. Geophysical data analysis indicates the presence of normal faults, notably the H fault, which may act as a conduit for the circulation of hydrothermal fluids and where the hanging wall can be a hydrogeological barrier within the hydrothermal system of the Asal Rift. The results from the 2D numerical flow and heat transfer modelling show the importance of groundwater flow responsible for thermal springs located at the periphery of Asal Lake. Reservoir temperature inferred by means of geothermometry ranging from 200 to 270 °C was shown to correspond to simulated temperature at potential reservoir depth. Moreover, simulated temperature between 600 and 1700 m depth is close to the temperature profile measured in the geothermal well Asal 6 of the area, with less than 20 °C difference. Simulations indicate that hydrothermal fluid circulation is likely influenced by the regional groundwater flow controlled by the topography and the major water bodies, the Ghoubbet Sea and Asal Lake, feeding buoyant fluids interacting with a deep magmatic source and where tectonic activity created normal faults offering a preferred path for fluid circulation.

**Citation:** Hassan Aden, A.; Raymond, J.; Giroux, B.; Sanjuan, B. New Insights into Hydrothermal Fluid Circulation Affected by Regional Groundwater Flow in the Asal Rift, Republic of Djibouti. *Energies* **2021**, *14*, 1166. <https://doi.org/10.3390/en14041166>

Academic Editor: Renato Somma

Received: 20 January 2021

Accepted: 17 February 2021

Published: 22 February 2021

**Keywords:** hydrothermal system; electrical conductivity; multiphase flow; numerical modeling; normal fault; heat source; Asal Rift

**Publisher's Note:** MDPI stays neutral with regard to jurisdictional claims in published maps and institutional affiliations.



**Copyright:** © 2021 by the authors. Licensee MDPI, Basel, Switzerland. This article is an open access article distributed under the terms and conditions of the Creative Commons Attribution (CC BY) license (<https://creativecommons.org/licenses/by/4.0/>).

## 1. Introduction

Extensive tectonic environments are known to host significant geothermal resources with large-scale fluid flows [1]. The Asal Rift is located in the central part of the Republic of Djibouti in the Afar depression, a tectonically active region where three major structures, the Great Rift Valley, the Red Sea, and the Gulf of Aden, are in extension and together form the Afar Triple [2,3], an emerged oceanic rift like that of Iceland. This region is a geological laboratory, where several scientific studies have been conducted to understand the processes and mechanisms related to the rifting phenomenon. The geological, geophysical, and geochemical studies carried out with French–Italian scientific collaboration between 1975 and 1988 guided the drilling of six deep geothermal exploration boreholes. A 3D geophysical model was built from passive seismic data [4] and indicated that the dip of normal faults far from the rift axis is about 50°–60° in the NE–SW direction, whereas normal faults close to the rift axis are sub-vertical. The tectonic activity of these faults and

the volcanism of the area, including the last eruption of the Ardoukoba volcano in 1978, are sources of seismic activity and drivers of hydrothermal fluid circulation. The results of seismic tomography indicate that most of the seismic events are located in the first 3 km below the surface [4]. Nevertheless, seismicity within the Asal Rift does not seem to be related to vertical fault planes, but rather to the opening of the fractures through a pressure gradient caused by hot fluids rising under the rift [5]. This mechanism implies that the planes of normal faults begin to tilt away from the rift axis [4] and could act as natural conduits allowing hydrothermal fluid circulation.

Asal Lake, which is 150 m below sea level, is affected by saline groundwater originating from the Ghoubbet sea located 12 km southeastward [2,3]. The role of normal faults in groundwater circulation in the Asal Rift appears important, especially for the circulation of groundwater interacting with Asal Lake, the Ghoubbet Sea, and the deep hydrothermal circulation of hot fluids, which has not been studied with modern physical models that can reproduce multiphase flow and heat transfer mechanisms. The present study is based on this hypothesis, for which work was conducted to better understand the importance of normal faults in the circulation of groundwater and hydrothermal fluids. This study was conducted in the context of geothermal exploration to provide fundamental knowledge analyzing the role of faults and considering the impact of groundwater flow between the Ghoubbet Sea and the Asal Lake. The work aims to define which faults can act as conduits or barriers to groundwater flow within the Asal Rift. To achieve this goal, electrical resistivity data were analyzed to build a conceptual model of the rift, followed by quantitative multiphase and heat transfer modelling of the hydrothermal system in 2D.

## 2. Geodynamic and Hydrogeological Context

The westward propagation of the Gulf of Aden at a velocity of 30 mm/year gave rise to the emergence of the Asal Rift [2]. The opening of the Asal Rift segment dates from the Miocene and its geology is characterized by the abundance of volcanic rocks formed in an environment of extension and opening. This emerged rift segment is 15 km long and 14 km wide. The opening velocity is approximately 16 mm/year [6] in the direction of N°45° E. The structure of this rift is characterized by a set of fracture networks and normal faults in the N130°E direction between Asal Lake and Ghoubbet Bay (Figure 1). Having a thin thickness and basaltic lavas at the surface in the form of basalt series, the land crust of the Asal Rift is considered transitional, i.e., an intermediate between the continental and nascent oceanic crust [4]. The first effusive event linked to the birth of the rift dates from 853,000 to 315,000 years ago [7]. Effusive magmatic activity continued in the northern part of the Asal Rift for 315,000 years and the southern part has been under seawater for 326,000 years, with the formation of hyaloclastites [7]. The activity of the central Fieale Caldera controlled the evolution of the rift between 326,000 and 100,000 years ago. Indeed, it allowed the injection of large volumes of basaltic lava into the interior floor that masked the previous faults [8]. Over the last 50,000 years, volcanic activity has decreased and the successive basaltic flow formations that make up Fieale Caldera have gradually been shifted by normal faults [7]. The modern rift structure began about 40,000 to 30,000 years ago with the development of the faults with outer margins H and  $\delta$  [9]. From this period, the Fieale Caldera gradually extinguished and volcanic activity continued along the interior floor with small volcanic edifices and eruptive fissures [7]. With the most recent magmato-tectonic event dated in November 1978, two earthquakes of magnitude 5 and 5.3 were recorded in the Asal-Ghoubbet Rift and, following this event, 0.7 m of vertical subsidence and 2 m of horizontal extension in the direction N°40 E occurred in the rift [9]. A one-week eruption accompanied by basaltic fissures to the northwest of the rift gave rise in November 1978 to the axial volcanic chain and then to the eruption of the Ardoukoba volcano (Figure 1). At present, most of the rift deformation is concentrated in its north-eastern part and around the edifice of the Fieale Caldera [4–6].

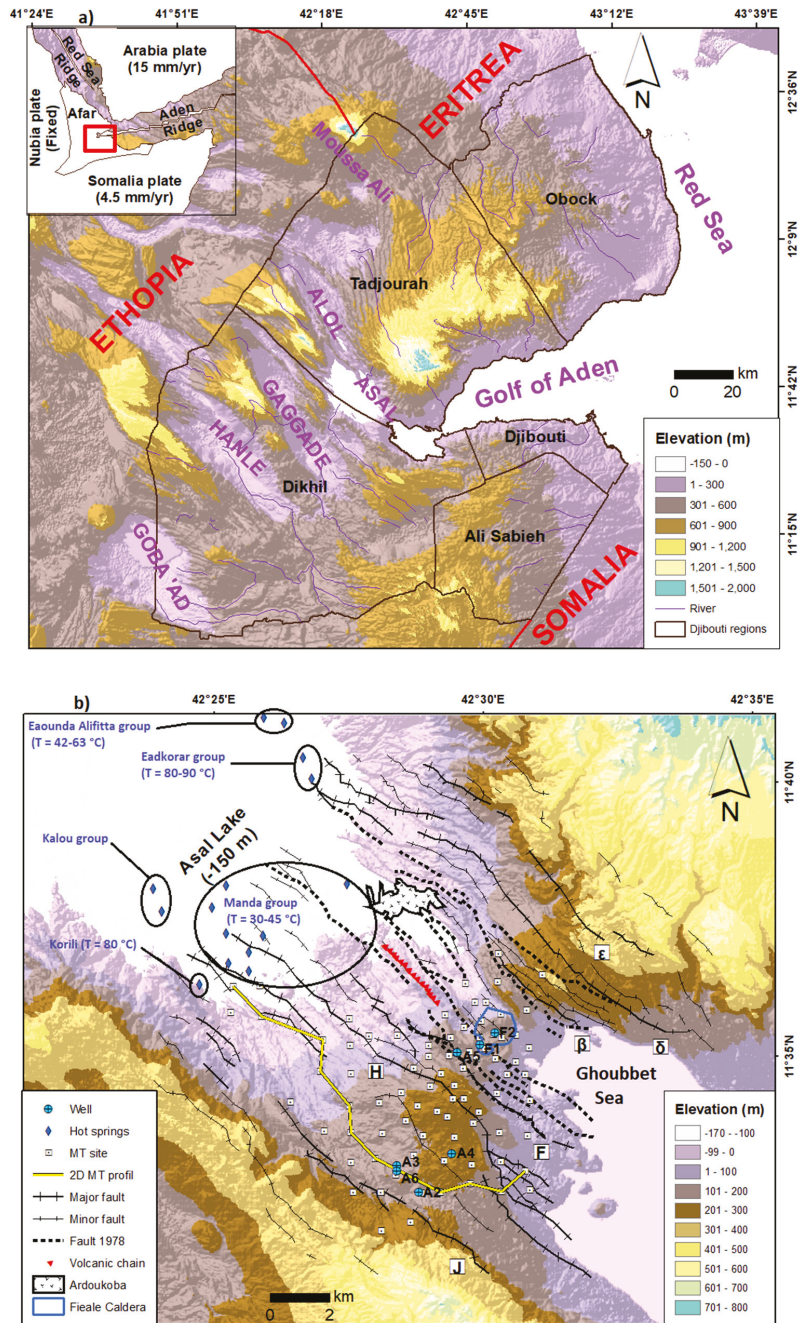


**Figure 1.** (a) Topographic map of Djibouti with the main geothermal potential sites. Red rectangle is Djibouti. (b) Structural map of the Asal Rift modified from [9]. EAR: East African Rift; MT: magnetotelluric.

Thermal springs, fumaroles, and the existence of alteration on the surface of the Asal Rift are indicators of volcanic activity and the presence of potential geothermal resources at depth. Hot springs are abundant around the Asal Lake, especially in the eastern part, with temperatures ranging from 30 to 90 °C (Figure 1). Between the Asal Lake and the Ghoubbet Sea, only fumaroles are observed at the surface because the hydrostatic level is below the topographic surface.

Chemical analyses of gases and determination of  $\delta D$  and  $\delta^{18}O$  water stable isotopes of steam condensate have been performed for some of these fumaroles [10,11]. The results allowed estimating the source temperature at a depth higher than 230 °C, and even than 300 °C, in the studied Asal Rift. The isotopic data from the steam condensate suggest the existence of primary steam (likely separated at high temperature) originating from a deep heavy brine in this area [11]. The existence of this primary steam is in good agreement with the presence of a dominant vapor zone in the conceptual geothermal model proposed by BRGM [10–12].

Owing to the high salinity of Asal Lake and according to geochemical analyses, about 90% of the recharge of Asal Lake is believed to be due to infiltration and evaporation of Ghoubbet seawater [3], depleted in sulfate because of  $CaSO_4$  precipitation [13]. From a geochemical study of water sampled from the rift thermal springs, the authors of [3] showed that the chemical and Sr isotope composition of these waters can be explained by variable seawater interaction with basaltic rocks at different temperatures and evaporation processes. Among thermal waters, those of the Manda group (Figure 1) indicate the lowest seawater–basalt interaction and evaporation degree, suggesting that their source temperature is not high and their circulation rate is relatively significant between the Ghoubbet Sea and the Asal Lake. The thermal waters of the Eadkorar group, located in the northeastern part of the lake (Figure 1), constituted by a mixing of seawater, Asal Lake water, and meteoric water, as suggested by the  $\delta D$  and  $\delta^{18}O$  water stable isotopes [14,15], indicate the highest seawater–basalt interaction grade and seem to be the only direct leaks of a deep fluid discharged from a geothermal reservoir at 200–210 °C, as estimated by chemical geothermometry [3]. The Korilii and Kalou thermal waters (Figure 1) can result from a mixing between the deep geothermal water at 260–270 °C with seawater and Asal Lake water. The stable isotopes suggest the Korilii water is also diluted by meteoric waters [14,15]. The Eounda Alifitta waters, located in the north-eastern most part of the lake (Figure 1), indicate relatively low basalt–seawater interaction degrees and significant contributions of Asal Lake water. A contribution of meteoric water is also suggested by the water stable isotopes [15].

The geothermal wells A1, A3, and A6 are within a radius of 300 m (Figure 1). These wells have confirmed the existence of an intermediate reservoir located between 300 and 700 m depth, with a maximum temperature of 185 °C, and another potentially deep reservoir located between 1200 and 2000 m depth, with a maximum temperature of 260–280 °C (Figure 2). However, production tests proved to be ineffective for a continuous commercial geothermal energy production over time for two reasons:

- The geothermal fluid produced in the wells drilled south-west of the rift (wells A1, A2, A3, and A6), which reached the deep reservoir, had a salinity ranging up to 120 g/L, and wells were subject to scaling and corrosion problems. The solutions considered at that time with chemical inhibitors were not satisfactory [16].
- The wells drilled in the center of the rift (wells A4 and A5) intercepted formations with low permeability, even if a higher temperature (345 and 360 °C, respectively) was measured at their base.

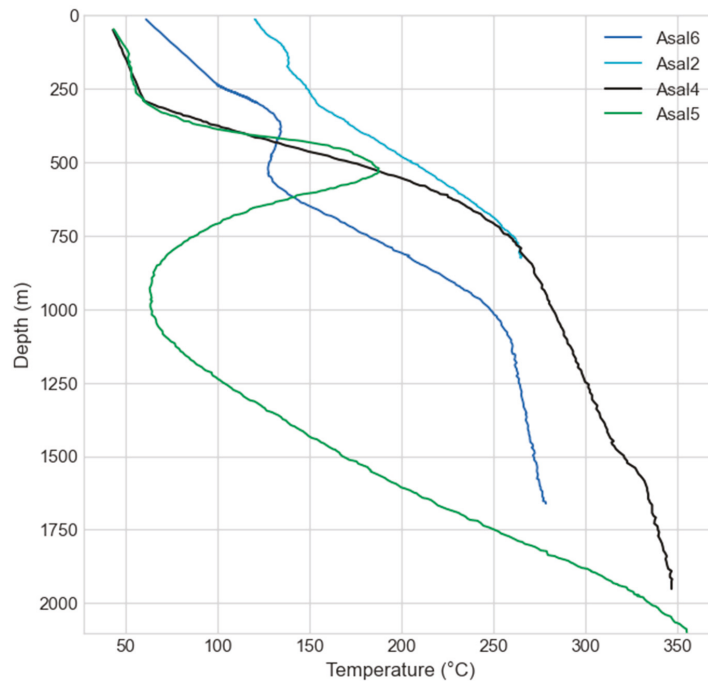


**Figure 2.** Temperatures measured at equilibrium in Asal geothermal wells.

The authors of [3] showed that the deepest geothermal fluid from the wells is constituted by a mixing of seawater and Asal Lake water, interacting with basalt rocks at 260–270 °C. The water stable isotopes also suggest a contribution of meteoric water [15], similar to that observed in the Korilii, Eadkorar, and Eounda Alifitta thermal waters, which could mainly be the meteoric water that transits from Asal local rift to Sakalol-Harralol depression, located at the north-west of Asal Lake, or/and the meteoric water coming from the deep circulating regional aquifers [11–14]. The low boron concentration observed in these deep waters suggests the existence of a steam phase in the geothermal system [3]. The existence of such a zone with dominant vapor is in agreement with the conclusions relative to the gas and steam condensate data drawn by [11] and the conceptual geothermal model proposed by BRGM [10–12]. The equilibrium temperature calculated from all gaseous reactive species associated with these well waters, except H<sub>2</sub>S, is very close to that measured at the bottom of the geothermal wells Asal 3 and Asal 6. This temperature corresponds to that of the identified geothermal reservoir and varies between 250 and 270 °C. According to [3], the geothermal waters located at a depth between 300 and 700 m correspond to a mixing between the deepest geothermal fluid and seawater. The circulation of hydrothermal fluids in the northern part of the rift is believed to happen deeper than in its southern part [17].

Assuming the highly saline water of Asal Lake contributes to the recharge of the geothermal reservoir, this contribution is relatively recent as the water of Asal Lake was fresh and its salinity was recently acquired [3–9]. This constrains the fluid circulation time in the deep hydrothermal system located between 1 and 3 km, having high enthalpy. The water level of Asal Lake 9 to 6 thousand years ago was 160 m above sea level. Over the past 5 to 6 thousand years, the level has declined by 310 m and the lake level is currently 150 m below sea level [9]. This level has remained constant for the last centuries. Therefore, this suggests that, despite the intense evaporation from the arid climate of the area and the infiltration of water from the lake, this evaporation of lake water is compensated by a constant recharge mainly supplied by the Ghoubbet Sea.

The Asal 2 and Asal 3 wells are believed to penetrate the potential deep reservoir unit, but Asal 2 well was non-productive, although a temperature of 230 °C was measured at a depth of 923 m, while the Asal 3 and Asal 6 (located with a distance of about 300 m) were producers with permeable zones at a depth of 1030 m (Figure 2). The fluid produced was hyper saline and essentially composed of liquid at 260° C [16].

### 3. Methods

An electrical resistivity model deduced from magnetotelluric surveys was used in this study to better understand the circulation of seawater through normal rift faults. Using the geoelectrical model, a 2D hydrogeological model was developed for numerically simulating multiphase flow and heat transfer, in order to better understand and quantify the flow dynamics and the development of possible hydrothermal reservoirs.

To better understand the role of seawater and the origin of thermal springs at the periphery of the Asal Lake, the 2D numerical model of coupled and multiphase flow and heat transfer was developed with the HYDROTHERM software provided by USGS [18,19].

#### 3.1. Magnetotelluric Data Acquisition and Processing

Generally, the presence of fluids in porous rocks and their interconnections, the types of minerals, and the temperature and pressure in the rocks contribute to the variation of electrical resistivity. Hydrothermal fluids and the existence of a layer of clay that acts as a cap rock present on the roof of a hydrothermal reservoir are usually identified as highly conductive areas, while, on the other hand, gas reservoirs and cooled magma are identified as less conductive areas [20].

Between 2007 and 2008, a survey including 81 magnetotelluric (MT) stations was carried out in the Asal Rift by the Icelandic company ISOR [16]. The geographical distribution of the MT stations, which are roughly 1 km apart, covers a large part of the Asal Rift (Figure 1). The instrument used to record the data was a Phoenix MTU-5 system and has the ability to record the temporal variation of the three components of the magnetic field ( $H_x$ ,  $H_y$ , and  $H_z$ ) and the two components of the telluric field ( $E_x$  and  $E_y$ ). A reference station, located 10 km from the study area, was used to correct and reduce the local noise of the MT signals [21]. The data collection time was 48 h. For each site, time series were converted from time domain to frequency domain impedance tensor [22]. The frequency range of the data varies from  $12.9 \times 10^{-6}$  Hz to 400 Hz and corresponds approximately to a depth of investigation of the MT signal of more than 12 km inside the earth.

In this study, a 1D inversion of each station of the MT data was achieved. The apparent resistivity of the squared sum of the components of the invariant impedance [23] was inverted using the Occam algorithm [24]. This impedance is expressed as follows:

$$Z_{SSQ} = \sqrt{\frac{Z_{xx}^2 + Z_{xy}^2 + Z_{yx}^2 + Z_{yy}^2}{2}} \quad (1)$$

where  $Z_{xx}$ ,  $Z_{xy}$ ,  $Z_{yx}$ , and  $Z_{yy}$  are the elements of the impedance tensor  $Z$ . Generally, the invariant determinant model is used, but, recently, ref. [25,26] have shown that the determinant model is affected by galvanic distortion at depth. These authors argue that this model tends to reveal more conductive geological structures in the presence of distortion. Another invariant type of model named SSQ (sum of squared elements) is used because it is less affected by the distortion and more appropriate to obtain a first representative approximation of the regional electrical resistivity [25,26].

In this study, an uncertainty of 10% apparent resistivity was assigned for several soundings, except seven soundings with up to 20% uncertainty. The signal in the so-called dead-band, which corresponds to the 5 to 20 s period interval, was low and the resulting uncertainty higher. Moreover, the uncertainty assigned for the phase was 2.5°. With this approach, an electrical resistivity model was developed, where data from all sites were interpolated and interpreted to infer concepts about underground fluid flow.

The inversion results of an electrical conductivity model are presented in Section 4 below, helping to evaluate the role of the Asal Rift in groundwater circulation interacting with deep hydrothermal fluids and to delineate the presence of a hydrothermal system located at a depth between 1.2 and 2 km.

### 3.2. Conceptual Model and Numerical Simulations

High enthalpy geothermal resources required to generate electricity are generally found in areas where magma is introduced into the shallow crust (<10 km) and hydrothermal convection takes place over intrusive hot bodies. For a convective-type geothermal system such as the Asal Rift, the most appropriate conceptual model consists of the following elements [27]. A deep magmatic intrusion that is covered by a host rock. The latter hosts permeable reservoir formations that are covered by a cap rock close to the surface. Based on the structure of this type of geothermal system and the results of the geothermal wells data (Figure 2), a conceptual model of the Asal Rift was set up, helping to approximate the thickness of the seawater intrusion towards Asal Lake. The 2D conceptual model used to define the geometry of the numerical model was based on an interpreted resistivity section inferred from the 1D electrical resistivity model developed in this study. This 2D section is parallel to the rift axis (Figure 1) and was chosen because of the presence of productive geothermal wells (Asal 3 and Asal 6) along this section, and is parallel to the believed direction of regional groundwater flow. The temperature profile of the Asal 6 well was used to calibrate the numerical model.

#### 3.2.1. Multiphase Flow and Heat Transport

Simulation of multiphase flow and heat transport is challenging because it is difficult to consider the critical point to set the appropriate thermodynamic state of the fluid in two phases. The pressure–enthalpy formulation that defines the thermodynamic state of the fluid in two phases can be used to avoid this problem, which was done in the HYDROTHERM code [28]. The governing equations used in the HYDROTHERM code are expressions of mass and energy conservation formulated in terms of pressure and enthalpy. As no potentiometric-head function exists for density fields that depend on temperature, pressure is chosen as the dependent variable for fluid flow. All pressures are expressed as absolute and the water-component flow equation is based on the conservation of water mass in a volume element, coupled with Darcy's law for multiphase flow through a porous medium [19]:

$$\frac{\partial}{\partial t} [\varphi(\rho_w S_w + \rho_s S_s)] - \nabla \cdot \frac{k k_{rw} \rho_{rw}}{\mu_w} [\nabla P + \rho_w g] - \nabla \cdot \frac{k k_{rs} \rho_{rs}}{\mu_s} [\nabla P_g + \rho_s g] - q_{sf} = 0 \quad (2)$$

where  $\varphi$  is the porosity (dimensionless),  $\rho$  is the fluid density ( $\text{kg m}^{-3}$ ),  $S_w$  is the saturation of liquid phase (water) and  $S_s$  is the saturation of the gas phase (steam or air; dimensionless),  $k$  is the porous-medium permeability tensor ( $\text{m}^2$ ),  $k_r$  is the relative permeability (dimensionless),  $\mu$  is the viscosity of fluid (Pa s),  $P$  is the fluid pressure in the liquid phase (Pa),  $P_g$  is the fluid pressure in the gas phase (Pa),  $g$  is the gravitational constant ( $\text{m s}^{-2}$ ),  $q_{sf}$  is the flow-rate intensity of a fluid-mass source (positive into the region;  $\text{kg s}^{-1} \text{m}^{-3}$ ),  $t$  is the time (s), and  $\nabla$  is the spatial gradient ( $\text{m}^{-1}$ ). The phase subscripts w and s refer to water (liquid phase) and steam (gas phase or vapor phase), respectively. In the single-component (water) zone,  $p_g = p$  because the capillary pressure is assumed to be zero. As any point in the mesh, it can be a single component or two component zone and the saturation constraint is  $S_w + S_g = 1$ .

The thermal-transport equation is based on the conservation of enthalpy in both the fluid phases and the solid phase of the porous medium, in a volume element of the region. So, enthalpy is a derived property containing both internal energy and flow energy. Thus,

$$\frac{\partial}{\partial t} [\varphi(\rho_w h_w S_w + \rho_s h_s S_s) + (1 - \varphi) \rho_r h_r] - \nabla \cdot K_a I \nabla T + \nabla \cdot \varphi(\rho_w h_w S_w v_w + \rho_s h_s S_s v_s) - q_{sh} = 0 \quad (3)$$

where  $h$  is the specific enthalpy of the fluid phase ( $\text{J kg}^{-1}$ ),  $h_r$  is the specific enthalpy of the porous-matrix solid phase ( $\text{J kg}^{-1}$ ),  $\rho_r$  is the density of the porous-matrix solid phase ( $\text{kg m}^{-3}$ ),  $K_a$  is the effective thermal conductivity of the bulk porous medium (combined liquid, gas, and solid phases) ( $\text{W m}^{-1} \text{K}^{-1}$ ),  $I$  is the identity matrix of rank 3 (dimensionless),  $T$  is the temperature ( $^{\circ}\text{C}$ ), and  $q_{sh}$  is the flow-rate intensity of an enthalpy source (positive into the region;  $\text{W m}^{-3}$ ).

The main assumptions underlying Equations (2) and (3) that are solved in HYDROTHERM are the following: capillary pressure effect is negligible, porous medium and fluid are in local thermal equilibrium, the fluid is pure water, heat transfer by radiation and dispersion can be neglected, Darcy's law is valid with two phase forms, and relative permeability is a nonhysteretic function of liquid volume saturation.

### 3.2.2. Spatial and Temporal Discretization

The 2D conceptual model to simulate extends 14 km horizontally (Figure 1) and 3 km vertically from the land surface. The model geometry in the HYDROTHERM simulator is discretized with a regular  $100 \times 100$  grid. The simulation time span to reach a quasi-steady state temperature regime was 100,000 years and an initial time step of 0.001 year was considered. An automatic time step algorithm is used in the simulator, where smaller time steps are selected when conditions are changing rapidly and maximum values for changes in pressure, enthalpy, and liquid saturation are specified before running the simulation [19]. In our study the maximum changes in pressure, enthalpy, and saturation are 10%, 5%, and 0.03, respectively. This results in a maximum time step of 1000 years. The independence of the mesh is presented to demonstrate the accuracy of the solution. In this study, two different grids were considered with two different initial time steps.

### 3.2.3. Initial and Boundary Conditions

Numerical modeling of continental or subaerial hydrothermal systems often considers the upper system flow boundary to be the water table of shallow aquifers affected by topography [18,29,30]. Therefore, initial conditions are an initial temperature of  $20\text{ }^{\circ}\text{C}$  with an atmospheric pressure of 1 atm at the surface of the 2D model, a geothermal gradient of  $49\text{ }^{\circ}\text{C}/\text{km}$ , and hydrostatic pressure increasing with depth. A heat flux of  $100\text{ mW}/\text{m}^2$  was fixed at the base of the model and the surface boundary has a constant temperature of  $20\text{ }^{\circ}\text{C}$ . A pressure of 1 atm was also considered at the surface boundary. The base of the model is considered impermeable with no flux. Constant temperature and pressure determined from the initial conditions were imposed on the lateral boundaries of the model in order to take into account the variation of the geothermal and the pressure gradients at depth. This allowed to establish the temperature and pressure gradients according to the topography and the water table depth inferred from the conceptual model. Five different simulation scenarios are presented below. For all scenarios, a deep resistive structure named R2 was taken as a magmatic intrusion or heat source, and a heat flux of  $2700\text{ mw}/\text{m}^2$  was fixed at the base of this R2 structure. This is the base case scenario where the boundary conditions presented above are used.

Numerical simulations conducted in magmatic hydrothermal systems [18,31] showed that the representation of the topography is an important factor to reproduce regional groundwater flow driven by the topography. This was taken into account to better evaluate the dynamic of groundwater flow between the Asal Lake and Ghoubbet Sea. In addition, the influence of infiltration from rainfall in geothermal systems is not negligible, but the impact of rainfall in the hydrothermal activity is commonly limited in the upper part [32] and may not prevail in the deeper part of the hydrothermal system, as in the case of Asal Rift. The impact of rainfall was not simulated as the numerical simulations considered confined flow.

### 3.2.4. Hydraulic and Thermal Properties

The geological units considered in the conceptual 2D model were interpreted from the 1D electrical resistivity model developed in this study. Hydraulic and thermal properties of each unit were defined according to Table 1, used as the base case scenario and noted as scenario 1. Then, four other different scenarios were conducted in order to evaluate the sensitivity of the results to changes in the main hydraulic parameter (permeability) of the geological units. Three permeable vertical conduits that can be associated with fault zones were added and coexist to evaluate the possible impact of fault zones. The choice of emplacement and geometry of these faults was based on the interpretation of the inverted electrical resistivity profile developed in this study. Thus, properties of faults remain the same of those of unit C1 (Table 1), but with higher isotropic permeability equal to  $2.17 \times 10^{-14} \text{ m}^2$ . In scenario 2, a permeability dependent temperature in the potential deep reservoir unit was adopted with an isotropic permeability of heat source equal to  $10^{-17} \text{ m}^2$ . Scenario 3 was simulated to understand the behaviour of the system in the deeper part without permeability dependent temperature. To do this, an isotropic permeability was assigned to both the heat source ( $10^{-17} \text{ m}^2$ ) and the potential deep reservoir unit ( $10^{-15} \text{ m}^2$ ). This permeability value assigned in the potential deep reservoir unit is of the same order of the one estimated from the production test of well Asal 3, which reached the potential deep reservoir, which was equal to  $6.3 \times 10^{-15} \text{ m}^2$  [33]. The conditions of scenario 4 are similar, but a permeability dependent temperature inside the heat source unit was used. Finally, scenario 5 was simulated with permeability anisotropy within the near-surface aquifer C1, which was assigned to the model to investigate how it can influence the regional groundwater flow. Horizontal permeability was set one order higher than the one of the base case scenario. The purpose of this scenario 5 was to simulate the predominance of horizontal fluid movements over vertical movements within this geological formation and hypothesize the behaviour of the system in such conditions. The properties of all units remain the same as those of scenario 1, except for the horizontal permeability in the unit C1, which was equal to  $2.17 \times 10^{-14} \text{ m}^2$ .

**Table 1.** Hydraulic and thermal properties for simulation of the base case scenario.

Formations	Unsaturated Formation: R1	Aquifer: C1	Cap Rock: C2	Potential Deep Reservoir	Heat Source: R2
Porosity (-)	0.12	0.12	0.12	0.27	0.12
Horizontal permeability ( $\text{m}^2$ )	$2.17 \times 10^{-16}$	$2.17 \times 10^{-15}$	$2.17 \times 10^{-18}$	Temperature dependent	Temperature dependent
Vertical permeability ( $\text{m}^2$ )	$2.17 \times 10^{-16}$	$2.17 \times 10^{-16}$	$2.17 \times 10^{-18}$	Temperature dependent	Temperature dependent
Thermal Conductivity ( $\text{W m}^{-1} \text{ k}^{-1}$ )	Temperature dependent	Temperature dependent	Temperature dependent	Temperature dependent	Temperature dependent
Density ( $\text{kg m}^{-3}$ )	2700	2700	2700	2800	2900
Specific heat ( $\text{J kg}^{-1}$ )	1000	1000	1000	Temperature dependent	Temperature dependent
Compressibility ( $\text{Pa}^{-1}$ )	$10^{-20}$	$10^{-20}$	$10^{-20}$	$10^{-20}$	$10^{-20}$

In the crust, thermal conductivity decreases with increasing temperature [34]. The formulation developed by [34] for crystalline rocks with a temperature range between 20 and 500 °C was taken into account, where the thermal conductivity value at 20 °C is  $2.5 \text{ W m}^{-1} \text{ }^\circ\text{C}^{-1}$ . To consider the effect of latent heat of crystallization, a linear temperature-dependent rock heat capacity relation was adopted, which doubles from 900 at temperatures below 100 °C to  $1800 \text{ J kg}^{-1}$  at temperatures greater than 500 °C. This linear relationship was based on the approach initially developed by [34] and then used by [35] for similar modeling work.

Temperature-dependent rock permeability was formulated for both the potential deep reservoir and heat source (Table 1). This formulation is the same as that developed by [29] for magmatic hydrothermal systems, where permeability increases with the decreasing temperature. Thus, the permeability of the heat source with a temperature range of 400–500 °C is one order of magnitude less than the one of the deep reservoir with a temperature range of 200–400 °C.

In such systems, fluid flow is mainly controlled by processes such as thermal pressurization, buoyancy, and magmatic exsolved fluid. Our hypothesis is based upon the existence of deep hydrothermal circulation in the Asal Rift and the absence of a magma chamber at a depth less than 5 km [4]. Thus, the fluid pressure originating from the heat source unit may have allowed rocks to fail and created permeability within the potential deep reservoir unit.

#### 4. Results

The results of 1D electrical conductivity model are initially presented and followed by the results of fluid flow simulations.

##### 4.1. 1D Electrical Resistivity Model

Observed and simulated electrical resistivity fits with an average root mean square (RMS) misfit of about 0.1. The match of electrical resistivity and phase at each MT station appears reasonable, as can be seen for resistivity, and phase curves of all MT sites along the 2D MT profile (Figure 1) are presented in Figure 3.

The H fault (Figures 1 and 4) delineates two distinct zones of electrical resistivity. The north-east part of this fault is defined as a conductive zone, while the south part is less conductive (more than 20  $\Omega\cdot\text{m}$ ). The geometry of the Fieale Caldera corresponds to a well-defined zone of electrical resistivity of the order 20–30  $\Omega\cdot\text{m}$  (Figures 1 and 4). The different electrical iso-resistivity maps in Figure 4 show a gradient of electrical conductivity that increases in the direction from the south-west to the north-east. This change of the conductivity gradient is clearly visible and evident at depths of 1640 and 1840 m (Figure 4).

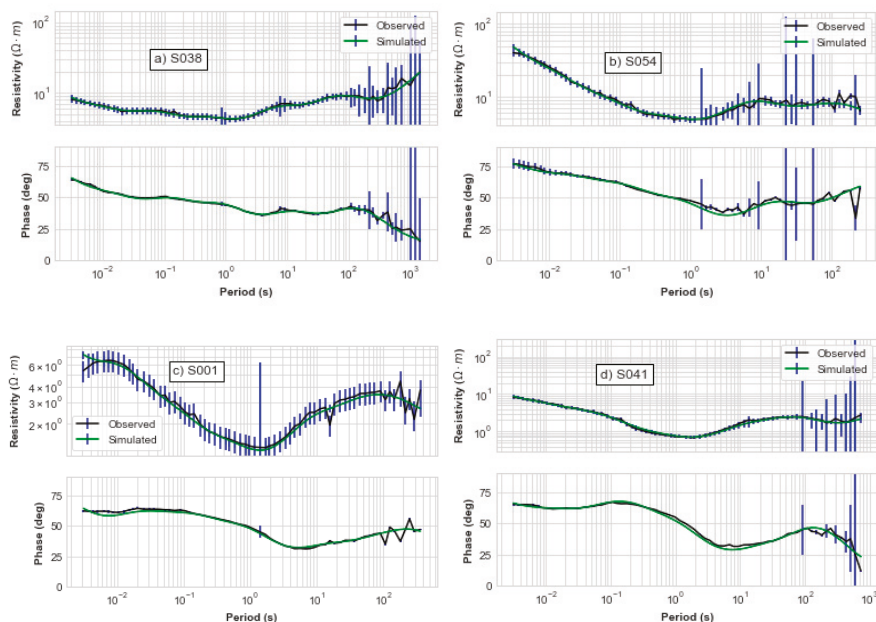


Figure 3. Cont.

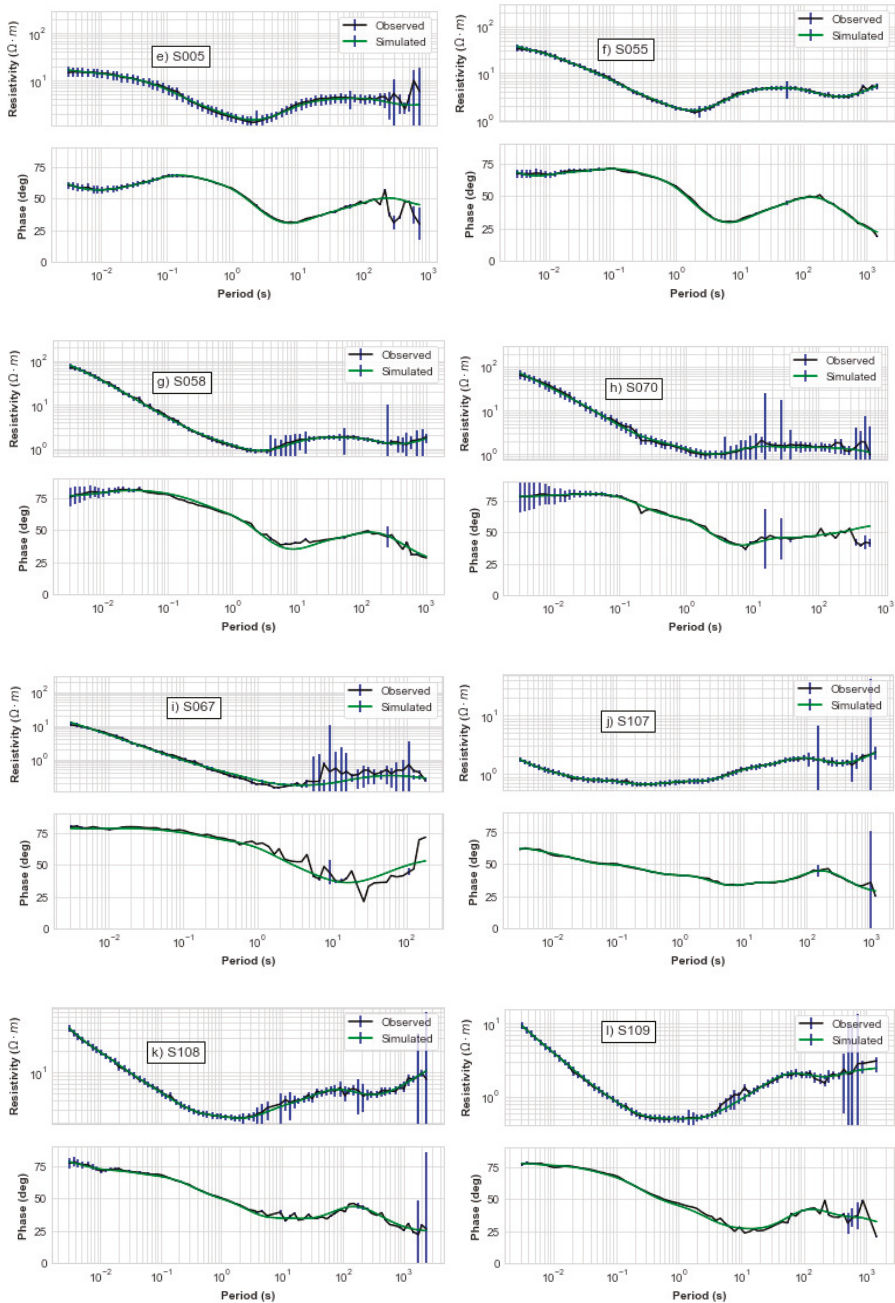


Figure 3. Comparison of observed and simulated electrical resistivity at MT sites along 2D MT profile in Figure 1.

#### 4.2. 2D Conceptual Model

The conceptual model of Figure 5 was defined using the available electrical resistivity data interpreted along a cross section more or less parallel to the Asal rift axis (Figure 1). A top layer of high resistivity (**R1**) is associated with unsaturated formation near the surface.

The underlying layer with a low resistivity **C1** is considered as an aquifer, which can host shallow or intermediate reservoirs, as evidenced by temperature profiles of wells Asal 6 and Asal 3 (Figure 2). These temperature profiles show convection cells with a change in geothermal gradient at a depth between 300 and 600 m that can only occur in permeable layers with fractures.

Layer **C2** can be a cap rock covering the formations hosting deep hydrothermal reservoirs, which is referred to here as the **potential deep reservoir** unit in the numerical model. The highly resistive **R2** structures can mostly likely be associated with intrusive bodies.

#### 4.3. Numerical Simulations

Mesh and time step independence were investigated to make sure numerical simulations are reliable. A comparison between different grids for scenario 1 at the location of Asal 6 well at a depth of 1500 m is presented in Appendix A. The results with a  $100 \times 100$  grid and initial time step of 0.001 year are presented in Figures 6 and 7. Furthermore, a mesh with a  $40 \times 100$  grid with an initial time step of 0.01 year was considered (Figure 6) and the patterns of flow and heat transport observed were similar to those of mesh with a  $100 \times 100$  grid (Figure 7). We can deduce and argue that our solution is independent of the choice of the grid and the choice of the initial time step. One should keep in mind that the HYDROTHERM software uses an algorithm allowing an automatic time step [19] in which only the initial time step is set by the user.

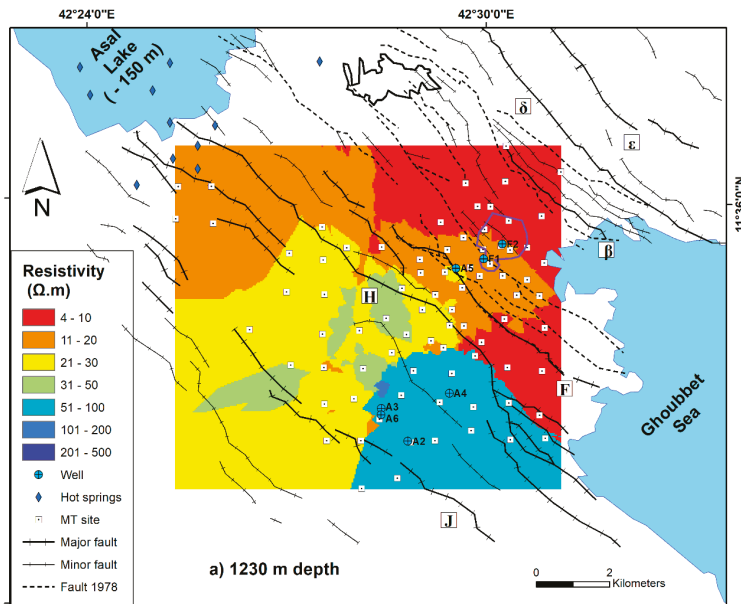


Figure 4. Cont.

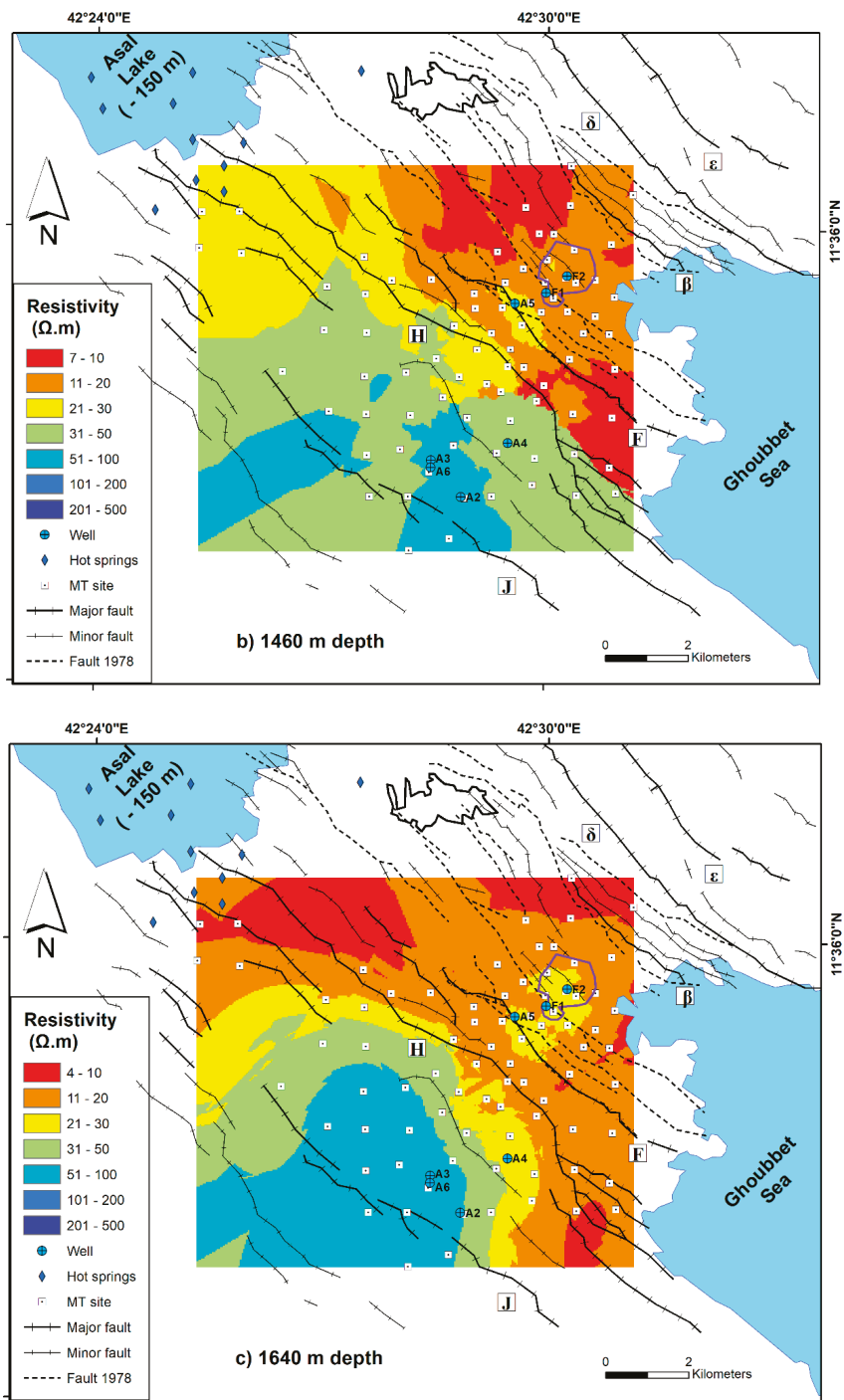


Figure 4. Cont.

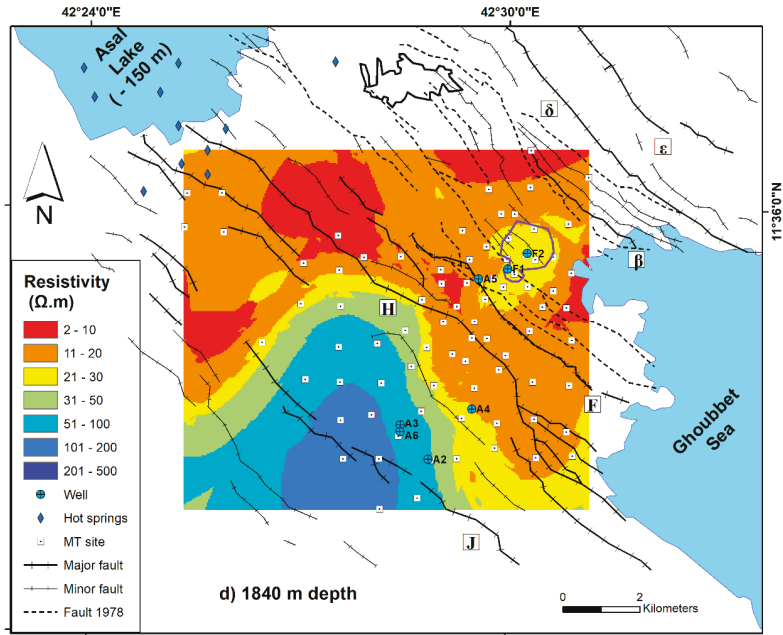


Figure 4. Interpolation at selected depth of inverted electrical resistivity.

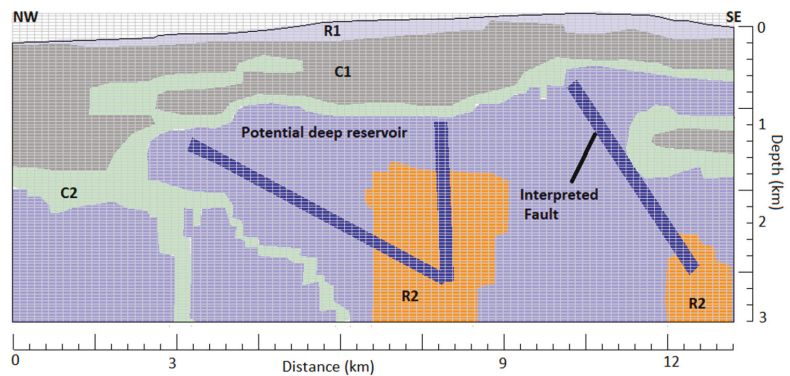
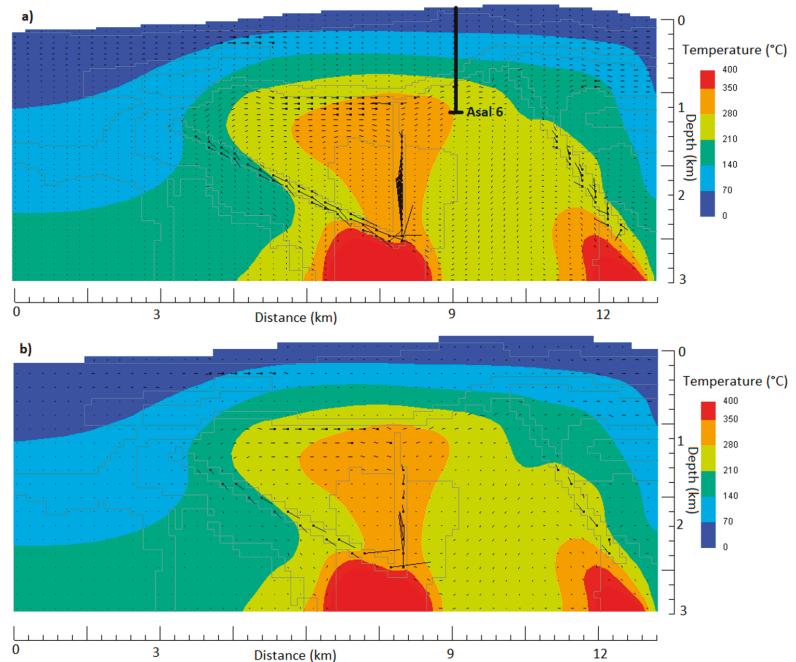


Figure 5. 2D conceptual model interpreted along 2D MT profile in Figure 1.

The simulation results of scenario 1 and scenario 2 (Figures 6 and 7) show the upwelling of a warm fluid or an upflow zone that propagates from the heat source at the model center toward Asal Lake and toward the sea, but to a lesser intensity. The development of convection movements is visible inside the deep potential reservoir unit that can likely host localized hydrothermal reservoirs. Scenarios 3 and 4 present similar flow and temperature patterns with the presence of three flow zones at a distinct depth. Groundwater circulation toward Asal Lake inside the aquifer C1 can be identified and the widening of the deep upflow zone of hydrothermal reservoir from the center to the sea can be observed. High velocity flow vectors also appear in the center of the rift at a depth between 900 and 1800 m, particularly inside the faults zones, where hot ascent fluid in the fault close to the sea and cold descendant fluid in the fault close to Asal Lake can be observed. This can be associated with a mixture of descending cold groundwater with

the ascending deep hydrothermal circulation over a depth of about 500 m and driven by the temperature gradient (Figure 7). Scenario 5 captures the same temperature patterns as the results of scenarios 1 and 2, but with strong flow vectors inside the unit called C1, noted here as a shallow aquifer. Obviously, the system behaviour remains the same in the deeper part even with the presence of significant lateral flow in the upper part of the system (Figure 7).

The Asal 3 and Asal 6 wells are believed to be penetrating the deep potential reservoir unit. The full comparison between simulated and observed temperature in well Asal 6 for each scenario is shown in Figure 8. The simulated temperature is about 255 °C in scenario 1 at a depth of 1600 m, which approximately corresponds to the measured temperature at the bottom of Asal 6 well (265 °C at a depth of 1700 m). In fact, the measured temperature matches with the simulated temperature of scenarios 1, 2, and 5, except in the upper part above 600 m depth (Figure 8). The comparison between the measured and simulated temperature for scenario 3 is not presented as it is the same as scenario 4 (Figure 8).



**Figure 6.** Simulated temperature and flow vectors at time equal to 100,000 years in scenario 1. The direction of flow is from the point to the end of the straight lines. The length of each line indicates the water flow vector magnitude, where  $1.2 \text{ km} = 1 \times 10^{-5} \text{ g (s}^{-1} \text{ cm}^{-2})$ . (a) Results with a grid of  $100 \times 100$  and initial time step of 0.001 year. (b) Results with a grid of  $40 \times 100$  and initial time step of 0.01 year.

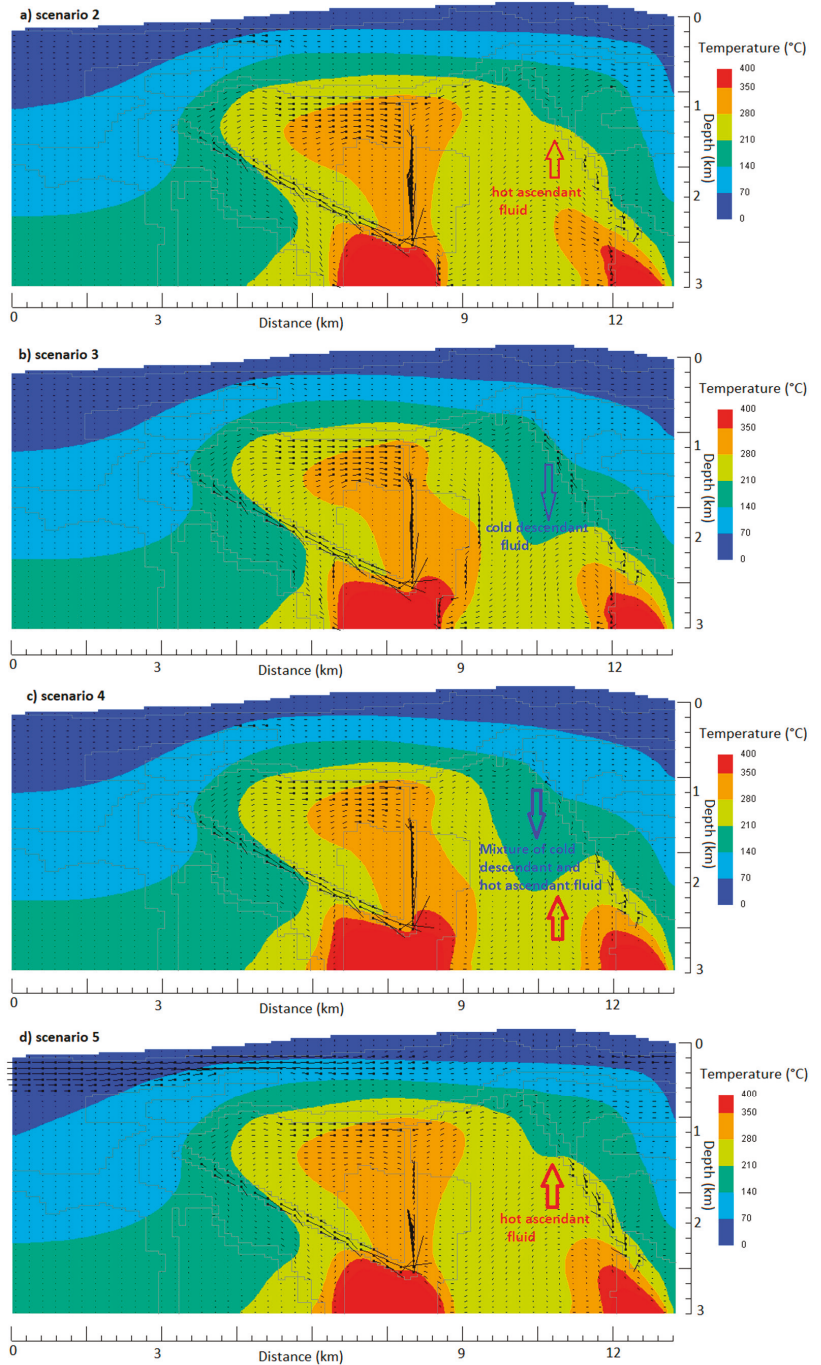


**Figure 7.** Simulated temperature and flow vectors at time equal to 100,000 years. The direction of flow is from the point to the end of the straight lines. The length of each line indicates the water vector magnitude, where  $1.2 \text{ km} = 1 \times 10^{-5} \text{ g (s}^{-1} \text{ cm}^{-2})$ .

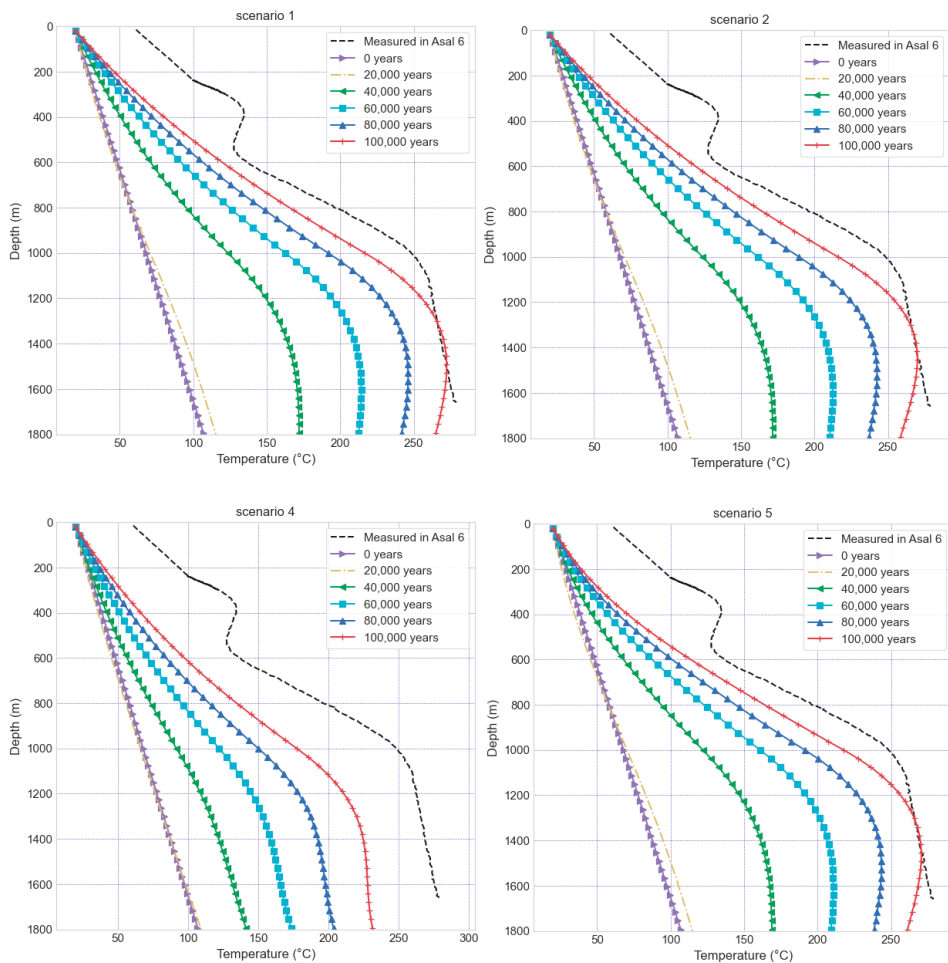


Figure 8. Comparison between the observed and simulated temperatures at well Asal 6.

## 5. Discussion

The directions of faults and fractures are parallel to the direction of believed groundwater flow (Figures 1 and 4). Unfortunately, the available MT data do not cover the entire area of the emerged Asal Rift. A lack of data in the area of the normal faults  $\epsilon$  and  $\delta$  to the north-east of the rift limits the interpretation (Figure 1). However, previous geochemical analyses conducted by [36] in littoral thermal springs could help to place our interpretations in a logical context and may explain the origin and the evolution of thermal waters that are not far at the eastern flank of the normal faults  $\epsilon$  and  $\delta$  located at the north-east of the rift. These authors conclude that a mixture of hot seawater with cold seawater emerges through the fractures. Moreover, the presence of deep hot seawater-derived geothermal fluid with a temperature of 210 °C was confirmed [37]. Despite the lack of data in this zone, our interpretation of pronounced fluid circulation at the north-east of the rift can be justifiable. The comparison between the  $^{87}\text{Sr}/^{86}\text{Sr}$  ratio and strontium concentration of the brine waters from the Red Sea bottom and Asal Lake have indicated that Asal Lake is a better location to study how hydrothermal fluids of seawater origin may evolve in the Red Sea rift [38].

The descriptive lithology of the wells drilled in the Asal Rift consists mainly of a succession of basaltic series, which were deposited over geological time and have different ages [39]. Even if the abundance of shale and/or graphite is known to cause a decrease in electrical resistivity [21], no significant quantity of the latter is found in the wells drilled, and more precisely between 1 and 2 km depth [39]. Within the Earth's crust, the dominant electrical conduction mechanism is electrolytic [21]. Therefore, low electrical resistivity in the context of the Asal Rift is generally interpreted as an indicator of the presence of a fluid. At depths of 1200 and 1400 m (Figure 4), groundwater seems to be present mainly between the H fault and the  $\delta$  fault according to the following evidence. In this zone, observed fractures were caused by the tectonic and volcanic activity associated with the eruption of the Ardoukoba volcano that occurred in 1978 (Figure 1). The low electrical resistivity suggests the presence of water and hence more important flow to the southeast between the H and F faults, and to the north-east of Fieale Caldera. The existence of dykes at a depth near the rift axis (between the F and  $\beta$  faults) has been hypothesized based on the deformations observed at the surface [9]. In this case, rift extension and subsidence are controlled by dyke injection. Moreover, the stretching model of Asal Rift is likely accommodated by the magma activity [40]. This extension can result in open cracks where groundwater flows easily. The proximity of the sea and the coexistence of recent open faults and fractures is a fair evidence for such flow illustrated with the simulations. The electrical resistivity model, especially images obtained at a depth between 1.2 and 2 km (Figure 4), indicates a possible hydrothermal system in the north-east part of the Asal Rift and with more pronounced regional groundwater flow in this area rather than in the south-west zone (Figure 4). Considering the contrast in electrical resistivity between the north-east and south-west parts of the Asal Rift, it seems likely that the hanging wall of the H fault acts as a hydrogeological barrier separating the Asal Rift between two zones. A first conductive zone, whose high electrical conductivity is due to the presence of groundwater, as well as a second less conductive zone with an increase of the electrical resistivity gradient towards the south of the rift, imply lower porosity and/or less groundwater in pore space and fractures. Only the major J fault and the minor fault passing through well Asal 4 exist in the south zone of the Asal Rift. In addition, according to the bathymetry map of the region, the J fault is not connected to the Ghoubbet sea. The absence of the open cracks or fractures observed with the November 1978 eruption in the southern zone of the Asal Rift is another argument that limits the possibility of possible fluid flow or water infiltration in this sector, while the presence of activated faults in 1978 in the northern part is dominant (Figure 1).

Wells A5, F1, and F2 were drilled in the north-east zone of the H fault, but only the temperature profile of well A5 was available for this study (Figure 2). This temperature profile shows a first convection cell from 300 to 500 m and a second convection cell from 500 to 1200 m, and then a constant geothermal gradient that can be related to heat conduction between 1.2 and 1.8 km. This information, therefore, correlates with the conductive zone to the north-east of fault H. Furthermore, the geothermal gradient estimated between 1.2 and 1.8 km in well Asal 5 is 18.7 °C/100 m. In addition, well Asal 5 is located in a relatively conductive zone with an electrical resistivity greater than 20  $\Omega$  m, which can corroborate the absence of groundwater that can have a high salinity associated with electrical resistivity less than or equal to a value of 10  $\Omega$  m [21]. This Asal 5 well can be close to a heat source where heat is transferred by deep conduction, resulting in a strong conductive geothermal gradient at a depth between 1.2 and 1.8 km. The absence of groundwater circulation between 1.2 and 2 km in this well is corroborated by both its temperature profile and the electrical resistivity model presented in this study. The latter also shows the Fieale Caldera in close proximity to well Asal 5 has a particular electrical resistivity range of 20–30  $\Omega$  m. It is highly probable that this resistivity is characteristic of the nature of the rock in this Caldera zone, which can be hot, but less permeable, limiting the circulation of fluid. Another important fact is that hydrothermal mineral assemblage is in good agreement with the measured temperatures in all geothermal wells of Asal Rift, except for well Asal 5 [39], where a chlorite-epidote mineral assemblage zone that normally

should exist at a high temperature was observed at a depth between 500 and 1200 m, where an important temperature inversion was measured (Figure 2). This information is helpful allows to assume that a pre-existing high temperature reservoir can have existed before the infiltration of cold sea water, and the temperature inversion may likely be related to a recent infiltration of seawater.

Geodetic measurements indicate that the opening of the Asal–Ghoubbet Rift has a velocity of 16 mm/year and an opening direction perpendicular to the rift axis, highlighting the asymmetrical behavior of the Asal Rift [6]. These authors studied the horizontal and vertical deformation of the rift in directions parallel and perpendicular to the rift axis. They consider that the north-eastern part of the Asal Rift is the site of significant continuous deformation, whereas for its south-western part, the deformation is weak and practically non-existent. These results corroborate the presence of active normal faults in the north-eastern part of the rift and the existing seismic activity [4]. The rate of deformation along the axis perpendicular to the rift axis increases towards the north-east of the rift [6]. This is a surprising correlation between the increase in this deformation rate and the increase in electrical conductivity highlighted by the model developed in this work pointing in the same direction (Figure 4).

The regional groundwater flow affected by sea water was believed to be the main source of recharge to Asal Lake [3], but our simulation results show the groundwater flow is directed toward both the Asal Lake and the Ghoubbet Sea, with a maximum point on the SE side diving flow in the two directions and a pronounced flow to Asal Lake. This can limit the pontifical depth of penetration of sea water intrusions near the surface. In this case, recharge of Asal Lake can occur through aquifer (C1), potentially containing fossil seawater that is likely fed by a deep hydrothermal circulation. In all the different simulation scenarios, it is important to highlight the evidence of groundwater flow into Asal Lake and hydrothermal circulation beneath Asal Lake and the Ghoubbet sea.

The superposition of three permeable zones with the predominance of flow towards Asal Lake and the Ghoubbet sea are important elements to advance the hypothesis of the existence of a large hydrothermal system under the rift that would be compartmentalized into these three permeable zones, which can be individualized under the tectonic activity and the injection of a deep heat source since the formation of the rift over the geological time. The subsurface flow at a depth between 300 and 700 m (Figure 7) can be influenced by the Ghoubbet sea and the local rift topography, while the intermediate flow at a depth between 1200 and 2000 m (Figure 7) is interpreted as the result of the development of a hydrothermal system, and the deep flow can be linked to a deep hydrothermal circulation feed by a heat source originating from a deep magmatic system (Figure 7). The presence of the cap rock layer limits possible communications between the second permeable layer, identified here as a potential deep reservoir, and the shallow aquifer C1 (Figures 5 and 7), and facilitates the development of a hydrothermal reservoir in the formation, where this cap rock layer covers and helps to contain thermal energy in the potential deep reservoir.

Similar simulation results obtained with scenario 5 (Figure 7) support the idea that regional flow variation is not strongly influenced by the permeability anisotropy in layer C1 of the conceptual model (Figure 5). In other words, the regional flow is mainly controlled by tectonics that affect deep structures and allow the deep heat source to be directed to shallower geological strata and formations. Simulations with an isotropic permeability of  $10^{-15}$  m<sup>2</sup> inside the deep reservoir and equal to  $10^{-17}$  m<sup>2</sup> inside the heat source were conducted for scenario 3 to indirectly evaluate the vertical dependence of permeability, which can decrease with depth. The development of hot convection cells within this unit was less pronounced than in scenarios 1 and 2 (Figures 6 and 7). Scenarios with permeability dependent temperature (scenarios 1, 2, and 5) seem to be more realistic than scenario 3 with isotropic permeability. However, the results from scenario 3 are not representative of conceptual hydrothermal models proposed in previous studies [41,42], where hydrothermal activity is concentrated in areas with elevated topography. Hydrothermal activity in permeability dependent temperature scenarios better correlates with the central zone of

high topography (Figures 6 and 7). In scenarios 1, 2, and 5, the lateral extension of the hydrothermal reservoir with the isotherm 210 °C becomes important compared with the results of scenarios 3 and 4 (Figures 6 and 7). This pattern is in good agreement with a previous study conducted in a tectonically active rift-ridge zone in Iceland [43]. The authors of this study confirm that emplacement and geometry of the upflow zones are mainly controlled by the location and the permeability values of fault zones. The geometry, location, and permeability values of fault zones remain the same in all the different scenarios for this study, but we deduce from our results that the permeability dependent temperature rock formulated in both heat source and potential deep reservoir can play a major role to reproduce a representative dynamic heat transfer in hydrothermal systems. Permeability dependent temperature formulated solely for the heat source unit may not produce significant variation when the potential deep reservoir is set with a constant permeability like the simulated conditions of scenario 4. In addition, the results are approximately the same as the results of scenario 3, where isotropic permeability was set for both the heat source and potential deep reservoir units. In such cases, we hypothesize that permeability dependent temperature would be an appropriate formulation in a hydrothermal system as in the Asal Rift, when it is adopted for both the heat source and potential deep reservoir or, uniquely, for the potential deep reservoir like in scenario 2.

The comparison between the temperature profile measured in the Asal 6 well and the temperature simulated appears more realistic with scenarios 1, 2, and 5 compared with other scenarios (Figure 8). This indicates that the conditions used are representative of the rift and the associated thermal anomaly can be related to the injection of a magma forming a heat source and the development of vertical conduits qualified as active faults to convey this internal thermal energy. In scenario 4 (Figure 8), the system at the end of the simulation began to cooled down, as the temperature at 100,000 years is less than the temperature measured in well Asal 6. It can be reasonable to interpret this as a consequence of an extinguished deep hydrothermal fluid circulation inside the heat source layer, where permeability could be higher than that assigned in scenario 4. However, the shape of the simulated temperature profile at the location of well Asal 6 is maintained and has the same appearance as the measured temperature in well Asal 6. Furthermore, the same reservoir was recognized at a depth between 1050 and 1300 m in three wells, Asal 1, 3, and 6, and the geologic formation hosting this reservoir is called Dalha basal, which has an average age of 4 to 9 My, where temperatures measured in this reservoir range from 260 to 280 °C [33] and are close to the simulated temperatures in this study. In addition, permeability anisotropy considered in scenario 5 inside the C1 layer does not lead to cooling of the system and the simulated thermal state at well Asal 6 is close to the measured one (Figure 8). It can be assumed that the thermal anomaly caused by this near-surface groundwater flow has less effect at the global scale of the system. Nevertheless, the assumption of pronounced horizontal flow near Asal Lake in scenario 5 is corroborated by our interpreted conceptual model based on electrical resistivity inversion (Figure 5), where the thickness of the shallow aquifer called C1 increases toward Asal Lake. As results of MT inversion and numerical simulations showed, this study is focused for the potential deep reservoir between 1 and 3 km. The developed 2D model simulate a regional groundwater flow that gives a capture of fluid circulation in a regional scale. Then, the lack of a better correlation between measured and simulated temperature at Asal 6 well for the shallow part of the system above 600 m of depth (Figure 8) may be related to a localized fractures or convections cells. Another possible interpretation would be resulted by the difference of density fluid between the upper part of the system and the lower part. May be if a higher density fluid (as saline fluid) was considered in the shallow part than the deeper part, the shallow part of temperature profile measured at Asal 6 well could be well represented.

Temperatures measured in the thermal springs emerging on the periphery of Asal Lake range from 30 to 90 °C [3], and the results of the different scenarios show approximate emergence temperatures that corroborate with those measured in the thermal springs (Figure 7). Based on the chemical and isotopic characteristic of water in the Asal region,

three main types of water may co-exist in the subsurface: seawater intrusion from Ghoubbet sea, Asal Lake water, and meteoric infiltration probably originating from the meteoric water that transits from Asal Rift to Sakalol-Harralol depression or/and the meteoric water coming from the deep circulating regional aquifer [14]. The low temperature emergence observed in the hot springs of group Manda [3], their chemical composition of which is close to that of seawater, and the high rate of flow show that seawater circulation through the faults and fractures is the main source of their recharge [15]. This information can be related to the emplacement of the hot springs group Manda that are close to the H fault and are aligned more or less to this H fault and with two other major faults located south of the H fault (Figure 1). Moreover, in this case, the information corroborates our hypothesis that seawater intrusion occurs where faults/fractures exist (Figures 1 and 4).

Dissolved salts in water can change the phase conditions of liquid–vapor system and the phase relation of saline water approximated by the  $H_2O$ -NaCl system is not the same as those of pure water considered in this study. In conditions of an  $H_2O$ -NaCl system such as that of the Asal Rift, the temperature and pressure of liquid–vapor co-existence are above the critical values of pure water [44]. Despite that the fluid simulated from HYDROTHERM code is pure water [19], for saline geothermal fluid, the emplacement depth of intrusion controls significantly whether phase separation is dominantly carried out by boiling or by condensation [35]. Obviously, in this case, numerical simulations considering a saline geothermal fluid are expected to reveal the presence of a vapor phase, as proposed by the BRGM conceptual model [17]. This model is in good agreement with the gas chemical results of the Asal fumaroles and the water stable isotope data of their steam condensates [11], as well as the decrease of boron concentrations in the well geothermal fluids evidenced by geochemical analyses [3].

The total flow rate of geothermal fluid produced in well Asal 3 showed a considerable decrease of production rate and a decrease of bottom hole pressure, which were related to sulphide and silica deposits in the well with a total dissolved solids (TDS) of 116,000 ppm [33], suggesting a high potential of permeability reduction.

The  $\delta D$  and  $\delta^{18}O$  water stable isotope data for the geothermal fluids of the Asal wells and for some hot springs (Korilii, Eadkorar, and Eounda Alifitta groups; Figure 1) indicated contributions of meteoric water [3]. This meteoric contribution probably originates from the meteoric water that transits from Asal Rift to Sakalol-Harralol depression or/and the meteoric water coming from the deep circulating regional aquifer [14]. These authors showed, in the area of Sakalol-Harralol, the presence of hot springs, with high TDS Na-Cl waters, aligned in NW-SE along the main faults like in the Asal Rift. The high altitude zones of rift margins at the north and south do not seem to be potential recharge sources. However, a more representative numerical model can incorporate these zones and be tested to confirm or invalidate these hypotheses. As suggested by [14], the existence of a deep regional aquifer that may have a wide extension in Djibouti and where the Asal geothermal water has apparently common features in terms of chemical and water-isotope compositions is a good argument to highlight the need for a numerical multiphase model developed at a large regional scale. Coastal aquifers in Djibouti hosted geothermal water that could be more evolved in terms of water–rock interaction between deep fossil water and sea water intrusions [38].

## 6. Conclusions

This study emphasizes the importance of fault activity and its role in hydrothermal circulation. More specifically, the hypothesis of groundwater infiltration into Asal Lake is supported by numerical flow and heat transfer simulations performed after considering an electrical resistivity model of the area. The electrical conductivity model obtained after inversion of MT data indicates that faults can act as conduits for the circulation of water, notably the H fault, where the hanging wall of the fault behaves as a hydrogeological barrier. The variation of the electrical conductivity gradient and its increase from the south-west to the north-east of the rift are in agreement with previous work that brings to light the

presence of horizontal and vertical deformation in the south-west to north-east direction. The 2D numerical model of flow and heat transfer developed in this study was used to better understand the groundwater flow and hydrothermal circulation. Furthermore, this model confirmed that flow is generally controlled by the presence of faults acting as conduits and driven by deep heat sources. Three flow zones were defined based on the interpretation of electrical resistivity and temperature profiles. The temperature simulated with our model having these three zones is correlated with the temperature measured in well Asal 6, and is thus considered representative of the heat transfer dynamics of the system. These three flow zones are shallow groundwater flow affected by seawater and topography, an intermediate flow with a hydrothermal circulation, and a deep flow related to the hot hydrothermal circulation originating from the magmatic heat source.

In the context of geothermal energy research, future exploration drilling can be located either along this major H fault or in the northeastern part of the rift to capture a significant flow of geothermal fluid that mainly comes from the underground circulation heated by the strong geothermal gradient existing under the Asal Rift. The target drilling zone could be the deep potential reservoir unit down to a depth of 3 km to better intercept permeable zones containing supercritical water or inside the potential deep reservoir at an intermediate depth between 1 and 2 km. The Fieale Caldera and its surrounding zones should be avoided as the presence of hot rocks is thought to produce low permeability in this area.

It could be interesting to complete the present study with a second electrical resistivity model including more MT sites covering the entire surface area of the Asal–Ghoubbet Rift and extending to the north-east of the rift, notably the north Ghoubbet zone, in order to better understand the limits of the hydrothermal system identified in our study and to establish a correlation on a larger scale between the electrical resistivity gradient and the deformation velocity gradient estimated by geodetic measurements [6]. In other words, such a complementary study will help estimate which are the underground circulation paths and proportions of seawater and meteoric water recharged through the faults in the hydrothermal systems identified in this study. According to the water stable isotopes data [14], infiltration of meteoric water can possibly occur from the meteoric water that transits from Asal Rift to Sakalol-Harralol depression or/and the meteoric water coming from the deep circulating regional aquifer. Similarly, the development of a 2D numerical model of flow and heat transfer down to a depth of 10 km can help to elucidate the role of magmatic intrusion in the deep hydrothermal circulation.

**Author Contributions:** Conceptualization, A.H.A., J.R., and B.G.; methodology, A.H.A.; validation, J.R., B.G., B.S., and A.H.A.; formal analysis, A.H.A.; investigation, A.H.A.; resources, J.R. and B.G.; data curation, A.H.A.; writing—original draft preparation, A.H.A., J.R., and B.G.; writing—review and editing, A.H.A., J.R., B.G., and B.S.; visualization, A.H.A.; supervision, J.R. and B.G.; project administration, J.R.; funding acquisition, J.R. and B.G. All authors have read and agreed to the published version of the manuscript.

**Funding:** This research was funded by the Islamic Development Bank through a PhD scholarship awarded to the first author as well as research funds attributed by the Natural Sciences and Engineering Research Council of Canada given to the second and third authors.

**Acknowledgments:** We would like to thank the contribution and support of the INRS. Gaeten Sakindi (Electricity Company of Rwanda), Abdourahman Haga, Awaleh Abdi, and Djama Robleh (Ministry of Energy and Natural Resources of the Republic Djibouti) are further acknowledged for their precious help on this project.

**Conflicts of Interest:** The authors declare no conflict of interest. The funders had no role in the design of the study; in the collection, analyses, or interpretation of data; in the writing of the manuscript; or in the decision to publish the results.

## Appendix A

Table A1. Verification of mesh independence for simulation of scenario 1.

Number of Elements	Temperature at 1600 m Depth in Asal 6 Well $T$ (°C)	Absolute Value of Relative Difference (%)
1200	238.931	—
2400	248.257	0.039
4000	254.387	0.024
4800	256.327	0.007
10,000	255.095	0.004

## References

- Bellani, S.; Gherardi, F. Thermal Overview of an Area NW of the Larderello Geothermal Field, Italy. *GRC Trans.* **2013**, *37*, 231–236.
- Mlynarski, M.; Zlotnicki, J. Fluid circulation in the active emerged Asal rift (east Africa, Djibouti) inferred from self-potential and Telluric–Telluric prospecting. *Tectonophysics* **2001**, *339*, 455–472. [[CrossRef](#)]
- Sanjuan, B.; Michard, G.; Michard, A. Origine des substances dissoutes dans les eaux des sources thermales et des forages de la région Asal-Ghoubbet (République de Djibouti). *J. Volcanol. Geotherm. Res.* **1990**, *43*, 333–352. [[CrossRef](#)]
- Dobre, C.; Manighetti, I.; Dorbath, L.; Dorbath, C.; Bertil, D.; Delmond, J.C. Crustal structure and magmato-tectonic processes in an active rift (Asal-Ghoubbet, Afar, East Africa): 2. Insights from the 23-year recording of seismicity since the last rifting event. *J. Geophys. Res. Space Phys.* **2007**, *112*. [[CrossRef](#)]
- Dobre, C.; Peltzer, G. Fluid-controlled faulting process in the Asal Rift, Djibouti, from 8 yr of radar interferometry observations. *Geology* **2007**, *35*, 69. [[CrossRef](#)]
- Vigny, C.; De Chabaliere, J.-B.; Ruegg, J.-C.; Huchon, P.; Feigl, K.L.; Cattin, R.; Asfaw, L.; Kanbari, K. Twenty-five years of geodetic measurements along the Tadjoura-Asal rift system, Djibouti, East Africa. *J. Geophys. Res. Space Phys.* **2007**, *112*. [[CrossRef](#)]
- Manighetti, I.; Tapponnier, P.; Gillot, P.Y.; Jacques, E.; Courtillot, V.; Armijo, R.; Ruegg, J.C.; King, G. Propagation of rifting along the Arabia-Somalia Plate Boundary: Into Afar. *J. Geophys. Res. Space Phys.* **1998**, *103*, 4947–4974. [[CrossRef](#)]
- Pinzuti, P.; Mignan, A.; King, G.C. Surface morphology of active normal faults in hard rock: Implications for the mechanics of the Asal Rift, Djibouti. *Earth Planet. Sci. Lett.* **2010**, *299*, 169–179. [[CrossRef](#)]
- Stein, R.S.; Briole, P.; Ruegg, J.-C.; Tapponnier, P.; Gasse, F. Contemporary, Holocene, and Quaternary deformation of the Asal Rift, Djibouti: Implications for the mechanics of slow spreading ridges. *J. Geophys. Res. Space Phys.* **1991**, *96*, 21789–21806. [[CrossRef](#)]
- Correia, H.; Demange, J.; Fabriol, R.; Gerard, A.; Varet, J. *Champ Géothermique d'Asal: Synthèse des Données Disponibles au 1er Janvier 1983*; Final BRGM Report 83 SGN 022 GTH; BRGM: Orleans, France, 1983.
- Marini, L. *Geochemistry of North Ghoubbet-Asal Region*; Geothermica Italiana Report 551-9-LUI; Geothermica: Reykjavík, Iceland, 1987.
- Gadalia, A.; Traineau, H. *Deux Champs Géothermiques de Rifts Océaniques Émergés: Krafla (Islande) et Asal (République de Djibouti). Une Étude Comparative des Contextes Géologiques et des Méthodes d'Exploration*; Final BRGM Report 84 SGN 216 IRG; BRGM: Orleans, France, 1984.
- D'Amore, F.; Giusti, D.; Abdallah, A. Geochemistry of the high-salinity geothermal field of Asal, Republic of Djibouti, Africa. *Geothermics* **1998**, *27*, 197–210. [[CrossRef](#)]
- Awaleh, M.O.; Boschetti, T.; Soubaneh, Y.D.; Baudron, P.; Kawalieh, A.D.; Dabar, O.A.; Ahmed, M.M.; Ahmed, S.I.; Daoud, M.A.; Egueh, N.M.; et al. Geochemical study of the Sakalol-Harralol geothermal field (Republic of Djibouti): Evidences of a low enthalpy aquifer between Manda-Inakir and Asal rift settings. *J. Volcanol. Geotherm. Res.* **2017**, *331*, 26–52. [[CrossRef](#)]
- Fouillac, C.; Fabriol, R.; Lundt, F. *Champ Géothermique d'Asal. Synthèse des Données Hydrogéologiques et Géochimiques Disponibles au 1er Janvier 1983*; Final BRGM Report 83 SGN 022 GTH; BRGM: Orleans, France, 1983.
- Houssein, D.E.; Axelsson, G. Geothermal resources in the Asal Region, Republic of Djibouti: An update with emphasis on reservoir engineering studies. *Geothermics* **2010**, *39*, 220–227. [[CrossRef](#)]
- Demange, J.; Puvilland, P. *Champ Géothermique d'Asal. Synthèse des Données*; Rapport C.F.G; BRGM: Orleans, France, 1993.
- Hayba, D.O.; Ingebritsen, S.E. Multiphase groundwater flow near cooling plutons. *J. Geophys. Res. Space Phys.* **1997**, *102*, 12235–12252. [[CrossRef](#)]
- Kipp, K.L.; Hsieh, P.A.; Charlton, S.R. *Guide to the Revised Ground-Water Flow and Heat Transport Simulator: HYDROTHERM—Version 3*; USGS: Reston, VA, USA, 2008.
- Yamaya, Y.; Alanis, P.K.B.; Takeuchi, A.; Cordon, J.M.; Mogi, T.; Hashimoto, T.; Sasai, Y.; Nagao, T. A large hydrothermal reservoir beneath Taal Volcano (Philippines) revealed by magnetotelluric resistivity survey: 2D resistivity modeling. *Bull. Volcanol.* **2013**, *75*, 729. [[CrossRef](#)]
- Simpson, F.; Bahr, K. *Practical Magnetotellurics*, 1st ed.; Cambridge University Press: Cambridge, UK, 2005.
- Sakindi, G. Three-Dimensional Inversion of Magnetotelluric Data: Geological-Geothermal Interpretation of Asal Geothermal Field, Djibouti. Master's Thesis, United Nations University, Reykjavik, Iceland, 2015.

23. Szarka, L.; Menvielle, M. Analysis of rotational invariants of the magnetotelluric impedance tensor. *Geophys. J. Int.* **1997**, *129*, 133–142. [[CrossRef](#)]
24. Constable, S.C.; Parker, R.L.; Constable, C.G. Occam's inversion: A practical algorithm for generating smooth models from electromagnetic sounding data. *Geophysics* **1987**, *52*, 289–300. [[CrossRef](#)]
25. Rung-Arunwan, T.; Siripunvaraporn, W.; Utada, H. On the Berdichevsky average. *Phys. Earth Planet. Inter.* **2016**, *253*, 1–4. [[CrossRef](#)]
26. Rung-Arunwan, T.; Siripunvaraporn, W.; Utada, H. Use of ssq rotational invariant of magnetotelluric impedances for estimating informative properties for galvanic distortion. *Earth Planets Space* **2017**, *69*, 80. [[CrossRef](#)]
27. Spichak, V.; Manzella, A. Electromagnetic sounding of geothermal zones. *J. Appl. Geophys.* **2009**, *68*, 459–478. [[CrossRef](#)]
28. Sanford, W.E. A simulation of the hydrothermal response to the Chesapeake Bay bolide impact. *Geofluids* **2005**, *5*, 185–201. [[CrossRef](#)]
29. Driesner, T.; Geiger, S. Numerical Simulation of Multiphase Fluid Flow in Hydrothermal Systems. *Rev. Miner. Geochem.* **2007**, *65*, 187–212. [[CrossRef](#)]
30. Raguanel, M.; Driesner, T.; Bonneau, F. Numerical modeling of the geothermal hydrology of the Volcanic Island of Basse-Terre, Guadeloupe. *Geotherm. Energy* **2019**, *7*, 1–16. [[CrossRef](#)]
31. Weis, P. The dynamic interplay between saline fluid flow and rock permeability in magmatic-hydrothermal systems. *Geofluids* **2015**, *15*, 350–371. [[CrossRef](#)]
32. Gaudin, D.; Finizola, A.; Delcher, E.; Beauducel, F.; Allemand, P.; Delacourt, C.; Brothelande, E.; Peltier, A.; Di Gangi, F. Influence of rainfalls on heat and steam fluxes of fumarolic zones: Six months records along the Ty fault (Soufrière of Guadeloupe, Lesser Antilles). *J. Volcanol. Geotherm. Res.* **2015**, *302*, 273–285. [[CrossRef](#)]
33. Jalludin, M. *State of Knowledge of Geothermal Provinces of Republic of Djibouti*; UNU training KENGEN: Naivasha, Kenya, 2007.
34. Vosteen, H.-D.; Schellschmidt, R. Influence of temperature on thermal conductivity, thermal capacity and thermal diffusivity for different types of rock. *Phys. Chem. Earth Parts A/B/C* **2003**, *28*, 499–509. [[CrossRef](#)]
35. Scott, S.; Driesner, T.; Weis, P. Boiling and condensation of saline geothermal fluids above magmatic intrusions. *Geophys. Res. Lett.* **2017**, *44*, 1696–1705. [[CrossRef](#)]
36. Houssein, I.; Sanjuan, B.; Michard, G. *Indices Géochimiques de l'Existence d'un Fluide à 210 °C dans la Région d'Obock (République de Djibouti)*; Note au C.R.A.S. t.316, Série II; Note au C.R.A.S. Paris, France, 1993; pp. 771–776.
37. Sanjuan, B. Use of a new Sodium/Lithium (Na/Li) geothermometric relationship for High-Temperature (HT) geothermal fluids derived from seawater/basalt interaction processes: Application to the Djibouti case. In Proceedings of the Third East African Rift Geothermal Conference, Djibouti, Djibouti, 22–25 November 2010; p. 22.
38. Boschetti, T.; Awaleh, M.O.; Barbieri, M. Waters from the Djiboutian Afar: A Review of Strontium Isotopic Composition and a Comparison with Ethiopian Waters and Red Sea Brines. *Water* **2018**, *10*, 1700. [[CrossRef](#)]
39. Zan, L.; Gianelli, G.; Passerini, P.; Troisi, C.; Haga, A.O. Geothermal exploration in the republic of djibouti: Thermal and geological data of the hanlé and asal areas. *Geothermics* **1990**, *19*, 561–582. [[CrossRef](#)]
40. Smittarello, D.; Grandin, R.; De Chabaliér, J.; Doubré, C.; Deprez, A.; Masson, F.; Socquet, A.; Saad, I. Transient deformation in the Asal-Ghoubbet Rift (Djibouti) since the 1978 diking event: Is deformation controlled by magma supply rates? *J. Geophys. Res. Solid Earth* **2016**, *121*, 6030–6052. [[CrossRef](#)]
41. Harris, R.N.; Fisher, A.T.; Chapman, D.S. Fluid flow through seamounts and implications for global mass fluxes. *Geology* **2004**, *32*, 725. [[CrossRef](#)]
42. Schardt, C.; Anderson, T.F.; Raiswell, R. Controls on Heat Flow, Fluid Migration, and Massive Sulfide Formation of an Off-axis Hydrothermal System—The Lau Basin Perspective. *Am. J. Sci.* **2006**, *306*, 103–134. [[CrossRef](#)]
43. Lupi, M.; Geiger-Boschung, S.; Graham, C.M. Hydrothermal fluid flow within a tectonically active rift-ridge transform junction: Tjörnes Fracture Zone, Iceland. *J. Geophys. Res. Space Phys.* **2010**, *115*. [[CrossRef](#)]
44. Bischoff, J.L.; Pitzer, K.S. Liquid-vapor relations for the system NaCl-H<sub>2</sub>O: Summary of the P-T-x surface from 300° to 500 °C. *Am. J. Sci.* **1989**, *289*, 217248. [[CrossRef](#)]

Article

# New Insights into Crust and upper Mantle Structure in Guangdong Province, China and Its Geothermal Implications

Jian Kuang <sup>1</sup>, Shihua Qi <sup>1,\*</sup> and Xiangyun Hu <sup>2</sup>

<sup>1</sup> State Key Laboratory of Biogeology and Environmental Geology, China University of Geosciences, Wuhan 430074, China; kuangjian@cug.edu.cn

<sup>2</sup> Hubei Subsurface Multiscale Imaging Laboratory, Institute of Geophysics and Geomatics, China University of Geosciences, Wuhan 430074, China; xyhu@cug.edu.cn

\* Correspondence: shihuaqi@cug.edu.cn

**Abstract:** Southeast Asia contains significant natural geothermal resources. However, the mechanism for generating geothermal anomalies by the crust–mantle structure still needs to define. In this study, we focused on Guangdong Province, China. We conducted three magnetotelluric profiles to interpret the crust and upper mantle structure beneath the Guangdong Province and its geothermal implications. Based on data analysis results, a two-dimension inversion was conducted on the dataset. The inversion model revealed that there is a presence of upwelling channels, and some channels are connected with shallow crustal fault zone; the thickness of crust and lithosphere in Guangdong Province is relatively thin. Such a special crust and upper mantle structure form high surface heat flow. Merged with previous research, our results imply that massive Late Mesozoic granites, which contain high radioactive heat generating elements, are distributed on the surface and underground of Guangdong Province. Based on the correlation between high radioactive Late Mesozoic granites, crust–upper mantle structure, surface heat flow, and locations of natural hot springs, we established a geothermal conceptual model to visualize the origin of a current geophysical and geothermal anomaly in Guangdong Province.

**Keywords:** magnetotellurics; 2D inversion; crust–upper mantle structure; Late Mesozoic granite; geothermal energy; Guangdong Province

**Citation:** Kuang, J.; Qi, S.; Hu, X. New Insights into Crust and upper Mantle Structure in Guangdong Province, China and Its Geothermal Implications. *Energies* **2021**, *14*, 2236. <https://doi.org/10.3390/en14082236>

Academic Editors: Renato Somma and Carlo Roselli

Received: 24 February 2021

Accepted: 14 April 2021

Published: 16 April 2021

**Publisher's Note:** MDPI stays neutral with regard to jurisdictional claims in published maps and institutional affiliations.



**Copyright:** © 2021 by the authors. Licensee MDPI, Basel, Switzerland. This article is an open access article distributed under the terms and conditions of the Creative Commons Attribution (CC BY) license (<https://creativecommons.org/licenses/by/4.0/>).

## 1. Introduction

Southeast Asia straddles the boundary between the Pacific/Philippine Plate and Eurasia Plate and locates in the South China fold belt. It is mainly located on the Cathaysian plate. The geology is highly diverse, and the tectonic setting ranges from the amalgamation between the Yangtze block and the Cathaysia Block during the Neoproterozoic [1] to the subduction of the Pacific/Philippine Plate in the Cenozoic [2]. Guangdong Province is located on the Cathaysian plate and has the same tectonic evolution as the Cathaysian plate (Figure 1). The crust and upper mantle structure of Guangdong Province in this area have shaped by these tectonic impacts, which are mainly manifested as follows:

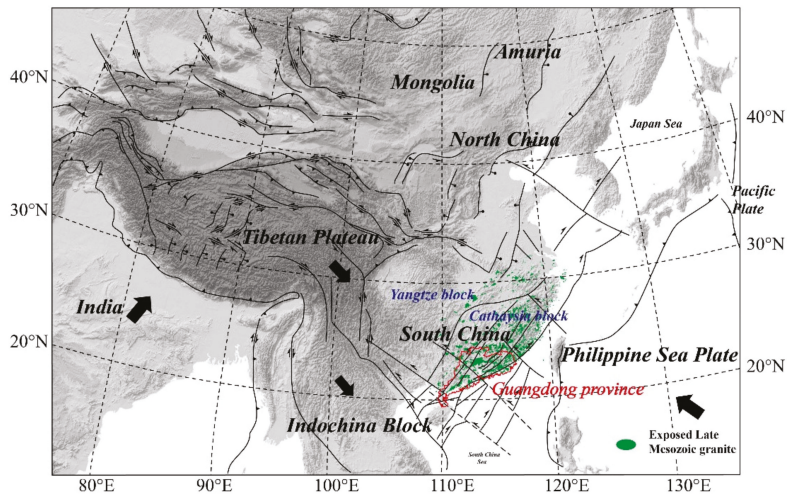


**Figure 1.** Tectonic map in East Asia and distribution of exposed Late Mesozoic granite in South China (modified from Kuang et al. [3]). The green area is the distribution of exposed Late Mesozoic granite, modified from Zhou et al. [4]. The red line is Guangdong Province.

First, the predominant feature in Guangdong Province is the widespread exposure of Mesozoic granite with an exposed area of 60,000 km<sup>2</sup>, accounting for about one-third of the area, considered the result of the multi-stage emplacement of magmatic rocks [3]. Such spatial-temporal distribution characteristics of the Mesozoic granites have been attributed to the dynamic mechanism associated with subduction and interaction with multiple plates [5,6]. These granites, Late Mesozoic granite, in particular, were formed by the remelting of the Neoproterozoic and Paleozoic crust [7] and extremely rich heat-producing elements (Th, U, and K) with average heat production of more than 5  $\mu\text{W}/\text{m}^3$  [8]. Second, various geophysical methods have led to the thin lithosphere (~80 km) present in South China [9–12]. Combining with studies on mantle peridotite enclaves/xenoliths in Paleozoic suggested that a lithospheric thinning process has occurred in Meso-Cenozoic [13–15]. Furthermore, there are abundant NE- and NW/WNW-trending faults and associated fold-and-fault zones in Southeast Asia ([6]; Figure 1). Consequently, these processes shaped Southeast Asia into a geothermally active region and southeast China into the second-largest high heat flow region in China, where there are many natural hot springs spanning an unusually large area ([16,17]; Figure 2). The large area geothermal anomaly constitutes an impressive geothermal utilization prospective area; however, it has not been well exploited due to the deficiency of comprehensive studies of the geothermal anomaly in southeast China.

Recently, a study based on Bouguer gravity data has suggested that the geothermal anomalies in Guangdong Province originated from the combined effect of asthenosphere upwelling and granite, which emplaced along the faults [18]. Another study based on heat flow data and tectonic setting stated that the high surface heat flow values correspond to the lithosphere's thinning [17]. However, these results do not fully explain the crust structure, geothermal anomalies, and their interrelationships. These results do not fully account for the crust structure, geothermal anomalies, and their interrelationships, which hinders the subsequent utilization of geothermal resources, the implementation of relevant simulation work, and analysis of the geothermal polygeneration system [19–21].

To solve these problems, the primary goals are to constrain the crust–mantle structure and to establish the association between geothermal anomalies and the crust–mantle structure. In this study, we conducted three magnetotelluric profiles in Guangdong Province, China, where these areas are abundant in the geothermal resource. Further, the granitic

intrusions and faults are available for analyzing the effects of different factors on the generation of hot springs. We present new imaging results of the crust and upper mantle structure across a major portion of Guangdong Province and establish a geothermal conceptual model to decipher geothermal formation in Guangdong Province.

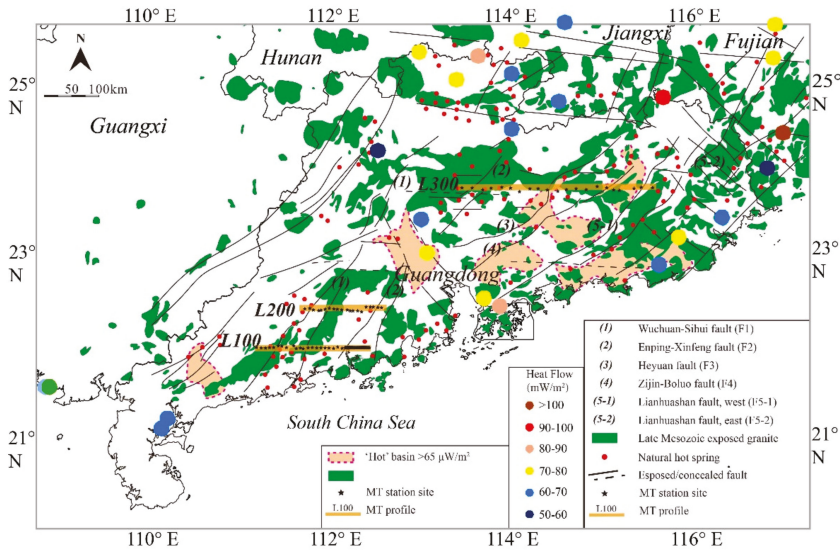


**Figure 2.** Tectonic map of Guangdong Province and adjacent area. The distribution of faults is modified from Wang et al. [6]. The yellow lines are the magnetotellurics profiles. The heat flow values and “hot” basin are modified from Jiang et al. [17].

## 2. Geological Setting

The Guangdong Province has narrowed due to three major convergent tectonic plates since the Mesozoic, which are the subduction of the Pacific Plate to the east, the subduction of the India Plate beneath the Eurasia Plate to the southwest, and the convergence between North and South China Blocks to the north (Figure 1). As a response to this tectonic event multi-plate interaction, this region underwent a widespread tectonic thermal event and intracontinental deformation. These events are characterized by massive magmatic emplacement, widespread shortening, thrusting, and decollement in the Mesozoic [4,6]. Specifically, these events could be evidenced by the widespread granitoid belts of different ages and large-scale fault zones. Such features were mainly caused by the multi-plate interaction [7] or by the advance and retreat of the Pacific Plate [6,22]. Later on, during the Cenozoic, a basin and range-like region and widely distributed basalt were generated in the coastal areas [23,24]. These tectonic events have been suggested to be formed by asthenospheric convection-driven extension and thinning of continental crust. Such asthenospheric convection is controlled by the collision between India Plate and Eurasia Plate (for a review, see [3]).

## 3. MT Data Acquisition

From July to August 2013, three MT profiles (L100, L200, and L300) with 440 km and 103 stations were established to obtain the electrical structure of crust and mantle in southeast China (Figure 2). The L100 is divided into two parts. The east part has a length of 40 km with an interval of 1 km. The west part has a length of 100 km with a station spacing of 5 km. L200 has a length of 100 km with a station spacing of 5 km. The L300 has a length of 200 km with a station spacing of 10 km. The L100 and L200 cross the Wuchuan-Sihui fault zone and the Enping-Xinfeng fault zone (Figure 2). The L300 crosses

the Enping-Xinfeng fault zone, Heyan fault zone, Zijin-Boluo fault zone, and Lianhuashan fault zone (south section of the Zhenghe-Dapu fault zone) (Figure 2). Extending direction of the MT profiles is designed to be east-west trending.

MT data were collected with Phoenix MTU-5 instruments. All 5 orthogonal components of the electromagnetic field (Ex, Ey, Hx, Hy, and Hz) were recorded. The x-axis and the y-axis are magnetic N-S trending and magnetic E-W trending, respectively. The horizontal electric (E) and magnetic (H) fields are measured in the time domain and converted to the frequency domain by Fourier transform to receive the MT response function. Before the field data collection, we performed calibration and consistency experiments on all the instruments and equipment used to ensure that the instruments invested during the construction process work properly. The first and second Supplementary Figures (Supplementary Figures S1 and S2) show the calibration results of the V5 system 2000 equipment box and probe, respectively. With a recording time no less than 18 h, MT data were obtained in an average period of 0.003–2000 s. The MT time-series were transformed into frequency domain with fast Fourier transform, and the frequency-dependent transfer function elements were calculated by standard remote reference [25], robust routines [26].

#### 4. MT Data Analysis, Inversion, and Result

##### 4.1. MT Data Analysis

In magnetotelluric analyses, the regional structure's response can be concealed by the galvanic distortion caused by small-scale inhomogeneities near the surface. In this work, the multi-site multi-frequency distortion decomposition, which is based on the Goom-Bailey (GB) decomposition method [27], was used to estimate the galvanic distortion of the MT response and the regional strike and dimension of magnetotelluric data before two-dimensional inversion and obtained the best electrical principal axis information of the three profiles in the study area according to this method (Supplementary Table S1). Under the assumption that the surface layer is partially covered by 3D on 2D structural paper, the observed impedance tensor ( $Z$ ) was decomposed [27], the formula is as follows:

$$Z = RCZ_{2-D}R^T = gRTSAZ_{2-D}R^T = CRZ_{2-D}R^T \quad (1)$$

$C$  is the frequency-independent local distortion matrix,  $g$  is a scalar factor,  $R$  is the rotation matrix,  $R^T$  is the transpose matrix of  $R$ ,  $T$  is the torsion matrix,  $S$  is the shear matrix,  $A$  is the decomposition tensor, and  $Z_{2-D}$  is the actual 2D impedance tensor of the region.  $T$  can be expressed as:

$$T = \begin{bmatrix} 1 & -t \\ t & 1 \end{bmatrix}, R = \begin{bmatrix} \cos \theta & \sin \theta \\ -\sin \theta & \cos \theta \end{bmatrix}, S = \begin{bmatrix} 1 & e \\ e & 1 \end{bmatrix}, A = \begin{bmatrix} 1+s & 0 \\ 0 & 1-s \end{bmatrix} \quad (2)$$

$t$  is the torsion factor,  $\theta$  is the strike angle,  $e$  is the shear factor, and  $s$  is the splitting scale factor.  $AZ_{2-D}$  is solved as a whole due to its nonuniqueness:

$$\begin{bmatrix} Z_{xx} & Z_{xy} \\ Z_{yx} & Z_{yy} \end{bmatrix} = \begin{bmatrix} \cos \theta & \sin \theta \\ -\sin \theta & \cos \theta \end{bmatrix} \begin{bmatrix} 1 & -t \\ t & 1 \end{bmatrix} \begin{bmatrix} 1 & e \\ e & 1 \end{bmatrix} \begin{bmatrix} 0 & Z_{TE} \\ -Z_{TM} & 0 \end{bmatrix} \begin{bmatrix} \cos \theta & -\sin \theta \\ \sin \theta & \cos \theta \end{bmatrix} \quad (3)$$

There are 8 equations and 7 unknowns when the impedance tensor is expanded in the form of a real part and an imaginary part. The parameters of regional impedance, strike, and distortion can be obtained by using the least-squares method. Furthermore, the whole frequencies of the MT data are rotated to the respective strike directions before inversion. The GB strike directions of all sites for whole frequencies were depict using the rose diagram (Figure 3). As shown in Figure 4, the calculated structural strike almost coincides with the strike of the large-scale fault in Guangdong Province, China. The main electrical axes of the three profiles are mainly NE, which are consistent with the large structural trend of southeast China [6].

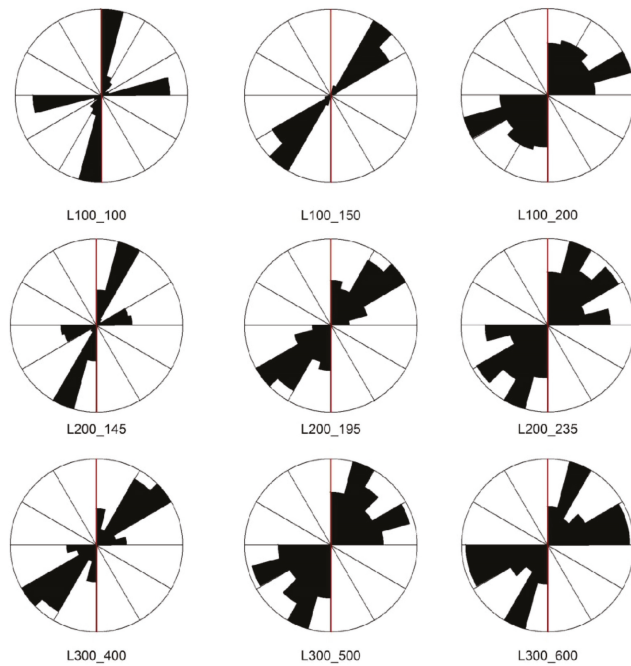


**Figure 3.** Multi-frequency rose diagrams of geoelectric strike direction of some stations by using the Goom–Bailey (GB) decomposition.

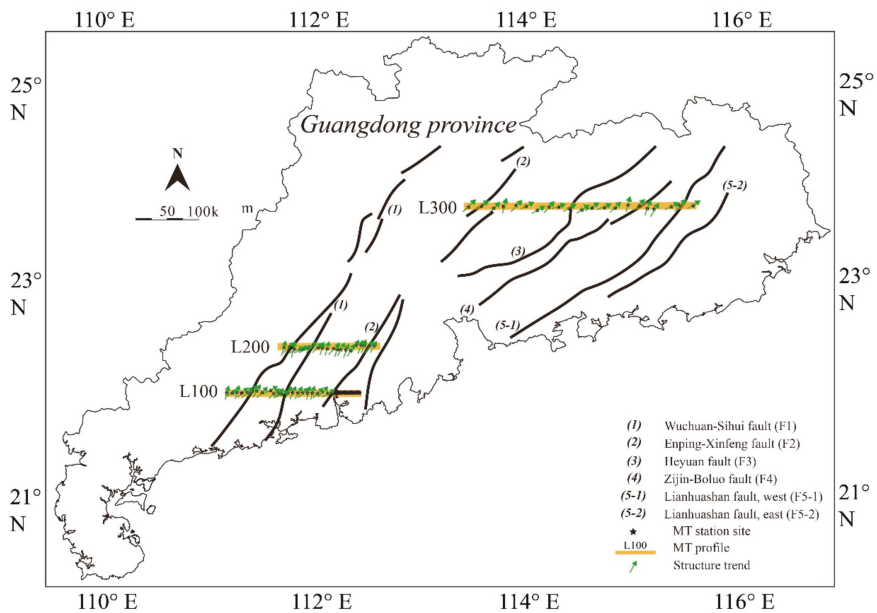


**Figure 4.** The structural trend of the survey points in the three profiles. The orange lines are major regional deep-seated fault, the yellow line is the MT profile, the pink arrow is the structure trend, and the black star is the MT station.

#### 4.2. MT Data Inversion

Using the nonlinear conjugate gradient algorithm developed by Rodi and Mackie [28], two-dimensional inversion analysis of the rotated data is carried out, and the algorithm is implemented in the data interpretation package WinGLink. Before calculating the final model, several inversion parameters should be set to fit the data.

The collected magnetotelluric data can be divided into two parts, which includes data with a magnetic field direction perpendicular to propagation direction (TM) and data with the electric field direction perpendicular to propagation direction (TE), and the inversion modes include TM mode, TE mode, and TE and TM joint inversion mode. For TM mode it is more sensitive to the low-resistance structure in the shallow part and is susceptible to the influence of static displacement, which mainly produces current-type distortion; the TE mode well reflects the deep and high-resistance structure and is less affected by the static displacement, which is prone to inductive distortion. For measured data, it is generally preferred to use TM model data for two-dimensional inversion [29,30]. Consequently, to select the inversion results more suitable for the geological parameters, TE model inversion, TM model inversion, and TE and TM joint model inversion were carried out for the L300, respectively (Figure 5). The TE model inversion has a good reflection on the shallow high-resistance layer. However, the low-resistance layer is missing, and it is impossible to analyze the fracture characteristics of the underground structure. The TM model highlights the low-resistance layer well and has a perfect correspondence with the deep-seated fault in the Guangdong Province. There is a certain similarity between TE and TM joint inversion model and the TM model. However, the result of joint inversion is not ideal due to the large fitting difference between the TE and TM joint model and TM model. Accordingly, in this study, the TM model of nonlinear conjugate gradient (NLCG) two-dimensional was selected for inversion. The NLCG inversion method has the advantages of fast operation layer speed, less memory occupation, multimode inversion, avoiding the single inversion mode and multi-solution of inversion results. The results are more comprehensive and selective, and the inversion model is more intuitive, reflecting the underground problems clearly.

To obtain the best regularization parameter ( $\tau$ ) values, we selected different  $\tau$  values ( $\tau = 1, 3, 5, 10, 20, 50$ ) for the L300, and carry out inversion, respectively. In the inversion process, the other parameters remain unchanged with the weighted parameter is 1.5 and the error range is 5%. Meanwhile, the fitting difference root-mean-square (RMS) value of each inversion is discriminated (Supplementary Table S2). Figure 6 displays that,  $\tau = 1$ , it can be seen from the figure that its reflection effect on the shallow part is better, however, for the deep information, the overall performance is low resistance, which does not achieve good results;  $\tau = 3$ , both the shallow part and the deep part have a good reflection effect;  $\tau = 5$  and  $\tau = 10$ , it can be seen from figures that there is no significant difference in the whole, and it also has a large similarity with  $\tau = 3$ . However, it does not obviously reflect the highly conductive upper mantle layer;  $\tau = 20$  and  $50$ , the inversion results are much smoother than that in others. Although it reflects well on deep electrical characteristics, it does weakly on shallow formation information. Therefore, 3 is the best  $\tau$  value, and it is used in the later inversion. Moreover, the initial resistivity was set as  $100 \Omega\cdot\text{m}$ ; the homogeneous half-space initial model was adopted; the WinGLink data inversion software was used for inversion.

#### 4.3. Inversion Results

The most notable feature of the 2D inversion result is the large area of low resistance area along with these profiles (Figure 7). Each profile's conductivity has a three-layered structure in vertical, and the low conductors are inserted between the high conductors across these profiles. The overall RMS of the L100, L200, and L300 are 4.4, 4.7, and 5.2, respectively. As demonstrated in Figure 7, the RMS value of most of the stations of the three profiles is below 4.5, and the RMS value of 90% of the station is less than 6. The 190 and 195 stations of the L100, which are located near Yangjiang City and Yangdong County, have

a relatively large RMS value and may be greatly disturbed by human activity, resulting in poor data fitting in two-dimensional inversion. Similarly, the 225 station of the L200, which is located near Enping City, has a relatively large RMS value. The overall RMS of the L300 is much larger than that of L100 and L200, and 20% of the L300 stations have high RMS values ( $>6$ ). However, there is no significant human disturbance near these stations with high RMS values. Thus, we speculate that there are complex fault systems near these stations, and the RMS is affected by a three-dimensional inhomogeneous geological body near the surface.

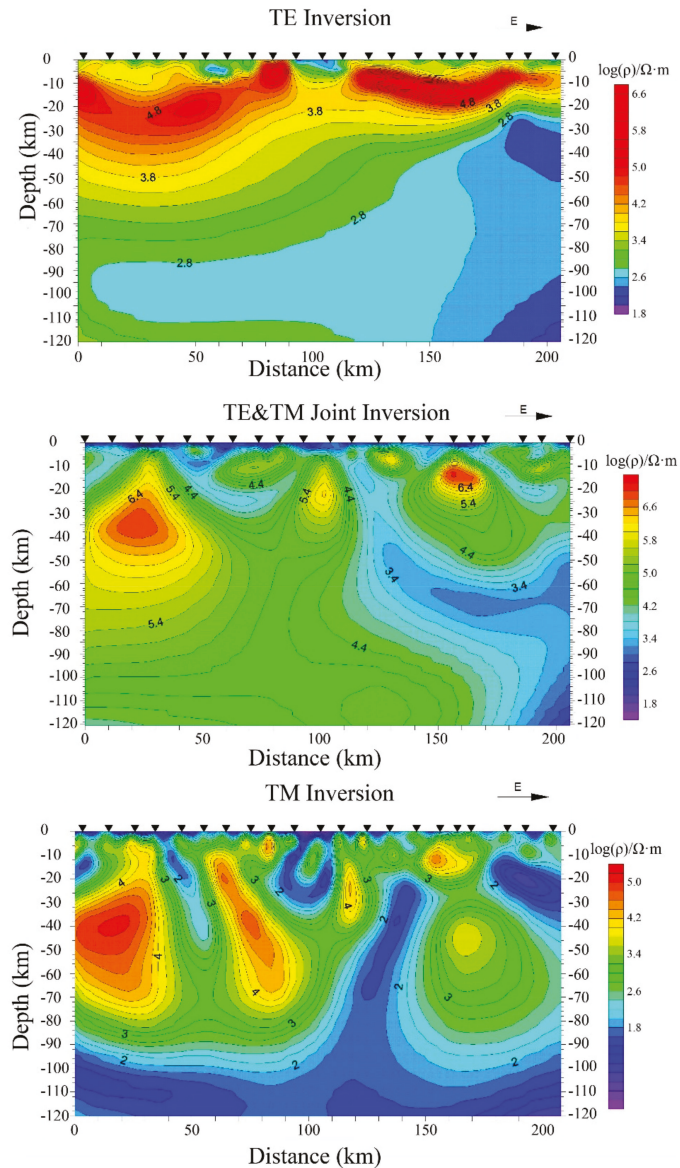


Figure 5. Compares of NLCG 2D inversion result of three inversion models (TE, TE and TM, and TM) of MT profile L300.

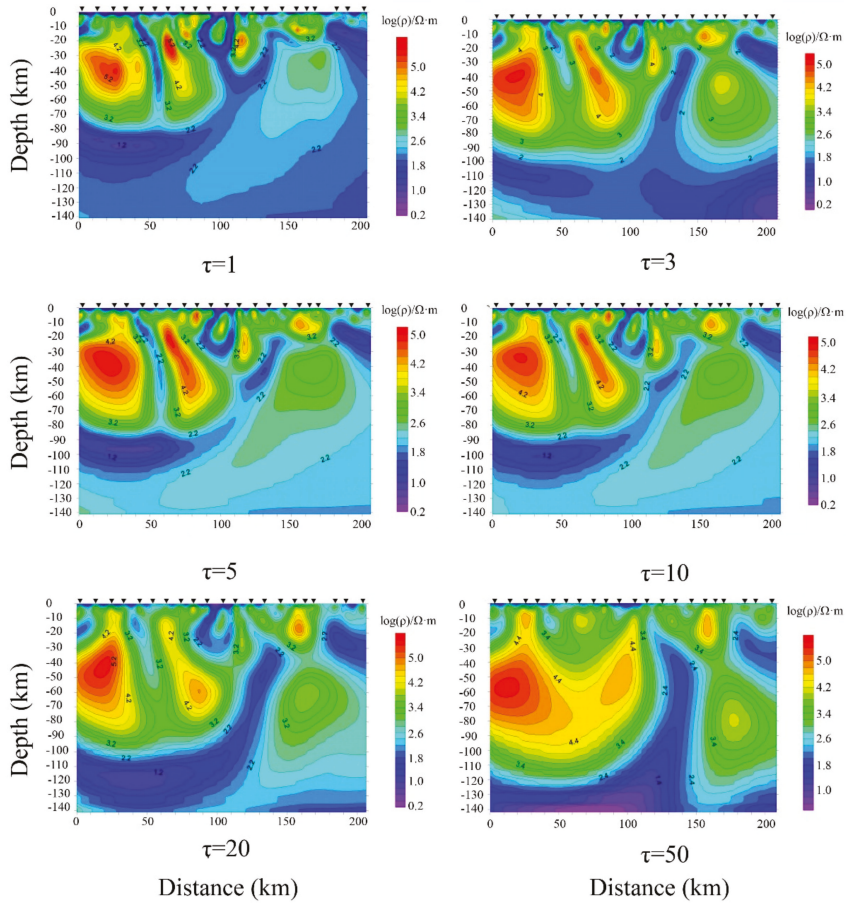


Figure 6. 2D inversion results of NLCG in L300 TM mode under different the regularization parameter ( $\tau$ ) values.

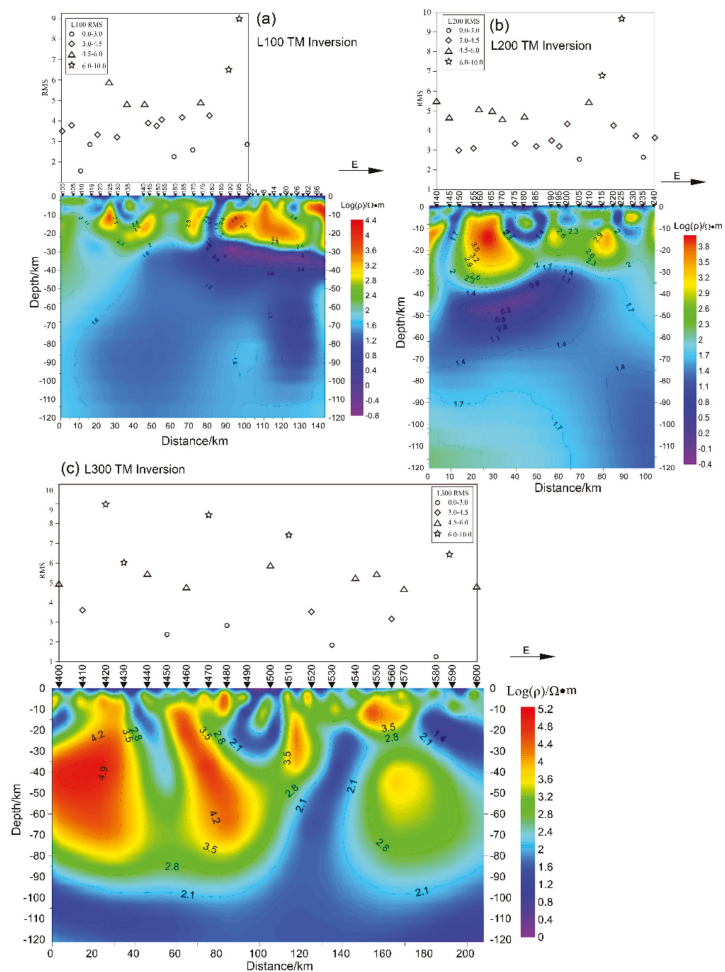


Figure 7. RMS distribution along these three profiles for the original 2D inversion.

## 5. Interpretations and Discussions

### 5.1. Interpretations of the Model

As can be seen from Figure 8, the resistivity increases with the depth in vertical profile, which contains three layers: crust sedimentary caprock in the top, middle and lower crust in the middle, and mantle to the bottom.

The top layer's thickness gradually thins from west to east in L100 and L200 profiles ranging from 9 km to 2 km thickness, while it is about 4 km thickness in the L300 profile. Similarly, crust thickness gradually thins from west to east in all profiles with an average of ~30 km even though the crust's thickness is various with 22 km in local. The high-resistance layer in the entire crust is cut into several blocks by the low-resistance bodies, forming a discontinuous spatial distribution of the high-resistance layer. A large area of low resistance layer has a resistivity value of 0.4–100  $\Omega \cdot m$  in the lower layer of L100 and L200 profiles, and it tends to extend to  $-120$  km or deeper. Furthermore, there is a large area of low resistivity in the upper mantle with a depth below 90 km, which is supposed to be asthenospheric. The presence of a discontinuous low resistivity layer in the range of  $-10$  to  $-30$  km suggests multiple channels for upwelling of the mantle sources or

recommends a high-conductor formed by the alteration or melting of wall rocks caused by mantle materials. Specifically, Figure 8 shows the  $F_3$  (Heyuan Fault) adjacent to Heyuan City is connected with the asthenospheric upwelling in the L300. Our previous geophysical exploration in the Heyuan Basin confirmed that the Heyuan Fault controls Cenozoic basalt occurrence [3]. Moreover, all the regional fault zones are well reflected in the inversion model, and the low resistance zone near the surface matches with the actual location of fracture exposure.

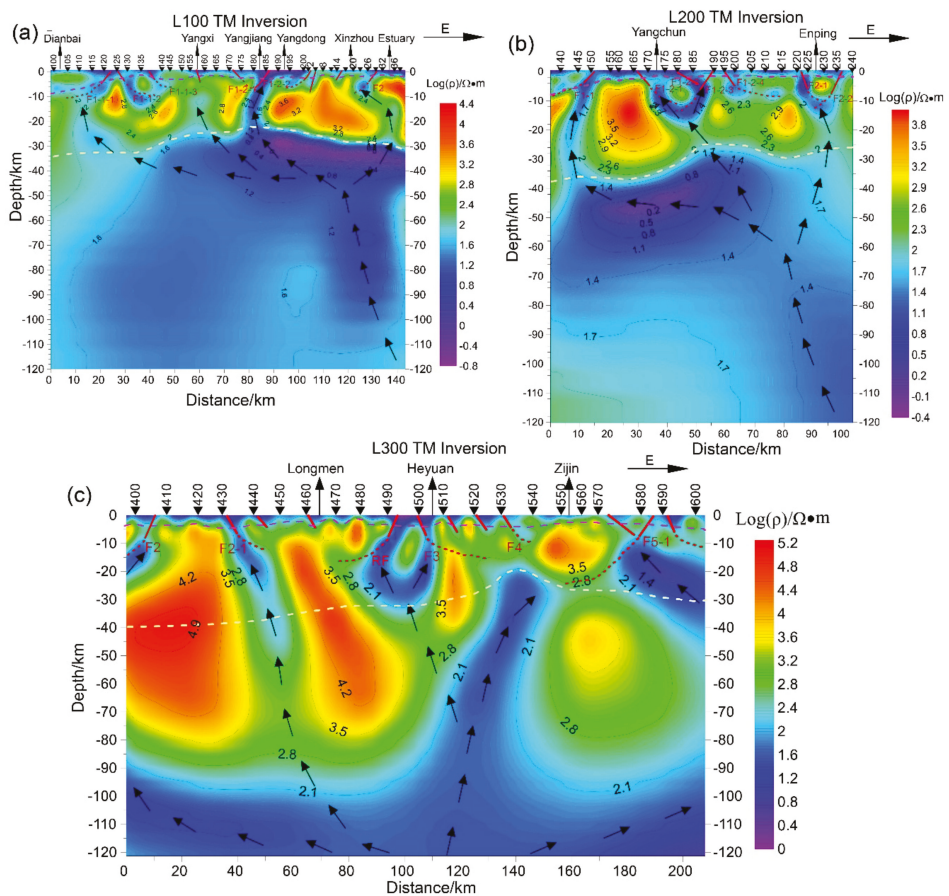


**Figure 8.** Preferred inversion model of electrical resistivity for the upper 120 km along the profiles with station locations and position of major tectonic features. F1-1, West part of F1; F1-2, East part of F1; F1, F2, F3, F4, and F5 are identical to that in Figure 2. The RF is the Renzishi Fault. The purple dotted line represents the inferred boundary between strata and Jurassic and Cretaceous granite; the yellow dotted line represents the inferred Moho boundary; the black arrow represents the upwelling direction of mantle material.

## 5.2. Lithosphere and Asthenosphere

### 5.2.1. Thickness of Lithosphere and Structure of the upper Mantle

The lithosphere thickness of the study areas and adjacent areas is around 80 km, as shown in this study. This result is similar to other geophysical observations in South China. For example, the ambient noise tomography work indicated that the lithosphere thickness in the Cathaysia Block is 60–70 km [9]. The receiver function results implied a lithosphere

thickness of ~65 km in southeast China [11,31]. Deng and Levandowski proposed that the depth of the lithosphere–asthenosphere boundary (LAB) is ranging around 100 km, which is estimated by the final density model and receiver functions [12]. A joint inversion of Rayleigh wave dispersion data, topography, geoid height, and terrestrial heat flow with a probabilistic Monte Carlo method predicts the recent lithosphere in South China is ranging from 80–105 km [10].

Notably, the depth of LAB in South China observed by different complex and commendably geophysical methods seems variable. The presence of multichannel of asthenosphere upwelling in the coastal area and adjacent area may well explain the variable depth of LAB as these upwelling channels interfered with geophysical interpretation to some extent. As shown in Figure 8, each profile has several asthenospheric upwelling channels along deep-seated faults whose influence width is tens of kilometers. Similarly, using the magnetotelluric method to detect the crust/mantle thermal structure shows that the asthenospheric upwelling is common in southeast China, including Fujian Province, Guangdong Province, etc. [32,33]. The impact of these widespread distributed multichannel asthenospheric upwelling on the lithosphere mainly reflects in the following two points. For one, the rigid lithosphere turns into a plastic state under the underplating of high-temperature materials. It is gradually eroded by the asthenosphere, resulting in thinning of the lithosphere. Additionally, the lithosphere undergoes partially melting due to the underplating of the asthenosphere with melttable material separate out from the lithosphere to the asthenosphere. The lithosphere's remaining rigid material undergoes rigid rupture under gravity and sinks into the asthenosphere [34,35]. These two mechanisms coexist in the upwelling process of the asthenosphere, and all have a significant impact on lithospheric thinning. Furthermore, Compared with other ancient cratons, U-Pb zircon geochronology dates the Cathaysian block where southeast China locates as Neoproterozoic in age [36] indicate the lithosphere is more vulnerable to erosion and destruction [32]. In summary, the asthenosphere's upwelling has completely modified the lithospheric structure, resulting in different thicknesses of the lithosphere and crust–mantle structures in Guangdong Province.

Guangdong Province straddles the boundary between three energetic tectonic domains: the Pacific subduction zone to the east, the collision zone between the Philippine Sea and the Eurasian plate to the southeast, and the spreading of the South China Sea to the south (Figure 1). Specifically, for the Pacific plate, previous receiver function images of mantle transition zone [37–39] and tomographic studies [40,41] indicate that the slab front extends into the area beneath the South China block (~105° E). Various geophysical and geochemical evidence has indicated that the Pacific plate stagnant in the mantle transition zone and has continuously released fluid material to destruct and reform the overlying lithospheric mantle [40,42,43]. The collision zone between the Philippine Sea and the Eurasian plate forms compressional uplifting and orogeny along the southeast coast area and Taiwan [44,45]. The evolution of the South China Sea has a significant impact on the surrounding continents, which is reflected in the formation of crustal uplifting or depression [2,46,47]. The interaction of these plates affects the activity of the asthenosphere in Guangdong Province and adjacent areas. For example, the force driven by the Pacific plate's subduction triggers the mantle convection, inducing the eastward asthenospheric flow beneath South China in the big mantle wedge. For one, during the flow process, the positive buoyancy causes asthenospheric upwelling accompanied by decompression melting and melt extraction [48]. This process will erode the overlying lithosphere. On another side, fluid released by the stagnant Pacific plate is added to the asthenosphere to promote the partial melting of the Upper mantle and Mantle transition zone [49–51].

Moreover, geophysical results imply that the present lithospheric thickness (~80 km) is much less than that of the Paleozoic lithosphere. Geochemistry and *P-T* studies on mantle peridotite enclaves/xenoliths entrained by Paleozoic kimberlite and basalt have indicated that there was a thick lithosphere (110–230 km) at that time beneath South China [13,15]. However, the study on Mesozoic Ningyuan mantle xenoliths implies a thin lithosphere

(<80 km) [52] and that on Cenozoic Xinchang mantle xenoliths intimate the mantle replacement and accretion is a common process in South China since the Mesozoic [14]. These pieces of geological evidence present a process of incessant lithospheric thinning and asthenospheric intrusion.

In summary, for a given tectonic domain mainly affected by subduction or collision, the evolution of the continent plate depends on the fluid (primarily water) content and forms of the subducting or colliding plate and the intrinsic properties of the continental block [32]. The structure of the upper mantle and thickness of the lithosphere in southeast China are affected by different motion types of different plates, fluid addition, and its crust–mantle properties, leading to regional large-scale asthenosphere upwelling, causing the South China lithosphere to be destructed and reformed by mantle-derived hot materials. As a consequence, a thin lithosphere (<80 km) is commonly present beneath southeast China and is consistent with the high heat flow (Q) [17].

### 5.2.2. Structure of the Crust

MT results thoroughly document the crustal electrical structure, the characteristics of deep-seated faults, and the variation of crustal thickness. As mentioned in previous (Section 5.1), numerous low electric resistance geological body is present in the crust where couples with deep-seated faults. The asthenosphere uplift's top interface corresponds well with the position of the fault zone in the crust. For example, the asthenospheric material can uplift to a shallow position where there are deep-seated faults in the superficial (Figure 8). In other words, deep-seated fault zones play an important role in controlling the upwelling of the asthenosphere. The thickness of the crust is generally around 30 km and tends to thin eastward.

The same geological structure feature was also reported in most other southeast China areas by different geophysics observations or numerical simulations. The MT results in other southeast China regions presented a similar crustal electrical structure, the characteristics of deep-seated faults, and the variation of crustal thickness of that in this study [33]. Based on deep seismic-sounding data, Zhang and Wang inferred that the crust thickness in the Cathaysia Block is around 33 km, and the crustal thickness tends to thin eastward [53]. Deep seismic-sounding data also displays such a thin eastward trend of crustal thickness and the crustal thickness ranging from 30 to 34 km; the result from receiver function analysis with teleseismic wavefield reconstruction suggested that Moho surface depth in southeast China ranges from 25–35 km [54]. Based on the numerical simulation in South China, Zhang et al. proposed the Moho temperature, and the Moho depth is ranged from 500 to 650 °C and from 27 to 32 km, respectively [55]. The joint inversion of receiver functions and surface wave dispersion indicated a crust thickness in southeast China is approximately 30 km [56]. These studies all show a relatively thin and electrical heterogeneity crust in Guangdong Province.

### 5.3. Interpretation of the Geothermal Anomalies in Guangdong Province

Heat flow is considered as one of the direct surface geothermal manifestations of subterranean thermal energy and is a key parameter used to interpret the crust–mantle structure and geodynamics [17,57,58]. Guangdong Province is located in the second-largest geothermal anomaly area in China, where surface heat flow ranges from 61.6 to 97 mW/m<sup>2</sup> with a mean average of 73 mW/m<sup>2</sup> [17]. The values of surface heat flow are greater than the mean heat flow of continental China (60 mW/m<sup>2</sup>, [17]), and the globe means heat flow of continental crust (65 mW/m<sup>2</sup>, [57]). High heat flow has formed many “hot” basins in Guangdong Province (Figure 2) and developed with numerous natural hot springs (recorded natural hot springs more than 300, Figure 2). However, the surface heat flow for Guangdong Province is limited by the small number of measurement sites (only 24 sites have been reported in the literature up to 2019 in Guangdong Province, Figure 2) and are affected by the local geothermal fluid convection [59]. Therefore, we use the surface heat

flow and the natural hot spring, which is a direct indicator to interpret the geothermal anomalies in Guangdong Province.

The high ratio of mean  $Q_{\text{mantle}}/Q_{\text{crust}}$  ( $\sim 1.33$ ) in southeast China implies that mantle heat causes surface geothermal anomalies in Guangdong Province [17]. As mentioned above, the thin lithosphere, which accompanies by multichannel asthenospheric upwelling, determines a high terrestrial heat flow in Guangdong Province. The upwelling channel of mantle-derived material is connected with the fault system of shallow crust in Guangdong Province. Source waters penetrate the fault system and reach deep into the places where the mantle-derived material is affected. These places have a high temperature, warming the cold water and resulting in fluid convection in the fault system. Fluid convection causes heat upwelling and the development of natural hot springs along with the fault system or adjacent areas (Figure 2).

It should be noted that many natural hot springs in Guangdong Province and its surroundings are distributed along with the faults system and the exposed areas of the Late Mesozoic granite. This is attributed to the high radioactive heat-producing elements (HPE, such as  $^{238}\text{U}$ ,  $^{232}\text{Th}$ , and  $^{40}\text{K}$ ) of the Late Mesozoic granites in South China. These Late Mesozoic granites in Guangdong Province are widely distributed with an exposed area of 60,000 km<sup>2</sup>, accounting for more than one-third of the area (Figure 2). These granites in Guangdong Province and adjacent areas were formed in a typical continental arc setting and were considered to associate with the advance of the Paleo-Pacific Plate in the Early Middle Jurassic and the retreat of the Paleo-Pacific Plate in the Late Jurassic to Cretaceous [2,5,22]. Importantly, subduction plate-derived materials and the decompression melting caused by stress relaxation promoted the reworking of terrane in South China [7,60]. Two-stage model age of Jurassic and Cretaceous granite Hf isotope ranges between 1.6 and 1.8 Ga, suggesting Late Mesozoic granites in Huizhou area were generated by remelting of Proterozoic crust [61]. This result is consistent with the two-stage model age of detrital zircons Hf isotope in Oujiang River, eastern Cathaysia, Fogang granites, and Nankunshan granites [7,60]. The remelting of differentiated crust material leads to redifferentiation occur. Consequently, the Late Mesozoic granites inevitably have high large ion lithophile elements. Statistics and calculation of the Th, U, and K content of Mesozoic granites in South China show an extremely high heat production with average values of 6.29  $\mu\text{W}/\text{m}^3$  for the Late Mesozoic granite in Guangdong [8,62]. The radioactive heat reservoirs calculated based on the heat production show the Mesozoic granite intrusions contain abundant radioactive heat production (Figure S3). As shown in Figure S3, compared with the Mesozoic granites in Guangdong Province and its surrounding areas, the Late Mesozoic granites in Nanling Range have the highest heat production (heat production more than 9  $\mu\text{W}/\text{m}^3$  of some granites, radioactivity heat reservoirs more than  $10^{16}$  J/a of some granite intrusions) and radioactive heat reservoirs and couple with numerous high-temperature ( $>80$  °C) natural hot spring. This finding reveals Late Mesozoic granite has a marked contribution to the regional geothermal anomaly.

The previous study inferred, based on low gravity anomalies, that there are massive concealed granitic bodies under the exposed Mesozoic granite and adjacent areas [18]. However, our previous study in the Huiyang-Meixian depression between Huizhou and Heyuan City revealed a continuous concealed granite under the depression [3] where Xi et al. [18] deduced there was an absence of concealed granite. Thus, we speculate that the scale of concealed granite under the Guangdong Province is larger than Xi et al. [17] suspected. In other words, due to the extremely high heat production of the Late Mesozoic granite, the Late Mesozoic granite under the Guangdong Province turned into a high-temperature geothermal reservoir. Large quantities of heat released from persistent radioactive decay are one of the most significant geothermal mechanisms in Guangdong Province.

By integrating the results and discussions above, a geothermal model is proposed to visualize the origin and evolution process of geothermic in Guangdong Province (Figure 9). For one, the arc tectonic setting in Guangdong had gradually changed into an intraplate rift

setting since Mesozoic [2,22], forming large-scale basins includes Heyuan Basin, Sanshui Basin, Lianping Basin, etc. [3,4,23], and accompanying with upwelling of mantle material. The thin lithosphere superimposed upwelling of mantle-derived material determines the high heat flow background in Guangdong Province. For another, voluminous Late Mesozoic granite generated by remelting of the Neoproterozoic and Paleozoic crust [7,61] contains an extremely high content of heat-producing elements. Large quantities of heat are released from the persistent radioactive decay of these heat-producing elements. Consequently, the special crust-upper mantle structure in Guangdong Province has led to the formation of numerous natural hot springs. These hot springs can be divided into two types (Figure 9). The first is type A, hot springs distributed near the fault of granite area, the Late Mesozoic granite is the key heat source. Typical examples are the hot springs in the Nanling Range. The second is type B, hot springs distributed along fault zones with mantle-derived material upwelling, the mantle material and the Late Mesozoic granite are the key heat source. Typical examples are the hot springs along the Heyuan fault, where noble gas evidence shows the upwelling of mantle material [63].

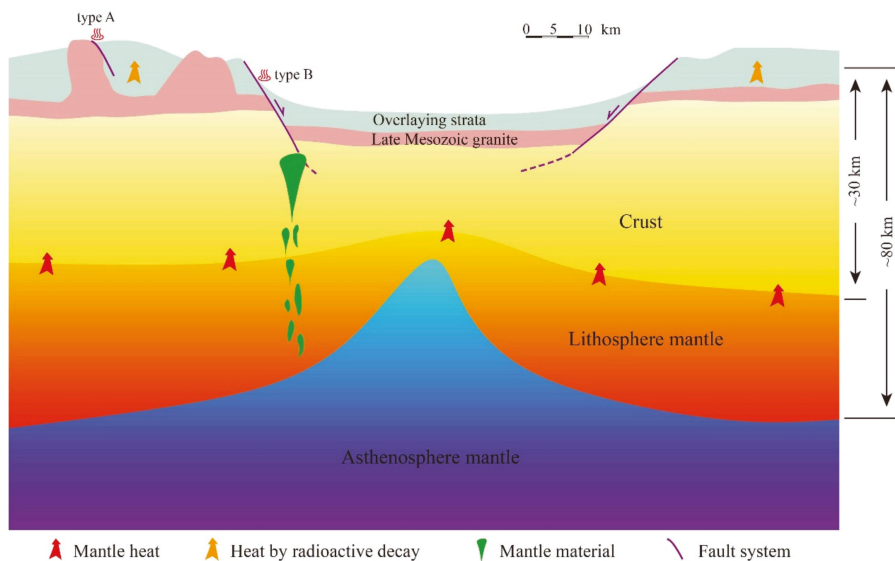


**Figure 9.** A model of the crust–mantle structure to decipher geothermal formation in Guangdong Province. The granite layer was modified from Kuang et al. [3].

## 6. Conclusions

In this study, we focused on the crust and upper mantle structure and its geothermal implications in Guangdong Province. The main results and conclusions are as follows:

1. Three new MT profiles with a total of 440 km long across the major portion of Guangdong Province were acquired to reconstruct crust and upper mantle structure. The TM model of the nonlinear conjugate gradient (NLCCG) two-dimensional inversion with  $\tau = 3$  was determined by data analysis;
2. Inversion results show that the low resistance zone on the shallow surface matches the actual location of the fault; there is the presence of multi upwelling channels of asthenosphere mantle, and some channels are connected with shallow crustal fault zone; the thickness of the crust and the lithosphere in Guangdong Province are relatively thin. The crust and upper mantle structure in Guangdong Province is the result of long-term (from Proterozoic to Cenozoic) tectonic magmatism, especially the

intense tectonic magmatism caused by multi-plate interaction since the late Mesozoic. Such special crust and upper mantle structure forms high surface heat flow and is one of the key factors for generating anomalies;

3. Massive Late Mesozoic granites, which contain high radioactive heat-producing elements, are distributed on the surface and underground of Guangdong Province. Large quantities of heat released from persistent radioactive decay of Late Mesozoic granite are another significant geothermal mechanism in Guangdong Province.

**Supplementary Materials:** The following are available online at <https://www.mdpi.com/article/10.3390/en14082236/s1>, Figure S1: Calibration results of V5 system 2000 equipment box, Figure S2: Calibration results of V5 system 2000 equipment probe, Figure S3: Radioactive heat reservoirs and radioactive heat production rate of the late Mesozoic exposed granite and the distribution of the hot springs in Guangdong province and adjacent area.

**Author Contributions:** Conceptualization, investigation and data curation, J.K.; methodology, software, validation, formal analysis, S.Q. and X.H.; writing—Original draft preparation, J.K.; writing—Review and editing, S.Q. and X.H.; supervision and project administration, S.Q. and X.H. All authors have read and agreed to the published version of the manuscript.

**Funding:** This research was funded by the Urban Underground Space Development and Utilization of Huizhou and China Geological Survey Project (1212011220014).

**Acknowledgments:** The first author would like to acknowledge Wang Shuai, Huang Xuelian, Xiao Zhicai, and Cheng Zihao for the support during the analyses. Special thanks go to three reviewers whose constructive comments help us a lot. Our deepest gratitude goes to the Academic Editors, Renato Somma and Raul Andreica, for their careful work and thoughtful suggestions that have helped improve this manuscript substantially. We appreciate Zhou Bing for the technical support.

**Conflicts of Interest:** The authors declare no conflict of interest.

## References

1. Zheng, Y.-F.; Xiao, W.-J.; Zhao, G. Introduction to tectonics of China. *Gondwana Res.* **2013**, *23*, 1189–1206. [[CrossRef](#)]
2. Suo, Y.; Li, S.; Jin, C.; Zhang, Y.; Zhou, J.; Li, X.; Wang, P.; Liu, Z.; Wang, X.; Somerville, I. Eastward tectonic migration and transition of the Jurassic-Cretaceous Andean-type continental margin along Southeast China. *Earth Sci. Rev.* **2019**, *196*, 102884. [[CrossRef](#)]
3. Kuang, J.; Wang, S.; Qi, S.; Xiao, Z.; Zhang, M.; Wang, Y. Cenozoic tectonic evolution of South China: A brief review, and new insights from the Huangshadong-Shiba area, south-east China. *Geol. J.* **2020**, *55*, 7716–7737. [[CrossRef](#)]
4. Zhou, X.; Sun, T.; Shen, W.; Shu, L.; Niu, Y. Petrogenesis of Mesozoic granitoids and volcanic rocks in South China: A response to tectonic evolution. *Episodes* **2006**, *29*, 26. [[CrossRef](#)] [[PubMed](#)]
5. Li, Z.-X.; Li, X.-H. Formation of the 1300-km-wide intracontinental orogen and postorogenic magmatic province in Mesozoic South China: A flat-slab subduction model. *Geology* **2007**, *35*, 179–182. [[CrossRef](#)]
6. Wang, Y.; Fan, W.; Zhang, G.; Zhang, Y. Phanerozoic tectonics of the South China Block: Key observations and controversies. *Gondwana Res.* **2013**, *23*, 1273–1305. [[CrossRef](#)]
7. Xu, X.; O'Reilly, S.Y.; Griffin, W.L.; Wang, X.; Pearson, N.J.; He, Z. The crust of Cathaysia: Age, assembly and reworking of two terranes. *Precamb. Res.* **2007**, *158*, 51–78. [[CrossRef](#)]
8. Zhou, Z.-M.; Ma, C.-Q.; Qi, S.-H.; Xi, Y.-F.; Liu, W. Late Mesozoic high-heat-producing (HHP) and high-temperature geothermal reservoir granitoids: The most significant geothermal mechanism in South China. *Lithos* **2020**, *366*, 105568. [[CrossRef](#)]
9. Zhou, L.; Xie, J.; Shen, W.; Zheng, Y.; Yang, Y.; Shi, H.; Ritzwoller, M.H. The structure of the crust and uppermost mantle beneath South China from ambient noise and earthquake tomography. *Geophys. J. Int.* **2012**, *189*, 1565–1583. [[CrossRef](#)]
10. Shan, B.; Afonso, J.C.; Yang, Y.; Grose, C.J.; Zheng, Y.; Xiong, X.; Zhou, L. The thermochemical structure of the lithosphere and upper mantle beneath south China: Results from multiobservable probabilistic inversion. *J. Geophys. Res. Solid Earth* **2014**, *119*, 8417–8441. [[CrossRef](#)]
11. Zheng, T.-Y.; Zhao, L.; He, Y.-M.; Zhu, R.-X. Seismic imaging of crustal reworking and lithospheric modification in eastern China. *Geophys. J. Int.* **2014**, *196*, 656–670. [[CrossRef](#)]
12. Deng, Y.; Levandowski, W. Lithospheric Alteration, Intraplate Crustal Deformation, and Topography in Eastern China. *Tectonics* **2018**, *37*, 4120–4134. [[CrossRef](#)]
13. Zhang, H.-F.; Sun, M.; Lu, F.-X.; Zhou, X.-H.; Zhou, M.-F.; Liu, Y.-S.; Zhang, G.-H. Geochemical significance of a garnet lherzolite from the Dahongshan kimberlite, Yangtze Craton, southern China. *Geochim. J.* **2001**, *35*, 315–331. [[CrossRef](#)]

14. Liu, C.-Z.; Liu, Z.-C.; Wu, F.-Y.; Chu, Z.-Y. Mesozoic accretion of juvenile sub-continental lithospheric mantle beneath South China and its implications: Geochemical and Re–Os isotopic results from Ningyuan mantle xenoliths. *Chem. Geol.* **2012**, *291*, 186–198. [\[CrossRef\]](#)
15. Zheng, J.P.; Lee, C.-T.A.; Lu, J.G.; Zhao, J.H.; Wu, Y.B.; Xia, B.; Li, X.Y.; Zhang, J.F.; Liu, Y.S. Refertilization-driven destabilization of subcontinental mantle and the importance of initial lithospheric thickness for the fate of continents. *Earth Planet. Sci. Lett.* **2015**, *409*, 225–231. [\[CrossRef\]](#)
16. Hu, S.; He, L.; Wang, J. Heat flow in the continental area of China: A new data set. *Earth Planet. Sci. Lett.* **2000**, *179*, 407–419. [\[CrossRef\]](#)
17. Jiang, G.; Hu, S.; Shi, Y.; Zhang, C.; Wang, Z.; Hu, D. Terrestrial heat flow of continental China: Updated dataset and tectonic implications. *Tectonophysics* **2019**, *753*, 36–48. [\[CrossRef\]](#)
18. Xi, Y.; Wang, G.; Liu, S.; Zhao, Y.; Hu, X. The formation of a geothermal anomaly and extensional structures in Guangdong, China: Evidence from gravity analyses. *Geothermics* **2018**, *72*, 225–231. [\[CrossRef\]](#)
19. Van der Zwaan, B.; Dalla Longa, F. Integrated assessment projections for global geothermal energy use. *Geothermics* **2019**, *82*, 203–211. [\[CrossRef\]](#)
20. Ceglia, F.; Macaluso, A.; Marrasso, E.; Roselli, C.; Vanoli, L. Energy, Environmental, and Economic Analyses of Geothermal Polygeneration System Using Dynamic Simulations. *Energies* **2020**, *13*, 4603. [\[CrossRef\]](#)
21. Ceglia, F.; Macaluso, A.; Marrasso, E.; Sasso, M.; Vanoli, L. Modelling of Polymeric Shell and Tube Heat Exchangers for Low-Medium Temperature Geothermal Applications. *Energies* **2020**, *13*, 2737. [\[CrossRef\]](#)
22. Tao, N.; Li, Z.-X.; Danišik, M.; Evans, N.J.; Batt, G.E.; Li, W.-X.; Pang, C.-J.; Jourdan, F.; Xu, Y.-G.; Liu, L.-P. Thermochronological record of Middle–Late Jurassic magmatic reheating to Eocene rift-related rapid cooling in the SE South China Block. *Gondwana Res.* **2017**, *46*, 191–203. [\[CrossRef\]](#)
23. Ren, J.; Tamaki, K.; Li, S.; Junxia, Z. Late Mesozoic and Cenozoic rifting and its dynamic setting in Eastern China and adjacent areas. *Tectonophysics* **2002**, *344*, 175–205. [\[CrossRef\]](#)
24. Gong, J.; Chen, Y.J. Evidence of lateral asthenosphere flow beneath the South China craton driven by both Pacific plate subduction and the India–Eurasia continental collision. *Terra Nova* **2014**, *26*, 55–63. [\[CrossRef\]](#)
25. Gamble, T.D.; Goubau, W.M.; Clarke, J. Magnetotellurics with a remote magnetic reference. *Geophysics* **1979**, *44*, 53–68. [\[CrossRef\]](#)
26. Egbert, G.D.; Booker, J.R. Robust estimation of geomagnetic transfer functions. *Geophys. J. R. Astron. Soc.* **1986**, *87*, 173–194. [\[CrossRef\]](#)
27. Groom, R.W.; Bailey, R.C. Decomposition of magnetotelluric impedance tensors in the presence of local three-dimensional galvanic distortion. *J. Geophys. Res. Solid Earth* **1989**, *94*, 1913–1925. [\[CrossRef\]](#)
28. Rodi, W.; Mackie, R.L. Nonlinear conjugate gradients algorithm for 2-D magnetotelluric inversion. *Geophysics* **2001**, *66*, 174–187. [\[CrossRef\]](#)
29. Berdichevsky, M.N. Marginal Notes on Magnetotellurics. *Surv. Geophys.* **1999**, *20*, 341–375. [\[CrossRef\]](#)
30. Ledo, J. 2-D versus 3-D magnetotelluric data interpretation. *Surv. Geophys.* **2005**, *26*, 511–543. [\[CrossRef\]](#)
31. Zhang, M.; Guo, Z.; Liu, J.; Liu, G.; Zhang, L.; Lei, M.; Zhao, W.; Ma, L.; Sepe, V.; Ventura, G. The intraplate Changbaishan volcanic field (China/North Korea): A review on eruptive history, magma genesis, geodynamic significance, recent dynamics and potential hazards. *Earth Sci. Rev.* **2018**, *187*, 19–52. [\[CrossRef\]](#)
32. Zhao, L.; Allen, R.M.; Zheng, T.; Zhu, R. High-resolution body wave tomography models of the upper mantle beneath eastern China and the adjacent areas. *Geochem. Geophys. Geosyst.* **2012**, *13*. [\[CrossRef\]](#)
33. Hu, X.Y.; Bi, B.T.; Liu, G.X.; Han, J.T.; Cai, J.C.; Peng, R.H.; Xu, S.; Liu, S.J. The lithospheric electrical structure of ji'an-fuzhou profile in the east part of south china. *Chin. J. Geophys.* **2017**, *60*, 532–543.
34. Menke, W.; Lamoureux, J.; Abbott, D.; Hopper, E.; Hutson, D.; Marrero, A. Crustal heating and lithospheric alteration and erosion associated with asthenospheric upwelling beneath southern New England (USA). *J. Geophys. Res. Solid Earth* **2018**, *123*, 8995–9008. [\[CrossRef\]](#)
35. Zheng, Y.; Xu, Z.; Zhao, Z.; Dai, L. Mesozoic mafic magmatism in North China: Implications for thinning and destruction of cratonic lithosphere. *Sci. China Earth Sci.* **2018**, *61*, 353–385. [\[CrossRef\]](#)
36. Yu, J.-H.; Wei, Z.-Y.; Wang, L.-J.; Shu, L.-S.; Sun, T. Cathaysia Block: A young continent composed of ancient materials. *Geol. J. China Univ.* **2006**, *12*, 440–447.
37. Ai, Y.; Zheng, T. The upper mantle discontinuity structure beneath eastern China. *Geophys. Res. Lett.* **2003**, *30*. [\[CrossRef\]](#)
38. Chen, L.; Ai, Y. Discontinuity structure of the mantle transition zone beneath the North China Craton from receiver function migration. *J. Geophys. Res. Solid Earth* **2009**, *114*. [\[CrossRef\]](#)
39. Xu, W.; Zheng, T.; Zhao, L. Mantle dynamics of the reactivating North China Craton: Constraints from the topographies of the 410-km and 660-km discontinuities. *Sci. China Earth Sci.* **2011**, *54*, 881–887. [\[CrossRef\]](#)
40. Huang, J.; Zhao, D. High-resolution mantle tomography of China and surrounding regions. *J. Geophys. Res. Solid Earth* **2006**, *111*. [\[CrossRef\]](#)
41. Li, C.; Hilst, R.D. Structure of the upper mantle and transition zone beneath Southeast Asia from travelttime tomography. *J. Geophys. Res. Solid Earth* **2010**, *115*. [\[CrossRef\]](#)
42. Zhao, D.; Maruyama, S.; Omori, S. Mantle dynamics of Western Pacific and East Asia: Insight from seismic tomography and mineral physics. *Gondwana Res.* **2007**, *11*, 120–131. [\[CrossRef\]](#)

43. Yan, D.; Tian, Y.; Zhao, D.; Liu, C.; Zhu, H.; Li, H. Upper mantle temperature structure of the North China Craton. *Phys. Earth Planet. Inter.* **2019**, *293*, 106269. [[CrossRef](#)]
44. Lallemand, S.; Theunissen, T.; Schnürle, P.; Lee, C.-S.; Liu, C.-S.; Font, Y. Indentation of the Philippine Sea plate by the Eurasia plate in Taiwan: Details from recent marine seismological experiments. *Tectonophysics* **2013**, *594*, 60–79. [[CrossRef](#)]
45. Wu, J.; Suppe, J.; Lu, R.; Kanda, R. Philippine Sea and East Asian plate tectonics since 52 Ma constrained by new subducted slab reconstruction methods. *J. Geophys. Res. Solid Earth* **2016**, *121*, 4670–4741. [[CrossRef](#)]
46. Ye, Q.; Mei, L.; Shi, H.; Camanni, G.; Shu, Y.; Wu, J.; Yu, L.; Deng, P.; Li, G. The Late Cretaceous tectonic evolution of the South China Sea area: An overview, and new perspectives from 3D seismic reflection data. *Earth Sci. Rev.* **2018**, *187*, 186–204. [[CrossRef](#)]
47. Ye, Q.; Mei, L.; Shi, H.; Shu, Y.; Camanni, G.; Wu, J. A low-angle normal fault and basement structures within the Enping Sag, Pearl River Mouth Basin: Insights into late Mesozoic to early Cenozoic tectonic evolution of the South China Sea area. *Tectonophysics* **2018**, *731*, 1–16. [[CrossRef](#)]
48. Raddick, M.J.; Parmentier, E.M.; Scheirer, D.S. Buoyant decompression melting: A possible mechanism for intraplate volcanism. *J. Geophys. Res. Solid Earth* **2002**, *107*, ECV 7-1–ECV 7-14. [[CrossRef](#)]
49. Zou, H.; Fan, Q.; Yao, Y. U–Th systematics of dispersed young volcanoes in NE China: Asthenosphere upwelling caused by piling up and upward thickening of stagnant Pacific slab. *Chem. Geol.* **2008**, *255*, 134–142. [[CrossRef](#)]
50. Sakuyama, T.; Tian, W.; Kimura, J.-I.; Fukao, Y.; Hirahara, Y.; Takahashi, T.; Senda, R.; Chang, Q.; Miyazaki, T.; Obayashi, M.; et al. Melting of dehydrated oceanic crust from the stagnant slab and of the hydrated mantle transition zone: Constraints from Cenozoic alkaline basalts in eastern China. *Chem. Geol.* **2013**, *359*, 32–48. [[CrossRef](#)]
51. Huang, J.; Li, S.-G.; Xiao, Y.; Ke, S.; Li, W.-Y.; Tian, Y. Origin of low  $\delta^{26}\text{Mg}$  Cenozoic basalts from South China Block and their geodynamic implications. *Geochim. Cosmochim. Acta* **2015**, *164*, 298–317. [[CrossRef](#)]
52. Liu, C.-Z.; Wu, F.-Y.; Sun, J.; Chu, Z.-Y.; Qiu, Z.-L. The Xinchang peridotite xenoliths reveal mantle replacement and accretion in southeastern China. *Lithos* **2012**, *150*, 171–187. [[CrossRef](#)]
53. Zhang, Z.; Wang, Y. Crustal structure and contact relationship revealed from deep seismic sounding data in South China. *Phys. Earth Planet. Inter.* **2007**, *165*, 114–126. [[CrossRef](#)]
54. Song, P.; Zhang, X.; Liu, Y.; Teng, J. Moho imaging based on receiver function analysis with teleseismic wavefield reconstruction: Application to South China. *Tectonophysics* **2017**, *718*, 118–131. [[CrossRef](#)]
55. Zhang, J.; Wang, B.; Tang, X.; Dong, M.; Ai, Y. Temperature structure and dynamic background of crust and mantle beneath the high heat flow area of the South China continental margin (in Chinese with English abstract). *Chin. J. Geophys.* **2018**, *61*, 16.
56. Deng, Y.; Li, J.; Peng, T.; Ma, Q.; Song, X.; Sun, X.; Shen, Y.; Fan, W. Lithospheric structure in the Cathaysia block (South China) and its implication for the Late Mesozoic magmatism. *Phys. Earth Planet. Inter.* **2019**, *291*, 24–34. [[CrossRef](#)]
57. Davies, J.H. Global map of solid Earth surface heat flow. *Geochem. Geophys. Geosyst.* **2013**, *14*, 4608–4622. [[CrossRef](#)]
58. Furlong, K.P.; Chapman, D.S. Heat Flow, Heat Generation, and the Thermal State of the Lithosphere. *Annu. Rev. Earth Planet. Sci.* **2013**, *41*, 385–410. [[CrossRef](#)]
59. Hu, S.-B.; He, L.-J.; Wang, J.-Y. Compilation of Heat Flow Data in the China Continental Area. *Chin. J. Geophys.* **2001**, *44*, 604–618. [[CrossRef](#)]
60. Li, X.-H.; Li, Z.-X.; Li, W.-X.; Liu, Y.; Yuan, C.; Wei, G.; Qi, C. U–Pb zircon, geochemical and Sr–Nd–Hf isotopic constraints on age and origin of Jurassic I- and A-type granites from central Guangdong, SE China: A major igneous event in response to foundering of a subducted flat-slab? *Lithos* **2007**, *96*, 186–204. [[CrossRef](#)]
61. Xiao, Z.; Wang, S.; Qi, S.; Kuang, J.; Zhang, M.; Tian, F.; Han, Y. Petrogenesis, Tectonic Evolution and Geothermal Implications of Mesozoic Granites in the Huangshadong Geothermal Field, South China. *J. Earth Sci.* **2020**, *31*, 141–158. [[CrossRef](#)]
62. Sun, Z.; Wang, A.; Liu, J.; Hu, B.; Chen, G. Radiogenic heat production of granites and potential for hot dry rock geothermal resource in Guangdong Province, Southern China. In Proceedings of the World Geothermal Congress, Melbourne, Australia, 19–25 April 2015; pp. 2–6.
63. Wang, S.; Kuang, J.; Huang, X.; Zhang, H.; Zhang, M.; Qi, S.; Han, Y.; Xiao, Z.; Wang, S.; Tang, L. Upwelling of Mantle Derived Material in Southeast China: Evidence from Noble Gas Isotopes. *Acta Geol. Sin. Engl. Ed.* **2021**. [[CrossRef](#)]



Review

# Review of Recent Drilling Projects in Unconventional Geothermal Resources at Campi Flegrei Caldera, Cornubian Batholith, and Williston Sedimentary Basin

Renato Somma<sup>1,2,\*</sup>, Daniela Blessent<sup>3</sup>, Jasmin Raymond<sup>4</sup>, Madeline Constance<sup>5</sup>, Lucy Cotton<sup>5</sup>, Giuseppe De Natale<sup>1</sup>, Alessandro Fedele<sup>1</sup>, Maria Jose Jurado<sup>6</sup>, Kirsten Marcia<sup>7</sup>, Mafalda Miranda<sup>4</sup>, Claudia Troise<sup>1</sup> and Thomas Wiersberg<sup>8</sup>

<sup>1</sup> Osservatorio Vesuviano, INGV, 80124 Naples, Italy; giuseppe.denatale@ingv.it (G.D.N.); alessandro.fedele@ingv.it (A.F.); claudia.troise@ingv.it (C.T.)

<sup>2</sup> IRISS, CNR, 80134 Naples, Italy

<sup>3</sup> Programa Ingeniería Ambiental, Universidad de Medellín, 050026 Medellín, Antioquia, Colombia; dblessent@udem.edu.co

<sup>4</sup> Institut National de la Recherche Scientifique, 490 Couronne St., Quebec City, QC G1K 9A9, Canada; jasmin.raymond@inrs.ca (J.R.); mafalda\_alexandra.miranda@ete.inrs.ca (M.M.)

<sup>5</sup> GeoScience Limited Unit 1 Falmouth Business Park, Bickland Water Road, Falmouth TR11 4SZ, UK; constance@geoscience.co.uk (M.C.); cotton@geoscience.co.uk (L.C.)

<sup>6</sup> Geosciences Barcelona CSIC, 08028 Barcelona, Spain; mjjurado@csic.es

<sup>7</sup> DEEP Earth Energy Production Corp. Box 6 Site 515 RR5, Saskatoon, SK S7K 3J8, Canada; kmarcia@deepcorp.ca

<sup>8</sup> Helmholtz-Zentrum Potsdam—Deutsches GeoForschungsZentrum GFZ, 14473 Potsdam, Germany; wiers@gfz-potsdam.de

\* Correspondence: renato.somma@ingv.it

**Citation:** Somma, R.; Blessent, D.; Raymond, J.; Constance, M.; Cotton, L.; Natale, G.D.; Fedele, A.; Jurado, M.J.; Marcia, K.; Miranda, M.; et al. Review of Recent Drilling Projects in Unconventional Geothermal Resources at Campi Flegrei Caldera, Cornubian Batholith, and Williston Sedimentary Basin. *Energies* **2021**, *14*, 3306. <https://doi.org/10.3390/en14113306>

**Academic Editor:**  
Paul Christodoulides

Received: 8 May 2021  
Accepted: 2 June 2021  
Published: 4 June 2021

**Publisher's Note:** MDPI stays neutral with regard to jurisdictional claims in published maps and institutional affiliations.



**Copyright:** © 2021 by the authors. Licensee MDPI, Basel, Switzerland. This article is an open access article distributed under the terms and conditions of the Creative Commons Attribution (CC BY) license (<https://creativecommons.org/licenses/by/4.0/>).

**Abstract:** Unconventional geothermal resource development can contribute to increase power generation from renewable energy sources in countries without conventional hydrothermal reservoirs, which are usually associated with magmatic activity and extensional faulting, as well as to expand the generation in those regions where conventional resources are already used. Three recent drilling experiences focused on the characterization of unconventional resources are described and compared: the Campi Flegrei Deep Drilling Project (CFDDP) in Italy, the United Downs Deep Geothermal Power (UDDGP) project in the United Kingdom, and the DEEP Earth Energy Production in Canada. The main aspects of each project are described (geology, drilling, data collection, communication strategies) and compared to discuss challenges encountered at the three sites considered, including a scientific drilling project (CFDDP) and two industrial ones (UDDGP and DEEP). The first project, at the first stage of pilot hole, although not reaching deep supercritical targets, showed extremely high, very rare thermal gradients even at shallow depths. Although each project has its own history, as well as social and economic context, the lessons learned at each drilling site can be used to further facilitate geothermal energy development.

**Keywords:** unconventional geothermal resources; geothermal drilling; communities; caldera; Enhanced Geothermal Systems

## 1. Introduction

Unlike other renewable energies, such as solar and wind, geothermal resources provide base-load power that can be generated continuously to meet the minimum level of power demand, independent of climate conditions. Resources are defined as conventional when found in hydrothermal systems related to magmatic activity and extensional faulting [1]. On the other hand, unconventional resources include Hot Sedimentary Aquifers (HSAs) with permeable layers at great depth (2–5 km), as well as Hot Dry Rocks (HDRs), which have been developed since the beginning of the 1970s and are now referred to as

Enhanced Geothermal Systems (EGSs), where hot low permeable crystalline rocks are stimulated at drillable depths [2]. Heat transfer mechanisms in HSA and EGS are dominated by conduction associated with near normal heat flow for such petrothermal plays. Forced convection can be induced in deep aquifer layers to extract heat [3]. Other geothermal resources gaining interest are associated with supercritical fluids, which are characterized by temperatures between 390 and 600 °C and processed with superheated dry steam plants [4], while those of EGS and HSA are exploited with binary power plants, since the fluid temperature is usually <150 °C. Supercritical geothermal resources have been proven to exist at technically and economically viable depths, and one well extracting those resources can significantly increase the production output [4]. However, the extraction of energy from these resources is challenging because the permeability of the host material is at the brittle–ductile transition and the magmatic fluids produced are highly corrosive [5]. Calderas are possible candidates for the presence of supercritical geothermal reservoirs at shallow depth that have been explored in several countries [6–8]. Drilling through supercritical fluids in the scope of geothermal energy production was achieved by the IDDP project (Iceland Deep Drilling Project) [9].

While geological, geochemical, and geophysical exploration methods are used to estimate the size and temperature of the resources during the initial exploratory phase, deep drilling and well testing are required to prove resource viability [1]. Results obtained from drilling projects at key locations can be applied to other areas worldwide [10]. Moreover, since the installed costs and capacity factors of geothermal power plants are project-specific, often the drilling of additional production wells is required to adjust the extraction mass flow rate and ensure the sustainability of the resource [11]. Deep drilling and reservoir stimulation can generate a negative social perception of geothermal energy within the communities living close to these kind of projects. Volken et al. [12] highlighted that geothermal energy acceptance in Switzerland decreased with increasing knowledge about geothermal development, probably as a result of learning about induced seismicity that occurred in the past [13]. Similarly, Malo et al. [14] demonstrated that the support to geothermal energy within the Quebec population in Canada can decrease by 10% when exposed to the potential impacts of reservoir stimulation. In contrast, Carr-Cornish and Romanach [15] showed a positive change in perception when people acquired more information and knowledge about geothermal energy. Pellizzone et al. [16] revealed that the perception of renewable energies, including geothermal energy, is generally positive and optimistic, but, like Carr-Cornish and Romanach [15], indicated that when a geothermal project is developed in the area, the confidence of the affected population decreases, giving rise to the phenomenon known as “Not in my backyard” (NIMBY). However, where deep drilling and subsurface exploration are a common practice, such as developed oil fields or mining regions, drilling for deep geothermal resources can be socially accepted given the local comfort from historical experience and transferable expertise to maintain jobs.

In this paper, three drilling geothermal exploration projects conducted in Italy, the United Kingdom, and Canada are described to provide an overview of recent geothermal development. The common element of these projects is that they target unconventional geothermal resources: the Campi Flegrei Deep Drilling Project (CFDDP) in the volcanic caldera located Southern Italy west to Naples metropolitan area, the United Downs Deep Geothermal Power (UDDGP) project in hot granite rocks located in the Cornwall county in South West England, and the DEEP Earth Energy Production Corp. project in Canada, targeting HSA in the Western Canadian Sedimentary Basin.

Although these three countries went forward with geothermal drilling projects, their geothermal power generation backgrounds are different. In Europe, geothermal power plants were installed by the beginning of 1900 in Italy, but there are not yet geothermal power plants in the United Kingdom. Likewise, no geothermal power plants are operating in Canada, but several recent exploration projects have been conducted [17]. While the CFDDP drilling activities were conducted in 2012, those of the UDDGP and DEEP projects are more recent, since they were concluded in 2019 and 2020, respectively. One of the

targets of the CFDDP were supercritical fluids, while the shallow pilot hole drilled so far has not reached those fluids. However, this area shows very high geothermal gradients at shallow depths, thus allowing unusually shallow, cheap, and powerful geothermal exploitation. On the other hand, the UDDGP and DEEP projects focus on geothermal resources outside volcanic areas reaching the same temperature of the CFDDP pilot hole far deeper. The social context and communication strategies with the local communities are also different: Campi Flegrei is a highly populated volcano, while the Cornwall county and the Saskatchewan province have a lower population density with local comfort and history from drilling oil and mining exploration wells. Therefore, the objective of this paper is to review the recent geothermal exploration work at those three key projects and synthesize new knowledge gained that can be used in other countries looking to expand geothermal energy production.

## 2. Geothermal Energy in Italy

Italy is the first country in the world where geothermal energy was used for power generation at the beginning of the twentieth century. Geothermal resources are mainly used for electricity generation in Tuscany. The installed electrical capacity at the end of 2020 was of 944 MW, leaving Italy outside the “1 GW geothermal country club” [18].

In the Neapolitan area (Southern Italy), 116 deep wells were drilled for geothermal exploration between 1930 and 1980, i.e., 26 of them in Campi Flegrei [19] and 90 of them on the Ischia island. At Campi Flegrei, it is expected that temperature exceeds the critical point of water at depths as shallow as 2.5–3.0 km, whereas the thermal output of Neapolitan volcanic areas exceeds 16 GWt [19]. The CFDDP project would contribute to further improve the knowledge about the geothermal resources in this area, from very high shallow geothermal gradients down to the supercritical areas [20].

### 2.1. The Campi Flegrei Project

The choice of Campi Flegrei as a target for the deep study of large calderas is justified by the evidence—from previous drillings and from recent deformation and seismic observations—that the main structures of volcanological interest are considerably shallower than in other well-studied similar calderas [21]. This also implies the presence of extremely high geothermal gradients, with supercritical temperatures found at depths as shallow as 2.5–3.0 km [19]. The Campi Flegrei caldera (CfC) (Figure 1) is a typical example of the most explosive volcanoes on the Earth, namely large collapse calderas. It was formed from a main collapse event related to an ignimbritic eruption occurring 15 ka ago [21,22], named Neapolitan Yellow Tuff (NYT).

In the framework of the International Continental Scientific Drilling Program (ICDP), the pilot hole of Campi Flegrei Deep Drilling Project (CFDDP) [20] was drilled down to a depth of 500 m for understanding the stratigraphy and eruptive history of the easternmost caldera border, which lacked previous drilling and remained less studied. One additional objective was to evaluate the possibility of drilling a 3500 m, deviated deep hole, with deviation starting at about 500 m of depth.

The CFDDP had passed through a long evaluation process by ICDP, before the approval of the scientific and technical project, to obtain the authorization and economic support to proceed. There was an important debate during this period in the local and international scientific communities because drilling in the caldera had not been conducted since the middle of the eighties. The area was further affected by uplift and frequent low-magnitude seismic activity (generally lower than magnitude 2, but with peaks of magnitude 4.2 in the 1980s). Such ground dynamics, with 0.76 m of uplift in the last fifteen years, increasing seismicity, together with the memory of the previous large unrest of the 1970s and 1980s, raised concern in the population about the usefulness and risks of CFDDP. Such a concern was first claimed by a local geologist and then shared and amplified by newspapers and media, worrying the community and the local authorities. In summary, while almost all the national and international scientific community agreed on

the usefulness of the project and on the absence of risks for the population, few geologists from Naples University argued in an unscientific way about risks due to the drilling of the CFDDP, not only the deep well, but also, specifically, the pilot hole targeting 500 m of depth only. Confusion was mainly associated with a possible volcanic eruption triggered by the pilot hole in the caldera, since a misunderstanding occurred when translating “gas blowout” that may occur during well drilling and this was confused with volcanic eruption. This potential risk was amplified by the media and rapidly spread worldwide. In 2010, the INGV, which is appointed to mitigate volcanic risk, was accused to endanger the community with its scientific activities. Although this situation was recognized as lacking any scientific background within the international scientific community, at the local level, the criticism made by geologists was influencing the opinion of local authorities and population. This situation, leading to unsuitable communication between scientists, authorities, and communities, resulted in a delay of about two years in the pilot hole drilling.

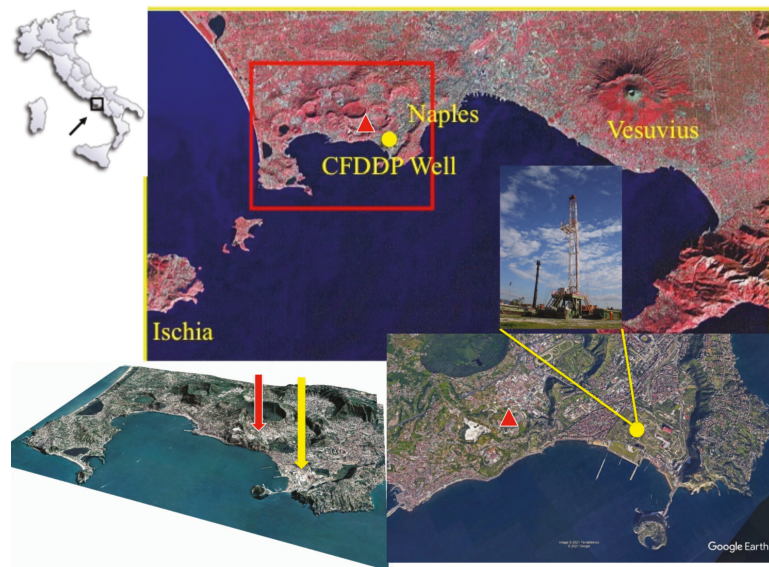


**Figure 1.** An overview of the Neapolitan volcanoes from a satellite image, with Campi Flegrei caldera evidenced in different points of view. The site of the Bagnoli 1 borehole CFDDP (yellow circle) and the Agnano geothermal well (red triangle) are also shown on the maps.

Drilling was conducted two years after, in 2012, in the Bagnoli plain: from 22 to 29 July until a depth of 222 m, and then from November 22 to December 2 to the depth of 506 m. This drilling site is an old dismantled industrial area located in Western Naples (Figure 1 of about 2 km<sup>2</sup> chosen for several scientific and logistic reasons [23]: the eastern part of the caldera had not been drilled before at a considerable depth, as this area is the most populated and faces the most geohazards. For these reasons, the aim of CFDDP was to study such an unexplored side of the caldera, where the local deposits are mostly unknown, although they pose the highest risk to the large city of Naples.

While the study of the rock properties helped to refine the thermo–hydro–mechanical modeling of the unrest processes [24], the stratigraphic studies and relative rock dating by radioisotope methods gave fundamental insight into the evolution of the area, as well as the caldera formation and extension [20]. At that time, the caldera was thought to have been formed by the Campanian Ignimbrite eruption (40 ka BP), and then collapsed again, in the innermost part, during the NYT eruption (15 ka BP). The Campanian Ignimbrite caldera was thought to include the city of Naples, so largely overcoming the Posillipo

Hill [24], which, on the other hand, was thought to represent the easternmost limit of the NYT caldera.

### 2.1.1. Pilot-Hole Mud-Gas Analysis

Real-time mud-gas analysis was performed during drilling to discuss the correlation between lithology and gas distribution. A detailed methodological description was given by Erzinger et al., 2006 [25]. In fact, on-line mud-gas monitoring is a reliable and cost-effective way of continuously investigating the distribution of gases versus depth, because it does not require rig-time. Because the mud gas may help to characterize origin of fluids and fluid interaction, the real-time mud-gas analysis can help to better understand the hydrothermal behavior with respect to CFC. Geochemical analysis in the CFDDP was conducted in a field laboratory to obtain information on gases and their composition in drill mud.

To dissolve the gas in the drilling mud, a custom-built water–gas separator was used and made of a steel cylinder (30 cm diameter, variable height) with an explosion-proof electrical motor on top that drives a stirring impeller mounted inside the cylinder [26]. The degasser was installed immediately behind the outlet of the mudflow line to reduce air contamination. The gas was then extracted and pumped with a membrane pump through a PTFE tube (4 mm inner diameter) into an on-site mud-logging cabin (about 20 m away from the hole) and led into an OmniStar® (Asslar, Germany) Quadrupole Mass Spectrometer (QMS; Pfeiffer Vacuum®, Alssar, Germany; Figure 2).

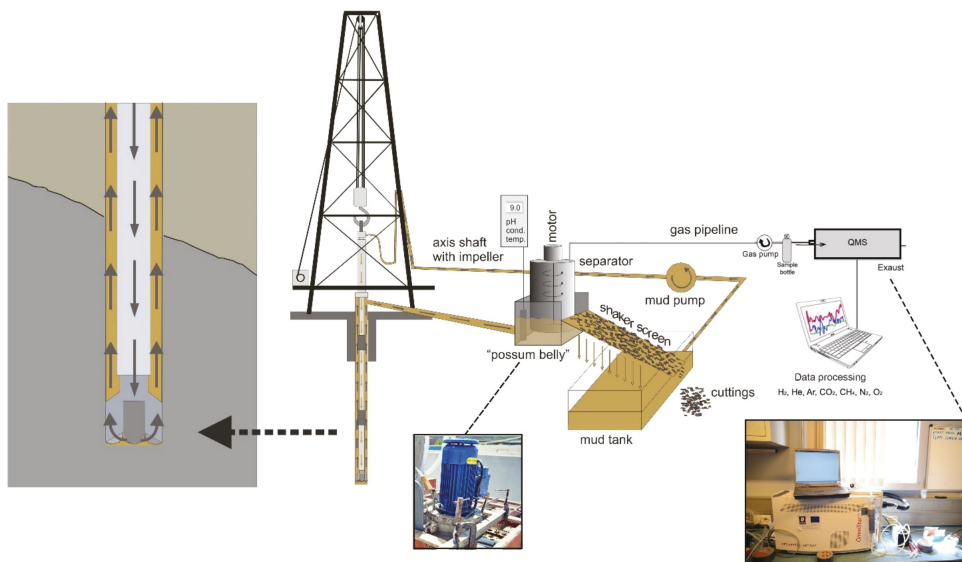


**Figure 2.** Sketch of the experimental setup. Gases entering the borehole are transported to the surface, together with the drill mud. A degasser extracts the gases from the drill mud. The gases are pumped to a lab trailer and analyzed in real time with a Quadrupole Mass Spectrometer (QMS).

Before introducing the gas into the QMS, the gas was passed through a water trap to remove moisture. The pressure of the gas to be measured is reduced from atmospheric down to  $4 \times 10^{-6}$  mbar by differential pumping through a 1.2 m long capillary with 0.15 mm diameter and an orifice (0.02 mm diameter). When gas flow into the mass spectrometer is interrupted, a background pressure of  $\sim 7 \times 10^{-8}$  mbar is achieved (for details, see Reference [27]).

The QMS was recalibrated, when necessary, with air, pure CO<sub>2</sub>, and certified gas mixtures, the compositions of which are selected according to the expected composition of mud gas. A time correction was applied to the gas composition data according to the measured and calculated mud-flow lag time, to compare the gas data to the drilling depth. A complete analysis of Ar, CO<sub>2</sub>, CH<sub>4</sub>, He, H<sub>2</sub>, O<sub>2</sub> and N<sub>2</sub> in the drilling mud gas was determined after an integration time of 20 s. However, measurements were recorded minutely to reduce the amount of data with detection limits of one ppm<sub>v</sub> and absolute analytical uncertainties of 1 ppm<sub>v</sub> for concentrations <10 ppm<sub>v</sub>, ~2–4 ppm<sub>v</sub> for concentrations <100 ppm<sub>v</sub>, ~5–20 ppm<sub>v</sub> for concentrations <ppm<sub>v</sub> and 0.02–0.1% for concentrations >1 vol.%. From all the analyzed gases, only CO<sub>2</sub>, CH<sub>4</sub>, and He are diagnostic of fluid inflow [25] because these gases are variably enriched in natural deep fluids but are only present in low concentration in the atmospheric air. Moreover, He, like all noble gases, is not affected by alteration of drilling mud or by chemical reactions. Although determination of Ar, H<sub>2</sub>, O<sub>2</sub>, and N<sub>2</sub> were also performed, relative concentrations of these gases can originate from sources other than fluid inflows, such as air contamination or chemical reactions with the drill mud, casing, and drill tools.

### 2.1.2. Correlation with Logging Measurements

A set of geophysical logging measurements were acquired by using hydrocarbon exploration standard borehole logging tools. Spectral natural gamma and acoustic logs, as well as resistivity-oriented images, were acquired to characterize rock composition, physical properties, structures, and geometries intersected by the CFDP-1 borehole. The logging data were acquired in two different surveys, using Schlumberger equipment, following the drilling of an upper and a lower section. The first logging operation performed in open-hole mode in July 2012 (31–170 m) (12.25 in borehole) in the upper section and included FMI (Full Bore Imaging) resistivity imaging and total natural gamma profile, as well as spectral gamma data with the HNGS Schlumberger tools and Sonic Scanner Schlumberger tool. In November 2012, additional geophysical logs were acquired during a second log-measurement operation (219–430 m section) in the open hole (8.5 in borehole).

The second logging run included imaging with the FMI tool HNGS spectral gamma measurements and acoustic profiling with the DSI (Dipole Shear Image) Schlumberger tool. This set of measurements is a unique continuous record that has been used to analyze and interpret the geological and petrophysical properties of the rocks drilled at the CFDDP drill hole [28]. The oriented resistivity images allowed the analysis of the geometries and orientation of the volcanic rock bodies, textures, structures, compositional changes, and the main discontinuities. To identify possible correlations between log measurements and gas anomalies, we used spectral natural gamma spectroscopic data as our first approach. This measurement yields gamma spectroscopy profiles in % for K, and ppm for U and Th [29–31]. These data are the expression of both the rock composition and the presence of radiogenic elements. It was observed that gas concentrations vary with different lithologies; therefore, we analyzed the correspondence and possible relationship with spectral data changes and fluctuations.

The data displayed on Figure 3 show overall total gamma value that is low with some increases related to compositional changes (e.g., at ~60 m) and in this case, the presence of organic-matter-rich levels [20,32].

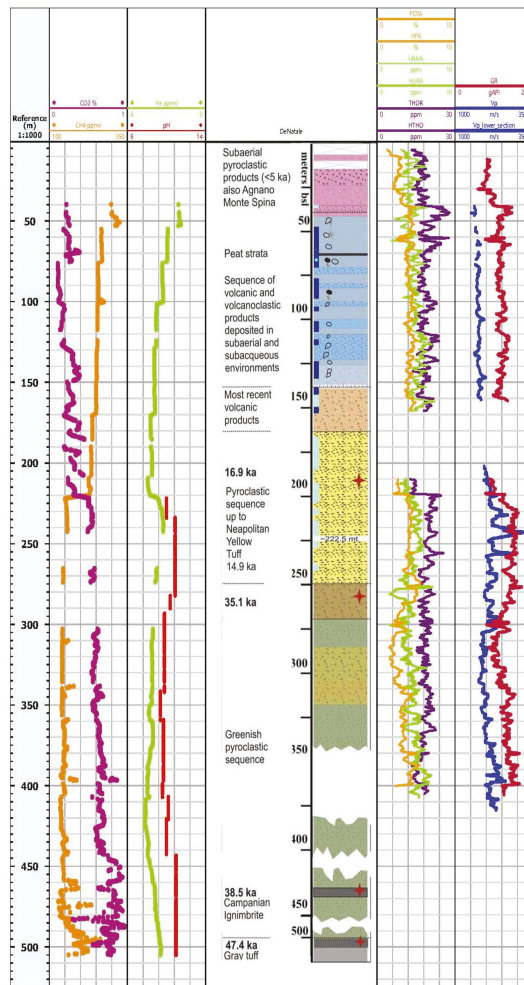


**Figure 3.** On the left-hand side, depth-profile of CO<sub>2</sub>, CH<sub>4</sub> and He, measured in the drill mud during drilling and associated lithology intercepted by the borehole. On the right-hand side (where the stratigraphic column is not scaled in the lower section and the logging data did not reach total depth of the well); wireline logging measurements (2 intervals) of spectral gamma radiation K, Th, and K content (first track); and total gamma radiation displayed with v<sub>p</sub> and v<sub>s</sub> acoustic velocities, on the second track.

At the boundary between pumice to scoria deposits at a depth of 160 m, a shift in gamma values from 160 to 180 gAPI is observed. Another change observed in total gamma values, as well as in the K, U, and Th concentrations, is observed at 280 m. In this case, the change can be related to the lithological boundary with the first appearance of the greenish tuff deposits. K (1 to 5.5 wt%), Th (10 to 28 ppm), and U (1 and 6 ppm) concentrations (Figure 3) agree with the range of values of surface sample analyses from Campi Flegrei [33–35]. The sonic velocity data’s quality is affected by the borehole conditions (irregular diameter) caused by the poorly consolidated rocks that can be inferred from the caliper log. Shear wave velocity measurements were especially affected by these borehole conditions. The compressional p-wave values are of good quality and can be used to analyse the rock properties. At a 260 m depth, and coincident with the base of the Neapolitan

Yellow Tuff sequence, increased  $V_p$  values are observed (3000 m/s). A good correlation is observed between the gamma radioactivity and pH along the Neapolitan Tuff formation at a depth ranging from 220 to 280 m (Figure 3).

## 2.2. From the Pilot Hole to the Deep Drilling

One of the aims of the pilot hole was to better understand the conditions of temperature, stress, and rock properties in the shallower substructure to plan the deep drilling, since the deviation towards the center caldera requires knowing the temperature at depth. In fact, electronic devices needed to perform the correct deviation cannot sustain temperature greater than about 150 °C. The temperature found at less than 500 m of depth in the former ENEL–AGIP drillings on the other side of the caldera exceeded 200 °C. Moreover, in the neighboring area of Agnano, about 2 km N–NW of Bagnoli, temperatures exceeding 100 °C can be found at depths as shallow as a few tens of meters. The Bagnoli borehole showed a temperature of about 110 °C at 500 m of depth, thus being compatible with the deep hole deviation at 500 m. Moreover, the high temperature gradient in parts of the caldera combined with seismic tomography [36,37] suggest highly pressured gas reservoirs may be found at a relatively shallow depth. However, the 500 m Bagnoli well did encounter such conditions. The CFDDP pilot hole, therefore, gave important results about the thermal and hydraulic rock properties and shallow stratigraphy indicating favorable conditions for a deep deviated drilling to find supercritical fluids deep down at the same site (Figure 4).

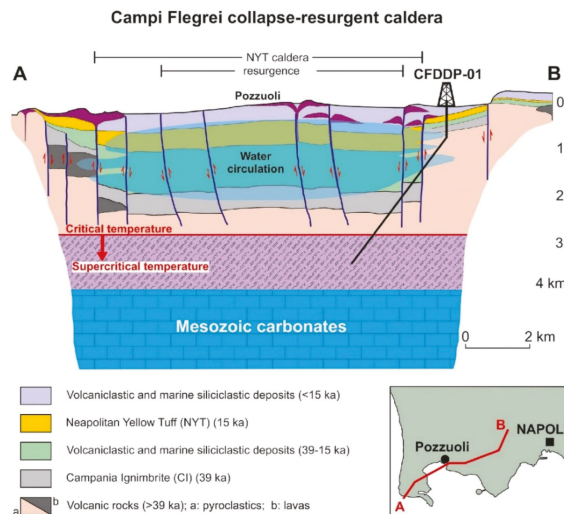


**Figure 4.** Schematic representation of the Campi Flegrei caldera structure indicating the proposed onshore deep inclined borehole CFDDP-01. Modified from Reference [38].

Following the results of the pilot hole, a further well, specifically aimed to find the areas of highest temperature gradients at very shallow depths, and hence the most suitable for inexpensive and powerful geothermal exploitation, was drilled in the Agnano–Pisciarelli area (red triangle in Figure 1). The measured temperature–depth profiles of the two wells are shown in Figure 5 [39]. The Agnano borehole samples the area of highest shallow geothermal gradient, with temperature exceeding 110 °C found at only 88 m of depth, showing the very high potential of this area, already quantified by Reference [19], even at very modest and inexpensive depths.

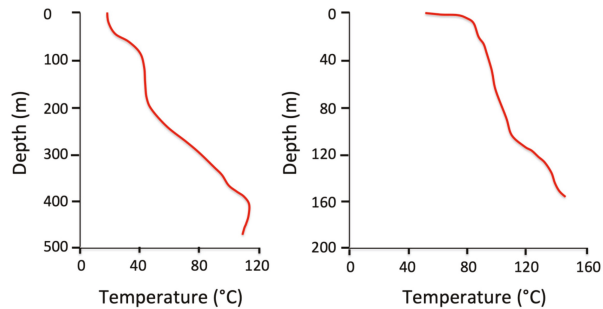


**Figure 5.** Temperature profiles of the Bagnoli 1 well ((left), Reference [39]) and of the Agnano well ((right), measured with thermocouple probe).

### 3. Geothermal Energy in the UK

The UK is not typically considered to be a country of significant geothermal energy potential, since it is located far from tectonic plate boundaries and is not volcanically active. Investigation into the UK's geothermal energy potential was instigated in the wake of the 1973 oil crisis. In the Cornwall region, characterized by a long mining history, elevated temperatures were measured in deep tin and copper mines [40]. These were later proven by heat-flow studies and geothermal assessments conducted by the BGS (British Geological Survey) [41,42]. In 1974, systematic heat-flow studies in the region revealed anomalously high values across the Cornubian Batholith (c.  $120 \text{ mWm}^{-2}$ ), more than double the UK average [43–45], due to the high concentrations of “heat producing” radioelements uranium, potassium, and thorium within the granites. Needless to say, it has long been known that the “rocks are hot down there”, and in the 1970s, the “Hot Dry Rock” project was conducted off the back of this knowledge to explore the potential of Cornwall's untapped geothermal resource. The HDR Geothermal Project (1974–1991) was pioneered by Camborne School of Mines and was located 7 km SSW of the recent UDDGP project [46]. The results from the HDR project were fundamental to the development of UDDGP, influencing both site selection and well design [47].

Cornwall is geologically known as the Cornubian Massif, part of the Variscan Massif, that is surrounded by Permian and younger offshore sedimentary basins [48]. Granites associated with the Cornubian batholith outcrop as six main plutons in the upland areas (Figure 6a). The thickness of the granite mass is not known, but from geophysical studies and the high heat-flow values, it is thought to be several kilometers. The granites of the Cornubian batholith, and Devonian host-rock formations, are crosscut by extensive NW–SE to NNW–SSE striking strike slip fault zones (Figure 6b). NW–SE to NNW–SSE striking fault zones displace earlier formed ENE–WSW striking extensional, magmatic hydrothermal lodes, and experienced selective post-Triassic reactivation and fluid migration [49]. The Porthtowan Fault (PTF) zone targeted at UDDGP is a NNW–SSE striking complex strike-slip fault zone belonging to this family of sub parallel fault structures in SW England.

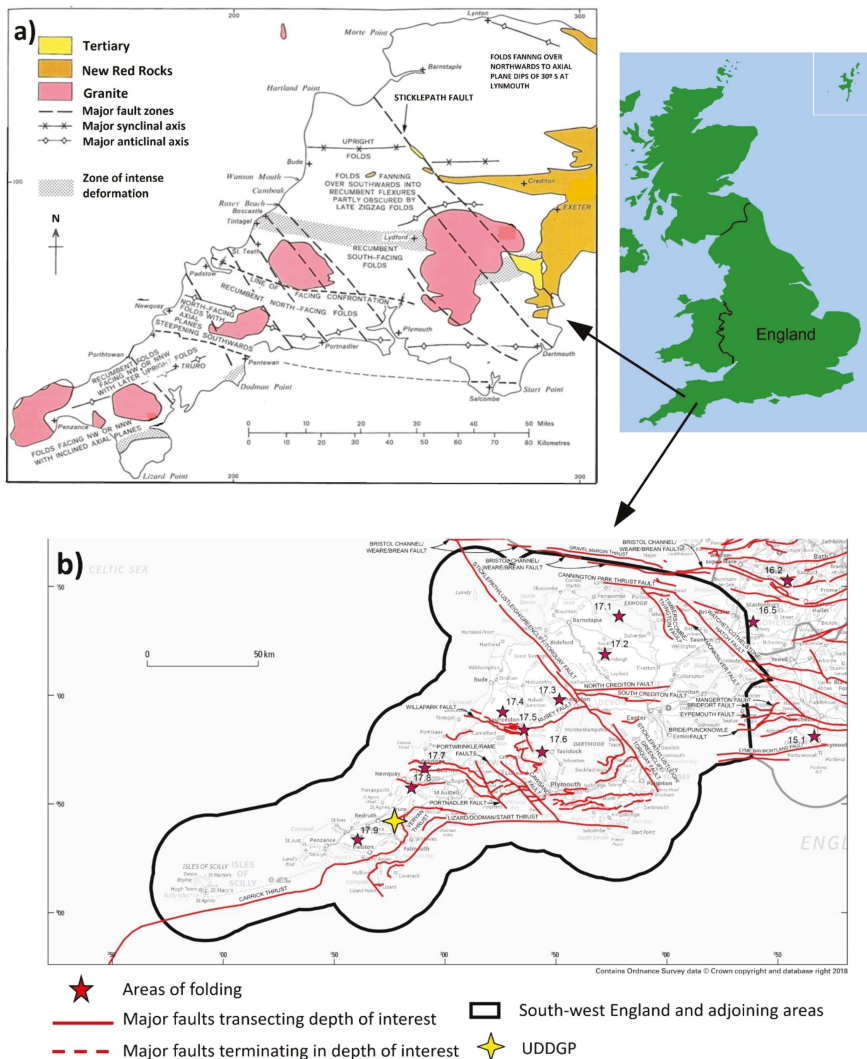


**Figure 6.** (a) Major faulting across the SW of England and granite location [50]. (b) Major faults and areas of folding in the South West England region, and location of the UDDGP project, Contains Ordnance Data © Crown Copyright and database rights 2018. Ordnance Survey License no. 100021290. Contains British Geological Survey digital data © UKRI 2018 [51].

### 3.1. The United Downs Deep Geothermal Power Project

The UDDGP project is the first of its kind in the UK and is located near Redruth in Cornwall. The project is predominantly funded by the European Regional Development Fund and Cornwall Council as well as some private match funding. The deeper production well (UD-1) is currently the deepest onshore well in the UK, at a vertical depth of 5057 m TVD, and was completed in April 2019. The injection well (UD-2) was completed 3 months later at the end of June 2019 to a depth of 2205 m TVD. These wells were drilled by using the Innovarig, a new-generation semi-automatic hydraulic rig (Figure 7a). The large well separation of over 2000 m is unique and was developed for two reasons: firstly, to help prevent the geothermal system from “short circuiting” and negatively impacting

the temperature performance (as was experienced in the 1980s HDR project) and secondly to try develop a deep geothermal system that is more economic and therefore commercially viable. Both wells are deviated towards the WSW at depth to intersect the PTF (Figure 7b). This steeply dipping NNW striking structure was identified as having enhanced permeability during the feasibility stage from the mining records, which showed both occurrences of hot springs along its strike length and hydrocarbon seeps close to the fault zone. When combining its surface expression with observations from the mining records and aeromagnetic data, the PTF is thought to have a strike length of >15 km and a nominal width of c. 400 m containing a complex zone of braided fault strands with relays, overstep, and jogs, with opposing dips and senses of displacement on individual strands [40].

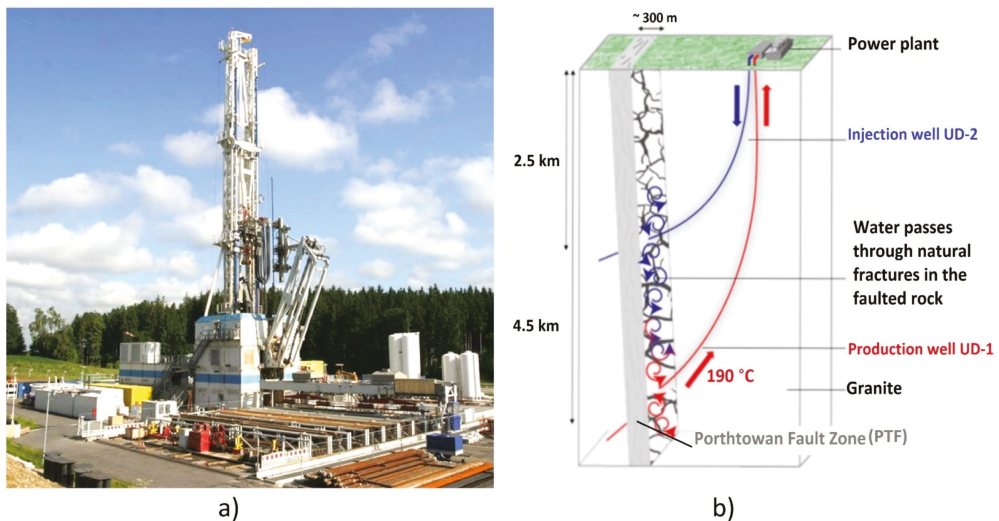


**Figure 7.** (a) The Innovarig hydraulic rig [52]; (b) schematic section with the production well (UD-1), injection well (UD-2), and Porthtown Fault (PTF), modified from Reference [53].

### 3.1.1. Analysis of Drill Cuttings

Samples of drill cuttings were collected every 10 m and every 5 m once in or close to the target structure. Further cuttings samples were taken at bit changes and at sudden changes in drilling parameters, mud samples were taken every 12 h. Upcoming lithology and fractures were hard to predict since mining records in the area ceased at 400 m and no geophysical data were available. For this reason, it was essential to collect as much down-hole data while drilling to predict and correctly identify the Porthtown Fault zone. Three main lithologies were encountered during the drilling of UD-1 and UD-2 at United Downs: metasediments (killas), microgranite, and granite.

Metasediments were found in the upper 210 m of UD-1 and were dominated by highly deformed, low-grade regionally metamorphosed and deformed mudstones of the Upper Devonian Mylor Slate Formation [54]. This lithology contains hard metamorphic quartz veins of late Variscan age, formed before the intrusion of the granite. QEMSCAN analysis of samples from the upper 210 m of UD-1 showed traces of mineral assemblages akin to those encountered during the formally mined steeply dipping lode systems within the slates of the United Downs mining district (Figure 8). The results included a range of oxide–sulfide mineralization, showcasing nearly every mineral that have been exploited in this area, including occurrences of tin, copper, zinc, and wolframite.

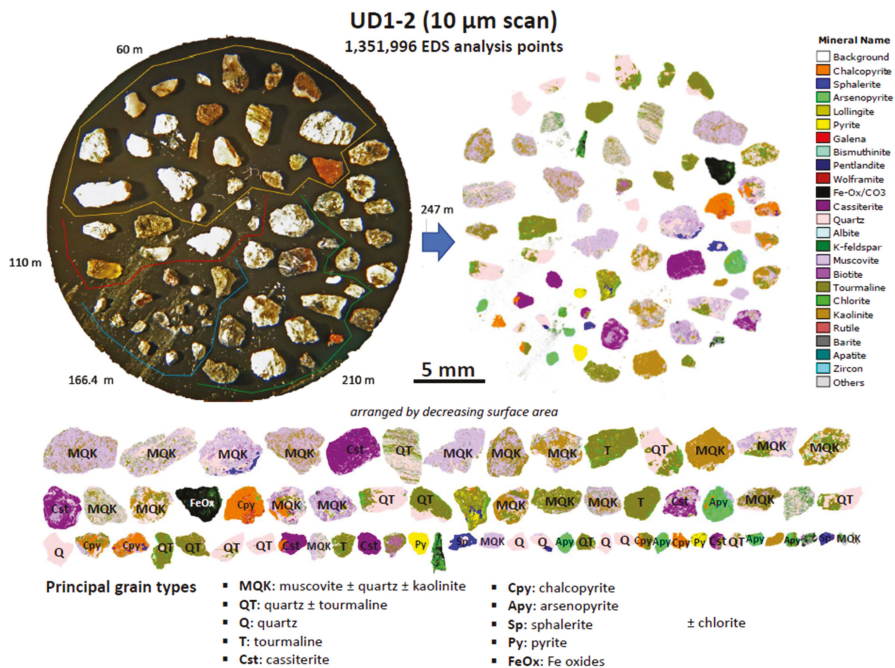


Figure 8. QEMSCAN analysis from the top 210 m of UD-1, accredited to CSM (Camborne School of Mines).

Both UD-1 and UD-2 penetrated heavily griesened and kaolinized fine grained “microgranite” from 210 m MD to c. 740 m MD. Although unexpected at the time, this lithology has since been accredited to NNW-dipping microgranite–rhyolite dyke, locally termed “Elvan” which was mapped at surface by the BGS in 1989.

Almost all unaltered samples of granite were muscovite dominant and corresponded with definitions of two mica granite and muscovite granite as recently redefined by the reclassification of Cornubian granites [55]. Further, nearly all coarse cuttings below 740 m plotted within the monzogranite field on the QAP classification which was consistent with the granites encountered during the HDR project at Rosemanowes some 5 miles away. Notable variations of texture and mineralogy with regard to the assemblage of accessory minerals led to further classification of the granite. The radiogenic classification of granites split the granite into four types, depending on their U/Th ratios from the spectral gamma data during wireline logging and helped to constrain and understand the heat-flow values.

### 3.1.2. Education and Community Outreach

The emphasis on community engagement from the outset of the project was critical to gain an SLO (Social License to Operate). The geothermal development was a high-profile project that attracted a lot of attention: communication was a high priority and was a unique and successful part of the project, which, if possible, should be emulated elsewhere. Since the UDDGP project is the first of its kind in the UK, the geothermal concept being tested at the site, as well as the associated deep-drilling technology, is new and unfamiliar, and unfamiliarity often leads to concern. Therefore, gaining a SLO was imperative to enable further development and growth of the industry. Although deep drilling for geothermal energy is relatively new to the region, subsurface exploration for natural resources is not unfamiliar to Cornwall given its long mining history. Effective science communication is key to the understanding and acceptance of new projects, and therefore high priority was given to education and communication of the project, with the overall objective of making

the maximum amount of information easily accessible to all members of public, and to encourage direct communications with project staff.

The UDDGP education program was designed around two key focuses: a gap in taught subjects and growing a new industry, with the aim of making education about geothermal and its potential in Cornwall, and the UDDGP concept available to all ages across all subject areas. It was designed for students between the ages of 7–21 years and split into specific age groups according to the English education system: KS2 (7–11 years), KS3 (11–14 years), KS4 (14 years+), and higher/further education, for example university students. For KS2 and KS3 students, respectively, lessons were created and delivered in a session either on site or in schools. The animation for younger ages features a character called “Miss Molecule”, who transports heat from the reservoir to the power plant for electricity generation [40].

A Raspberry Shakes program was launched in 2018 and incorporated into the KS4 by providing nine local secondary schools with a Raspberry Shake seismograph and Raspberry Pi computers with geophones to measure ground vibration. The Raspberry Shake seismographs formed a Cornish Schools Microseismic Monitoring Network that highlighted the level of natural background seismicity in the region, which helped “normalize” discussions around the potential for induced seismicity from the geothermal project. Overall, the education program has reached 3000 students from 46 educational institutions. Positive feedback has been received from teachers, particularly from primary schools.

The outreach program was designed to ensure public engagement throughout the duration of the project, and clarity and accessibility of project information to the communities closest to the project site, as well as the wider population of Cornwall. A significant focus of the outreach was the drilling phase of the project, due to the likelihood for public concern surrounding the potential for environmental and social disturbances [40]. Due to the rise in anti-fracking protests and subsequent ban of “fracking” by the UK Government in late 2019, it was anticipated that a false association might be drawn between the targeting of natural fault zones for permeability at UDDGP and “fracking” technology used by the oil and gas industry. A Community Relations Manager was employed during the early stages of the project to work within the community. This enabled new relationships to be built between project staff and the local community. Public visits were also hosted on site, including both organized group visits to the site and site “drop-in” days. A website was created during the early stages of the project to provide information on geothermal energy and specific information about the project. Social media channels also provided a constant, reliable source of information. Short films and animation videos included a “seismicity explainer” video that was created to address initial concerns regarding induced seismicity and “fracking”.

The response to this community outreach program has been overwhelmingly positive, with growing enthusiasm for geothermal development and the establishment of a new sustainable industry in Cornwall. Strong communication channels established between the project team and local community have led to the initial fears of the residents being unfounded.

#### 4. Geothermal Energy in Canada

The Canadian interest for the development of geothermal energy sources started around 1972/1973 as a consequence of the diesel price rise and reserves decline forecasts [56]. Prior to the 1970s, geothermal energy sources were restricted to direct use applications, such as hot springs and spas in Western Canada [57]. The first governmental program to investigate the geothermal potential of Canada, the Geothermal Energy Program, began in 1976 but was terminated a decade later in 1986, motivated mostly by the oil-price drop, but also due to the perception of geothermal energy as a high capital risk [57–59]. Almost 5 decades have passed since Canada started seeing geothermal energy sources from an industrial point of view, rather than only for ludic activities. In the Western Canadian Sedimentary Basin, three major deep geothermal direct-use and power projects

are progressing: the Clarke Lake geothermal project, the Alberta #1 Greenview project, and the DEEP Earth Energy Production project.

#### 4.1. The Saskatchewan DEEP Project's Geological Context

The Williston Basin is an inter-cratonic basin centrally located on the North American continent straddling the Canadian American border (Figure 9). It is an ellipsoidal bowl-shaped depression that forms the southwest extremity of the Western Canadian Sedimentary Basin. Oil was first discovered in the Williston Basin in Southeastern Montana in the 1920s and in North Dakota in 1951 and subsequently, more than 115,000 wells have been drilled. The sedimentary section of the Williston Basin reaches a thickness of over 4800 m in Northern North Dakota and the stratigraphic section demonstrates that the predominant depositional environment was a shallow sea from the Cambrian until the late Cretaceous. DEEP is developing its geothermal project from an HSA at the base of the Williston Basin, known as the Deadwood Formation.

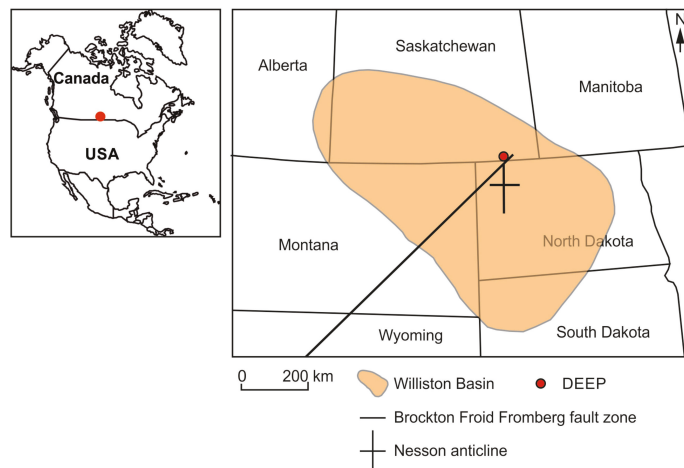


**Figure 9.** Williston Basin and DEEP project (red dot) location map.

The Deadwood Formation basal clastics in the Williston Basin were deposited after a long period of Precambrian erosion. The Deadwood sands represent a thick package of mature sandstones that accumulated on the Precambrian surface. The lower Cambrian Deadwood formation represents the first transgressive event as Cambrian seas transgressed the low relief and irregular Precambrian surface. Deadwood sedimentation initially started in an aeolian and dune environment directly on the Precambrian basement. This is overlain by a thick package of mature porous deltaic and fluvial sediments which grade upwards to offshore sands (informally referred to as the DEEP Sands). At this time, the deltaic focus shifted, and we see a drop in sea level and sedimentation of longshore-drift-influenced brackish lagoons and fluvial channels capped by aeolian sands and complete exposure. Final sedimentation of the Deadwood by a marine transgression resulted in deposition of a tight tidal flat carbonate package.

In the DEEP project area, the Deadwood is unconformably overlain by transgressive sandstones, siltstones and shales of the middle Ordovician Winnipeg formation. The deposition of the Winnipeg formation is contemporaneous with the initiation of the structural depression that forms the basin. The sediments of the Williston Basin are representative of all periods of the Phanerozoic. Silica diagenesis precludes porosity in parts of the Deadwood and Winnipeg Formations. Intense silica cementation takes place at updip-exposure surfaces. The texture is reminiscent to quartzite and makes an effective seal. Silicification is prevalent in the initial aeolian and dune sediments directly overlying the Precambrian

basement and in the basal Winnipeg sands. The geochemistry of silica precipitation is associated with acidic conditions and elevated temperature, suggesting that the Deadwood may have been subjected to an even higher temperature in the past.

#### 4.2. DEEP Earth Energy Production Corp. Project Overview

Injection wells for water disposal in Saskatchewan and gas wells in North Dakota demonstrate a basin-scale resource with reservoir characteristics suitable for large fluid production and injection rates; however, temperatures greater than 100 °C are only found in the southeasterly most part of Saskatchewan and Western North Dakota. The project is unique in that it targets deep hot water in a highly productive oil region. The project has thousands of horizontal oil wells as neighbors and is located in the renowned Bakken oil trend.

DEEP's long-term strategy is to build geothermal power facilities along with direct use applications. This strategy complies with a vision of a cleaner energy future for Saskatchewan and simultaneously supports SaskPower's goal to reduce 2005 emission levels by 40% by 2030. Produced electricity from the first facility will be sold under an existing Power Purchase Agreement with SaskPower. DEEP is exploring additional revenue streams including a commercial greenhouse development, which would be a new opportunity for the Saskatchewan agricultural sector. To date, the project has advanced with ~CAD\$30M of Federal and Provincial funding and ~CAD\$20M of private investment. Federal funding was announced in person in Regina, Saskatchewan, by Prime Minister Trudeau, the first renewable energy funding announcement ever made by a Prime Minister in the history of Canada. The studies performed show that the resources in this geothermal reservoir can potentially be used by power plants with capacities of more than 100 MWe. Construction of the first 20 MW facility is planned to commence in August 2021 and fully commissioned by March 2023. The DEEP project is certainly an important step toward Canada's energy transition. These first 20 MWe would reduce about 114,000 metric t of CO<sub>2</sub>/year.

#### 4.3. Drilling and Completion of Deep Wells

The drilling rig is shown in Figure 10a, where, subsequent to the Border-1 discovery well completed in December 2018, four more vertical/directional wells were drilled over the 2019/2020 winter: Border-2A, Border-2B, Border-3, and Border-4 (Table 1 and Figure 10b). Border-2B was drilled starting from well Border-2A and then deviating to acquire additional data. Then, well Border-3 was directionally drilled from the location of Border-1, while the vertical well Border-4 is located southwest of the previous wells and outside the domain shown of Figure 10b.

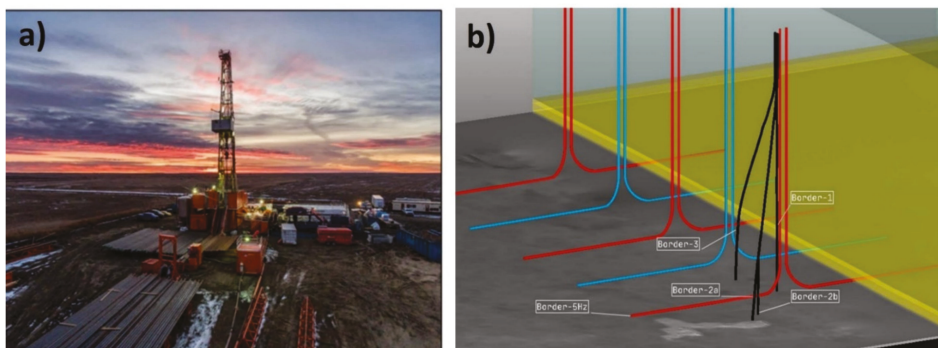


Figure 10. (a) Drilling rig for the DEEP project and (b) schematic representation of drilled wells [60].

**Table 1.** Main characteristics of wells drilled to date at DEEP project.

Well Name	Border-1	Border-2A	Border-2B	Border-3	Border-4	Border-5
Type	Vertical	Directional	Whipstock Directional	Directional	Vertical	Horizontal
Drilling Days	38	37	26	22	30	43
Drilling Costs (\$M)	3.53	3.60	1.99	2.25	2.60	4.60
Liner Type	Slotted/Solid	n/a	Slotted/Solid	Solid	Solid	Solid w/Frac Sleeves
Bottom Hole Temp. (°C)	125	117	121	122	120	127
Well TD (mMD/mTVD)	3530	3840/3496	3890/3624	3681/3560	3731	5672/3731

The total amount of new hole drilled (minus above the Border-2B whipstock) was 12,279 m. There was 185 m of core cut and 10 drill stem flow tests (includes 2 misruns). The intermediate section of the wells was cased with 177.8 mm (7") casing. The results of this drilling program were determined in an extensive 2020 summer testing program that included a combination of flowing and injectivity tests.

A sixth horizontal well, Border-5, was drilled and hydraulically stimulated in October 2020. This was the first 90° horizontal fluid production well in the world to be drilled and hydraulically stimulated for the purposes of geothermal power generation. The horizontal well was drilled to a total measured depth of 5672 m (3450 m vertical depth) which includes a 2000 m horizontal section. The well was completed with a cemented liner and a 20-stage multicycle stimulation sleeve system, and hydraulically stimulated using the latest horizontal well techniques. The highest temperature measured during open-hole logging was 127 °C. No significant issues were encountered during drilling and the geological, operations and directional staff were able to maintain the well trajectory in the reservoir target zone for a significant portion of the lateral length. This well demonstrates the viability of horizontal drilling for geothermal resources in Hot Sedimentary Aquifers, supports the geophysical analysis, and further demonstrates reservoir continuity. The open hole well was tested by using a coil tubing nitrogen lift test, which indicated high permeability and flow capability with an absolute open flow capacity in the order of 20,000 m<sup>3</sup>/d or a productivity index of 0.55 m<sup>3</sup>/d/kPa. Successful mechanical stimulation and production modeling indicate a highly productive well—twice the productivity of an unstimulated well. This well will sustain commercial production rates (100 L/s), while minimizing fluid drawdown. Drilling and testing results indicate that temperature and potential flow rates are sufficient to support multiple 20 MWe geothermal power facilities (enough power to supply approximately 20,000 households).

#### 4.4. Social and Economic Implications

The province of Saskatchewan has a long history of developing its natural resources with oil and gas being one of the leading industries as well as being the world's largest producer of potash and one of the world's largest producers of uranium. Saskatchewan is the second-largest oil-producing jurisdiction in Canada and seventh-largest onshore oil-producing jurisdiction in Canada and the United States. Improvements to horizontal oil well drilling and completion techniques have greatly improved production in the last several years. There have been ~90,000 oil and gas wells drilled in the Williston Basin on both sides of the Canadian and American border in Saskatchewan and North Dakota combined. In Saskatchewan alone, including the Williston Basin and other oil reservoirs, there has been a total of ~270,000 oil and gas wells drilled in the province [61]. The resource industry is a key economic driver in the province through royalty payments to the province from producers and major industry and job creation. As such, there is strong local support to develop provincial geothermal resources and a robust regulatory environment already exists to support it. This strong provincial regulatory environment for drilling and exploration is a key strength in the DEEP geothermal project. Licensing for drilling deep wells is a commonplace activity, which is not the case elsewhere in the world, since it is

benefiting from the enormous experience of Canada’s oil and gas mining industry and it is converting the workforce to new forms of clean, renewable, and sustainable energy.

The project is attracting, for the first time, a diverse and innovative labor force that has been previously geared only to fossil fuel production. DEEP’s geothermal project has been locally championed as a way to both literally and figuratively develop a new clean energy industry on the backs of the oilfield industry and has been benefited from co-funding and continued logistical and authorization support from Natural Resources Canada. The effects on the labor market in the country have seen the redeployment of workers with high technological and scientific profiles on a renewable energy project.

## 5. Discussion and Conclusions

The three geothermal drilling projects presented here, the CFDDP in Italy, the UDDGP in the United Kingdom, and the DEEP in Canada, show that the development of unconventional resources can be achieved with proper scheduling, scientific knowledge, technical expertise, and communication with local communities and stakeholders. The characterization of caldera-hosted geothermal resources, Enhanced Geothermal Systems in granite basement, and Hot Sedimentary Aquifers are the three different geological contexts described here. The drilling depth reached in each site is different, but the enthalpy of the fluids is comparable, since the geothermal gradient is higher in the Campi Flegrei Caldera (about 220 °C/km) than in the UK and Canadian sites, where almost the same gradient is observed (37 °C/km), as shown in Table 2.

**Table 2.** Summary of the main characteristic of the three geothermal drilling projects considered.

Project Acronym	Country	Maximum Drilled Depth TVD	Bottom/Hole Temperature (°C)	Geothermal Gradient (°C/km)	Period of Drilling Activities	Number of Wells Drilled to Date in Each Project
CFDDP	Italy	500	~110	220	2012	1
UDDGP	United Kingdom	5057	187	37.2	2019	2
DEEP	Canada	3450	127	36.8	2019–2020	6

From the technical point of view, the CFDDGP allowed the application of real-time mud-gas analysis technique, which has been shown to be a valuable and operationally simple way to obtain qualitative information about the fluid contents in a specific drilled section. The method described above is operationally simple and relatively inexpensive. Because the mud-gas samples are taken during drilling, it also helped to decide if and at what depth, rock or fluid samples should be taken. A good correlation between the fluid’s changes and lithology of the drilling core has been identified. CH<sub>4</sub>, He, and with limitations CO<sub>2</sub> and H<sub>2</sub> are most suitable for detection of fluid-bearing horizons, such as shear zones, open fractures, and sections of enhanced permeability. This technique can be used with other gas of interest depending on the industrial application (i.e., geothermal, oil and gas, etc.).

At the UDDGP project, detailed analysis of the cuttings allowed for a qualitative overview of the relationship between mineralogy and the concentration of radiogenic components, which helped to constrain local heat-flow data and led to a new classification of granite types based on their Th, U, and K ratios. Significant peaks in gamma correlated with mineral rich lodes (veins) provided additional evidence for fractures. Other structural features were indicated by notable changes in the cuttings, which corresponded to zones of losses recorded whilst drilling. QEMSCAN and SEM analysis were used to establish the mineralogical differences between the fractured zones and surrounding granite.

DEEP’s subsurface “fishbone” geothermal field design is globally unique and is a transformative application of modern oil and gas drilling, completion, stimulation design, and field execution techniques applied for the first time on a renewable energy project. The drilling for this project is being advanced by local world class oilfield expertise and redeploying that uniquely skilled workforce into a new clean energy industry for Canada.

Stimulated horizontal wells drilled at a similar elevation are planned in the final completion phase of the project to implement production and injection well doublets. This anticipated well-field design is significantly different from what was used at the UDDGP project, with production and injection wells at different elevation levels.

The activities conducted in these three projects highlight the importance of proper communication and establishment of outreach programs. In Italy, the CFDDP experience shows that misunderstanding about technical aspects can stop a research project. A lesson learnt from the shallow pilot hole drilling is that a better communication among academia, politicians, stakeholders, and communities is required for the second phase of the project, whose target is a 3500 m–deep well, aiming to reach supercritical fluids inside the caldera. In contrast, in the UK, the outreach program was established one year before drilling started, and the phased approach taken, helped to build trust in the project leading to its increased acceptance.

The developers of deep geothermal projects, as well as of any other energy generation plant, have the responsibility to clearly share the information about their projects, indicating the potential environmental impacts and their mitigation measures, the employment opportunities, and the benefits of electricity generation from renewable sources. The comparison among different energy sources, the divulgation of basic scientific and technical topics, and the promotion of public consciousness of our energy need and consumption are important aspects that should be included in community outreach programs. However, the obstacles that can be encountered with the opposition of local communities are site-specific, besides being related to economic, social, and political context of each country. Considering the three sites analyzed here, the population density is very different, which may explain the local communities' reactions to each project (Table 3).

**Table 3.** Population density in the regions of the three geothermal projects reviewed.

Country	Site	Population Density Residents/km <sup>2</sup>	Year	Source
Italy	City of Naples	8091	2020	ISTAT [62]
United Kingdom	Cornwall county	161	2018	Office for National Statistics [63]
Canada	Southern Saskatchewan province	<2	2020	Statistics Canada [64]

A further aspect to be considered for social acceptability is also the vocation of the territory, which differs greatly in the various cases analyzed of Campi Flegrei (its volcanic context and geothermal manifestations), Cornwall (its mining heritage) and Southern Saskatchewan (its oil and gas history). The Phlegraean Fields represent a portion of the famous Campania Felix defined by the Romans where numerous centers of Greek civilization first and then Roman civilization settled. The fertility of the soil of volcanic nature and the availability of geothermal resources has been a focal point for the development of the area. In the 1970s, there were two periods of strong bradyseism (1970–1972 and 1983–1984) in which there has been a gradual relocation of the inhabitants of the area of Pozzuoli in neighboring areas. It is precisely during this period that there was a resumption of geothermal exploration with the drilling of wells reaching considerable depths (Table 4). However, this research activity was abandoned for reasons related to the phenomena of bradyseism, until 2012 with the drilling of the CFDDP pilot well. In Cornwall, the two wells of the UDDGP project are the only ones drilled in the area aside from mining exploration boreholes (Table 4). Geothermal development is looking to restore jobs and boost the local Cornwall economy producing electricity, heat, and, hopefully, lithium [65]. The bottom hole temperature of 187 °C from the production well was ascertained during production testing in August 2020. The project is currently in its testing phase with plans to build a commercial power plant supplying 3 MW of electricity later in the year.

**Table 4.** Main characteristic of the drilling activities (geothermal and oil and gas) at each site.

Site	Country	Period of Drilling Activities	Number of Wells Drilled to Date
Campi Flegrei [19,22]	Italy	1939–2020	28
Cornwall [24]	United Kingdom	2019	2
Williston Basin [61]	Canada	1982–2020	~90,000

A drilling project is therefore site- and technology-specific: in the UDDGP project, the community outreach and education program played a central role in achieving drilling goals, while for DEEP licensing was straightforward because of the numerous oil and gas wells in the region. In CFDDP, on the other hand, a serious controversy was generated, involving the population, scientists, and politicians, in a densely populated area. Finally, while the CFDDP is a scientific project, those in the UK and Canada are industry driven and this review is a first initiative to compare scientific and industrial geothermal drilling projects. This comparison shows that each geothermal drilling project has its own history, not only because of the different geological context and technical challenges, but also because the different approaches with the local communities, as well as cultural aspects related with history, economy, and politic of each country.

Among other recent experiences, the ongoing IDDP project in Iceland has provided interesting new insights for the scientific community. The IDDP-2 well drilled in 2017 is the first well that exceeds not only critical temperatures, which was already observed in countries such as Italy, Mexico, or Japan, but also critical pressures, in the history of geothermal drilling [66]. On the other hand, EGS development in France has shown successful experiences, with the Soultz-sous-Forêts power plant [67], where, after 30 years of research, a binary power plant has started operation in 2016, as well as with the Rittershoffen geothermal heat plant, successfully providing an average of 22.5 MWt and 180 GWh/year of heat since June 2016 [68]. Successful examples of unconventional geothermal development are also given by Croatia, with the plant in Velika Ciglena [69], and Germany, with the Landau plant [70].

However, in several regions of France, people opposed to hydraulic stimulation for geothermal energy, since they point out the risk of induced seismicity, as it happened according to recent news [71]. On the other hand, the interest for geothermal power production is growing in the oil and gas industry whose technical drilling expertise and innovations can readily be applied to develop geothermal reservoirs, as in the case of the DEEP project. Other recent technological development for geothermal systems includes closed deep borehole heat exchangers, such as the Advanced Geothermal Systems described by Wang et al. [72] and the Closed-Loop Geothermal (CLG) technologies, in their early commercialization stages, that use deep ground heat exchangers for power generation [73].

The motivation for promoting this kind of drilling projects lies in the transition from fossil fuels to green energies, particularly in in Canada and the UK; in Italy, although the Naples area has no oil and gas or mining tradition, as it is the case of the UDDPG and DEEP projects, the use of geothermal resources can contribute to the development of geoenery in that area. The three case studies described here indicate that drilling techniques and reservoir characterization methods are currently available for the development of unconventional geothermal resources (EGS, HSA, and supercritical fluids), contributing to the transition between non-renewable resource development (mineral in the UK, and oil and gas in Canada, just to highlight the examples given here), to renewable geothermal resources.

**Author Contributions:** Conceptualization, D.B., J.R., and R.S.; methodology, L.C., M.C., A.F., M.J.J., R.S., and T.W.; validation, D.B., L.C., M.C., G.D.N., M.J.J., K.M., M.M., J.R., R.S., and T.W.; formal analysis, D.B., L.C., M.C., G.D.N., A.F., M.J.J., K.M., M.M., J.R., R.S., C.T., and T.W.; investigation, L.C., M.C., G.D.N., A.F., M.J.J., K.M., M.M., J.R., R.S., C.T., and T.W.; resources, D.B., L.C., M.C., A.F., M.J.J., K.M., M.M., J.R., R.S., and T.W. data curation, D.B., L.C., M.C., G.D.N., A.F., M.J.J., K.M., M.M., J.R.,

R.S., and T.W.; writing—original draft preparation, D.B., L.C., M.C., G.D.N., A.F., M.J.J., K.M., M.M., J.R., R.S., and T.W.; writing—review and editing, D.B., L.C., M.C., G.D.N., M.J.J., K.M., M.M., J.R., R.S., and T.W.; supervision, D.B., J.R., and R.S.; project administration, G.D.N., R.S., C.T. (CFDDP), K.M. (DEEP), L.C., and M.C. (UDDGP); funding acquisition, G.D.N. (CFDDP), K.M. (DEEP), L.C., and M.C. (UDDGP). All authors have read and agreed to the published version of the manuscript.”

**Funding:** This research was co-funded by ICDP consortium and INGV for the CFDDP. Grant number CFDDP 05-2008.

**Institutional Review Board Statement:** Not applicable.

**Informed Consent Statement:** Not applicable.

**Data Availability Statement:** Not applicable.

**Acknowledgments:** We acknowledge Sebastian Cordoba for helping to format the references and the IGCP636 project “Geothermal resources for energy transition” belonging to the International Geoscience Program funded by United Nations Educational, Scientific and Cultural Organization (UNESCO) and International Union of Geological Sciences (IUGS) to which RS, DB, JR, LC, MC are members. We acknowledge 6 anonymous reviewers who contributed to the improvement of this manuscript.

**Conflicts of Interest:** The authors declare no conflict of interest.

## Abbreviations

API	American Petroleum Institute
BGS	British Geological Survey
CFc	Campi Flegrei caldera
CFDDP	Campi Flegrei Deep Drilling Project
CFDP-1	Campi Flegrei Deep Project Pilot hole
DEEP	Earth Energy Production in Canada
EGS	Enhanced Geothermal System
ENEL	Ente nazionale per l’energia elettrica
AGIP	Azienda Generale Italiana Petroli
FMI	Full Bore Imaging
HSA	Hot Sedimentary Aquifer
HDRs	Hot Dry Rocks
ICDP	International Continental Drilling Project
IDDP-2	Iceland Deep Drilling Project well-2
INGV	Istituto Nazionale di Geofisica e Vulcanologia
ISTAT	Istituto Nazionale di Statistica
NYT	Neapolitan Yellow Tuff
PTF	Porthtown Fault
QMS	Quadrupole Mass Spectrometer
SLO	Social License to Operate
UD-1	Deep production well UDDGP
UD-2	Injection well UDDGP
UDDGP	United Downs Deep Geothermal Power
UNESCO	United Nations Educational, Scientific and Cultural Organization

## References

1. Simmons, S.F. Geothermal Resources. In *Encyclopedia of Geology*, 2nd ed.; Alderton, D., Elias, S.A., Eds.; Elsevier: Amsterdam, The Netherlands, 2021; pp. 708–722. ISBN 978-0-08-102909-1.
2. Saemundsson, K.; Axelsson, G.; Steingrímsson, B. Geothermal systems in global perspective. In Proceedings of the Short Course on Surface Exploration for Geothermal Resources, Santa Tecla/Ahuachapán, El Salvador, 17–30 October 2009.
3. Moeck, I. Catalog of geothermal play types based on geologic controls. *Renew. Sustain. Energy Rev.* **2014**, *37*, 867–882. [[CrossRef](#)]
4. Kruszewski, M.; Wittig, V. Review of failure modes in supercritical geothermal drilling projects. *Geotherm. Energy* **2018**, *6*, 1–29. [[CrossRef](#)]
5. Fajar, A.; Yamada, R.; Uno, M.; Okumura, S.; Tsuchiya, N. Evaluation of Caldera Hosted Geothermal Potential during Volcanism and Magmatism in Subduction System, NE Japan. *Geofluids* **2019**, *19*, 14. [[CrossRef](#)]

6. Chiodi, A.; Tassi, F.; Báez, W.; Filipovich, R.; Bustos, E.; Glok Galli, M.; Suzaño, N.; Ahumada, F.M.; Viramonte, J.G.; Giordano, G.; et al. Preliminary conceptual model of the Cerro Blanco caldera-hosted geothermal system (Southern Puna, Argentina): Inferences from geochemical investigations. *J. South Am. Earth Sci.* **2019**, *94*, 102213. [CrossRef]
7. Tsuchiya, N. Potential Candidates of Supercritical Geothermal Reservoir. In Proceedings of the Geothermal Resources Council 41st Annual Meeting—Geothermal Energy: Power To Do More (GRC 2017), Salt Lake City, UT, USA, 1–4 October 2017; pp. 1587–1598.
8. Goff, F.; Janik, C.J. *Geothermal Systems*; Academic Press: Cambridge, MA, USA, 2000; p. 1415.
9. Friðleifsson, G.O.; Elders, W.A.; Zierenberg, R.A.; Stefánsson, A.; Fowler, A.P.G.; Weisenberger, T.B.; Harðarson, B.S.; Mesfin, K.G. The Iceland Deep Drilling Project 4.5 km deep well, IDDP-2, in the seawater-recharged Reykjanes geothermal field in SW Iceland has successfully reached its supercritical target. *Sci. Drill.* **2017**, *23*, 1–12. [CrossRef]
10. Harms, U.; Emmermann, R. History and status of the international continental scientific drilling program. In *Continental Scientific Drilling*; Harms, U., Koeberl, C., Zoback, M.D., Eds.; Springer: Berlin/Heidelberg, Germany, 2007; pp. 1–52. ISBN 978-3-540-68778-8.
11. Franco, A.; Vaccaro, M. Sustainable Sizing of Geothermal Power Plants: Appropriate Potential Assessment Methods. *Sustainability* **2020**, *12*, 3844. [CrossRef]
12. Volken, S.; Xexakis, G.; Trutnevyte, E. Perspectives of informed citizen panel on low-carbon electricity portfolios in Switzerland and longer-term evaluation of informational materials. *Env. Sci. Technol.* **2018**, *52*, 11478–11489. [CrossRef]
13. Häring, M.O.; Schanz, U.; Ladner, F.; Dyer, B.C. Characterisation of the Basel 1 enhanced geothermal system. *Geothermics* **2008**, *37*, 469–495. [CrossRef]
14. Malo, M.; Malo, F.; Bédard, K.; Raymond, J. Public perception regarding deep geothermal energy and social acceptability in the province of Québec, Canada. In *Geothermal Energy and Society*; Allansdottir, A., Manzella, A., Pellizzone, A., Eds.; Springer: Berlin/Heidelberg, Germany, 2018; pp. 91–103. ISBN 978-3-319-78286-7.
15. Carr-Cornish, S.; Romanach, L. Differences in Public Perceptions of Geothermal Energy Technology in Australia. *Energies* **2014**, *7*, 1555–1575. [CrossRef]
16. Pellizzone, A.; Allansdottir, A.; De Franco, R.; Muttoni, G.; Manzella, A. Geothermal energy and the public: A case study on deliberative citizens' engagement in central Italy. *Energy Policy* **2017**, *101*, 561–570. [CrossRef]
17. Huang, K.K.; Hickson, C.J.; Cotterill, D.; Champollion, Y. Geothermal Assessment of Target Formations Using Recorded Temperature Measurements for the Alberta No. 1 Geothermal Project. *Appl. Sci.* **2021**, *11*, 608. [CrossRef]
18. Richter, A. ThinkGeoEnergy's Top 10 Geothermal Countries 2020—Installed Power Generation Capacity (MWe). Thinkgeoenergy. Available online: <https://www.thinkgeoenergy.com/thinkgeoenergys-top-10-geothermal-countries-2020-installed-power-generation-capacity-mwe/> (accessed on 10 February 2021).
19. Carlino, S.; Somma, R.; Troise, C.; De Natale, G. The geothermal exploration of Campanian volcanoes: Historical review and future development. *Renew. Sustain. Energy Rev.* **2012**, *16*, 1004–1030. [CrossRef]
20. De Natale, G.; Troise, C.; Mark, D.; Mormone, A.; Piochi, M.; Di Vito, M.A.; Isaia, R.; Carlino, S.; Barra, D.; Somma, R. The Campi Flegrei Deep Drilling Project (CFDDP): New insight on caldera structure, evolution and hazard implications for the Naples area (Southern Italy). *Geochim. Geophys. Geosyst.* **2016**, *17*, 4836–4847. [CrossRef]
21. Deino, A.L.; Orsi, G.; De Vita, S.; Piochi, M. The age of the Neapolitan Yellow Tuff caldera-forming eruption (Campi Flegrei caldera—Italy) assessed by 40 Ar/39 Ar dating method. *J. Volcanol. Geotherm. Res.* **2004**, *133*, 157–170. [CrossRef]
22. Rosi, M.; Sbrana, A. Phlegrean fields. In *Quaderni di la Ricerca Scientifica*; Rosi, M., Sbrana, A., Eds.; Consiglio Nazionale Ricerche: Rome, Italy, 1987; Volume 114, pp. 1–175.
23. Orsi, G.; De Vita, S.; Di Vito, M. The restless, resurgent Campi Flegrei nested caldera (Italy): Constraints on its evolution and configuration. *J. Volcanol. Geotherm. Res.* **1996**, *74*, 179–214. [CrossRef]
24. De Natale, G.; Troise, C.; Somma, R. Invited perspectives: The volcanoes of Naples: How can the highest volcanic risk in the world be effectively mitigated? *Nat. Hazards Earth Syst. Sci.* **2020**, 2037–2053. [CrossRef]
25. Erzinger, J.; Wiersberg, T.; Zimmer, M. Real-time mud gas logging and sampling during drilling. *Geofluids* **2006**, *6*, 225–233. [CrossRef]
26. Erzinger, J.; Wiersberg, T.; Dahms, E. Real-time mud gas logging during drilling of the SAFOD Pilot Hole in Parkfield, CA. *Geophys. Res. Lett.* **2004**, *31*. [CrossRef]
27. Fedele, A.; Pedone, M.; Moretti, R.; Wiersberg, T.; Somma, R.; Troise, C.; De Natale, G. Real-time quadrupole mass spectrometry of hydrothermal gases from the unstable Pisciarelli fumaroles (Campi Flegrei): Trends, challenges and processes. *Int. J. Mass Spectrom.* **2017**, *415*, 44–54. [CrossRef]
28. Erzinger, J.; Kilburn, C.R.J.; Sammonds, P.R.; Gudmondsson, A.; Friðleifsson, G.O.; Troise, C. Drilling at Campi Flegrei Caldera (Southern Italy). Available online: [https://www.icdp-online.org/index.php?id=2126&no\\_cache=1&label=ICDP-2006/12](https://www.icdp-online.org/index.php?id=2126&no_cache=1&label=ICDP-2006/12) (accessed on 14 February 2021).
29. Goldberg, D. *Well Logging for Physical Properties: A Handbook for Geophysicists, Geologists and Engineers*, 2nd ed.; Eos Transactions American Geophysical Union: New York, NY, USA, 2001; Volume 82. [CrossRef]
30. Rider, M.; Kennedy, M. *The Geological Interpretation of Well Logs*, 3rd ed.; Rider-French Consulting Limited: Sutherland, UK, 2018; ISBN 9780954190682.
31. Serra, O. *Fundamentals of Well-Log Interpretation: The Acquisition of Logging Data*; Elsevier: Amsterdam, The Netherlands, 1984; ISBN 9780444426208.

32. Tang, L.; Luo, L.Q.; Lao, C.; Wang, G.; Wang, J.; Huang, Y. Real time fluid analysis during drilling of the Wenchuan Earthquake Fault Scientific Drilling Project and its responding features. *Tectonophysics* **2014**, *619*, 70–78. [CrossRef]
33. D'antonio, M.; Civetta, L.; Orsi, G.; Pappalardo, L.; Piochi, M.; Carandente, A.; De Vita, S.; Di Vito, M.A.; Isaia, R. The present state of the magmatic system of the Campi Flegrei caldera based on a reconstruction of its behavior in the past 12 ka. *J. Volcanol. Geotherm. Res.* **1999**, *91*, 247–268. [CrossRef]
34. Pabst, S.; Wörner, G.; Civetta, L.; Tesoro, R. Magma chamber evolution prior to the Campanian Ignimbrite and Neapolitan Yellow Tuff eruptions (Campi Flegrei, Italy). *Bull. Volcanol.* **2008**, *70*, 961–976. [CrossRef]
35. Piochi, M.; Kilburn, C.R.J.; Di Vito, M.A.; Mormone, A.; Tramelli, A.; Troise, C.; De Natale, G. The volcanic and geothermally active Campi Flegrei caldera: An integrated multidisciplinary image of its buried structure. *Int. J. Earth Sci.* **2014**, *103*, 401–421. [CrossRef]
36. Vinciguerra, S.; Trovato, C.; Benson, M.; Troise, C.; De Natale, G. Understanding the Seismic Velocity Structure of Campi Flegrei Caldera (Italy): From the Laboratory to the Field Scale. *Pure Appl. Geophys.* **2006**, *163*, 2205–2221. [CrossRef]
37. Vanorio, T.; Virieux, J.; Capuano, P.; Russo, G. Three-dimensional seismic tomography from P wave and S wave microearthquake travel times and rock physics characterization of the Campi Flegrei Caldera. *J. Geophys. Res.* **2005**, *110*. [CrossRef]
38. Sacchi, M.; De Natale, G.; Spiess, V.; Steinmann, L.; Aocella, V.; Corradino, M.; de Silva, S.; Fedele, A.; Fedele, L.; Geshi, N.; et al. A roadmap for amphibious drilling at the Campi Flegrei caldera: Insights from a MagellanPlus workshop. *Sci. Dril.* **2019**, *26*, 29–46. [CrossRef]
39. Somma, R.; Troise, C.; Zeni, L.; Minardo, A.; Fedele, A.; Mirabile, M.; De Natale, G. Long-Term Monitoring with Fiber Optics Distributed Temperature Sensing at Campi Flegrei: The Campi Flegrei Deep Drilling Project. *Sense* **2019**, *19*, 1009. [CrossRef]
40. Cotton, L.; Gutmanis, J.; Shail, R.K.; Dalby, C.; Batchelor, A.; Foxford, A.; Rollinson, G. Geological Overview of the United Downs Deep Geothermal Power Project, Cornwall, UK. In Proceedings of the World Geothermal Congress, Reykjavik, Iceland, 24–27 October 2020.
41. Downing, R.A.; Gray, D.A. *Geothermal Energy the Potential in the United Kingdom*; HMSO: Nottingham, UK, 1986; p. 187.
42. Francis, M.F. Investigation of the South West England Thermal Anomaly Zone. Ph.D. Thesis, Imperial College, London, UK, 1980.
43. Tammemagi, H.Y.; Wheildon, J. Terrestrial heat flow and heat generation in the south-west England. *Geophys. J. Int.* **1974**, *38*, 83–94. [CrossRef]
44. Tammemagi, H.Y.; Wheildon, J. Further data on the South-west England heat flow anomaly. *Geophys. J. Int.* **1977**, *49*, 531–539. [CrossRef]
45. Sams, M.S.; Thomas-Betts, A. 3-D numerical modelling of the conductive heat flow of SW England. *Geophys. J.* **1988**, *92*, 323–334. [CrossRef]
46. Parker, R.H. *Hot Dry Rock Geothermal Energy: Phase 2B Final Report of the Camborne School of Mines Project*; Pergamon Press: Oxford, UK, 1989.
47. MacDonald, P.; Stedman, A.; Symons, G. The UK geothermal hot dry rock R & D programme. In Proceedings of the Seventeenth Workshop on Geothermal Reservoir Engineering, Stanford University, Stanford, CA, USA, 22–24 January 1992.
48. Evans, C.D.R. *The Geology of the Western English Channel and Its Western Approaches*; British Geological Survey; HMSO: London, UK, 1990.
49. Chen, Y.; Clark, A.; Farrar, E.; Wasteneys, H.; Hodgson, M.; Bromley, A. Diachronous and independent histories of plutonism and mineralization in the Cornubian Batholith, southwest England. *J. Geol. Soc. Lond.* **1993**, *150*, 1183–1191. [CrossRef]
50. Beamish, B.; Busby, J. The Cornubian geothermal province: Heat production and flow in SW England estimates from boreholes and airborne gamma-ray measurements. *Geotherm. Energy* **2016**, *4*, 4. [CrossRef]
51. British Geological Survey TellusSW. Airborne Geophysical Data WMS. Available online: <https://www.bgs.ac.uk/technologies/web-map-services-wms/tellusw-airborne-geophysical-data-wms/> (accessed on 17 February 2021).
52. United Downs Deep Geothermal Power Project. Available online: <https://geothermalengineering.co.uk/united-downs/> (accessed on 20 February 2021).
53. Ledingham, P.; Cotton, L.; Law, R. The United Downs Deep Geothermal Power project. In Proceedings of the 44th Workshop on Geothermal Reservoir Engineering, Stanford University, Stanford, CA, USA, 11–13 February 2019.
54. Leveridge, B.E.; Holder, M.T.; Goode, A.J.J. Geology of the country around Falmouth. In *Memoir of the British Geological Survey*; England and Wales: Nottingham, UK, 1990; Sheet 352.
55. Simons, B.J.; Shail, R.K.; Anderson, J. The petrogenesis of the Early Permian Variscan granites of the Cornubian Batholith. Lower plate post-collisional peraluminous magmatism in the Rhenohercynian Zone of SW England. *Lithos* **2016**, *260*, 76–90. [CrossRef]
56. Souther, J.G. Geothermal power, the Canadian potential. *Geosci. Can.* **1976**, *3*, 14–20.
57. Thompson, A. Geothermal development in Canada: Country update. In Proceedings of the World Geothermal Congress, Bali, Indonesia, 25–29 April 2010.
58. Jessop, A.M. Geothermal energy in Canada. *Geosci. Can.* **1998**, *25*, 33–41. [CrossRef]
59. Jessop, A. *Review of National Geothermal Energy Program Phase 2—Geothermal Potential of the Cordillera (Report No.: Open File 5906)*; Natural Resources Canada: Ottawa, Canada, 2008. [CrossRef]
60. DEEP Earth Energy Production Corp. Available online: <https://deepcorp.ca/gallery/> (accessed on 15 February 2021).
61. Geoscut Data Base. Available online: <https://www.geologic.com/products/> (accessed on 22 February 2021). (license required for access).

62. Geo Demo ISTAT. Available online: <http://demo.istat.it/popres/index.php?anno=2020&lingua=ita> (accessed on 20 February 2021).
63. Cornwall Population Statistics. Available online: <https://www.plumplot.co.uk/Cornwall-population.html> (accessed on 20 February 2021).
64. Population and Demography Statistics. Available online: [https://www.statcan.gc.ca/eng/subjects-start/population\\_and\\_demography](https://www.statcan.gc.ca/eng/subjects-start/population_and_demography) (accessed on 20 February 2021).
65. Taylor, K. Electricity, Heat and Lithium: Geothermal Offers New Hope for Old Mining County. 2021. Available online: <https://www.euractiv.com/section/energy/news/electricity-heat-and-lithium-geothermal-offers-new-hopes-for-old-mining-county/> (accessed on 25 February 2021).
66. Kruszewski, M. IDDP-2 Well: A Significant Milestone for the Geothermal Industry. Available online: <https://www.geoenergymarketing.com/tag/criticaltemperatures/> (accessed on 25 February 2021).
67. Gérard, A.; Genter, A.; Kohl, T.; Lutz, P.; Rose, P.; Rummel, F. The deep EGS (Enhanced Geothermal System) project at Soultz-sous-Forêts (Alsace, France). *Geothermics* **2006**, *35*, 473–483. [[CrossRef](#)]
68. Douzief, M.; Ravier, G.; Perez Lopez, P.; Blanc, I. Environmental impacts of geothermal, natural gas and biomass used for heat generation at a starch plant. In Proceedings of the 1st Geoscience & Engineering in Energy Transition Conference, Strasbourg, France, 16–18 November 2020.
69. Richter, A. The 17.5 MW Velika Ciglena Geothermal Power Plant Starts Operation in Croatia. 2018. Available online: <https://www.thinkgeoenergy.com/the-17-5-mw-velika-ciglena-geothermal-power-plant-starts-operation-in-croatia/> (accessed on 25 April 2021).
70. Sanjuan, B.; Négrel, G.; Le Lous, M.; Poulmarch, E.; Gal, F.; Damy, P.C. Main geochemical characteristics of the deep geothermal brine at Vendenheim (Alsace, France) with constraints on temperature and fluid circulation. In Proceedings of the World Geothermal Congress, Reykjavik, Iceland, 24–27 October 2020.
71. Ehkirch, V. Après Les Séismes En Alsace, Menace Sur La Géothermie. Available online: [https://lexpansion.lexpress.fr/actualite-economique/apres-les-seismes-en-alsace-menace-sur-la-geothermie\\_2142307.html](https://lexpansion.lexpress.fr/actualite-economique/apres-les-seismes-en-alsace-menace-sur-la-geothermie_2142307.html) (accessed on 25 February 2021).
72. Wang, K.; Yuan, B.; Jia, G.; Wua, X. A comprehensive review of geothermal energy extraction and utilization in oilfields. *J. Petrol. Sci. Eng.* **2018**, *168*, 465–477. [[CrossRef](#)]
73. Van Horn, A.; Amaya, A.; Higgins, B.; Muir, J.; Scherer, J.; Pilk, R.; Ross, M. New Opportunities and Applications for Closed-Loop Geothermal Energy Systems. *Grc Trans.* **2020**, *44*, 1123–1143.



Article

# Small Unconventional Hydrocarbon Gas Reservoirs as Challenging Energy Sources, Case Study from Northern Croatia

Tomislav Malvić<sup>1</sup>, Uroš Barudžija<sup>1</sup>, Borivoje Pašić<sup>1</sup> and Josip Ivšinić<sup>2,\*</sup>

<sup>1</sup> Faculty of Mining, Geology and Petroleum Engineering, University of Zagreb, HR-10000 Zagreb, Croatia; tomlav.malvic@rgn.unizg.hr (T.M.); uros.barudzija@rgn.unizg.hr (U.B.); borivoje.pasic@rgn.unizg.hr (B.P.)

<sup>2</sup> Field Development, INA-Industry of Oil Plc., Av. V. Holjevca 10, HR-10000 Zagreb, Croatia

\* Correspondence: josip.ivsinovic@ina.hr

**Abstract:** Small possible hydrocarbon gas reservoirs were analysed in the Bjelovar Subdepression in Northern Croatia. This area includes the Neogene–Quaternary, mostly clastics, sequences, reaching 3000+ metres in the deepest part. The shallow south-eastern part of the Drava Depression contains a subdepression characterised with several, mostly small, discovered hydrocarbon fields, where the majority are located on the northern subdepression margin. The reason is the large distance from the main depressional migration pathways and main, deep, mature source rock depocenters. However, two promising unconventional targets were discovered inside the subdepression and both were proven by drilling. The first are source rocks of Badenian, of kerogen type III in early catagenesis, where partially inefficient expulsion probably kept significant gas volumes trapped in the source rock during primary migration. Such structures are the Western Bjelovar (or Rovišće) and the Eastern Bjelovar (or Velika Ciglena) Synclines. The second promising unconventional reservoir consists of “tight” clastic lithofacies of mostly Lower Pontian located on the north-eastern margin of the subdepression. These are fine-grained sandstones with frequent alternations in siltites, silty and clayey sandstones. They are located on secondary migration pathways, but were never evaluated as regional reservoirs, although numerous drilling tests showed gas “pockets”.

**Keywords:** hydrocarbon gas; unconventional reservoirs; drilling; Neogene; Croatia

**Citation:** Malvić, T.; Barudžija, U.; Pašić, B.; Ivšinić, J. Small Unconventional Hydrocarbon Gas Reservoirs as Challenging Energy Sources, Case Study from Northern Croatia. *Energies* **2021**, *14*, 3503. <https://doi.org/10.3390/en14123503>

Academic Editor: Felix Barreras

Received: 4 April 2021

Accepted: 10 June 2021

Published: 12 June 2021

**Publisher’s Note:** MDPI stays neutral with regard to jurisdictional claims in published maps and institutional affiliations.



**Copyright:** © 2021 by the authors. Licensee MDPI, Basel, Switzerland. This article is an open access article distributed under the terms and conditions of the Creative Commons Attribution (CC BY) license (<https://creativecommons.org/licenses/by/4.0/>).

## 1. Introduction

The main general background for this research is the fact that the era of oil and gas as dominant energy sources will not be obsolete in the next human generation. The role of renewable energies, generated by wind, Sun or tide, will be more and more important and their share in total production will probably reach 20–30% in many countries. The main reason for their growth is tax policy, supporting clean or “green” energy sources to decrease atmospheric pollution and the danger to the environment. Such a danger is relatively the highest for coal and nuclear based power plants, processing or transport. Unconventional reservoirs of hydrocarbon gases chemically contain the same gases as in the conventional reservoirs. In fact, it can be claimed that such “unconventional” gas reserves remained trapped in the source rocks where they were generated and later mostly migrated into more permeable rocks. The second unconventional source of such gas is reservoir rocks where the hydrocarbons migrated, but generally they are rocks of marginally low permeability and porosity for them to be considered as a reservoir. In both cases, especially in the second, the recovery of such gas does not demand large additional costs, because the unconventional reservoirs are often located in the same field alongside conventional reserves.

Moreover, as a second claim, unconventional reservoirs can often be accompanied by deep geothermal sources, especially where hydrocarbon reservoirs are in high-temperature zones (late catagenesis, metagenesis). Such geothermal energy could be directly used for an electrical power plant. However, numerous geothermal reservoirs are available worldwide

at low–medium temperatures. Such sources could be used through the installation of small-size power plants providing power or heat-applying Organic Rankine Cycles technology [1], where high efficiency could be reached with working fluid in the tubes side. In fact, the optimal combination of fluid, layout and polymer could save 73% of evaporator costs [1].

Economic optimisation of Organic Rankine Cycles for the exploitation of low to medium enthalpy geothermal brines has been explained, e.g., in [2]. The developed tools allowed for a techno-economic analysis with numerous scenarios of production from geothermal reservoirs with temperatures in the range of 120–180 °C, reaching the optimum temperature for the number of cycles and fluid types, which lead to the minimal electricity production costs. Supercritical cycles, fluids with a critical temperature slightly lower than the reservoir temperature, resulted in minimal expenses [2].

At a time when oil and gas production in Croatia, from onshore and offshore fields, is continuously decreasing and energy needs are growing, the development of small unconventional reservoirs can be a very important agenda for energy policy. At least, the new gas reserves and their production increase national energy stability and decrease the dependence on imported gas. Moreover, well known technology for oil and gas production from the unconventional reservoirs and years of practice in Croatia make gas production possible from considered unconventional reservoirs, which easily increase the total proven hydrocarbon reserves, decrease future drilling, completion and production costs for such reservoirs types, as well as the price of the gas on the domestic market.

## 2. Methods

The methods in this analysis could be divided into majorly qualitative and minorly quantitative. The potential unconventional reservoirs, in the researched area, are presented mostly qualitatively using geological descriptions, regional stratigraphy and qualitative data obtained by cited sources, such as core and log tests, mapping and structural interpretation. The same approach is applied for the description of potential petroleum development of such a reservoir system, mostly on drilling types and procedures. The main qualitative part, also originally created for this research, was petrological analysis and interpretation. The representative samples were selected describing potential clastics reservoir units, conventional as well as unconventional.

The quantitative data represent the geochemical variables, putting them in the context of structural and depositional frameworks. They were especially important for one of the main qualitative achievements of this work, expressed as a hydrocarbon migration map in the analysed subdepression.

## 3. Geological Properties of the Neogene Source and Reservoir Rocks in the Bjelovar Subdepression

The crucial condition for thermogenic generation of oil, gas and condensate is the existence of a subsurface system, which consists of several geological categories, and defining recoverable reserves. Such a system is often called a “hydrocarbon system” or “petroleum system”. Those geological categories represent specific rock types in the subsurface, mechanism and time responsible for fluid migration. Essentially, five of them could be outlined: trap, reservoir, source rocks, migration and hydrocarbon preservation (see Figure 1). Inside the analysed Bjelovar Subdepression, all are defined in Neogene and Quaternary sediments and divided into several lithostratigraphic and chronostratigraphic units (see Figure 1) with clearly defined ages [3,4]. Although the source, reservoir and isolator rocks range from Lower Badenian to Upper Pontian age, the main source interval is linked to Middle to Upper Badenian, and the dominant reservoir/isolator sequence is a sandstone/marl alternation of Upper Pannonian and Lower Pontian.

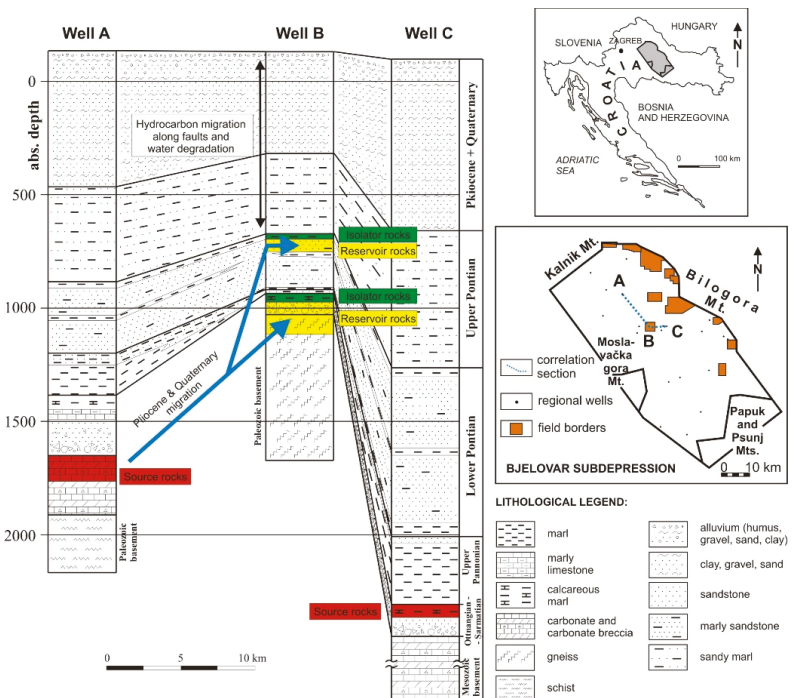


**Figure 1.** Location and typical hydrocarbon system in the Bjelovar Subdepression [5–7].

The conventional approach considers reservoirs as the rocks with reservoir properties, where effective porosity and permeability make hydrocarbon recovery possible. Due to wettability, capillary forces and saturation, part of the total hydrocarbon reserves (original hydrocarbons in place, abbr. OHIP) can be recovered from the reservoirs. Source rocks are considered as the place where hydrocarbons are generated mostly through a period of catagenesis. Migration from source to reservoir rocks is crucial for the accumulation of oil and gas in the trap, which can be divided into primary and secondary migration. Primary means migration inside the source rocks, which is initiated by capillary forces and pressure. Secondary migration comprises permeable pathways, gravitational separation and trapping. The length of the first one is on a scale of hundreds of metres, and the second is on a kilometre scale.

Here, both kinds of possible unconventional gas reservoirs are analysed inside the subdepression, from the group of weakly permeable sandstones and siltstones where gas is accumulated by secondary migration, but also source rocks where hydrocarbons are generated. Both types are strongly connected with migration. So, in order to evaluate them, it was also necessary to evaluate source rock potential inside the subdepression, migration pathways inside and outside the area, and possible unconventional source reservoirs as a secondary target. Possible source chronostratigraphic units are Badenian to Lower Pannonian pelitic rocks. They lithostratigraphically belong to the Mosti and Križevci Members of the Moslavačka Gora Formation (see Figure 1), and they are regionally proven as mature source rocks in the Croatian part of the Pannonian Basin System (CPBS). Five geochemical variables were studied, as follows: Corg (organic matter content), S<sub>2</sub> (genetic potential), HI (hydrogen index), OI (oxygen index) and Ro (vitrinite reflection). Their thermal maturity was also calculated and compared with regional geothermal maps. Possible “tight” sandstone reservoirs are younger—of Lower Pontian, even Pliocene—and belong to the Poljana and Pepelana Sandstones of the Kloštar Ivanić Formation.

Large quantities of hydrocarbon remained in reservoirs due to irreversible saturation or due to the high content of water in production. Some average recoveries are about 60% for gas and 20–30% for oil reservoirs, but not all generated hydrocarbons are expelled from the source rocks. It depends on the quality of the organic matter, natural fracturing of the source rocks and on the pressure gradient. Part of these volumes can be recovered, using artificial fracturing of rocks. The major problem in this procedure is the complex calculation of well drainage radius because rock permeability is distributed highly stochastically and often clustered. Despite the technological problems and uncertainties in reserve calculation, the total thickness of source and “tight” rocks in the entire hydrocarbon system can be considerable. Here, an example from the Croatian part of the Pannonian Basin System (CPBS), i.e., the area of the Bjelovar Subdepression, is given as a part of the Drava Depression.

### 3.1. Petrological and Sedimentological Properties of Outcrop and Subsurface Rocks

Characteristic Neogene sedimentary rocks from the surface outcrops in the wider research area (see Figure 2a–f) are presented as potential source rocks and collectors of hydrocarbon gas in the west of the Croatian part of the Pannonian Basin System (CPBS) (e.g., [7–11]). These are the Middle and Upper Miocene fine-grained marls (see Figure 2a,b), middle coarse-grained sandstones and calcarenites (Figure 2c,d), and coarse-grained clastics (see Figure 2e,f).

Properties of characteristic sedimentary rocks from the subsurface are shown as well (see Figure 3a–h). They comprise fine-grained sedimentary rocks (see Figure 3a–d) as the potential source rocks: interlaminated marlstones and siltites/shales, laminated calcitic shales, lithic greywacke sandstones to mudstones and silty marlstones as well, all enriched in kerogen in various amounts. Potential collectors determined in the subsurface are mainly coarse and middle coarse-grained sedimentary rocks (see Figure 3e–h): lithic and quartz arenitic sandstones, calcarenites and calcarenitic sandstones, and various types of petromictic conglomerates as well.

Interlaminated black globigerinid marlstone and pale grey sandy siltite/shale (see Figure 3a). Black marlstone laminae are enriched in kerogen and contain fine angular quartz grains and micas, as well as small planktic foraminifera. Pale grey sandy laminae contain angular quartz grains and lithic fragments, bound together with calcite cement. It is interpreted as the final sandy and pelitic intervals (Td and Te) of Bouma turbiditic sequence deposits and considered as a potential source rock for kerogen maturation and hydrocarbons generation (so-called “oil shale”). This sample was taken around the 3500 m subsurface depth interval.

Dark grey, laminated dense marlstone to calcitic shale (see Figure 3b) containing a thin interchange of clayey-calcitic laminae and laminae with mica flakes and fine quartz grains, tightly packed due to compaction and burial diagenesis. This sample was taken around the 1500 m subsurface depth interval.

Dark grey, fine-grained silty lithic greywacke sandstone to mudstone (see Figure 3c) containing fine angular quartz grains and various lithic fragments, floating within clay and silty matrix. This sample was taken around the 1000 m subsurface depth interval.

Well-lithified, pale grey to brown silty marlstone, enriched in kerogen (see Figure 3d) containing abundant globigerinid foraminifera skeletons, as well as some pyrite grains developed in diagenesis. This sample was taken around the 3500 m subsurface depth interval.

Middle coarse-grained, well-sorted lithic arenite sandstone (see Figure 3e) containing predominantly angular quartz grains and lithic fragments of quartzites, cherts and sandstones, densely packed and intercalated with mica flakes. Intergranular spaces are partly filled with microcalcite cement. This sample was taken around the 3500 m subsurface depth interval.

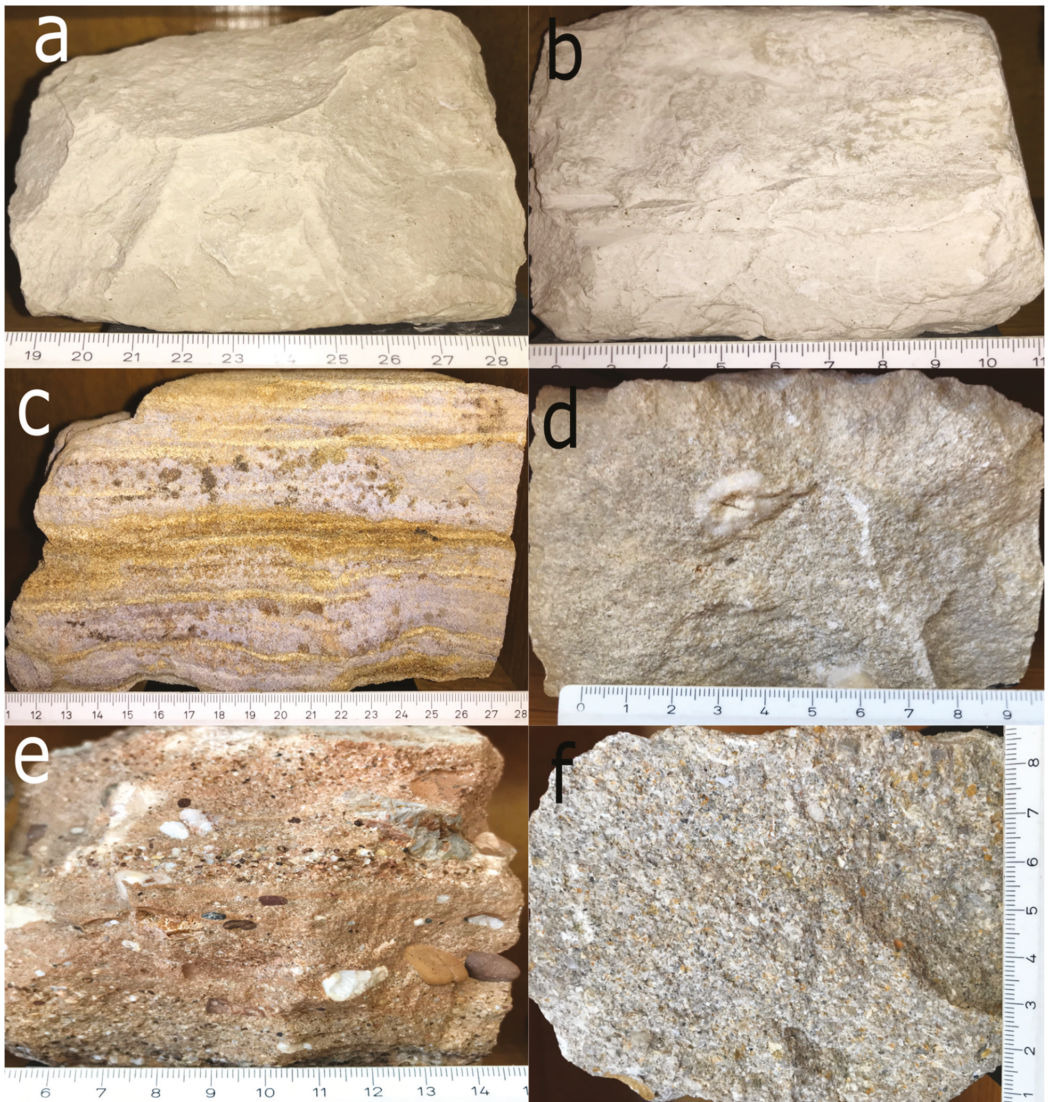


**Figure 2.** (a–f). Specimens of the characteristic Middle and Upper Miocene sedimentary rocks taken from the surface outcrops: (a, b)—marls; (c)—laminated sandstone; (d)—calcarenitic sandstone; (e)—interlayered conglomerate and sandstone; (f)—coarse-grained calcarenitic sandstone to fine-grained conglomerate. Samples are taken from the surface, at localities: SW Medvednica Mt. (a, d, e); SE Medvednica Mt. (b); Jerovec (c); Breznički Hum (f); all at the western margin of the CPBS. All samples are from the referent and demonstrational Minerals and Rocks Collection, situated at the Department of Mineralogy, Petrology and Mineral Resources (Faculty of Mining, Geology and Petroleum Engineering, University of Zagreb).

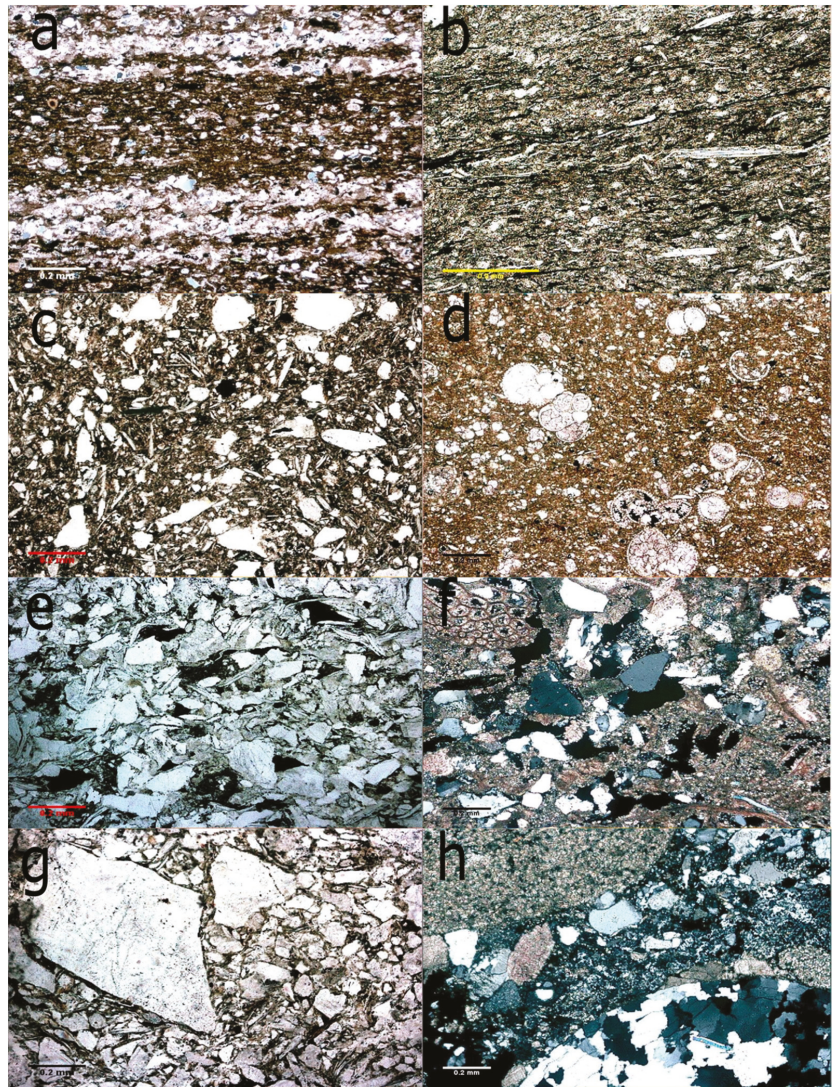


**Figure 3.** (a–h). Microphotographs of the characteristic source rocks and collectors taken from the subsurface samples (scale bars = 0.2 mm). (a–d)—source rocks (marlstones, siltites and shales); (e–g)—collectors (sandstones, calcarenites and conglomerates). Samples are taken from the subsurface at localities Mosti (b, d, f), Fančev mlin (a, c, g), and Mičetinac (e, h) in the Drava Depression.

Fossiliferous lithic arenite sandstone (see Figure 3f) contains fine-grained, semi-consolidated, grey semi-calcareous sandstone, which includes predominantly siliciclastic grains (quartz and metamorphics) and subordinate fossil detritus (bryozoans and bivalves), also having laminated micas and randomly dispersed glauconitic grains, bound together in calcite cement. This sample was taken around the 1000 m subsurface depth interval.

Coarse-grained, densely packed, clast-supported lithic arenite sandstone to petromictic breccia/conglomerate (see Figure 3g) containing poorly sorted, angular lithic fragments of metamorphics and quartz grains, together with micas and some feldspars. Intergranular spaces are partly filled with fine marly matrix, and grains are bound together with

cryptocrystalline calcite cement. This sample was taken around the 3500 m subsurface depth interval.

Well-lithified, clast-supported petromictic conglomerate (see Figure 3h) containing well-rounded clasts of various rocks (magmatics, metamorphics and dolomites), bound together in sandy matrix of various angular grains, together with dispersed glauconitic grains and mica flakes. This sample was taken around the 3000 m subsurface depth interval.

### 3.2. Geochemical Values in the Source Rocks

In the analysed area, as well as in the entire CPBS and the Pannonian Basin System (PBS) in general (e.g., [11–15]), from the Upper Badenian to the Lower Pannonian age, characteristic sedimentation of pelitic rocks, such as marlstone, limestone, calcitic marlstone and marly limestone, prevailed. The mostly shallow, calm, and brackish environment favoured the preservation of organic matter and its transformation into kerogen. Such a transformation was mostly unsuccessful due to the relatively small depths in the sub-depression (today less than 3000 m), but where it was effective, kerogen of types II and III were formed. The generation potential of source rocks is described by geochemical variables (see Table 1). It is clear, that Middle Miocene pelites can be considered as regional weak source rocks, mostly due to very low average carbon content (low margin for clastic source rocks for generation is about 0.5–1.0%, which is similar to the subdepression's mean value). Moreover, the organic carbon content is very variable, from 0.31 to 7.28% (the means are given in Table 1). Higher values of HI ( $S_2/C_{org}$ , i.e., mg HC/g  $C_{org}$ ) indicate that samples could be taken locally with significant hydrocarbons obtained during laboratory pyrolysis (420–460 °C). Generally, though, organic matter is shallow and oxidated, showing high values of OI ( $S_3/C_{org}$ , i.e., mg  $CO_2$ /g  $C_{org}$ )—Figure 4.

**Table 1.** Geochemical variable values in potential source rocks in the Bjelovar Subdepression, Croatia [16].

Variable	Mean	−95%	95%	Minimum	Maximum	Variance	
Badenian and Sarmatian rocks (16.4–11.5 Ma)							
$C_{org}$ (wt%)	1.14	0.15	2.14	0.01	5.3	2.2	
(pyrolytic peak mg HC/g rock)	$S_2$	6.91	0.00	19.17	0.01	22.91	97.4
HI (mg HC/g org. C)	237.81	45.67	429.94	120.00	397.78	$14.6 \times 10^3$	
OI (mg $CO_2$ /g org. C)	447.83	0.00	1851.32	107.30	1100.00	$3.2 \times 10^5$	
Upper Pannonian rocks (11.5–9.3 Ma)							
$C_{org}$ (wt%)	0.61	0.35	0.87	0.19	1.41	0.11	
(pyrolytic peak mg HC/g rock)	$S_2$	1.64	1.07	4.34	0.92	2.89	1.18
HI (mg HC/g org. C)	271.74	0.00	619.11	184.0	433.0	$19.6 \times 10^3$	
OI (mg $CO_2$ /g org. C)	76.70	0.00	650.64	31.53	121.87	4080.66	

As kerogen type III (terrigenous material from the higher plants) predominates, hydrocarbon generation mostly produced gas with an efficiency of usually less than 20%, where the main process happened at 120–150 °C. Such a temperature range had been proven on the single deep locality inside the depression, in the Velika Ciglena or Eastern Bjelovar Syncline, where catagenesis occurred before approx. 4.5 Ma, and “oil windows” were activated in the last 0.2 Ma [16]. Moreover, generation in leaner source rocks is a less efficient process, and most of the created hydrocarbons remain inside, especially oil [17]. The thickness of the source intervals rich in organic carbon inside the subdepression is

mostly a few metres, so the efficiency of expulsion is low and most of the generated gas probably remained within the source facies.

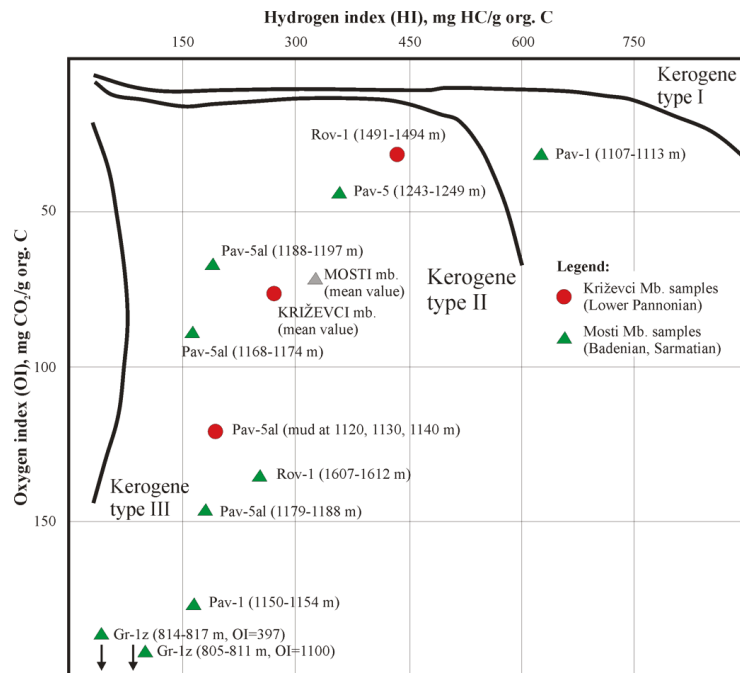


**Figure 4.** Van Krevelen diagram of kerogen samples. The Bjelovar Subdepression, Croatia [16].

### 3.3. Migration Pathways

Migration occurrence and pathways are the critical factors for the creation of any conventional as well as weakly permeable reservoirs (conditionally permeable clastics such as fine-grained silty sandstones and siltstones). The fluid physics directionally depend on permeable migration zones in the subsurface as well as geothermal gradients, i.e., subsurface temperatures (hydrocarbon generation “per se”, but also the heating of subsurface fluids). The Bjelovar Subdepression belongs to the hotter part of the Pannonian Basin System. The authors of [18] and [19] showed that geothermal gradients vary between 4.5 and 7.7 °C/100 m.

Inside the subdepression, the locally developed source rocks are mudstones, shales, and siltites of Badenian to Lower Pannonian age, appearing from 811 to 3255 m depth, and they are mostly thermally immature. In deeper, predominantly clastic rock sequences, high thermal altered terrestrial organic matter appears, which presently would reach the late catagenesis and early metagenesis stage (according to Figure 5). They are, in fact, still currently in the early catagenesis stage, due to a lower gradient in the past. Such areas are the Velika Ciglena Syncline and marginally Western Bjelovar or Rovišće Synclines (see Figure 1, well A) and Eastern Bjelovar or Velika Ciglena Synclines (see Figure 1, well B). There was not enough volume to feed all the discovered hydrocarbon reservoirs, even only to saturate them with gas. So, the proposed migration map for the subdepression is given in Figure 5.

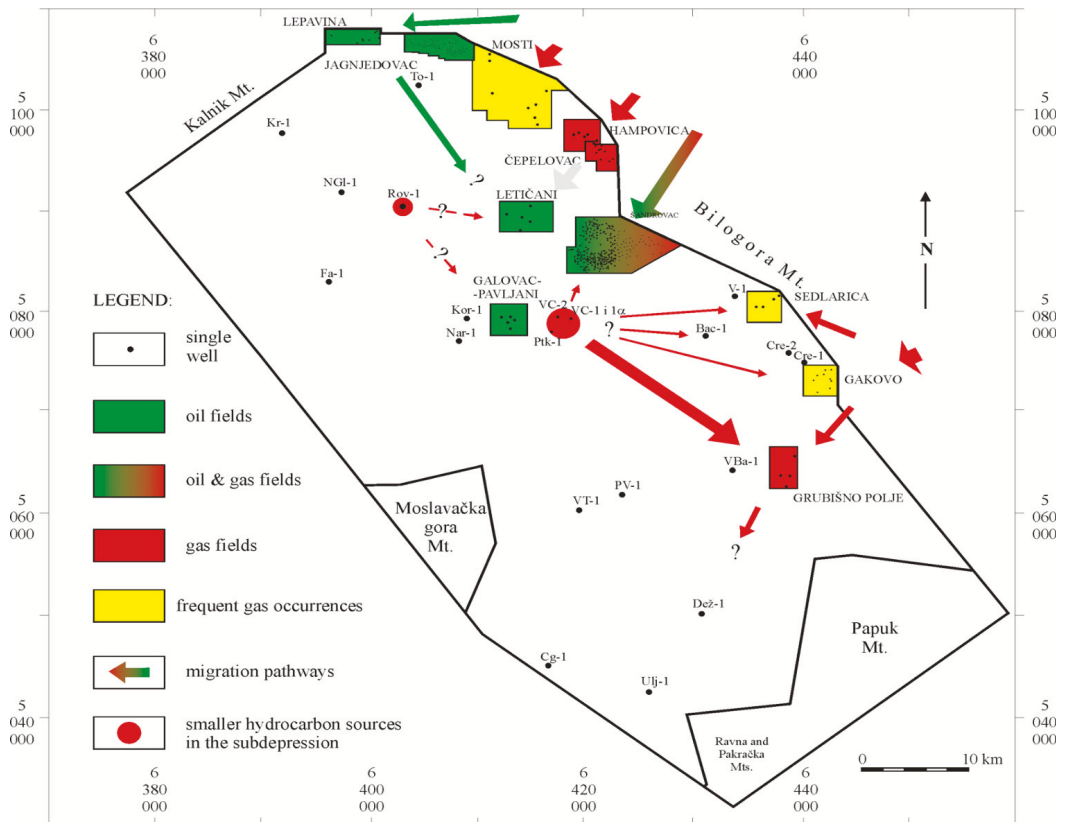


**Figure 5.** The proven and assumed hydrocarbon migration pathways for fields and occurrences inside the subdepression.

It is obvious that, besides several smaller fields, there are several localities with proven gas occurrences, but they are not yet in production, situated on the north–north-eastern margin of the subdepression. The reasons are relatively small possible estimated reserves, based on the low gas saturation and/or small porosities/permeabilities as a result of numerous alternations of the “tight” sandstone lithofacies. Such possible producing horizons are situated at depths of 800 to 1000 m, with a predominance of weakly permeable sandstones of Upper Miocene age.

From a geochemical point of view, some parameters indicate high-quality paraffinic oils, originating from a terrestrial precursor, which is also confirmed by carbon isotopic ratios with a slight predominance of light isotope  $^{12}\text{C}$  ( $>\delta^{13}\text{C} -25.1\%$ ). There is also proven oil where bimodal hydrocarbon distribution reflected both sapropelic and terrestrial origin. The larger differences in physical and chemical properties of hydrocarbons can be attributed to differences in source facies type and maturity, but post-generative processes, particularly subsurface water washing, water flooding and evaporative fractionation, also altered them.

Reservoir gases could be wet with a concentration of higher hydrocarbon homologs (about 2–22%), but much more importantly, they could be represented by migrated thermogenic gases associated with oils or mixed gases (bacterial/thermogenic sources) in shallow reservoirs. They are the promising unconventional targets where some migration could form significant gas occurrences in “tight” lithofacies of Upper Miocene, even Lower Pliocene. Such rocks are proven in the north-eastern part (see Figures 1 and 5, localities 3, 9,

10) and are saturated with gasses, which have slightly lower wetness and higher maturity than gasses in the western part of the subdepression.

The crucial variable in such reservoirs is porosity, i.e., permeability. For example, from 20 to 25% in conventional reservoirs in weakly permeable sandstones, tight sands or sandy marls of Upper Miocene, it can be reduced to about 10% (e.g., 12.86 on locality A, 12.03 on B or 6.14% on C, Figure 1). Consequently, the permeability is reduced to less than  $10^{-3} \mu\text{m}^2$  (or 1 millidarcy). As an example, a qualitative representation of sudden and often changing lithofacies from medium-grained sandstone into marly sandstone and vice versa is given in Figure 6, where Poljana Sandstone represents a typical regional proven reservoir rock sequence of Lower Pontian (Upper Miocene) age.

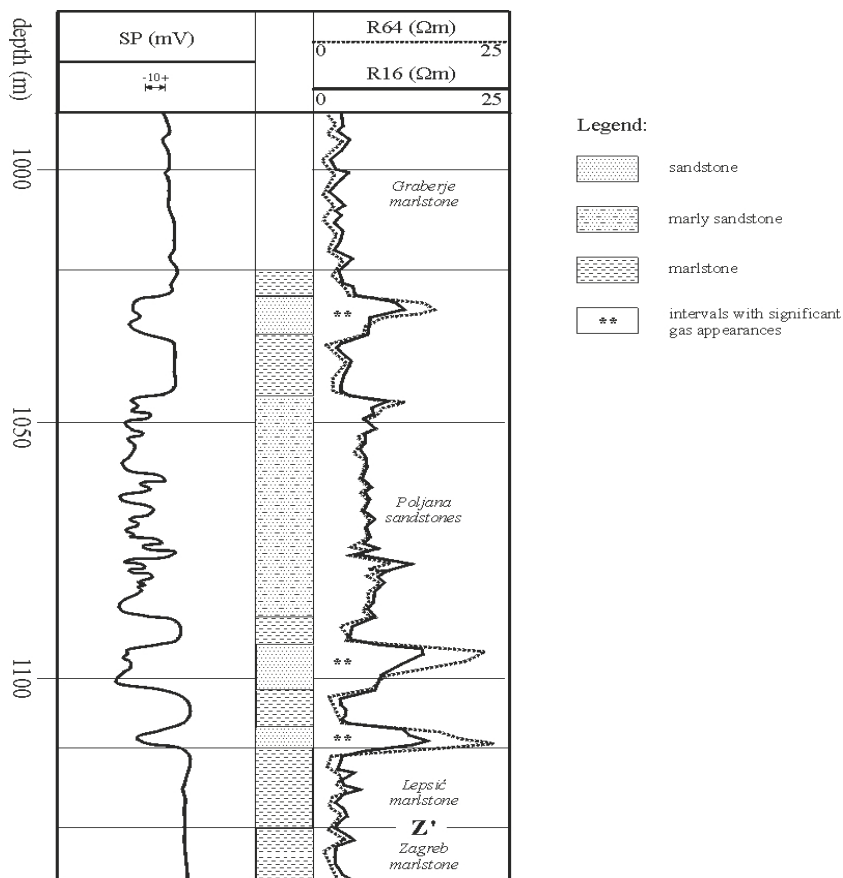


**Figure 6.** Sudden changes between medium-grained and marly sandstone layers inside a single lithostratigraphic member showed qualitatively on SP/R e-logs.

For such lithofacies [20], a numerical analysis of possible regional porosity-based log resistivity curves was performed. The Cremušina Structure (locality no. 10, Figure 5) is selected on the north-eastern part of the subdepression. The results outlined that in the alternation of fine-grained sandstones with silty marly sandstones, i.e., in a section considered as an unconventional potential reservoir, regionally can be described with a porosity of about 10%. That is high enough to support gas migration and form smaller “tight” gas reservoirs.

### 3.4. Geothermal Potential of the Investigated Area

According to the characteristics of the investigated area, the possibility of finding a geothermal potential is in geopressed reservoirs. The hydrostatic pressure is proportional to the weight of water and increases with depth. From the aspect of geothermal exploitation, geothermal reservoirs are characterized by three important properties [21]: high pressure, high temperature, and dissolved methane. The CPBS has the greatest geothermal potential, as well as significant technological opportunities for the exploitation of geothermal energy in agriculture and the food industry. The average geothermal temperature gradient in the CPBS is  $0.049\text{ }^{\circ}\text{C}/\text{m}$  [22], while in the rest of Europe it is  $0.03\text{ }^{\circ}\text{C}/\text{m}$  [23]. Data on geothermal reservoirs were obtained from exploration wells that were primarily intended for locating oil and gas reservoirs. Great potential for the exploitation of geothermal energy is found in negative oil and gas wells, then in mature oil and gas reservoirs as well as in aquifers. Geothermal deposits in the Republic of Croatia (see Figure 7) are divided according to the temperature of geothermal liquid at the wellhead into [24] reservoirs with a temperature higher than  $100\text{ }^{\circ}\text{C}$  and reservoirs with a temperature lower than  $100\text{ }^{\circ}\text{C}$ .

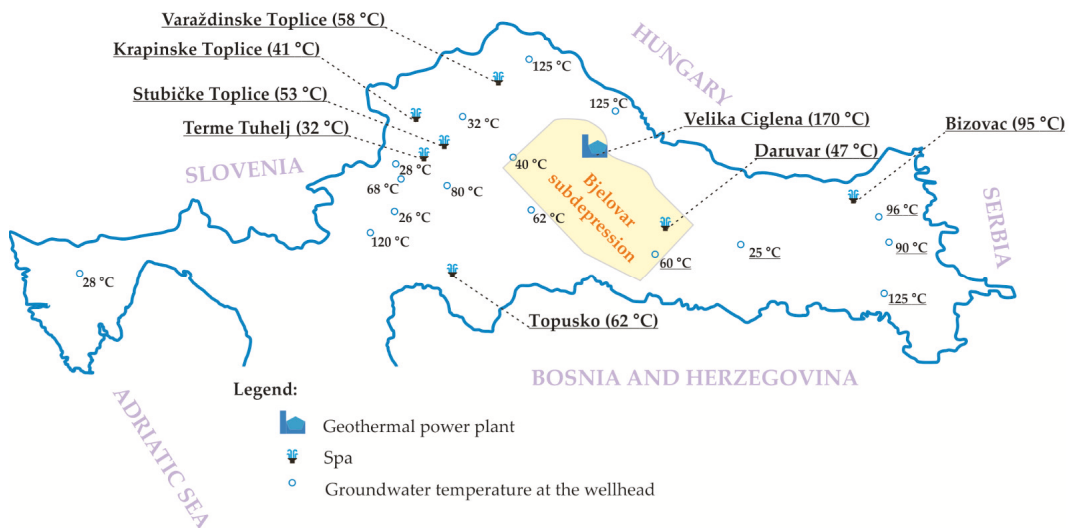


Figure 7. Temperature values in proven geothermal reservoirs modified after [25].

According to the authors of [26,27], the possible thermal power from geothermal energy is between  $750\text{ MW}_t$  and  $1,300\text{ MW}_t$  for the CPBS area. In the researched area of the Bjelovar Subdepression, the geothermal field Velika Ciglena was put into production in 2018. The installed capacity of the geothermal power plant Velika Ciglena is  $>16.5\text{ MWe}$  [28].

### 4. Challenges and Solutions for Drilling in Clastic Alternation of Conventional and Unconventional Reservoirs

Due to the specific properties of the unconventional reservoirs, their development cannot be successfully completed without the application of two well-known technologies in drilling and completion operations, horizontal drilling, and multi-stage hydraulic fracturing. Moreover, some relatively rarely used technologies for conventional reservoirs, such as natural dump flooding wells [29], could be considered in low-permeable sandstone lithofacies, in the late recovery phase.

The horizontal drilling technology allows petroleum companies to economically develop different types of reservoirs which have hitherto been unprofitable or out of reach.

Despite highly developed different techniques and technologies in the petroleum industry, the development of the unconventional reservoirs demands the adjustment of these commercial techniques and technologies to the specificities of the unconventional reservoirs [30]. As in the case of the development of conventional oil and gas reservoirs, the success of unconventional reservoir development, especially drilling and completion activities, distinctly depends on the available data. Some well investigated areas, where significant oil and gas production from conventional reservoirs exist together with unconventional reservoirs, were neglected at first and, thus, insufficiently researched.

Drilling and completion campaigns in unconventional reservoirs, as well as subsequent oil and gas production, depend on the available data about lithology, pore pressure and in situ stress distribution in the areas under consideration. This information is very important from a geomechanical point of view, especially for engineering demanding operations, such as horizontal drilling or hydraulic fracturing [31]. Building a mechanical earth model (MEM) for the specific underground location based on the available seismic data and proper calibration should be a starting point in the development of any unconventional reservoirs. The mentioned model includes a 1–3D structural model, mechanical stratigraphy, elastic properties, and strength parameters, as well as earth stress (magnitude and direction) and pore pressure. Moreover, improvement in any visualisation, such as advance mapping [32], is a useful addition to such a model, outlining unconventional lithofacies and their structures. A high-quality mechanical earth model would be very useful in the planning stage, and it would significantly reduce operational risks, time, and costs. The available information from the earth model for petroleum systems directly affects the successful development of unconventional reservoirs [33], and this emphasizes the importance of geochemical data, especially from the Middle Miocene source lithofacies.

A well-developed mechanical earth model represents a starting point (input) for wellbore stability analyses. During the drilling operation, stress redistribution takes place in the vicinity of the wellbore wall, whereby in situ stresses (vertical, maximum, and minimum horizontal) are replaced with axial, radial and hoop stresses. Aside from stress redistribution along the wellbore wall, the wellbore stability strongly depends on the wellbore orientation (inclination and azimuth) and the existence of different specific circumstances such as anisotropy, heterogeneity, the existence of fractures, faults, etc. In some circumstances, alternation in pore pressure and rock properties require the application of a specific drilling technique, such as managed pressure casing drilling (MPCD) or managed pressure cementing (MPC), which involve a closed-loop mud circulation system and carefully balancing pore pressure during the entire drilling operation [34]. In the presented analysis, the stability of the unconventional series would not be problematic in Badenian to Lower Pannonian source lithofacies, due to the high level of consolidation. It is valid both for carbonates as well as clastics (sandstones and marls). In all such permeable lithofacies (lime breccia, coarse-grained sandstones), conventional hydrocarbon reservoirs are already proven (Letični, Galovac-Pavljani and Grubišno Polje structures; Figure 5). However, such stability could be significantly less during drilling in low-permeable sandstones on the north-eastern margin of the explored subdepression (Mosti, Sedlarica, Gakovo structures; Figure 5). Such lithofacies are significantly more weakly consolidated, especially ones determined at the very end of Lower Pontian or in Upper Pontian. Consequently, the stability breakdown or even “sand flows” into the wellbore could occur.

Unlike the development of conventional reservoirs, the development of an unconventional reservoir usually requires horizontal wells with a long horizontal section properly placed in the space, which implies the use of some advanced drilling technology such as measurement while drilling (MWD), logging while drilling (LWD) or geosteering and a different completion design with multistage hydraulic fracturing. The completion design of a well in an unconventional reservoir includes one of the following solutions: cased and cemented hole, open hole completion, hole cased with perforated casing and cemented casing with stimulation sleeves [35].

Another risk associated with unconventional reservoirs is, as previously mentioned, possible rock damage problems. It is more pronounced in unconventional lithofacies (than in conventional ones) because of well construction, often with a long horizontal open hole section through the reservoir. The unconventional lithofacies are characterized by low porosity (here less than 10%) and a pore throat (10–1000 nm) which makes most of the filtration control additives (size in mm and  $\mu\text{m}$  range) inapplicable [36]. Drilling fluid invasion within a near-wellbore zone can cause a pore pressure change and wellbore instability problems as a result of a physicochemical reaction between the drilling fluid filtrate and clay minerals, especially in presented marls of Middle Miocene. This process can be accelerated in the presence of natural or induced fractures, as observed in the subdepression along structures closer to main fault zones. Recent developments in drilling fluid technology involve the application of smart drilling fluids in combination with nanoparticles and the application of environmentally acceptable water-based drilling fluids in the drilling of unconventional reservoirs [37].

Generally, several techniques can be applied for the evaluation of drilled, completed and stimulated wells such as production logging, proppant tracers, fluid tracers, hydrocarbon tracer, microseismic, distributed temperature survey (DTS) and distributed acoustic survey (DAS) [38]. During production logging, it is possible to obtain different data such as temperature, pressure, fluid density, formation fluid inflow points and the type of produced fluid. Proppant, fluid and hydrocarbon tracer, as well as microseismic, are used for full characterisation of the fractured area covered by hydraulic fracturing. The last studies indicate the possible application of unconventional nanotechnology-based tracers (Carbon Quantum Dots (CQDs), function silica nanoparticle synthesis, surface modification of upconversion nanoparticles) instead of traditional radioactive tracers [39]. Unlike conventional radioactive tracers, nanoparticles are environmentally more acceptable and have many other advantages, such as inertness, chemical stability, the formation of stable dispersion, etc. The appropriate selection of the evaluation technique can be very useful in cost reduction, completion design optimisation and production improvement. Machine learning and data mining can also be valuable tools in fluid production prediction from an unconventional reservoir, and validation of the applied completion system. All these methods could be applied for the development of unconventional reservoirs in the Bjelovar Subdepression. Unfortunately, potential unconventional reservoirs are, probably, in the range of very small ( $<10,000\text{ m}^3$ ) to small ( $10,000\text{--}100,000\text{ m}^3$ ) fields, regarding the classification of Croatian fields and recoverable reserves [40]. Consequently, many of the advance techniques would not be affordable and profitable for such reserves, and balancing between “standard” and advanced logging programs is a viable option.

## 5. Discussion

Regionally proven mature source rocks in the Croatian part of Pannonian Basin System (CPBS), mainly weakly permeable sandstones, siltstones and marls of Badenian to Lower Pontian age, are potential sources for unconventional gas reservoirs inside the Bjelovar Subdepression. Gas could be accumulated during catagenesis or by secondary migration.

Micropetrographic analysis of the characteristic sedimentary rocks from the subsurface (see Figure 3a–h) reveals their composition and fabric, suitable for kerogen maturation and hydrocarbons generation. Two groups of sedimentary rocks are distinguished, according to their potential as the source rocks or as the reservoirs of hydrocarbons, by primary or secondary migration pathways.

Predominantly fine-grained sedimentary rocks (see Figure 3a–d), mainly enriched in kerogen, are marked as the potential source rocks. These include interlaminated marlstones and siltites/shales, laminated calcitic shales, lithic greywacke sandstones to mudstones and silty marlstones. Their origin is closely related to deep-water sedimentary environments and processes in the sedimentary basin (CPBS), deposited in the basin itself (i.e., well-lithified, pale grey to brown silty marlstone with abundant globigerinid foraminifera skeletons and enriched in kerogen, shown in Figure 3d), or at the distal parts of the vaning

gravity currents from the basin margins (i.e., interlaminated black globigerinid marlstone and pale grey sandy siltite/shale, shown in Figure 3a).

Mainly coarse and middle coarse-grained sedimentary rocks are marked as potential reservoirs determined in the subsurface (see Figure 3e–h). These are lithic and quartz arenitic sandstones, calcarenites and calcarenitic sandstones, as well as various types of petromictic breccias/conglomerates. Their relatively broad grain-size range (from coarse- to middle-grained clastics and calcareous clastics), as well as their various fabric (from clast-supported breccias/conglomerates, shown in Figure 3g,h) to various arenitic and greywacke sandstones (shown in Figure 3e,f), place them as, more-or-less, suitable for hydrocarbons emplacement.

Porosity ranges of potential reservoirs encourage this hypothesis. However, their permeability ranges partly limit migration pathways to secondary, including oblique/vertical migration of hydrocarbon gas during burial, from the source rocks placed at the greater burial depths in the subdepression toward the potential reservoirs at the lower depths (see Figure 1). Sedimentary sequences with thin collector units followed by seal rock units, such as sandstone and marl units appearing in the upper parts of the Upper Miocene sequences in the CPBS, make a suitable sedimentary architecture for the development and emplacement of so-called unconventional hydrocarbon gas reservoirs.

The considered unconventional reservoirs are placed in the Croatian part of the Pannonian Basin System (CPBS), an area with a long history in oil and gas production from conventional reservoirs. This fact represents the main advantage in further consideration of gas production from unconventional reservoirs because of the wells and the surface infrastructure on the existing fields in the area. The existing wells provide the possibility for additional research and the data gathering necessary for the economically and technically feasible development of unconventional reservoirs. Except for additional logging, fluid sampling and observation for downhole changes, the existing wells can be used for re-entry in horizontal drilling; thus, significantly reducing the cost of the drilling and completion of the operation.

## 6. Conclusions

Qualitative and quantitative analyses of some aspects belonging to small unconventional hydrocarbon gas potential reservoirs are given here. Potential reservoirs were analysed in the relatively isolated Neogene Subdepression in Northern Croatia, where depths are rarely larger than 3000 m and clastic sedimentation was dominated with pelitic detritus. As conventional discoveries were limited on several fields, the further research and investments highly depend on new discoveries, smaller but profitable. As migration pathways supported the idea that not all possible (P3), even probable (P2), reserves are proven, analysis of this type confirmed the following summarised results:

1. The deepest Eastern Syncline (also named as the Velika Ciglena Syncline), is a single place where gas was generated and migration started to feed smaller surrounding structures. The gas-prone source rocks of that structure could be studied in detail as sources of unconventional lithofacies. As there is a proven high geothermal gradient and a geothermal reservoir below the source facies, the maturation process could obviously take a long time, currently reaching early catagenesis.
2. The north-eastern margin of the subdepression is characterized with numerous structures where gas occurrences were often observed during drilling through “tight” sandstones, reaching from a small percentage up to 10 percent methane. The volume of potential unconventional reservoirs in the zone is several times larger than the reservoir in the Velika Ciglena Syncline.
3. This north-eastern margin is represented with an alternation of fine-grained with silty and marly sandstones. Consequently, porosity varies in a wide range of 10–25%, but a single layer is often no thicker than 1 m. It makes the zones hard to test and develop, due to potential instability during drilling. Moreover, logging would hardly reach

true saturated rock values (such as for spontaneous potential or resistivity). So, any production and reserve calculation is a potentially highly uncertain task.

4. As a marginal target could be outlined for the Upper Badenian “tight” but consolidated sandstones, as sporadic unconventional Badenian lithofacies. Unfortunately, these lithofacies are still not regionally well explored and are highly uncertain regarding their unconventional potential.
5. Taking into account experience in oil and gas production on a considered area, and existing well and surface facilities, the development of a small unconventional gas reservoir in the future can be a promising solution for the growing energy demand in Northern Croatia.

**Author Contributions:** Conceptualization, T.M. and U.B.; methodology, T.M., U.B., B.P. and J.I.; validation, T.M., U.B., B.P. and J.I.; investigation, T.M., U.B., B.P. and J.I.; writing—original draft preparation, T.M., U.B. and B.P.; writing—review and editing, T.M., U.B., B.P. and J.I.; visualization, T.M., U.B. and B.P.; supervision, T.M.; funding acquisition, T.M. All authors have read and agreed to the published version of the manuscript.

**Funding:** This research was conducted as part of a project funded by the University of Zagreb “Mathematical methods in geology V” (led by T. Malvić).

**Conflicts of Interest:** The authors declare no conflict of interest.

## References

1. Ceglia, F.; Marrasso, E.; Roselli, C.; Sasso, M. Effect of layout and working fluid on heat transfer of polymeric shell and tube heat exchangers for small size geothermal ORC via 1-D numerical analysis. *Geothermics* **2021**, *95*, 102118. [CrossRef]
2. Astolfi, M.; Romano, M.C.; Bombarda, P.; Macchi, E. Binary ORC (Organic Rankine Cycles) power plants for the exploitation of medium–low temperature geothermal sources—Part B: Techno-economic optimization. *Energy* **2014**, *66*, 435–446. [CrossRef]
3. Ldi, K. Paleogeography and climate of the Badenian (Middle Miocene, 16.4–13.0 Ma) in the Central Paratethys based on foraminifera and stable isotope ( $^{18}O$  and  $^{13}C$ ) evidence. *Int. J. Earth Sci.* **2006**, *95*, 119–142.
4. Haq, B.U.; Eysinga, F.W.B. (Eds.) *Geological Time Table*, 5th ed.; Wall Chart; Elsevier Science: Amsterdam, The Netherlands, 1998; ISBN 0444828656.
5. Malvić, T.; Velić, J.; Peh, Z. Qualitative-quantitative analyses of the influence of depth and lithological composition on Lower Pontian sandstone porosity in the central part of Bjelovar Sag (Croatia). *Geol. Croat.* **2005**, *58*, 73–85.
6. Malvić, T.; Rusan, I. Potential Hydrocarbon Discoveries in Bjelovar Subdepression, Croatia. *Search Discov.* **2007**, *16*. Available online: <https://www.searchanddiscovery.com/documents/2007/07098malvic/> (accessed on 11 June 2021).
7. Malvić, T.; Rusan, I. Investment Risk Assessment of Potential Hydrocarbon Discoveries in a Mature Basin, Case Study from the Bjelovar Sub-Basin, Croatia. *OIL GAS Eur. Mag.* **2009**, *2*, 67–72.
8. Malvić, T. Regional geological settings and hydrocarbon potential of Bjelovar sag (Subdepression), R. Croatia. *Nafta* **2004**, *55*, 273–288.
9. Malvić, T. Review of Miocene shallow marine and lacustrine depositional environments in Northern Croatia. *Geol. Q.* **2012**, *56*, 493–504. [CrossRef]
10. Pavelić, D. Tectonostratigraphic model for the North Croatian and North Bosnian sector of the Miocene Pannonian Basin System. *Basin Res.* **2001**, *13*, 359–376. [CrossRef]
11. Velić, J. Geologija ležišta nafte i plina (Geology of Oil and Gas Reservoir). In *Faculty of Mining, Geology and Petroleum Engineering*; University of Zagreb: Zagreb, Croatia, 2007; 311p. (In Croatian)
12. Royden, L.H. Late Cenozoic Tectonics of the Pannonian Basin System. In *AAPG Memoir 45 (Chap. 3)—The Pannonian Basin*; Royden, L.H., Horváth, F., Eds.; AAPG: Tulsa, OK, USA, 1988; pp. 27–48.
13. Rögl, F. Stratigraphic Correlation of the Paratethys Oligocene and Miocene. *Mitt. Ges. Geol. Bergbaustud. Osterr.* **1996**, *41*, 65–73.
14. Rögl, F. Palaeogeographic Consideration for Mediterranean and Paratethys Seaways (Oligocene to Miocene). *Ann. Naturhist. Mus. Wien* **1998**, *99a*, 279–310.
15. Vrbanac, B. Paleostrukturalne I Sedimentološke Analize Gornjopanskih Naslaga Formacije Ivanić Grad U Savskoj Depresiji Palaeostruktural and Sedimentological Analyses of Upper Pannonian Sediments Ivanić Grad Formation in the Save Depression—In Croatian. Ph.D. Thesis, Faculty of Natural Sciences, University of Zagreb, Zagreb, Croatia, 1996; 121p.
16. Malvić, T. Naftnogeološki Odnosi I Vjerojatnost Pronalaska Novih Zaliha Ugljikovodika U Bjelovarskoj Uleknini [Oil-Geological Relations and Probability of Discovering New Hydrocarbon Reserves in the Bjelovar Sag]—In Croatian. Ph.D. Thesis, Faculty of Mining, Geology and Petroleum Engineering, University of Zagreb, Zagreb, Croatia, 2003; 139p.
17. Cooles, G.P.; Mackenzie, A.S.; Quigley, T.M. Calculation of petroleum masses generated and expelled from source rocks. *Org. Geochem.* **1986**, *10*, 235–245. [CrossRef]
18. Jelić, K.; Kevrić, I.; Krsić, O. Temperatura i toplinski tok u tlu Hrvatske. In *Zbornik Radova, 1. Hrvatski Geološki Kongres*; Croatian Geological Institute and Croatian Geological Society: Zagreb, Croatia, 1995.

19. Jelić, K.; Pavičić, H. Heat flow and hydrocarbon reservoirs in Croatia. *Nafta* **1999**, *50*, 257–260.
20. Malvić, T.; Sučić, A.; Cvetković, M. Low permeability Neogene lithofacies in Northern Croatia as potential unconventional hydrocarbon reservoirs. *Cent. Eur. J. Geosci.* **2014**, *6*, 182–194. [[CrossRef](#)]
21. DiPippo, R.; *Geothermal Power Plants*, 4th ed.; Butterworth-Heinemann: Oxford, UK, 2016; pp. 3–22. [[CrossRef](#)]
22. Tumara, D.; Kolbah, S.; Škrlec, M.; Živković, S. Korištenje resursa geotermalne energije u Republici Hrvatskoj. *Nafta i plin* **2019**, *39*, 51–56. (In Croatian)
23. Lund, H. Renewable energy strategies for sustainable development. *Energy* **2007**, *32*, 912–919. [[CrossRef](#)]
24. Bošnjak, R. GEOEN—Program korištenja geotermalne energije: Osnovni rezultati i buduće aktivnosti (GEOEN—Geothermal Energy Use Program: Basic Results and Future Activities). *Hrvat. Vode* **1998**, *6*, 363–369. (In Croatian)
25. Guzović, Z.; Lončar, D.; Ferdelj, N. Possibilities of electricity generation in the Republic of Croatia by means of geothermal energy. *Energy* **2010**, *35*, 3429–3440. [[CrossRef](#)]
26. Kolbah, S.; Škrlec, M.; Gloub, M. Kvantifikacija indiciranog geotermalnog potencijala RH za proizvodnju električne energije. *Inženjerstvo Okoliša* **2018**, *5*, 61–68. (In Croatian)
27. Tumara, D.; Pavlović, D. Geotermalna energija i njezin potencijal u vremenu energetske diversifikacije i tranzicije Republike Hrvatske. *Nafta i plin* **2019**, *39*, 53–62. (In Croatian)
28. Živković, S.; Kolbah, S.; Škrlec, M.; Tumara, D. *Geothermal Energy Use, Country Update for Croatia 2019*; European Geothermal Congress: Hague, The Netherlands, 2019.
29. Zadravec, D.; Brkić, V. Intelligent natural dump flooding well—Case study from the area of the western Persian/Arabian Gulf and possible application in the Croatian mature oil field Beničanci. *Rudarsko-geološko-naftni Zbornik. Min. Geol. Pet. Bull.* **2020**, *35*, 21–31. [[CrossRef](#)]
30. Kudryashov, A.; Povzhik, P. A Comprehensive Study of Unconventional Reservoirs: The Case of Rechitskoe Field Sediments of Rock Units I-III; paper SPE-201820-MS. In Proceedings of the SPE Russian Petroleum Technology Conference, Moscow, Russia, 12–14 October 2020. [[CrossRef](#)]
31. Sayers, C.; Dasgupta, S.; Gofer, E.; Hearn, R.; Koesoemadinata, A.; Sudhakar, V. Seismic Inversion for Risk Reduction in Drilling and Production in Unconventional Reservoirs; paper SPE-201530-MS. In Proceedings of the SPE Annual Technical Conference & Exhibition, Denver, CO, USA, 5–7 October 2020. [[CrossRef](#)]
32. Šapina, M. A Comparison of Artificial Neural Networks and Ordinary Kriging depth maps of the Lower and Upper Pannonian stage border in the Bjelovar Subdepression, Northern Croatia. *Rudarsko-geološko-Naftni Zbornik. Min. Geol. Pet. Bull.* **2016**, *31*, 75–86. [[CrossRef](#)]
33. Debashree, P.; Rajnish, S.; Rajeev Ranjan, K.; Joseph, Z.; Ajit, K.; Agarwal, P.; Surey, K.S.; Bandyopadhyay, A.; Talreja, R.; Nandi, A.; et al. Advanced Acoustic Measurements Aided Rock Mechanics Calculation for Successful Hydrofracturing Design and Wellbore Stability Analysis in Unconventional Reservoirs of Western Onshore, India; paper SPE-202802-MS. In Proceedings of the Abu Dhabi International Petroleum Exhibition & Conference, Abu Dhabi, United Arab Emirates, 9 November 2020. [[CrossRef](#)]
34. Balanza, J.A.; Justiniano, L.C.; Poletzky, I. Implementation of Managed Pressure Casing Drilling and Managed Pressure Cementing Techniques in Unconventional Reservoirs; paper SPE/IADC-173080-MS. In Proceedings of the SPE/IADC Drilling Conference and Exhibition, London, UK, 17–19 March 2015. [[CrossRef](#)]
35. Jaripatke, O.; Samandarli, O.; McDonald, B.; Richmond, P. Completion Optimisation of an Unconventional Shale Play: Implementation of a Successful Completion Design Optimization Plan and the Results; paper SPE-170764-MS. In Proceedings of the SPE Annual Technical Conference and Exhibition, Amsterdam, The Netherlands, 27–29 October 2014. [[CrossRef](#)]
36. Dorman, J.; Lakatos, I.J.; Szentes, G.; Meidl, A. Mitigation of Formation Damage and Wellbore Instability in Unconventional Reservoirs Using Improved Particle Size Analysis and Design of Drilling Fluids; paper SPE-174260-MS. In Proceedings of the SPE European Formation Damage Conference and Exhibition, Budapest, Hungary, 3–5 June 2015. [[CrossRef](#)]
37. Li, S.; Osisanya, S.; Haroun, M. Development of New Smart Drilling Fluids Using Nano-Materials for Unconventional Reservoirs; paper SPE-183509-MS. In Proceedings of the Abu Dhabi International Petroleum Exhibition & Conference, Abu Dhabi, United Arab Emirates, 7–10 November 2016. [[CrossRef](#)]
38. Senters, C.W.; Warren, M.N.; Squires, R.A.; Woodroof, R.A.; Leonard, R.S. Reducing Costs and Optimizing Drilling and Completion Efficiencies in Unconventional Plays Using Completion Diagnostics; paper SPE-174844-MS. In Proceedings of the SPE Annual Technical Conference and Exhibition, Houston, TX, USA, 28–30 September 2015. [[CrossRef](#)]
39. Murugesan, S.; Suresh, R.; Agrawal, D.; Darugar, Q.; Khabashesku, V. Unconventional Nanotechnology-Based Tracers for Drilling and Completion Applications; paper IPTC-19600-MS. In Proceedings of the International Petroleum Technology Conference, Dhahran, Saudi Arabia, 13–15 January 2020. [[CrossRef](#)]
40. Velić, J.; Malvić, T.; Cvetković, M.; Vrbanac, B. Reservoir geology, hydrocarbon reserves and production in the Croatian part of the Pannonian Basin System. *Geol. Croat.* **2012**, *65*, 91–101. [[CrossRef](#)]

## Article

# Multidisciplinary Approaches for Assessing a High Temperature Borehole Thermal Energy Storage Facility at Linköping, Sweden

Max Hesselbrandt <sup>1</sup>, Mikael Erlström <sup>2,3</sup>, Daniel Sopher <sup>4</sup> and Jose Acuna <sup>1,5,\*</sup>

<sup>1</sup> Bengt Dahlgren AB, Hammarby Allé 47, SE-120 30 Stockholm, Sweden; max.hesselbrandt@bengt Dahlgren.se

<sup>2</sup> Geological Survey of Sweden, Kiliansgatan 10, SE-223 50 Lund, Sweden; mikael.erlstrom@sgu.se

<sup>3</sup> Department of Geology, Faculty of Science, Lund University, Sölvegatan 12, SE-223 62 Lund, Sweden

<sup>4</sup> Geological Survey of Sweden, Box 670, SE-751 28 Uppsala, Sweden; daniel.sopher@sgu.se

<sup>5</sup> Department of Geoscience and Petroleum, Faculty of Engineering, Norwegian University of Science and Technology, S.P. Andersens veg 15a, 7031 Trondheim, Norway

\* Correspondence: jose.acuna@ntnu.no; Tel.: +46-762-320-008

**Citation:** Hesselbrandt, M.; Erlström, M.; Sopher, D.; Acuna, J. Multidisciplinary Approaches for Assessing a High Temperature Borehole Thermal Energy Storage Facility at Linköping, Sweden. *Energies* **2021**, *14*, 4379. <https://doi.org/10.3390/en14144379>

Academic Editors: Renato Somma and Daniela Blessent

Received: 20 February 2021

Accepted: 7 July 2021

Published: 20 July 2021

**Publisher's Note:** MDPI stays neutral with regard to jurisdictional claims in published maps and institutional affiliations.



**Copyright:** © 2021 by the authors. Licensee MDPI, Basel, Switzerland. This article is an open access article distributed under the terms and conditions of the Creative Commons Attribution (CC BY) license (<https://creativecommons.org/licenses/by/4.0/>).

**Abstract:** Assessing the optimal placement and design of a large-scale high temperature energy storage system in crystalline bedrock is a challenging task. This study applies and evaluates various methods and strategies for pre-site investigation for a potential high temperature borehole thermal energy storage (HT-BTES) system at Linköping in Sweden. The storage is required to shift approximately 70 GWh of excess heat generated from a waste incineration plant during the summer to the winter season. Ideally, the site for the HT-BTES system should be able to accommodate up to 1400 wells to 300 m depth. The presence of major fracture zones, high groundwater flow, anisotropic thermal properties, and thick Quaternary overburden are all factors that play an important role in the performance of an HT-BTES system. Inadequate input data to the modeling and design increases the risk of unsatisfactory performance, unwanted thermal impact on the surroundings, and suboptimal placement of the HT-BTES system, especially in a complex crystalline bedrock setting. Hence, it is crucial that the subsurface geological conditions and associated thermal properties are suitably characterized as part of pre-investigation work. In this study, we utilize a range of methods for pre-site investigation in the greater Distorp area, in the vicinity of Linköping. Ground geophysical methods, including magnetic and Very Low-Frequency (VLF) measurements, are collected across the study area together with outcrop observations and lab analysis on rock samples. Borehole investigations are conducted, including Thermal Response Test (TRT) and Distributed Thermal Response Test (DTRT) measurements, as well as geophysical wireline logging. Drone-based photogrammetry is also applied to characterize the fracture distribution and orientation in outcrops. In the case of the Distorp site, these methods have proven to give useful information to optimize the placement of the HT-BTES system and to inform design and modeling work. Furthermore, many of the methods applied in the study have proven to require only a fraction of the resources required to drill a single well, and hence, can be considered relatively efficient.

**Keywords:** methodology; crystalline bedrock; energy storage; boreholes; logging; thermal properties; magnetic measurements; VLF; drone photogrammetry

## 1. Introduction

Waste heat is an inevitable byproduct generated during the process of energy conversion. An estimated 50% of the global primary energy production is dissipated as exhaust losses, with the main portion being relatively low-grade heat at temperatures below 100 °C [1]. Thermal energy storage (TES) systems provide a possibility to harness this wasted heat and correct temporal phase differences between heat supply and demand in single buildings, as well as in large-scale district heating systems. One such system

is borehole thermal energy storage (BTES), which uses the ground as a storage medium together with shallow vertical borehole heat exchangers (BHE). A heat transfer fluid is circulated through the BHE network, which exchanges heat with the surrounding subsurface. These systems have been used successfully for a couple of decades for storing and recovering heat, as well as cold, in residential and commercial buildings [2]. Typically, these systems operate at temperatures that are relatively close to the undisturbed or natural temperature of the subsurface. Only a few high temperature BTES (HT-BTES) systems, which operate at temperatures significantly above ambient conditions, have been built [3]. However, due to social, environmental, and economic drivers, interest in using HT-BTES systems for storing large amounts of waste heat at high temperatures (50 to 100 °C) is presently increasing. In such systems, the size, performance, and economic feasibility rely strongly on the capacity of the subsurface to store and transport heat.

This study investigates the potential to implement an HT-BTES system in the city of Linköping, Sweden. The average yearly temperature in Linköping is 7.4 °C, where the monthly average temperatures range between −1.9 °C in the winter and 17.9 °C in the summer [4]. The number of yearly heating degree days (HDD) for the period 2011–2016 in the Linköping area is 3602, which is significantly higher in comparison to Central Europe, where the typical HDD value is less than 2500 [5]. The relatively high HDD value results in a great need for heating of housing in Linköping, which is typical for urban areas in the Nordic countries. Presently, the heating demand in Linköping is met mainly by a district heating system powered primarily by energy from a waste incineration plant. This plant has a heat capacity of 510 GWh, which corresponds to the heating required for about 25,000 houses [6]. Today most of the excess heat produced during electricity generation in the summertime cannot be utilized, and is, thus, wasted. During the wintertime, fossil-fueled plants are used to cover the peak heating demand.

Presently, Tekniska Verken in Linköping AB (a large energy company in Sweden) is assessing the option to store excess heat (about 70 GWh) from their combined heat and power (CHP) operation in an HT-BTES during the summer period and to utilize it during the peak-load periods in the winter. Such a system could increase the flexibility and efficiency of the energy system. In addition, it could make it possible to phase out the fossil-fueled plants, used to generate additional heat during the winter. If the geological, social, and techno-economical prerequisites are met for the site, it could become one of the largest HT-BTES systems in the world. Earlier modeling work of a potential HT-BTES system in Linköping is described in [7], where the Precambrian crystalline bedrock is considered as the storage medium. According to that study, a heat pump-supported HT-BTES system consisting of 1300 to 1500 BHEs with 300 m depth shows a potential to store and extract up to c. 90 GWh annually. In this study, a system with up to 1400 BHEs, borehole depth of about 300 m, and well separation of five meters is assumed.

The design of an HT-BTES plant is a complex and challenging endeavor that involves social, environmental, techno-economical, and practical aspects. The design work involves calculations of the energy efficiency, as well as energy and exergy balance. Hence, as input to this process, it is important to understand the thermal properties of the bedrock, the amount of fracturing and its orientation, groundwater conditions and water chemistry, as well as the thermal impact on the system design [8].

With regards to the potential storage site, there are several factors that would be desirable for the efficient operation of a potential HT-BTES system. Since the TES solution is based on the storage of sensible heat, a high volumetric heat capacity of the bedrock is desirable as this will ultimately lead to a higher thermal energy storage potential for the site. Furthermore, high thermal conductivity of the subsurface is beneficial, since it promotes rapid heat transfer within the storage, and will, thus, contribute to the higher short-term performance of the BHEs [2]. It is, however, important to note that high rates of conductive heat transfer also promote heat losses to the surrounding subsurface, and consequently reduce the long-term performance of the storage [9,10]. In addition, HT-BTES systems in fractured rock can be subject to substantial advective losses in the presence of groundwater

flow [11]. Extensive fracturing in some cases can also complicate drilling and lead to well integrity problems. Hence, site conditions characterized by low-permeability bedrock combined with low hydraulic gradients are also desirable.

Often, there is uncertainty as to the best available methodology for assessing the suitability of a potential site for a large-scale HT-BTES. Historically, closed-loop shallow geothermal energy system development has primarily been driven as a subset of heating, ventilation, and air-conditioning (HVAC) research, focusing on energy performance, heat pump technology, and the design of mechanical devices, etc. As a result, the characteristics of the geological and hydrogeological environment surrounding the boreholes have typically been of lesser concern [12,13]. Presently, standard assumptions about bedrock composition, overburden thickness, and thermal properties are often made based on regional data from geological maps combined with thermal response test data from one or a few scattered test boreholes. Furthermore, most existing design methodologies assume the homogeneous rock mass [14]. These general assumptions are often enough for the design of smaller and low temperature BTES. However, to optimally position, as well as better prognose the performance and reliability of large-scale high temperature systems that can hypothetically be connected to district heating production, better characterization of the bedrock storage medium is required. Concerns about the environmental impact of BTES systems are also increasing as subsurface resources are more exploited in parallel with population growth and urbanization. As pointed out by [13], sustainable BTES development requires a profound understanding of the full range of concerns associated with the technical, geological, and hydrogeological aspects of the ground-coupled system and its interaction with subsurface processes. This could be achieved by deeper integration between mechanical and geosciences disciplines to use their combined expertise in the fields involved.

Immediately north of the city of Linköping, Sweden, a relatively large area (about 2 km<sup>2</sup>), referred to as the Distorp site, has been identified within which a potential HT-BTES system could be situated. Based on the previously available geological information, both the type of bedrock and distribution of fractures is expected to vary significantly within the area. Heterogeneity within a storage medium, which has not been adequately characterized, is known to be a factor that can reduce the accuracy of modeling and design efforts. For example, [15] shows that a better understanding of subsurface heterogeneity in the modeling of BTES systems can reduce uncertainty in energy balance calculations. Similarly, work by [11,16] showed that groundwater movement can also significantly impact the performance of a BTES facility. Therefore, to place investigation boreholes optimally and efficiently and subsequently locate and accurately model the performance of a full-scale HT-BTES system, improved knowledge of the subsurface geology across the study area is required.

In this study, a multidisciplinary approach is adopted to investigate the geology of the Distorp site and to provide information to help optimize future investigation work, as well as the design of a potential HT-BTES system. Surface-based geological and geophysical measurements, not typically included in pre-investigation surveys for BTES systems, are combined with more conventional, as well as state-of-the-art measurements in several boreholes. Finally, some of the merits and limitations of the different methods applied in this study are discussed in the context of pre-site investigation for an HT-BTES system. Hence, the aims for the study are: (1) To provide a case study of multidisciplinary pre-investigation work at the Distorp site to exemplify how this information can be used to reduce risk in the placement and planning of an HT-BTES system; (2) to test and evaluate the applicability of many different field methods, not typically applied in pre-investigation work for BTES systems, to guide as to what information can and should be collected during field study and design of HT-BTES.

## 2. Geological Setting at Distorp, Linköping

The site to be addressed in this study has previously been identified as a potential area for constructing a high temperature BTES. The site lies within a small region of farmland called Distorp, located a few kilometers north of Linköping. The terrain in Distorp can be characterized as a low-lying hilly landscape, which is like the terrain of much of the surrounding region.

The bedrock in Distorp is typically draped by less than ten meters of Quaternary deposits, consisting of clay, silty clay, and clayey till. The terrain altitude in the site area varies between 38 and 47 m above mean sea level. Relatively thick Quaternary clay-dominated deposits are mainly found in the lower parts of the terrain, while thin deposits of till are associated with topographic highs. In several places, the Quaternary deposits are absent, and the underlying bedrock is exposed. These bedrock outcrops often exhibit smooth and rounded geometries, due to glacial erosion, and can be observed at several locations within the Distorp site and surrounding area. In addition, the main N–S direction of the ice during the last glaciation has created a corresponding lineation of the landscape. The terrain also clearly portrays the presence of regional NW–SE- and NNW–SSE-oriented fracture and deformation zones that have been further contoured by Quaternary glacial erosion and deposition. These zones are related to a structural belt of folded and metamorphosed rocks affected by the Svecokarelian orogen (c. 1.86 Ga) [17].

Overall, the bedrock is strongly affected by ductile deformation and amphibolite to locally granulite facies metamorphism. Metabasaltic rocks of amphibolite and gabbro, as well as diorite, are found within domains of variably gneissic and granitoid intrusive rocks. Besides these, a series of post-Svecokarelian (c. 1.85–1.65 Ga) variably porphyric, granulitic, and gneissic granites intrude the previous rock suites. Within the Linköping area there are also subordinate occurrences of Svecofennian supracrustal (c. 1.91–1.86 Ga) metamorphosed felsic rhyolitic volcanoclastics [18]. Based on modal data presented in the description of the bedrock map of Linköping NE [19], the average SiO<sub>2</sub> content (which largely influences the thermal conductivity of the rock) is 68–75% for the gneissic and granitoid rocks, and 45–52% for the metabasaltic rocks.

The predominance of NW–SE-oriented structures (fractures, faults, and deformation zones) is related to the Loftahammar–Linköping regional deformation zone (LLDZ) marking the boundary between the Bergslagen (to the NE) and Småland (to the SW) lithotectonic units [17]. This 7–10 km wide zone includes, besides a break in the topography, a series of ductile and brittle deformation zones. The LLDZ is clearly visible in the Geological Survey of Sweden's (SGU) geophysical data, as a broad NW–SE-oriented region with anomalously low values in the magnetic data. In the gravity data it appears as a region with a distinct N–S-oriented gradient with higher gravity values occurring in the north [18]. Since the Distorp site is located within the LLDZ, adjacent to the N–E boundary, several NE–SW-oriented lineaments parallel to the main orientation of the zone are expected (Figure 1).

The Distorp site also lies in the periphery of an area to the west with Lower Paleozoic platform cover strata [20]. As the outer eastern part of this area is located immediately north of the site area (Figure 1), scattered and thin deposits of Cambrian sandstone can be expected on top of the Precambrian bedrock.

The groundwater resources in the area are mainly associated with the bedrock, since the overburden is dominated by thin fine-grained deposits with low transmissivity and storage capacity. Data from the publicly available well information database at the Geological Survey of Sweden show that wells drilled in the granite-dominated areas give capacities between 1000 and 2000 L/h, while wells in metabasite and gabbroid bedrock areas show capacities <600 L/h [21].

It is clear from the regional geological information that variations in the lithology and level of deformation of the crystalline basement are expected to occur across the area of the Distorp site. Furthermore, in some areas, the crystalline basement can be overlain by variable, albeit relatively thin sequences of Cambrian strata or Quaternary sediments.

Hence, it is important to consider these anisotropic bedrock conditions when performing future appraisal investigations and during the design of the energy storage.

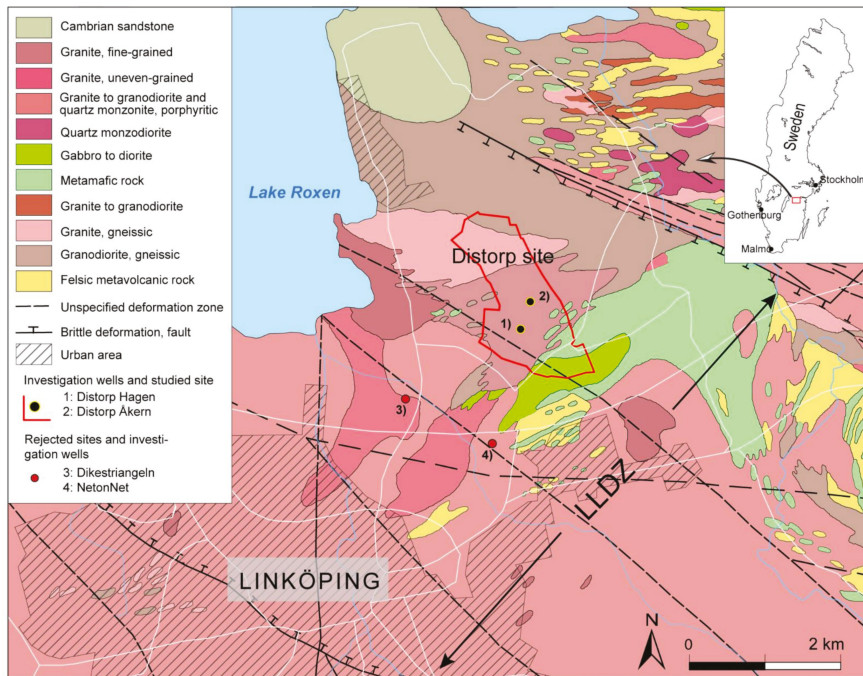


**Figure 1.** Bedrock geological map of the Distorp site (red frame) and surroundings extracted from the Geological Survey of Sweden’s bedrock database. LLDZ, Loftahammar–Linköping deformation zone. Map modified with permission after [18]. © Sveriges geologiska undersökning.

### 3. Methods

The primary aim for pre-investigation in any HT-BTES project is to evaluate the geological and thermal conditions of the subsurface with respect to their suitability for the potential development of an HT-BTES facility. In this study, we discuss and present exhaustive pre-investigation work which has been done at the Distorp site, Linköping.

Prior to selecting the Distorp site for more detailed investigations in this study, four different locations were selected as preliminary sites. The choice of these four sites was essentially based on the availability of accessible land areas at a suitable distance from Tekniska Verken in Linköping AB’s waste incineration plant Gärstadverket, i.e., the heat waste source for the possible HT-BTES. This first phase of the investigations was carried out in 2017 and started with the completion of one 300 m deep percussion borehole (115 mm Ø) in each of the four locations, i.e., Dikesträngeln, NetonNet, Distorp Åkern, and Distorp Hagen (Figure 1). The work included collecting samples of drill cuttings, measuring drilling time per drilling rod, and monitoring groundwater levels. Furthermore, temperature measurements, hydraulic capacity tests, thermal response tests (TRT), and distributed thermal response tests (DTRT) were also performed [22]. Two of the four preliminary locations were disregarded, due to the presence of relatively thick overburden, the occurrence of biogenic gas in the soil, and comparatively low thermal conductivity. The remaining two sites, referred to as Distorp Åkern and Distorp Hagen, were subsequently merged into one larger prospect site for further investigations in this study, i.e., the ca 2 km<sup>2</sup> large Distorp site (Figure 1).

In the Distorp site, three investigation wells have been established [22], including the two 300 m deep boreholes drilled during the first investigation phase in 2017 (Distorp Hagen and Distorp Åkern). In 2018, an additional investigation well (89 mm Ø) was drilled adjacent to the Distorp Hagen well using a water-driven down-the-hole (DTH) system to a depth of approximately 240 m [23]. These two wells were selected for conducting field experiments intended for investigating and applying permeation grouting techniques as a means of reducing fluid loss in open-loop BHEs. With a surface distance of only around 2.5 m between the Distorp Hagen wells, the well configuration represents typical conditions in BTES construction where very dense drilling grids are common.

Figure 2 presents the various steps of the multidisciplinary investigations and methodologies used at the Distorp site as part of this study. Figure 2 also presents the associated information or data obtained from applying these methods, which are relevant to evaluating the site and input to the HT-BTES design work.

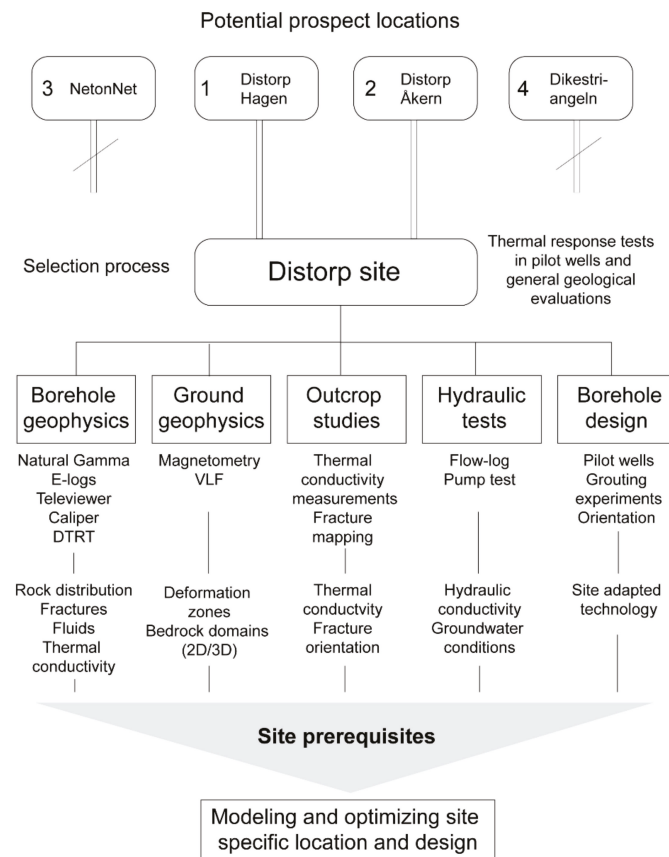


**Figure 2.** Diagram illustrating the various aspects of the site investigation, as well as the methodologies used. The parameters obtained from the various investigations, used as input to the modeling and site assessment are also shown. The different prospect locations are shown in Figure 1.

The main objectives for the in-depth multidisciplinary studies in the Distorp site were: (1) To apply a range of different methods to obtain the best possible characterization of the Distorp site with the resources available to the project; and (2) to evaluate these methods with regards to their suitability and capacity to provide essential information required for optimizing the modeling, site selection, and design of the final HT-BTES

system. This was done to improve the understanding of the applicability of these methods to future BTES projects.

The in-depth multidisciplinary studies started in late 2018, beginning with a detailed geological and geophysical survey of the boreholes. Initially, descriptions of the cuttings collected every three meters in the two 300 m deep boreholes Distorp Åkern and Distorp Hagen were made. Furthermore, geophysical wireline logging was also performed in the two boreholes. During 2019 and 2020, geological observations and ground geophysical measurements were performed. This included geological descriptions of the rock types at outcrop, sampling for petrophysical and measurements of the thermal conductivity on rock samples, as well as measurements of the natural gamma radiation and magnetic susceptibility. Additionally, magnetic field and VLF (Very Low-Frequency) measurements were collected across the study area. Some outcrops were photographed using a drone to generate high resolution orthographic images for fracture interpretation. Figure 3 shows a map with the location of data acquired during this work. Note that the black dashed line highlights the study area in the figure.

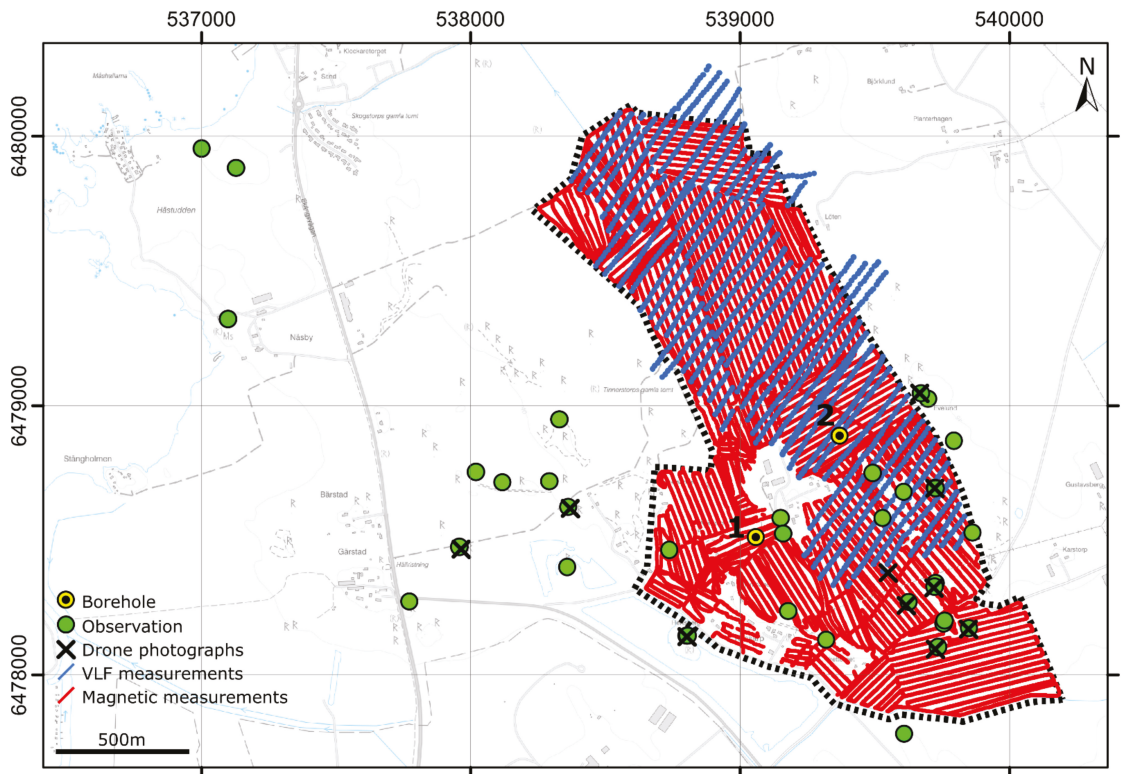


**Figure 3.** Base map showing the location of data acquired during this study. Borehole 1: Distorp Hagen, 2: Distorp Åkern.

Although this study addresses many methods, it is important to note that the data were collected across a range of projects with varying scopes and resources. Hence, the data collection strategy across the lifetime of the site investigation has been somewhat suboptimal. For example, the investigation wells and the TRT and DIRT were already performed prior to most of the surface measurements and analyses. As a result, the flow chart in Figure 2 illustrates a parallel execution of the methods, which was the case in this study. Ideally, this would not be the case for an optimized pre-investigation strategy,

where data from different methods would be acquired sequentially and used to inform and guide decisions throughout the workflow. Hence, ideally, the placement of the investigation wells would be decided and optimized based on the surface measurements, instead of being placed arbitrarily, as they were in this study.

A table summarizing the methods and equipment, as well as brief comments about accuracy and resolution, is provided in the supplementary data (Table S1).

### 3.1. Ground Geophysics

Variations in subsurface composition or rock type are often associated with changes in physical properties. Through physical measurements (for example, the magnetic or gravitational field), ground-based geophysical methods aim to characterize these variations in physical properties, and hence, infer changes in the subsurface composition. Often these measurements can be performed relatively quickly across an area. Furthermore, they do not require the bedrock to be exposed. Hence, together with bedrock observations at outcrop and borehole data, ground-based geophysical methods can be a powerful tool to map the bedrock geology over an area.

Ground-based magnetic field measurements can be made to infer variations in the magnetic properties of the subsurface. Some rock types which are highly magnetized can give rise to anomalies in the total magnetic field, which can be measured and mapped across an area. In the case of induced magnetization, the strength of the observed anomaly is related to the magnetic susceptibility of the rock [24]. The Very Low-Frequency method is an electromagnetic geophysical method that utilizes radio frequencies within the range of 3–30 kHz. If an electrically conductive subsurface structure exists, with an appropriate size and orientation to the incoming radio waves, an electrical field will be induced within the subsurface conductor. This electrical field, in turn, gives rise to a secondary magnetic field, which can, in turn, be measured. Hence, VLF measurements can be utilized to infer the presence of conductive subsurface structures, such as water-bearing fracture zones [24].

Airborne magnetic field and VLF measurements are available from the study area, collected in 1999 and 2003 by SGU as part of bedrock mapping projects. These data indicate the presence of regional deformation zones, as well as variations in the magnetic susceptibility of the bedrock within and around the Distorp area. However, these data do not provide the level of resolution required for this study, hence, ground-based magnetic field and VLF measurements were collected over the study area.

The ground-based magnetic field and VLF measurements were collected using a GEM GSMV-19 instrument. For the magnetic measurements, data points were collected continuously at one second intervals whilst walking along profiles with a nominal spacing of about 30 m (Figure 3). After acquisition, the data were corrected for diurnal variations using base station measurements from SGU's Fiby observatory. Minor line-leveling and filtering corrections were also then applied to the data.

VLF measurements were collected every 15 m along a series of profiles with a nominal spacing of 40 m. A profile azimuth of 30° and VLF frequencies of 19.6 and 24.0 kHz were used, to be sensitive to potential deformation zones with an NW–SE-orientation. A VLF frequency of 16.4 kHz was also measured to provide measurements from an approximately orthogonal direction to the first two frequencies. Power lines located in the southern part of the study area generated too much noise for data to be collected. Hence, VLF data was only acquired in the central and northern parts of the study area (Figure 3). After acquisition, some simple filtering was applied to the data before it was inverted to generate a 3D resistivity model of the subsurface. As the terrain across the study area is primarily farmland, the magnetic and VLF measurements could be collected relatively quickly and efficiently over about 5–7 days.

In addition to the VLF and magnetic field measurements, natural gamma radiation was measured at several outcrop locations using a handheld RS-125/230 spectrometer. A minimum of three measurements was made for each rock type at the outcrops, which were

investigated. Based on these measurements, the spectrometer estimates the amounts of potassium, uranium, and thorium in the different rock types.

Ground-based gravity surveying can be a powerful method for characterizing variations in bedrock geology. With this method, local anomalies in the earth's gravitational field can be used to infer changes in subsurface density [24]. Regional gravity data has previously been acquired across the Distorp area and is available from the Geological Survey of Sweden [25]. However, the average spacing between measurement points for this part of Sweden is about 2.5 km. Hence, only one gravity measurement was performed within the study focus area. Therefore, the resolution of these regional gravity data is too low for detailed mapping of the geology at the Distorp site. Acquisition of additional ground gravity measurements likely would have contributed to our assessment of the site. However, due to limitations in resources and accessibility of the measurement equipment, this was not performed as part of this study.

### 3.2. Drone Photography of Outcrops

A Mavic 2 pro drone was used to take photographs of several outcrops within the study area for the purpose of generating detailed orthophotos (orthographic composite photos) for fracture interpretation. During acquisition, the drone was flown at a height of 10 m, and a series of pictures was collected over the outcrop of interest using a front overlap of 80% and side overlap of 60%. The images were later processed in photogrammetry software to generate georeferenced orthographic images. The orthophotos of each outcrop were then imported into GIS software (ArcMap 10.7.1) where the fractures were mapped. Subsequently, a custom MATLAB (R2020b) script was used to perform a statistical analysis of the interpreted fractures and generate diagrams for visualization of the results.

### 3.3. Thermal Conductivity Measurements

The thermal conductivity of the various rock types occurring in the investigated area has been measured by the Geological Survey of Sweden using a Thermal Conductivity Scanner (TCS). The equipment used is manufactured by Lippmann and Rauhen GbR in Germany. In total, 17 rock samples from outcrops inside or in the proximity of the Distorp site were analyzed. In some cases, multiple measurements were performed on a single sample, to scan in different orientations. This led to a total of 23 measurements being made for the Distorp area. The TCS measures the thermal conductivity (TC) and thermal diffusivity (TD) by applying optical scanning technology to plane or cylindrical surfaces (along the cylinder axis) of rock or core specimens. The TCS uses a focused, mobile, and continuously operated heat source in combination with infrared temperature sensors [26]. These sensors measure the sample temperature before and after heating. Typically, two reference probes with known thermal properties are analyzed together with the sample. TC and TD are determined by comparing the temperatures assessed from the certified standard samples with temperatures measured on the rock sample.

During operation, individual TC measurements are made along a scan line at a specified sampling rate across the rock sample. From these measurements, a mean average, as well as maximum and minimum TC values are calculated for the sample. Thermal diffusivity TD can also be measured together with the TC measurements.

### 3.4. Petrophysical Measurements on Rock Samples

During the project, measurements of both magnetic susceptibility and density were performed on 14 samples collected from outcrops in the Distorp area, in SGU's petrophysics laboratory. The density was calculated by comparing measurements of weight and volume. The weight of the samples was measured using a precision scale (FX-3200) and the volume using the Archimedes principle (displacement of water). The magnetic susceptibility was measured using a GTK K4/GSF-93 instrument, built by the Finnish Geological Survey (GTK). Here the magnetic susceptibility is measured using the deviation method, utilizing an AC bridge. Based on repeat measurements of a typical bedrock

sample, of standard size and relatively low susceptibility, the standard deviation of these instruments is about  $5 \text{ kg/m}^3$  and  $20 \times 10^{-6} \text{ SI}$  for density and magnetic susceptibility, respectively. In addition to these lab measurements, magnetic susceptibility was measured at outcrop locations using a hand susceptibility meter (SM20). To assess the variability and obtain a representative average value, at least 10 measurements were made at different points across each outcrop location.

Furthermore, pre-existing petrophysical data and outcrop magnetic susceptibility measurements from the Distorp site and surrounding area were extracted from SGU's databases. These pre-existing data were combined with the newly acquired data to form a petrophysical database for use in this study.

### 3.5. Wireline Logging

The wireline logging was performed by Engineering Geology at Lund University with equipment from Robertson Geologging Ltd. Two runs were performed in each borehole, the first with Natural Gamma, Temperature, Long and Short Resistivity, Single Point Resistance, and the second with Acoustic Televiwer (ATV).

The Natural Gamma log is the most widely used log for lithological characterization of successions within boreholes. The log is a passive radiometric log that uses a scintillation counter that detects the natural gamma radiation coming from the rocks in the borehole wall [27]. The radiation originates from the potassium-40, radium-uranium, and thorium series. For crystalline rocks like granites and metabasites there is a significant difference in the potassium content, which can be detected in the Natural Gamma log. The relatively potassium-rich granites (high in mica and feldspars) will consequently result in a higher gamma-ray level in comparison to the generally potassium-poor mafic rocks [28]. The purpose of this log was, with the support from descriptions of the rock cuttings, to get a detailed picture of the rock type distribution in the boreholes. The gamma-ray results can also indirectly be used as a measure of the thermal properties of the rocks within the borehole, since most in situ heat production are related to the amount of naturally occurring radioactive elements mentioned above [29].

The Single Point Resistance tool measures the electrical resistance of the subsurface in the immediate vicinity of the borehole. The tool operates by measuring the difference in voltage between two electrodes using a constant current. Single-point logs are sensitive to the resistivity of the lithology adjacent to the electrodes, regardless of electrical influences caused by varying thicknesses and composition of beds; thus, they have, in general, a very high vertical resolution.

The Short and Long Resistivity tool measures (as opposed to resistance) the resistivity of the formation volume (rock and formation fluids) outside the immediate proximity of the borehole. The vertical resolution is less than for the Single Point Resistance tool. The tool works best in sedimentary bedrock with relatively thick beds where the focus lies on determining the thickness of the mud invaded zone in porous rocks, as well as properties of any reservoir fluids present.

Several properties affect the resistivity of a rock volume, for example, porosity, the resistivity of the fluid within fractures and pores, mineral composition, and the texture of the rock. Granitic rocks have, in general, slightly lower resistivity compared to mafic rocks. Although, it should be noted that there is a significant variation in the resistivities of mafic and felsic intrusive rock types [30].

The Acoustic Televiwer generates an acoustic image of the borehole wall by detecting the arrival time for a reflected sound wave generated by a rotating piezoelectric source. Besides the arrival time, the log registers the amplitude of the measured acoustic wave. The measurement gives a continuous, 360 degrees image of the borehole wall, which is geographically orientated. After processing, fractures and variations in the density of the borehole wall can clearly be identified. A major advantage of the Acoustic Televiwer is that it can be run in boreholes where the drilling fluid is opaque, for example drilling mud. Within this project, Acoustic Televiwer data has been used to map the in-situ fractures

to assess the hydraulic properties, borehole integrity and to determine the deviation and direction of the investigation boreholes. Vertical boreholes with minimal deviation are essential in a multiwell HT-BTES where the distance between the individual boreholes is commonly only a few meters. Too much deviation can cause undesirable thermal interaction between boreholes, as well as increase the risk of collision between boreholes during drilling operations [31].

### 3.6. Thermal Response Tests

Thermal measurements, including thermal response tests and distributed thermal response tests, were performed. Conventional TRT is a relatively simple and well-established pre-investigation method in the shallow geothermal industry. It is utilized for quantifying effective underground properties, and thereafter, provides input for system design [32].

TRTs are commonly performed by injecting the heat into the borehole at a constant rate by circulating a heated secondary fluid through a closed-loop borehole heat exchanger. The effective thermal conductivity ( $\lambda^*$ ) and effective borehole thermal resistance ( $Rb^*$ ) are estimated through an inverse modeling procedure. During this process, measurements of the heat exchanger inlet- and outlet temperature in response to the heat injection over time are matched with the equivalent temperature response obtained from a parameterized model. For this purpose, under the common assumption of pure conduction heat transfer in a homogeneous medium, the infinite line source (ILS) model was used [33]. This test procedure implies that the experimental data and the best-fit parameter values obtained only represent spatially averaged predictions of the thermal characteristics of the subsurface and BHE performance. In other words, no information about subsurface heterogeneity is provided.

Application of distributed temperature sensing (DTS) technology, based on Raman optical time-domain reflectometry allows for downhole temperature measurements to be recorded along the full length of the borehole during the response test. One or multiple fiber optic cables may be installed in the test borehole, while performing a TRT. The processed temperature data acquired from the DTS system consist of discrete (averaged) representations of the continuous temperature distribution over a sampling interval. The sampling resolution, i.e., the sampling interval spacing over which signals are collected and averaged along the fiber, can be as low as 0.125 m for high performance devices [34]. Distributed temperature measurements can also be carried out with other types of sensors, but optical fiber cables, when properly used, offer significant advantages [35]. This type of TRT is often referred to as a Distributed Thermal Response Test.

In contrast to conventional TRT, based on BHE inlet- and outlet temperature measurements, the DTRT permits evaluation of  $\lambda^*$  and  $Rb^*$  locally along the borehole using time series of downhole temperature profiles acquired from DTS data as input to the response model [36]. The DTS instrument used in this study has a sampling resolution of 203 cm, which enabled TRT evaluation at around 150 sample intervals along the two 300 m deep investigation wells. Temperature profiles are also obtained during the test phases before and after heat injection, which allow for evaluating additional factors that affect the temperature conditions in the borehole, such as vertical groundwater movement and the presence of water-bearing fractures. Passive DTS measurements taken under undisturbed ground conditions can be used for characterizing near-surface seasonal temperature propagation effects, and at greater depths, the geothermal gradient.

### 3.7. Hydraulic Tests

Hydraulic tests were performed in connection with an experimental grouting project conducted in parallel with the present study [23]. The aim of the field experiments was to explore the use of permeation grouting techniques to implement open-loop BHEs. The primary objective of the hydraulic tests was to characterize near-borehole hydraulic conditions in the rock mass.

In the 240 m and 300 m deep Distorp Hagen wells, the hydraulic testing procedure involved the performance of single-hole, short-duration water loss measurements, which were carried out by injecting water into the test section under a constant pressure of 200 kPa. The pressure was maintained until the injection flow rate had stabilized (i.e., reached quasi-stationary condition), which typically occurred within time periods of the order of minutes. The pressure and flow data were evaluated through steady state flow analysis using Moye's formula to estimate a transmissivity value for the test section [37].

A double-packer system was used to isolate sections of interest within the borehole to perform the investigation. Measurements using 50 m section lengths were performed at regular intervals between about 10 m depth and the base of the borehole. Additional measurements were also carried out using a smaller packer spacing of 5 m in four sections within the shallowest 50 m of the borehole. These sections were selected based on the wireline logs, which indicate intervals with a high fracture density or the occurrence of single conductive water-bearing fractures.

## 4. Results

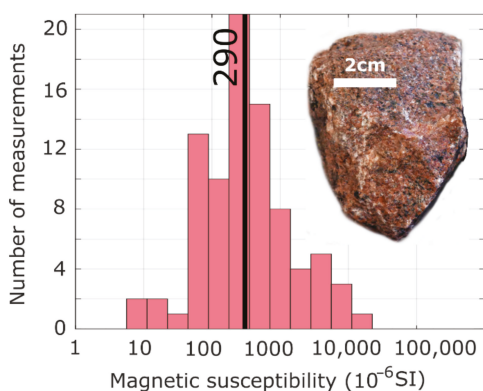
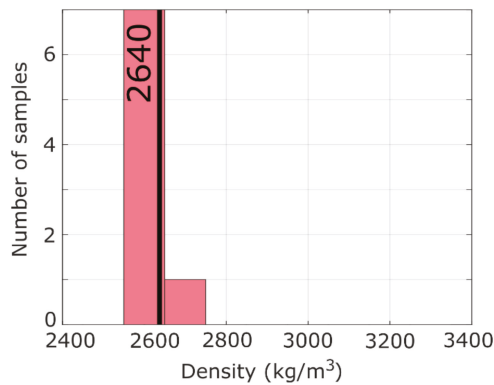
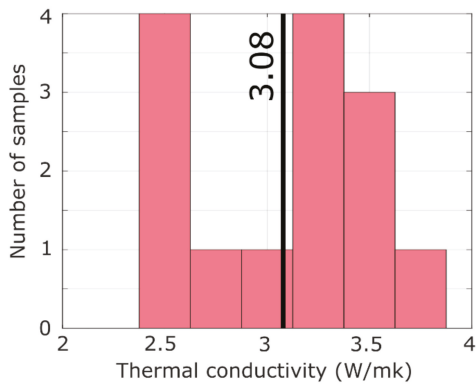
### 4.1. Bedrock Composition and Thermal Properties

The dominant rock types expected within the site area are, according to the bedrock map [18], grey and red fine- and medium-grained granite, greyish granite-granodiorite, and dark grey to black gabbro and metabasite (Figure 1). Different orogenic phases with granitoid intrusions deformation and metamorphism have resulted in a heterogeneous rock mass which in places also consist of folded migmatite gneiss.

The regional bedrock map (Figure 1) shows that smaller areas with metabasite and gabbro occur in the southeastern most parts of the site area, while most of the bedrock surrounding the investigation wells is composed of fine-grained red and grey granite. In the northwest parts of the site, the bedrock is dominated by variably gneissic granite and granodiorite. However, it should be noted that there are relatively few outcrops in the northern part of the area where geological observations can be made. Hence, the map in this area is primarily based on regional geophysical data and is consequently somewhat uncertain [18]. Most outcrops occur in the southeast and southern part of the study area. In total, 22 of these outcrops, dominated by variably grey and red, fine- and medium-grained granite, were sampled in this study (Figure 3). In addition, a few outcrops with mafic rocks were sampled to the southeast and west of the site area.

Considering the regional bedrock map, the composition of the uppermost bedrock within the site area should be dominated by various granitoid rock types with minor volumes of mafic rocks. Hence, an average thermal conductivity close to that of granite would be anticipated across the study area. Thermal data within a c. 5 km radius from the Distorp site, based on modal mineralogical analysis of rock samples, indicate that the average thermal conductivity for the granites in the area is 3.36 W/mK (Std Dev 0.20 W/mK), while the mafic rocks show an average of 2.61 W/mK (Std Dev 0.14 W/mK). Results from the laboratory TCS measurements on rock samples from the study area fall within the same range as the values from the modal-based regional database. A statistically reliable relationship between thermal conductivities based on modal mineralogical analyses and results from TCS-measurements have also been shown by [38]. The TCS-analyses give a mean thermal conductivity of 3.08 W/mK for the granites, while the mafic rocks give a significantly lower mean value of 2.42 W/mK (Figure 4). The results from the thermal conductivity lab measurements and the calculated values from modal analyses are presented as supplementary data (Tables S2 and S3).

### a) Granitoids



### b) Mafic rocks

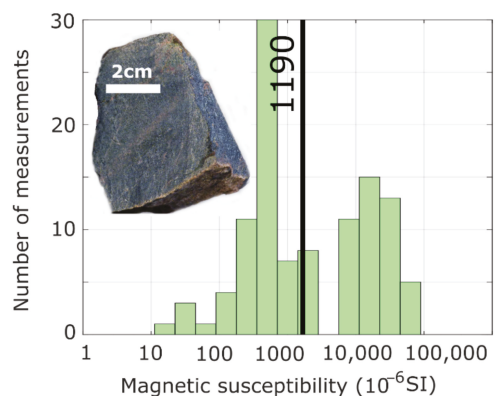
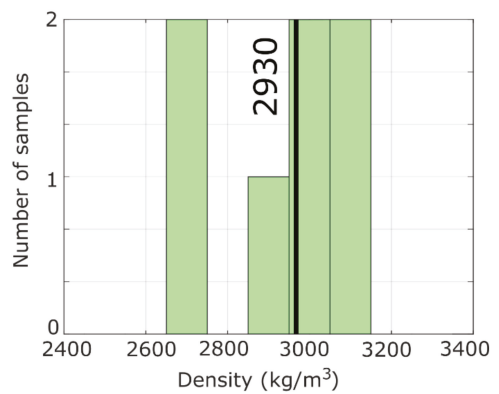
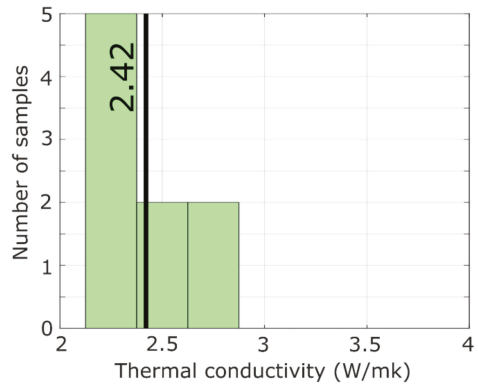


**Figure 4.** Petrophysical data for granite and mafic rock types. Histograms showing thermal conductivity data (top), density data (center), and magnetic susceptibility data (bottom), are shown for each rock type. The thick black lines display the average values for each plot. The mean average value is shown for the thermal conductivity and density data, while the median average is shown for the magnetic susceptibility data. A close-up image of each rock type is shown on the magnetic susceptibility graph. (a) Graphs on the left are for Granitoids. (b) Graphs on the right are for Mafic rocks.

The two 300 m deep investigation wells reveal that the subsurface bedrock mass is not as uniform as expected from the bedrock map. It should be noted especially that the two wells show quite different rock successions, despite being in the same type of granite on the geological map. The DTRT measurements also demonstrated differences in thermal conductivities that relate to the rock type distribution in the two wells. The Distorp Åkern well gave thermal conductivities between 3.09 and 3.58 W/mK with an average of 3.30 W/mK (Figure 5), while the Distorp Hagen well had values ranging between 2.85 and 3.64 W/mK with an average of 3.43 W/mK (Figure 6). TRT measurements show that the effective thermal conductivity at Distorp Hagen is slightly lower than Distorp Åkern, with values of 3.05 and 3.28 W/mK, respectively. The error in this type of in situ thermal conductivity measurement is known to be 5–15% [39]. Although it is possible that error in the presented results is within this range, it should be noted that the thermal conductivity values above have been measured/calculated during the heat injection phase of the DTRT and that the injected heat per unit length has been assumed to be the same in all sections of the borehole. In [36], it is stated that firstly, higher accuracy is obtained when tests are evaluated during thermal recovery after heat injection (with no radial temperature gradient in the borehole and avoiding the presence of thermosyphon effects). Secondly, it is stated that local thermal conductivity calculations should be performed using local heat injection rates, which were not measurable in the tests presented in this paper. The increase of thermal conductivity with depth observed in one of the two boreholes and the difference between average thermal conductivity values from the DTRT and the effective value obtained from a standard TRT are attributed to these two factors. More details about the factors affecting TRT results can be found in [39,40]. DTS data obtained during TRT on the Distorp Åkern well are provided as supplementary material (Spreadsheet S1).

When comparing the natural gamma logs for the two wells, a clear difference can be seen in the measurements. The gamma response is mainly related to the presence of potassium in these types of rock. Hand spectrometer measurements give a mean potassium content of about 4.0% for the granites, while the mafic rocks have a potassium content of about 2% (Supplementary Table S4). Relatively low gamma values are thus interpreted to represent rock types with a lower amount of potassium, thus primarily mafic rock types in this geological setting. Hence, the regions with low gamma values, within the somewhat variable gamma signature are interpreted to indicate metamafic or gabbro rocks in the Distorp Åkern well. It was also indicated in the cuttings material that there is a greater volume of mafic rocks occurring in the Distorp Åkern well (Figure 5) than in the Distorp Hagen well (Figure 6). In the Distorp Hagen well, the gamma values are on average higher than in the Distorp Åkern well and exhibit less variability. This is interpreted as a more homogeneous sequence of granite and granodiorite. This interpretation is also verified by the cuttings that indicate a relatively homogeneous rock succession of fine- and medium-grained granite in this well.

The difference in the number of mafic rock types encountered in the two wells and the associated thermal rock properties lead to a different thermal response in the two wells.

Based on the petrophysical data from this study, a significant difference between the magnetic properties of the granitic and mafic rocks exists (Figure 4). Here it can be observed that in the histograms, both rock types have a peak at about  $300 \times 10^{-6}$  SI, which is most likely due to the presence of iron-bearing paramagnetic minerals (such as biotite). However, the mafic rocks have an additional peak at about  $20,000 \times 10^{-6}$  SI, which is likely due to the presence of magnetic minerals (such as magnetite). Hence, strong magnetic anomalies within the study area are likely to be associated with mafic rock types. Figure 7 shows maps of the total magnetic field over the study area, and the average resistivity of the upper 300 m of the subsurface. The black dashed line highlights the study area in the figure.

### Distorp Åkern

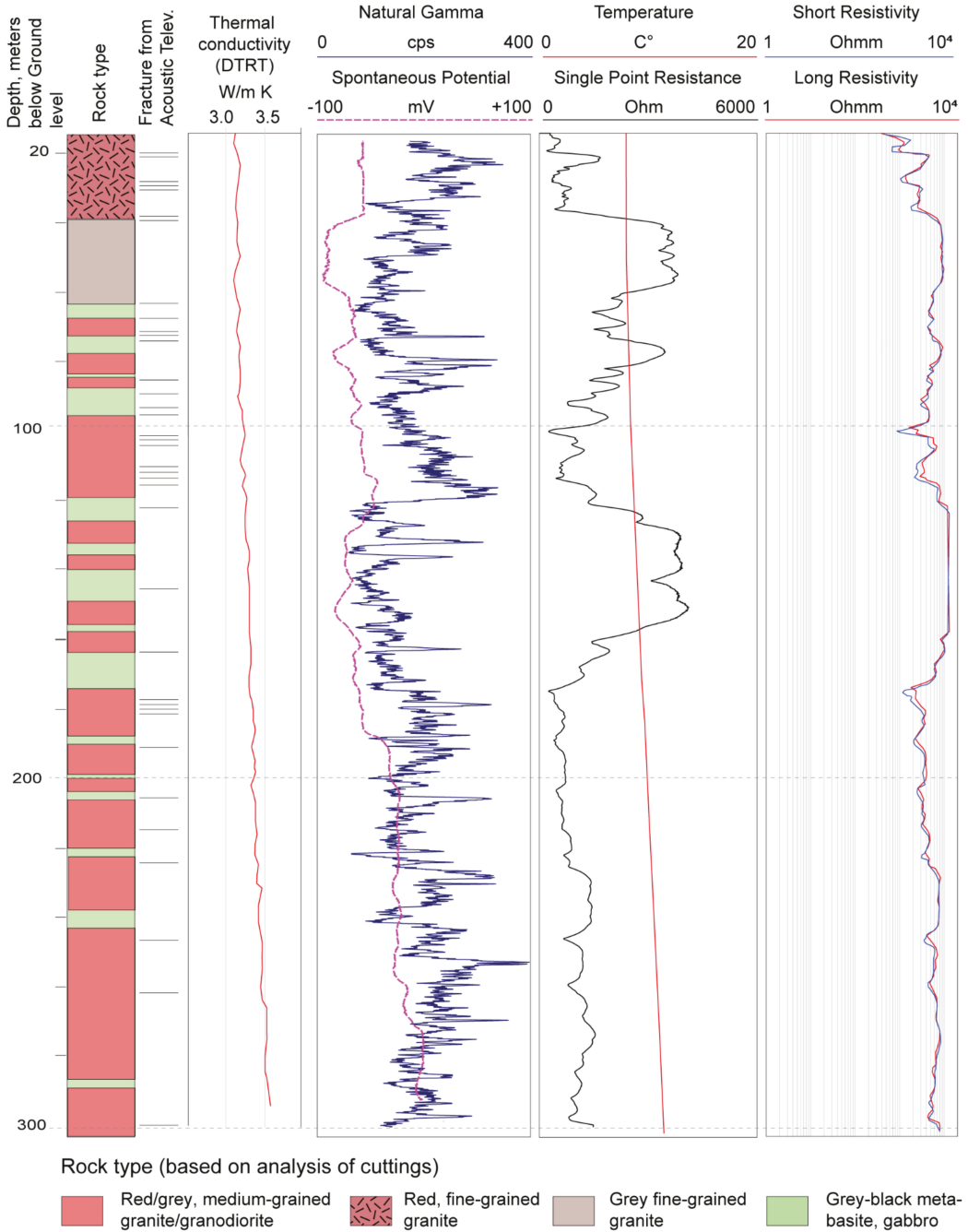


Figure 5. Composite log of the 300 m deep Distorp Åkern well.

## Distorp Hagen

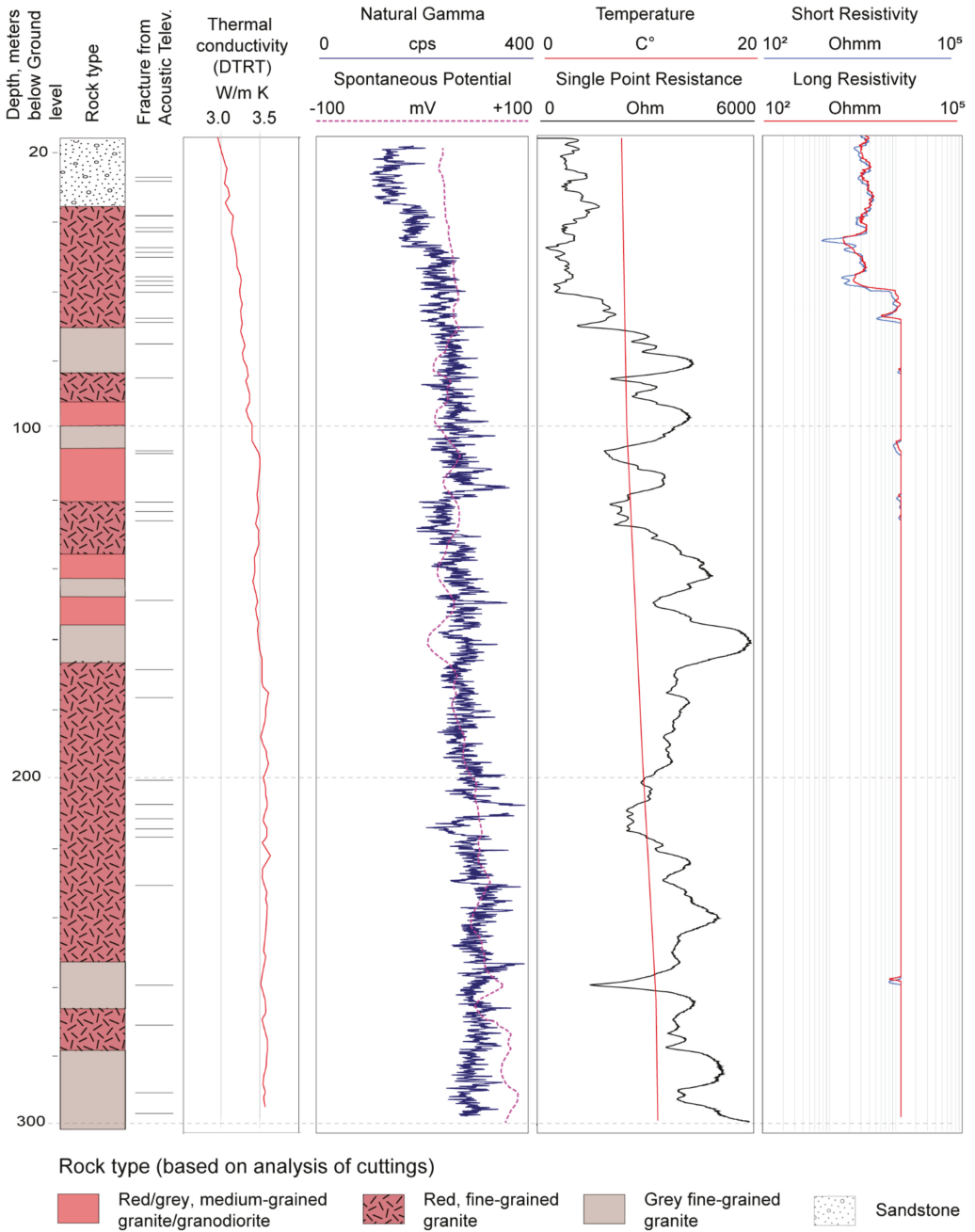
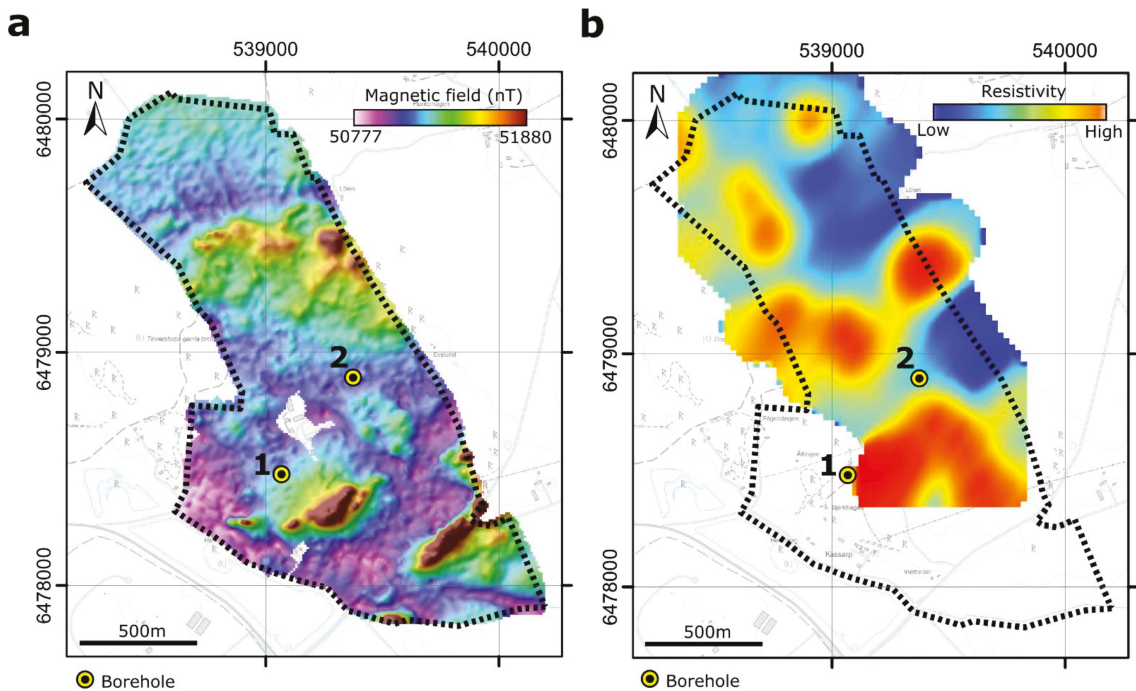


Figure 6. Composite log of the 300 m deep Distorp Hagen well.



**Figure 7.** (a) A map of the total magnetic field over the study area. (b) Map of the average resistivity of the upper 300 m of the subsurface derived from the 3D resistivity model generated from VLF measurements. Borehole 1: Distorp Hagen, 2: Distorp Åkern.

On inspection of the map of the magnetic field measurements (Figure 7a), several regions with positive magnetic anomalies (relatively high values) can be identified in the southern part of the study area. These anomalies coincide with outcrops where mafic rocks have been observed. Hence, considering the petrophysical data, it is likely that these positive magnetic anomalies are due to the presence of mafic rocks. A broad positive magnetic anomaly is also present to the north of the Distorp Åkern well, which can also be interpreted as a region with more mafic rock types. Such an interpretation of this anomaly is supported by outcrop observations to the west of this anomaly, where isolated units of mafic rocks have been mapped within the predominantly granitic rocks. The remaining parts of the study area characterized by relatively low magnetic field values can be interpreted to be predominantly granitic rocks. Figure 8 shows a detailed interpretation of the bedrock geology of the study area based on the new data collected in this study, here the regions of more mafic rock types (green) are interpreted to correspond broadly to regions with high magnetic field values.

In the magnetic field data shown in Figure 7a, several linear zones can be identified, over which a sharp change in the magnetic field values occurs (discontinuities). These are most notable in the southern part of the study area. Specifically, two zones with an NW–SE-orientation exist; the first is located between the two investigation wells, while the second lies about 300 m south of the Distorp Hagen well. A more subtle discontinuity in the magnetic data with an N–NW-orientation can be interpreted about 100 m to the west of the Distorp Hagen well. These are interpreted to represent deformation zones over which the geology has been displaced and are shown in Figure 8 as black lines. The orientation of these discontinuities is consistent with the large-scale deformation zones mapped from airborne geophysical data (Figure 1).

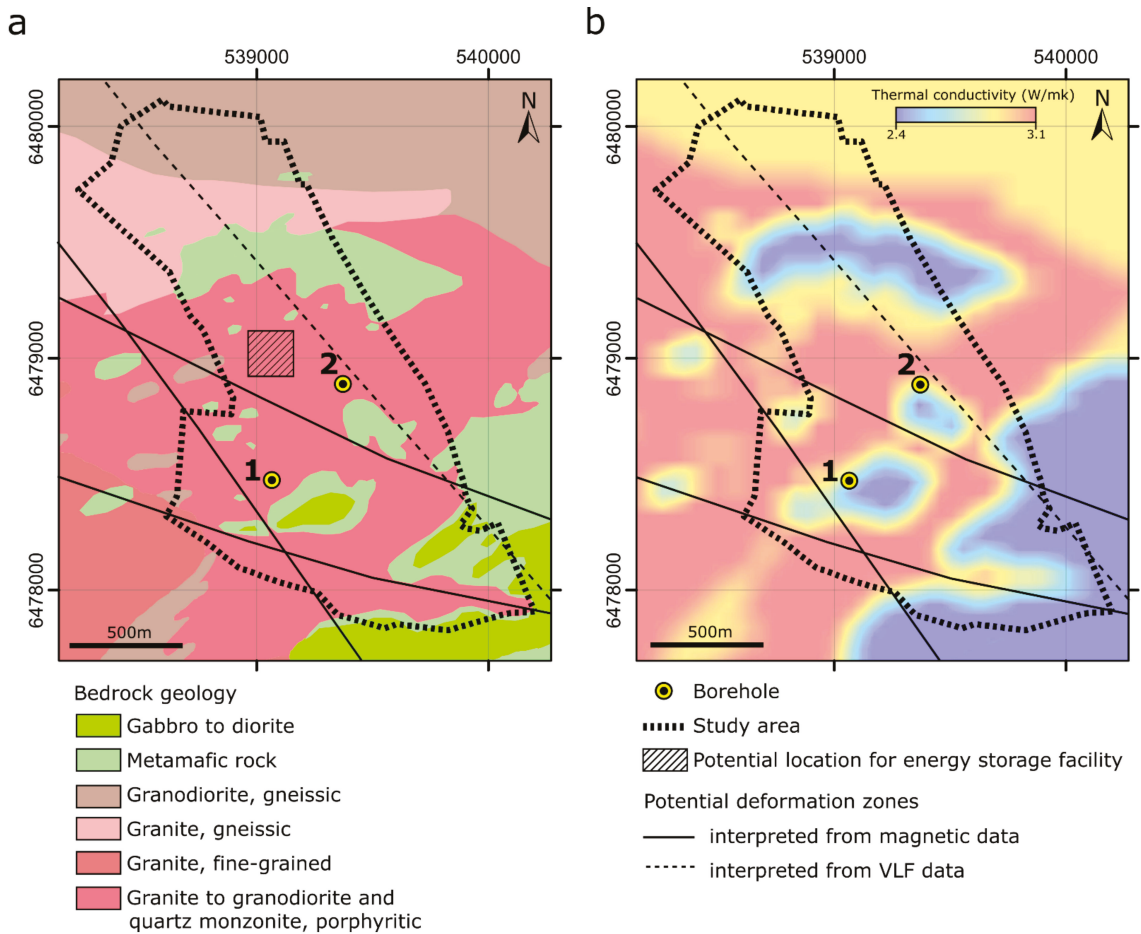


**Figure 8.** (a) Interpretation of the Bedrock geology based on geological and geophysical observations made in this study. A potential location for the energy storage facility is highlighted. (b) A map showing the prognosed bedrock thermal conductivity based on the data and observations from this study. Borehole 1: Distorp Hagen, 2: Distorp Åkern.

On inspection of the resistivity map, generated from the VLF data shown in Figure 7b, a general transition from higher resistivities in the west to lower resistivities in the east can be observed. This is interpreted to be largely due to variations in the surface sediment layer, where more resistive sandy and silty moraine are mapped to the west, and less resistive glacial clay is mapped to the east of the study area. Furthermore, several high resistive anomalies can be observed in Figure 7b. Two of these, one to the southeast of the Distorp Åkern well and another to the northwest, correspond to areas where outcrops exist. Hence, these can be interpreted as regions where the resistive bedrock is relatively close to the surface, and the more conductive sediment layer is thin. A linear region with relatively low resistivity values and an NW–SE-orientation can potentially be interpreted in the resistivity map. This zone is most notable directly to the north of the Distorp Åkern well, where it intersects a region of relatively high resistivity. This zone could potentially indicate the presence of a more conductive zone in the bedrock, such as a water-filled fracture system (deformation zone). This potential zone is shown in Figure 8 as a dashed black line.

If both the detailed bedrock interpretation of the study area (Figure 8a) and the thermal conductivity lab results (Figure 4) are considered, it is possible to make a simple prognosis

of the thermal conductivity of the bedrock across the study area, which is shown in Figure 8b. Here the mean average thermal conductivities (from the TCS measurements) of 3.08 and 2.42 W/mK are assigned to granitic and mafic rocks, respectively. An intermediate thermal conductivity was assigned to granodiorite rocks. Some smoothing was applied to account for the mixing and interlayering of these two rock types in transitional areas. It should be noted that there is significant uncertainty in this map of prognosed thermal conductivity. This is due to the large variation in thermal conductivity values measured from samples, as well as the uncertainty in the detailed bedrock map, which is based largely on geophysical data, rather than outcrop observation. Despite this, it can be a useful tool to visualize the anticipated bulk thermal conductivity values based on the updated geological map.

#### 4.2. Fracturing and Fracture Orientation

Figure 9 shows an example of an orthophoto that was generated for an outcrop located on the southwestern edge of the study area. At this outcrop, a clear contact between coarse-grained granite and more mafic fine-grained granodiorite can be observed. An example of the fractures interpreted for this outcrop are shown in Figure 9b. Similar fracture interpretation was performed on all outcrops where drone photographs were available to generate a database of about 1500 fractures. A rose diagram showing the distribution of fracture directions, weighted by fracture length, for all fractures which were interpreted in the study is shown in Figure 9c.

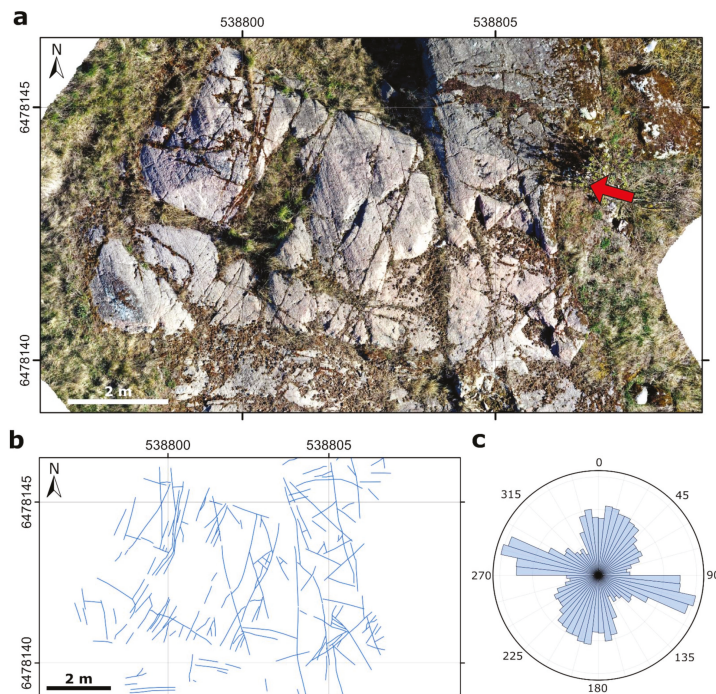


**Figure 9.** (a) Example section of a drone orthophoto of an outcrop within the study area. A contact between fine-grained granodiorite rocks (grey) and coarse-grained granite rocks (pink) is marked with a red arrow. (b) interpreted fractures (blue lines) for the portion of the orthophoto shown in (a). (c) Rose diagram showing the orientation of fractures mapped on all outcrops within the study area, where drone photographs were taken.

Here it can be observed the predominant fracture set in the study area has an azimuth of about  $105^\circ$ . Secondary fracture sets appear to exist with azimuths of  $15^\circ$  and  $165^\circ$ . A primary fracture orientation of  $105^\circ$  corresponds well to the orientation of the regional deformation zones mapped from airborne geophysical data (Figure 1), as well as several of the potential deformation zones mapped from the ground-based magnetic data (Figure 8). The secondary fracture set with an azimuth of about  $165^\circ$  corresponds well to the potential deformation zone mapped with the VLF data and one of the deformation zones mapped with the magnetic data (Figure 8).

Downhole fracture mapping by visual inspection of Acoustic Televiewer images and geoelectric data sets collected in the 300 m and 240 m deep Distorp Hagen wells indicates relatively high fracture density at shallow depths to around 60 m. Estimates of the lineal fracture density ( $P_{10}$ ) [41] at discrete 1 m intervals within the depth section of 10–60 m of the boreholes are shown in Figure 10. A maximum fracture density of 7 fractures per meter can be observed in both boreholes. At larger depths, only single or groups of few fractures were identified in scattered intervals along the boreholes. Although not described in this study, additional information on fracture characteristics (e.g., strike and dip) can be acquired from Acoustic Televiewer data with additional analysis. This is possible because the tilt and orientation of the instrument are logged during measurement. The ATV image logs for both Distorp Hagen wells are provided in the supplementary data (Figures S1 and S2).

#### 4.3. Groundwater Conditions

The estimated capacities of the two 300 m deep investigation wells within the Distorp site were 1200 L/h and 1500 L/h based on air-lift yields measured during the completion of the wells. The groundwater table is relatively shallow and was observed to be about 2 to 3 m below ground level within the study area. Borehole transmissivity data, based on hydraulic testing in the 300 m and 240 m deep Distorp Hagen wells, are presented in Figure 10. The range of estimated transmissivities, using measurement intervals of 50 m, spans from  $8.4 \times 10^{-7} \text{ m}^2/\text{s}$  to  $2.6 \times 10^{-5} \text{ m}^2/\text{s}$  in the 300 m deep well, and from  $3.3 \times 10^{-7} \text{ m}^2/\text{s}$  to  $1.0 \times 10^{-5} \text{ m}^2/\text{s}$  in the 240 m deep well. The medians of these ranges are  $1.4 \times 10^{-5} \text{ m}^2/\text{s}$  and  $5.3 \times 10^{-6} \text{ m}^2/\text{s}$ , respectively.

A trend of decreasing transmissivity with depth can be observed. An exception to this is seen in the lowermost two sections (which overlap to some degree) of the 300 m well. Qualitative interpretation of ATV and geoelectric data indicates that the water loss within these sections is dominated by a single fracture located at a depth of approximately 260 m (Figure 10). The maximum transmissivity estimates occur in the shallowest test interval of both wells, corresponding to the regions where the maximum fracture densities are also estimated (Section 4.2). This agrees with the common observation that bedrock transmissivity is often depth-dependent. Possible explanations for this include, near-surface fracturing, due to stress release and dissolution of fracture filling minerals. Another explanation is the closure of fractures, due to increasing overburden stress at greater depth [42,43].

Thermal anomalies that can be observed in the temperature-depth profiles obtained during DTRT may be indicative of possible groundwater movements. The DTS data can provide a useful means to distinguish the flow state of fractures that are detected from geophysical logs. In the example shown in Figure 11, the combined Acoustic Televiewer and single point resistance logs indicate the presence of multiple water-bearing fractures within the considered interval (e.g., at depths of 79 m, 85 m, and 109 m, as indicated in (Figure 11)). However, a prominent temperature anomaly is only associated with one of these fractures, at a depth of around 85 m. Hence, the DTS temperature profile detects fractures with the most significant fluid flow. The DTS temperature profile records can also be used for quantitative assessment of cross-hole and in-hole groundwater flow velocities [44,45]. However, groundwater flow velocities based on DTS data were not addressed in this study.

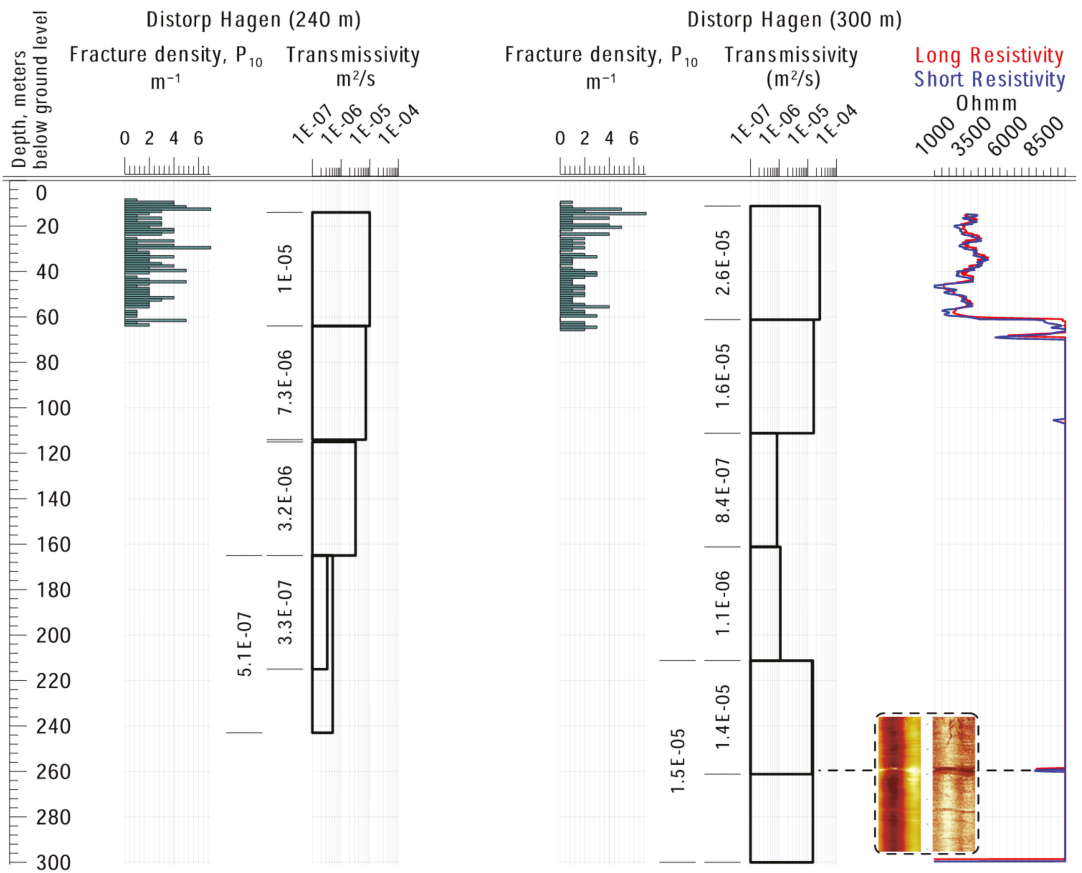
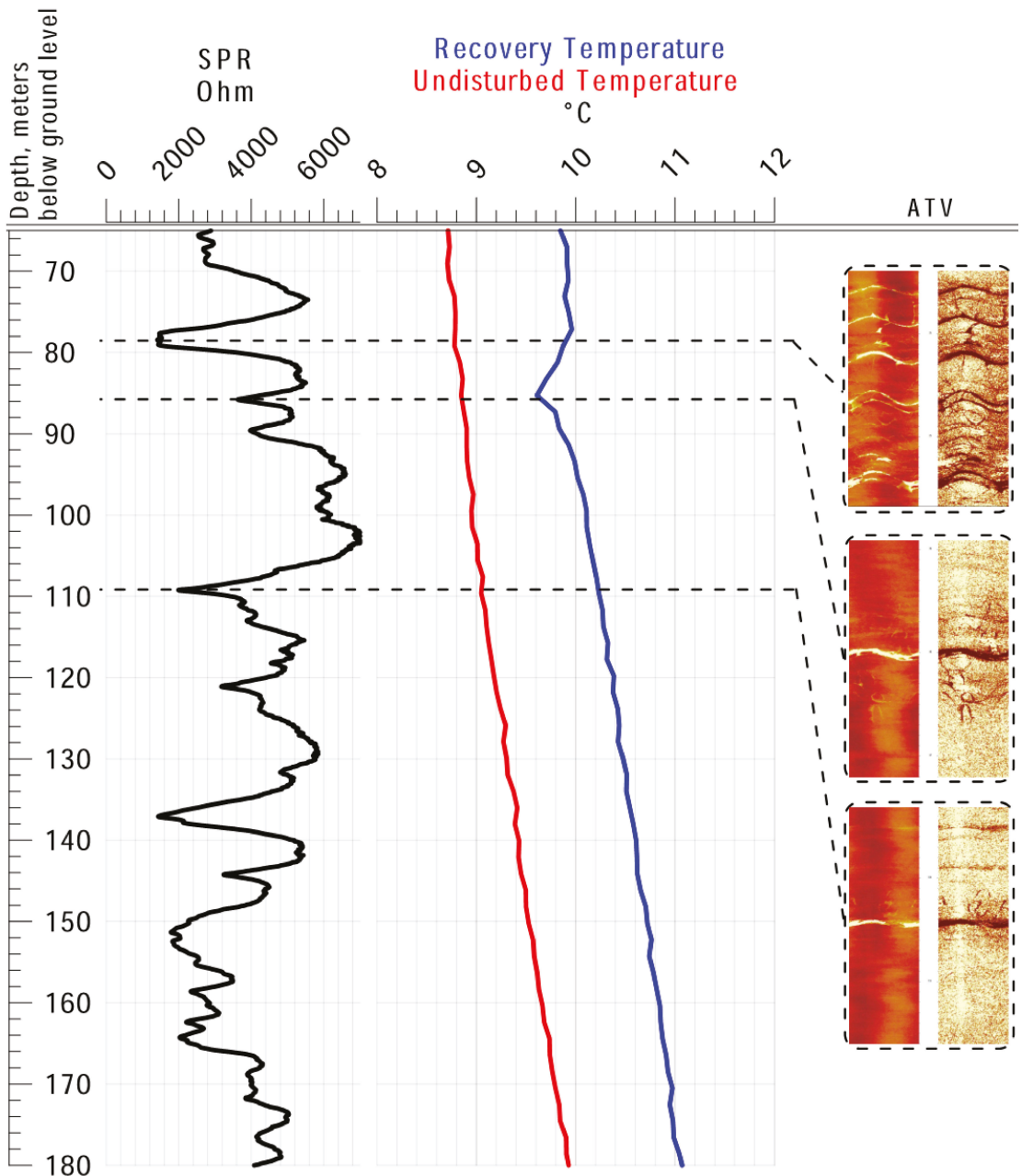


Figure 10. Transmissivity estimates with measured depth below ground level for the 240 m and 300 m deep Distorp Hagen wells.



**Figure 11.** Detection of flowing fractures using single point resistance (SPR) logs and temperature profiles acquired during DTRT in the 240 m deep Distorp Hagen well.

### 5. Discussion

It is known that the investment cost associated with multiwell HT-BTES systems is substantial. As such systems may be designed and built for large scale installations,

an arbitrary assessment of design and placement, based on limited data, can lead to high risks regarding performance, longevity, and impact on the surrounding environment. Anisotropic geological conditions are especially common in a crystalline rock mass, like the conditions in the Distorp site. When considering sites with sedimentary strata, a certain degree of predictability in the geological conditions parallel to bedding is reasonable to assume, despite variability perpendicular to the bedding direction. However, the anisotropy observed in crystalline rocks is, in comparison to sedimentary rocks, often considerably greater. As a result, the anisotropy in thermal properties anticipated within crystalline rocks is also typically higher than in sedimentary rocks. The frequency and predominant orientation of fractures and fracture zones are also important factors that can have an impact on the groundwater flow, and hence, the size and shape of the rock mass thermally affected during the operation of an HT-BTES system. Hence, a strategy relying only on single investigation wells for appraisal and design of a large-scale HT-BTES facility in an anisotropic crystalline bedrock setting is unlikely to provide accurate information required to assess potential performance, longevity, and environmental impact.

To fully characterize the anisotropic geological conditions (i.e., to obtain a more solid base for design), a multidisciplinary approach in the pre-investigation phase is recommended, especially for HT-BTES systems that utilize large well clusters.

However, characterization of anisotropic conditions in a crystalline rock mass on a local scale is challenging and can be resource-demanding. Thickness and composition of the soil cover, petrophysical properties of the rock mass, groundwater conditions, and the accessibility of outcrops all govern the possibility to collect information, as well as the methods that can be applied. The approach in this study has been to test and evaluate a comprehensive range of methods that may be appropriate for improving the empirical data set on various properties in a crystalline bedrock domain. It is not recommended that all the methods addressed in this study should be applied in all pre-site evaluations. In fact, it is important to emphasize that several aspects of the data collection and investigation strategy within this study are suboptimal. This is largely because the data in this study have been collected across various separate and sequential projects, which have had varying individual scopes and objectives. For example, in this study, the boreholes were drilled prior to the surface geophysical and geological investigations. Ideally, the results of the relatively quick and resource effective ground geophysical and geological investigations should have been available to optimize the location of the relatively expensive boreholes. Furthermore, in this study, many methods have been tested in parallel to investigate various aspects of the HT-BTES site. It is recommended, however, that in future investigations, a more sequential and integrated data acquisition and analysis strategy be adopted. Hence, it is not suggested that the workflow presented in this study be considered best practice for a pre-investigation study for an HT-BTES system. Instead, we aim to showcase and exemplify a range of available methods which, if appropriate, can be selected to form part of an HT-BTES investigation strategy.

It is important to highlight that the choice of methods should be tailored to the scenario being assessed. When designing an investigation strategy, it is important to consider the physical characteristics of the bedrock, as well as the anticipated level of subsurface uncertainty when selecting methods. The limitations of the different methods should also be considered. Furthermore, the investigations should be of an appropriate scale, bearing in mind the resources available for the project and the eventual size of the HT-BTES system. Finally, the investigations should form part of an integrated and sequential site evaluation strategy.

In the following discussion, the performance and limitations of the different methods applied at the Distorp site are discussed, with the aim of providing information that can be useful for the design of pre-site investigations strategies for future HT-BTES systems within crystalline bedrock.

At the Distorp site, regional bedrock maps and petrophysical data from SGU indicate that the bedrock is dominated by granitoids, which typically have low magnetic suscepti-

bilities and relatively high thermal conductivities. Within these granitic rocks, occurrences of more mafic gabbroid rock types can occur, which can have higher magnetic susceptibilities and typically have significantly lower thermal conductivities (cf. Figures 1 and 4). Hence, in the case of the Distorp site, the magnetic survey proved to be the most useful ground geophysical tool for pre-investigation. Firstly, it allowed regions with more mafic rocks to be mapped in more detail, as these rocks often exhibit relatively high magnetic susceptibility values. The magnetic data also allowed several local deformation zones to be interpreted based on linear discontinuities in the measurements. Updates to the bedrock geology map for the Distorp site, although based on all the available data from the study, relied heavily on the newly acquired ground magnetic data (Figure 8a).

The VLF-survey gave complimentary information on the occurrence of deformation zones which appear as low resistive features in the data. In the Linköping area, a single potential water-bearing deformation zone was interpreted. Although there is uncertainty in the interpretation of this data, it is beneficial to avoid such potential features when planning an HT-BTES well-cluster. The ground-based geophysical investigations, which required only a fraction of the time and resources required to drill an investigation well, can therefore be considered relatively efficient tools for assessing the lateral anisotropy of the bedrock across the Distorp site. However, it is important to note that interpretation of these ground geophysical data is to some degree subjective, and hence, uncertain. Furthermore, to interpret the ground geophysical data effectively, a good understanding of the petrophysical properties of the rock types in the study area is required. A limitation of ground magnetic and VLF measurements is that they are affected by the presence of infrastructure. Hence, due to the presence of powerlines, it was not possible to acquire VLF data in the entire southern part of the study area. Furthermore, magnetic measurements close to infrastructure or large metallic objects (such as farming machinery or fences) could not be used. Therefore, ground geophysical methods are likely to be most effective as a pre-investigation tool when there is some flexibility in the placement of the HT-BTES system within a larger investigation area with anisotropic bedrock conditions and sparse infrastructure.

Ground gravity measurements were not collected as part of this investigation, due to limitations with resources and equipment availability during the project. However, based on the petrophysical data, there is a clear difference in density values between the mafic and felsic rocks in the study area (Figure 4). Hence, the regions with mafic rocks would likely have generated a series of gravity anomalies which could have been mapped by a grid of gravity measurements across the study area. Therefore, the acquisition of gravity measurements would be recommended for further geophysical investigations at the Distorp site or for pre-site investigations of other HT-BTES projects within similar geological settings.

Outcrop studies have also provided valuable information during the investigations at the Distorp site and have proven to be essential for the interpretation of the ground geophysical data and revision of the bedrock geology map. The use of drone photographs to image and map outcrops proved to be an efficient method for generating a statistical assessment of the primary fracture orientations in the study area, which is valuable data for subsequent modeling work. During the study, lab measurements of thermal conductivity and petrophysical properties, such as density and magnetic susceptibility, have provided highly valuable information which can be useful for calibrating subsequent modeling efforts, as well as interpreting other data collected in the project. A downside of these observations is that measurements are often constrained to specific outcrop locations, which are not evenly distributed across the study area. Hence, this can lead to bias in the subsequent analysis of these data.

The updated geological map for the study area (Figure 8) is assessed to be an improvement from the pre-existing geological map (Figure 1). This is primarily because the more regional map shown in Figure 1 is based on relatively few geological observations and relatively low resolution airborne geophysical measurements. The more detailed map in Figure 8 incorporates and is consistent with additional outcrop observations. Further-

more, some of the geological boundaries have been re-interpreted to be consistent with the detailed ground magnetic data.

However, it is important to note that this geological interpretation could be further improved with additional modeling and analysis of the data. In this project, the results from the different geophysical methods were largely used separately to update the geological map of the study area. This was mainly due to resource constraints during the project. However, in other studies, it has been shown that more accurate and consistent geological interpretations can be achieved if the ground geophysical data is combined, with the available borehole and outcrop data to generate a single 3D geological model [46,47]. In such approaches, it is also possible to process (invert) the data from various geophysical methods together to obtain a more robust result [48,49]. Hence, additional 3D modeling work and joint processing of the data could lead to improvements in the assessment of the site geology and hence, better placement of a potential HT-BTES system.

The use of percussion-drilled investigation wells is not the best way to collect measurements of the subsurface properties. Although data from TRT and DTRT measurement and geophysical wireline logging provide valuable information, there is a problem in correlating the precise rock type to the geophysical and thermal properties. Hence, it is challenging to combine the well results with the ground geophysical measurements. Acquisition of drill core, along with measurements of the susceptibility and analyses of the thermal conductivity coupled to rock type, would greatly enhance the understanding of how the lithological and physical properties of the bedrock are related. Although it is a relatively expensive method, the quality of the information justifies that at least one fully cored borehole is drilled in pre-investigations for larger HT-BTES projects. Wireline logging of the cored borehole could then be used as a reference to interpret log data acquired in additional (relatively cheap) percussion boreholes strategically placed within the site area.

The wireline log data were important, together with the cuttings, to interpret the lithology in the wells. However, they were also used to identify fracturing, water-bearing zones, and assess the orientation of the boreholes. Furthermore, if spectral gamma-ray measurements are used in percussion drilled boreholes, this would enable calculations of heat productivity and more clearly distinguish potassium-poor mafic rock types, such as gabbro, from potassium-rich granitoids.

The geological prerequisites play an important role in the borehole design. Vertical wells are important as the intersection between wells can cause problems when installing the well collector tubing. Strongly deviated wells will also typically not reach the designed depth and bottomhole temperature. A foliated and fractured rock may increase the risk of deviation.

Within the site selection and the BTES design process, the use of conceptual and simulation models is central in assessing the thermal performance and environmental impact of the system. In this context, data collected from extensive field observations provide a useful base for selecting appropriate model parameters, as well as for model validation purposes. In particular, the validity of the common assumptions made in system modeling (e.g., conduction-only heat transfer in homogeneous porous media) can be assessed. Furthermore, it allows for evaluating the applicability of conventional field investigation methods (e.g., TRT) typically employed for collecting data to determine requisite model input parameters.

In this study, the geophysical and geological observations indicate that substantial lateral heterogeneity in the subsurface thermal properties occurs on a scale smaller than that of a typical large-scale BTES facility (Figure 8). It is also the case that a typical-duration TRT only samples a small portion of the storage volume. Given these factors, there is a high probability that a homogeneous model based on TRT data alone, with limited spatial coverage, would not be capable of accurately representing the global characteristics of the large-scale system. The potential limitation of assuming a single TRT-based thermal conductivity estimate to be representative at storage-scale was demonstrated by [15]. Here [15] compared the long-term prediction accuracy of a homogeneous TRT-based

finite element model with that of a vertically layered heterogeneous model with material properties inferred from inverse modeling of long-term soil temperature observational data.

The use of ground geophysical and outcrop studies in the early stage of the pre-investigation process could provide useful information on storage-scale heterogeneity for optimization of subsequent borehole investigations (e.g., DTRT and thermal core analysis, wireline logging, etc.). The combined storage- and borehole-scale data could ultimately be used for parameter estimation, e.g., by geostatistical analysis (see for example [50–52]). Furthermore, the use of hydraulic testing and fracture mapping techniques (e.g., borehole televiewer, outcrop, and core studies) for hydrogeological characterization could provide valuable model input data in the design and environmental assessment processes.

In the final part of this section, the optimal placement of a potential future HT-BTES system at the Distorp site is discussed, considering the available data. The potential HT-BTES in Linköping would involve drilling approximately 1400 wells, with an equidistance of five meters, which would take up an area of approximately  $0.04 \text{ km}^2$  ( $200 \times 200 \text{ m}$ ). Thus, this would require considerably less space than the entire site area of approximately  $2 \text{ km}^2$ , presenting the opportunity to optimize the proposed location of the HT-BTES system. Ideally, such a facility would be located within granitic rocks (with high thermal conductivity) and within a region with relatively few fractures. Therefore, based on the updated bedrock geology map of the study area (based on a range of measurements collected in this study), a location approximately 500 m north of the Distorp Hagen well can be suggested (Figure 8a). The specified area is interpreted to consist of relatively homogeneous granite. In the VLF data, this location lies within a region of relatively high resistivity, which could indicate that it is relatively unfractured. This location is also characterized by relatively low magnetic field values, which likely indicate more granitic rocks. Hence, this area would be a good potential target for further investigation. However, due to uncertainty in the bedrock geology map and the potential for heterogeneity at depth, additional investigation wells at this location are required to further assess the suitability of this location.

## 6. Conclusions

In this study, a multidisciplinary approach has been applied to further assess the anisotropic crystalline bedrock at the Distorp site at Linköping as a potential storage medium for an HT-BTES system. The investigations conducted include surface-based geophysical measurements, outcrop observations, and lab measurements of samples. Furthermore, detailed investigations within two boreholes inside the study area were conducted, including geophysical well logging, DTRT, flow logs, and pump tests. This multidisciplinary approach has proved invaluable in characterizing the anisotropic bedrock and its anticipated thermal properties across the approximately  $2 \text{ km}^2$  study area. Based on these results, a subregion of the study area is highlighted for further investigation as a potential site for an HT-BTES system. As well as highlighting the strengths of a multidisciplinary approach, the suitability of the different methods utilized in this study for BTES appraisal work are discussed with regards to their strengths and limitations.

Traditionally, pre-site investigations for BTES systems only involve observations in one or several investigation wells. However, when considering large scale HT-BTES systems that utilize anisotropic crystalline bedrock as a storage medium, a pre-investigation strategy based only on well observations is likely to be inadequate. In such situations, leverage of a range of methods that can adequately characterize the variability of the bedrock properties is important for the successful assessment of performance and design of a BTES facility. Hence, this multidisciplinary study has shown that re-evaluating the way pre-investigations are typically performed is necessary when it comes to the optimization of large HT-BTES.

**Supplementary Materials:** The following are available online at <https://www.mdpi.com/article/10.3390/en14144379/s1>, Figure S1: Distorp Hagen 240 m Acoustic televiwer, Figure S2: Distorp Hagen 300 m Acoustic televiwer, Table S1: Supplementary information on the equipment used for the various methods, Table S2: Mean, minimum and maximum values for each of the lab based TCS measurements performed on samples from the Distorp area, Table S3: Calculated thermal conductivity based on the modal analyses of the mineral composition on rock samples of various typical rock types within five-kilometer radius from the Distorp site, Table S4: Individual measurements from the gamma spectrometer for the different rock types in the Distorp area, Spreadsheet S1: DTRT data Distorp Åkern.

**Author Contributions:** Conceptualization, M.E., J.A., M.H. and D.S.; methodology, M.E., M.H. and D.S.; software, D.S. and M.H.; validation, M.H., J.A. and D.S.; formal analysis, M.H., D.S. and M.E.; investigation, D.S., M.H. and M.E.; resources, J.A. and M.E.; data curation, M.H. and D.S.; writing—original draft preparation, M.H., M.E. and D.S.; writing—review and editing, M.H., M.E., D.S. and J.A.; visualization, D.S., M.H. and M.E.; supervision, J.A. and M.E.; project administration, M.E. and J.A.; funding acquisition, J.A. and M.E. All authors have read and agreed to the published version of the manuscript.

**Funding:** This research was funded by the European Union’s Horizon 2020 research and innovation program under grant agreement No. 731166 and under the terms of the GeoERA program—ERANET Cofund Action, and by Energiforsk and the Norwegian University of Science and Technology (NTNU).

**Institutional Review Board Statement:** Not applicable.

**Informed Consent Statement:** Not applicable.

**Data Availability Statement:** The regional geological and geophysical measurements as well as the newly acquired measurements over the study area are publicly available via the Swedish Geological survey’s customer service (<https://www.sgu.se/en/products/>, accessed on 12 July 2021).

**Acknowledgments:** We especially want to thank Tekniska Verken in Linköping AB and Henrik Lindståhl for the support and letting us use information from and access to the Distorp site as a pilot site within the GeoERA MUSE project.

**Conflicts of Interest:** The authors declare no conflict of interest. The funders had no role in the design of the study; in the collection, analyses, or interpretation of data; in the writing of the manuscript, or in the decision to publish the results.

## References

- Forman, C.; Muritala, I.K.; Pardemann, R.; Meyer, B. Estimating the global waste heat potential. *Renew. Sustain. Energy Rev.* **2016**, *57*, 1568–1579. [CrossRef]
- Gehlin, S. 11-Borehole thermal energy storage. In *Advances in Ground-Source Heat Pump Systems*; Rees, S.J., Ed.; Woodhead Publishing: Cambridge, UK, 2016; pp. 295–327. ISBN 978-0-08-100311-4.
- Malmberg, M. Transient Modeling of a High Temperature Borehole Thermal Energy Storage Coupled with a Combined Heat and Power Plant. Master’s Thesis, Royal Institute of Technology, Stockholm, Sweden, 2017.
- Linköping Climate: Average Temperature, Weather by Month, Linköping Weather Averages—Climate-Data.Org. Available online: <https://en.climate-data.org/europa/sverige/oestergoetlands-laen/linkoeeping-80/> (accessed on 14 June 2021).
- Statistics | Eurostat. Available online: [https://ec.europa.eu/eurostat/databrowser/view/nrg\\_chddr2\\_a/default/table?lang=en](https://ec.europa.eu/eurostat/databrowser/view/nrg_chddr2_a/default/table?lang=en) (accessed on 15 June 2021).
- Lejonpannan. Available online: <https://www.tekniskaverken.se/om-oss/anlaggningar/kraftvarmeverk/lejonpannan/?login=reset> (accessed on 15 June 2021).
- Malmberg, M.; Mazzotti, W.; Acuña, J.; Lindståhl, H.; Lazzarotto, A. High temperature borehole thermal energy storage—A case study. In Proceedings of the IGSHPA Research Track, Stockholm, Sweden, 18–19 September 2018; pp. 380–388.
- Acuña, J.; Lazzarotto, A.; Garcia, J.; Mazzotti-Pallard, W.; Topel, M.; Hesselbrandt, M.; Malmberg, M.; Abuasbeh, M. *Tools For Design of High Temperature Borehole Storage in District Heating Production*; Termiska Energilager; Energiforsk: Stockholm, Sweden, 2021; ISBN 978-91-7673-770-5.
- Catolico, N.; Ge, S.; McCartney, J.S. Numerical Modeling of a Soil—Borehole Thermal Energy Storage System. *Vadose Zone J.* **2016**, *15*, 1–17. [CrossRef]
- Welsch, B.; Rühak, W.; Schulte, D.O.; Bär, K.; Sass, I. Characteristics of medium deep borehole thermal energy storage. *Int. J. Energy Res.* **2016**, *40*, 1855–1868. [CrossRef]

11. Nguyen, A.; Pasquier, P.; Marcotte, D. Borehole thermal energy storage systems under the influence of groundwater flow and time-varying surface temperature. *Geothermics* **2017**, *66*, 110–118. [CrossRef]
12. Schincariol, R.A.; Raymond, J. Borehole Heat Exchangers—Addressing the Application Gap with Groundwater Science. *Ground Water* **2021**. [CrossRef] [PubMed]
13. Dehkordi, S.; Schincariol, R. Guidelines and the design approach for vertical geothermal heat pump systems: Current status and perspective. *Can. Geotech. J.* **2014**, *51*, 647–662. [CrossRef]
14. Spitler, J.D.; Bernier, M. 2—Vertical borehole ground heat exchanger design methods. In *Advances in Ground-Source Heat Pump Systems*; Rees, S.J., Ed.; Woodhead Publishing: Sawston, UK, 2016; pp. 29–61. ISBN 978-0-08-100311-4.
15. Tordrup, K.W.; Poulsen, S.; Bjørn, H. An improved method for upscaling borehole thermal energy storage using inverse finite element modelling. *Renew. Energy* **2017**, *105*, 13–21. [CrossRef]
16. Banks, D. A review of the importance of regional groundwater advection for ground heat exchange. *Environ. Earth Sci.* **2015**, *73*, 2555–2565. [CrossRef]
17. Stephens, M.B.; Jansson, N.F. Chapter 6 Paleoproterozoic (1.9–1.8 Ga) syn-orogenic magmatism, sedimentation and mineralization in the Bergslagen lithotectonic unit, Svecokarelian orogen. *Geol. Soc. London, Memoirs* **2020**, *50*, 155–206. [CrossRef]
18. Claeson, D.; Antal Lundin, I.; Sukotjo, S. *K 438 Beskrivning till Berggrundskartan Delar Av Mjölby, Linköpings Och Norrköpings Kommuner*; Sveriges Geologiska Undersökning: Uppsala, Sweden, 2013; ISBN 978-91-7403-223-9.
19. Gorbatshev, R.; Fromm, E.; Kjellström, G. *Af 107 Description to the Map of Solid Rocks Linköping NO.*; Geological Survey of Sweden: Stockholm, Sweden, 1976; ISBN 91-7158-093-X.
20. Wickström, L.M.; Stephens, M.B. Tonian–Cryogenian rifting and Cambrian–Early Devonian platformal to foreland basin development outside the Caledonide orogen. In *Sweden: Lithotectonic Framework, Tectonic Evolution and Mineral Resources*; Stephens, M.B., Bergman Weihed, J., Eds.; Geological Society of London: London, UK, 2020; Volume 50, pp. 451–477. ISBN 978-1-78620-460-8.
21. Brunnar. Available online: <http://resource.sgu.se/service/wms/130/brunnar> (accessed on 15 June 2021).
22. Acuña, J.; Stokuca, M.; Mazzotti, W.; Munter, E. Förundersökningar För Högtemperaturlager. Provboring och Responsmätning Vid NetonNet, Dikesträngeln, Distorp Åker Och Distorp Hagen (in Swedish). Unpublished.
23. Hesselbrandt, M.; Acuña, J.; Funehag, J. *Impermeable Boreholes for High Temperature Thermal Energy Storage*; Termiska Energilager; Energiforsk: Stockholm, Sweden, 2020; ISBN 978-91-7673-666-1.
24. Kearey, P.; Brooks, M.; Hill, I. *An Introduction to Geophysical Exploration*, 3rd ed.; Blackwell Science: Malden, MA, USA, 2002; ISBN 0-632-04929-4.
25. Geofysiska Markmätningar, Tyngdkraft. Available online: <http://resource.sgu.se/service/wms/130/markgeofysik-tyngdkraft> (accessed on 15 June 2021).
26. Popov, Y.A.; Berezin, V.; Semionov, V.G.; Korosteliov, V.M. Complex Detailed Investigations of the Thermal Properties of Rocks on the Basis of a Moving Point Source. *Izv. Earth Phys.* **1985**, *21*, 64–70.
27. Liu, H. *Principles and Applications of Well Logging*, 2nd ed.; Springer Geophysics; Springer: Berlin/Heidelberg, Germany, 2017; ISBN 978-3-662-54976-6.
28. Geological Log Analysis. Available online: [http://www.kgs.ku.edu/Publications/Bulletins/LA/09\\_igneous.html](http://www.kgs.ku.edu/Publications/Bulletins/LA/09_igneous.html) (accessed on 15 June 2021).
29. Bücker, C.; Rybach, L. A simple method to determine heat production from gamma-ray logs. *Mar. Pet. Geol.* **1996**, *13*, 373–375. [CrossRef]
30. Loke, M.H. Tutorial: 2-D and 3-D Electrical Imaging Surveys. Available online: <https://www.geotomosoft.com/coursenotes.zip> (accessed on 19 July 2021).
31. Skarphagen, H.; Banks, D.; Frengstad, B.S.; Gether, H. Design Considerations for Borehole Thermal Energy Storage (BTES): A Review with Emphasis on Convective Heat Transfer. *Geofluids* **2019**, *2019*, 1–26. [CrossRef]
32. Spitler, J.D.; Gehlin, S.E. Thermal response testing for ground source heat pump systems—An historical review. *Renew. Sustain. Energy Rev.* **2015**, *50*, 1125–1137. [CrossRef]
33. Carslaw, H.S.; Jaeger, J.C. *Conduction of Heat in Solids*; Oxford University Press: Oxford, UK, 1959; ISBN 978-0-19-853303-0.
34. Simon, N.; Bour, O.; Lavenant, N.; Porel, G.; Nauleau, B.; Pouladi, B.; Longuevergne, L. A Comparison of Different Methods to Estimate the Effective Spatial Resolution of FO-DTS Measurements Achieved during Sandbox Experiments. *Sensors* **2020**, *20*, 570. [CrossRef] [PubMed]
35. Aranzabal, N.; Martos, J.; Stokuca, M.; Pallard, W.M.; Acuña, J.; Soret, J.; Blum, P. Novel instruments and methods to estimate depth-specific thermal properties in borehole heat exchangers. *Geothermics* **2020**, *86*, 101813. [CrossRef]
36. Acuña, J. Distributed Thermal Response Tests—New Insights on U-Pipe and Coaxial Heat Exchangers in Groundwater-Filled Boreholes. Ph.D. Thesis, Royal Institute of Technology, Stockholm, Sweden, 2013.
37. Moye, D.G. Diamond Drilling for Foundation Exploration. *Civ. Eng. Trans.* **1967**, *CE9*, 95–100.
38. Andolfsson, T. Analyses of Thermal Conductivity from Mineral Composition and Analyses by Use of Thermal Conductivity Scanner : A Study of Thermal Properties of Scania Rock Types. Master’s Thesis, Lund University, Lund, Sweden, 2013.
39. Witte, H.J.L. Error Analysis of Thermal Response Tests. *Appl. Energy* **2013**, *109*, 302–311. [CrossRef]
40. Gustafsson, A.-M. Thermal Response Tests: Influence of Convective Flow in Groundwater Filled Borehole Heat Exchanger. Ph.D. Thesis, Luleå Tekniska Universitet, Luleå, Sweden, 2010.

41. Dershowitz, W.S.; Herda, H.H. Interpretation of Fracture Spacing and Intensity. In Proceedings of the The 33th U.S. Symposium on Rock Mechanics (USRMS), Santa Fe, NM, USA, 3–5 June 1992; American Rock Mechanics Association: Santa Fe, NM, USA, 1992.
42. Mäkelä, J. Drilled Well Yield and Hydraulic Properties in the Precambrian Crystalline Bedrock of Central Finland. Ph.D. Thesis, University of Turku, Turku, Finland, 2012.
43. Cheema, T. Depth dependent hydraulic conductivity in fractured sedimentary rocks—a geomechanical approach. *Arab. J. Geosci.* **2015**, *8*, 6267–6278. [[CrossRef](#)]
44. Bense, V.F.; Read, T.; Bour, O.; Le Borgne, T.; Coleman, T.; Krause, S.; Chalari, A.; Mondanos, M.; Ciocca, F.; Selker, J.S. Distributed Temperature Sensing as a downhole tool in hydrogeology. *Water Resour. Res.* **2016**, *52*, 9259–9273. [[CrossRef](#)]
45. Bakx, W.; Doornenbal, P.J.; van Weesep, R.J.; Bense, V.F.; Oude Essink, G.H.P.; Bierkens, M.F.P. Determining the Relation between Groundwater Flow Velocities and Measured Temperature Differences Using Active Heating-Distributed Temperature Sensing. *Water* **2019**, *11*, 1619. [[CrossRef](#)]
46. Finn, C.A.; Bedrosian, P.; Cole, J.C.; Khoza, T.D.; Webb, S.J. Mapping the 3D extent of the Northern Lobe of the Bushveld layered mafic intrusion from geophysical data. *Precambrian Res.* **2015**, *268*, 279–294. [[CrossRef](#)]
47. Claeson, D.; Sopher, D. *Investigation of Layered Gabbroic Intrusions, Bergslagen*; Geological Survey of Sweden: Uppsala, Sweden, 2021.
48. Gallardo-Delgado, L.A.; Pérez-Flores, M.A.; Gómez-Treviño, E. A versatile algorithm for joint 3D inversion of gravity and magnetic data. *Geophysics* **2003**, *68*, 949–959. [[CrossRef](#)]
49. Pilkington, M. Joint inversion of gravity and magnetic data for two-layer models. *Geophysics* **2006**, *71*, L35–L42. [[CrossRef](#)]
50. Focaccia, S. Characterization of Geothermal Reservoirs' Parameters by Inverse Problem Resolution and Geostatistical Simulations. Ph.D. Thesis, Università di Bologna, Bologna, Italy, 2012.
51. Rūhaak, W.; Guadagnini, A.; Geiger, S.; Bär, K.; Gu, Y.; Aretz, A.; Homuth, S.; Sass, I. Upscaling thermal conductivities of sedimentary formations for geothermal exploration. *Geothermics* **2015**, *58*, 49–61. [[CrossRef](#)]
52. Linde, N.; Chen, J.; Kowalsky, M.B.; Hubbard, S. Hydrogeophysical Parameter Estimation Approaches for Field Scale Characterization. In *Applied Hydrogeophysics*; Vereecken, H., Binley, A., Cassiani, G., Revil, A., Titov, K., Eds.; NATO Science Series; Springer: Dordrecht, The Netherlands, 2006; Volume 71, pp. 9–44. ISBN 978-1-4020-4912-5.



Article

# Exergoeconomic Optimization of Polymeric Heat Exchangers for Geothermal Direct Applications

Alberto Carotenuto <sup>1</sup>, Francesca Ceglia <sup>2</sup>, Elisa Marrasso <sup>2,\*</sup>, Maurizio Sasso <sup>2,\*</sup> and Laura Vanoli <sup>1</sup>

<sup>1</sup> Department of Engineering, University of Naples Parthenope, 80143 Naples, Italy; alberto.carotenuto@uniparthenope.it (A.C.); laura.vanoli@uniparthenope.it (L.V.)

<sup>2</sup> Department of Engineering, University of Sannio, 82100 Benevento, Italy; fceglia@unisannio.it (F.C.); marrasso@unisannio.it (E.M.)

\* Correspondence: sasso@unisannio.it

**Abstract:** The highest economic costs of a geothermal plant are basically related to well drilling and heat exchanger maintenance cost due to the chemical aggressiveness of geothermal fluid. The possibility to reduce these costs represents an opportunity to push toward geothermal plants development. Such challenges are even more important in the sites with a low-medium temperature geothermal fluids (90–120 °C) availability, where the use of these fluids for direct thermal uses can be very advantageous. For this reason, in this study, a direct geothermal heating system for a building will be investigated by considering a plastic plate heat exchanger. The choice of a polymeric heat exchanger for this application is upheld by its lower purchase cost and its higher fouling resistance than the common metal heat exchangers, overcoming the economic issues related to conventional geothermal plant. Thus, the plastic plate heat exchanger was, firstly, geometrical and thermodynamical modeled and, after, exergoeconomic optimized. In particular, an exergoeconomic analysis was assessed on the heat exchanger system by using a MATLAB and REFPROP environment, that allows for determination of the exergoeconomic costs of the geothermal fluid extraction, the heat exchanger, and the heating production. A sensitivity analysis was performed to evaluate the effect of main design variable (number of plates/channels) and thermodynamic variable (inlet temperature of geothermal fluid) on yearly exergoeconomic product cost. Then, the proposed methodology was applied to a case study in South of Italy, where a low-medium enthalpy geothermal potential exists. The plate-heat exchanger was used to meet the space heating requests of a single building by the exploitation of low-medium temperature geothermal fluids availability in the selected area. The results show that the inlet temperature of geothermal fluid influences the exergoeconomic cost more than the geometrical parameter. The variation of the exergoeconomic cost of heat exchanger with the inlet geothermal fluid temperature is higher than the change of the exergoeconomic costs associated to wells drilling and pumping with respect to the same variable. This is due the fact that, in the selected zone of South of Italy, it is possible to find geothermal fluid in the temperature range of 90–120 °C, at shallow depth. The product exergoeconomic cost is the lowest when the temperature is higher than 105 °C; thus, the smallest heat exchange area is required. The exergoeconomic optimization determines an optimum solution with a total product cost of 922 €/y for a temperature of geothermal fluid equal to 117 °C and with a number of plates equal to 15.

**Keywords:** geothermal energy; direct heating system; plastic plate heat exchanger; exergoeconomic analysis

**Citation:** Carotenuto, A.; Ceglia, F.; Marrasso, E.; Sasso, M.; Vanoli, L. Exergoeconomic Optimization of Polymeric Heat Exchangers for Geothermal Direct Applications. *Energies* **2021**, *14*, 6994. <https://doi.org/10.3390/en14216994>

Academic Editor: Angelo Zarrella

Received: 17 September 2021

Accepted: 21 October 2021

Published: 25 October 2021

**Publisher's Note:** MDPI stays neutral with regard to jurisdictional claims in published maps and institutional affiliations.



**Copyright:** © 2021 by the authors. Licensee MDPI, Basel, Switzerland. This article is an open access article distributed under the terms and conditions of the Creative Commons Attribution (CC BY) license (<https://creativecommons.org/licenses/by/4.0/>).

## 1. Introduction

Today, the ambitious energy and environmental European Union (EU) target is to limit global temperature increase below 2 °C. Among the different sectors involved in the decarbonization by 2050, such as transport, industry, civil, and agriculture, the building sector causes 36% of greenhouse gas (GHG) emissions, and it represents the pivotal sector

to achieve the energy transition [1]. The highest share of energy demand in EU building sector has been caused by space heating in 2018; in fact, it covers 64% of energy building consumption in EU. Moreover, EU space heating requests are met 5% by electricity, 5% by solid fuel, 10% by derived heat, 4% by oil and petrol product, 23% by renewable and waste heat, and 43% by natural gas [2]. For these reasons, the EU promotes the replacement of fossil-fuel-based heating systems with renewable-based one in order to mitigate the building sector environmental impact. A massive use of renewable energy sources (RESs) to activate space heating system is a good strategy to obtain the EU targets. The renewable energy use for heating purposes in 2018 amounted to 2270 TJ of solar energy, 44,411 TJ of geothermal energy, 477,666 TJ of waste heat recovery, and 641,308 TJ of biofuels [3].

The use of RESs to meet the space heating needs could be significantly improved with the exploitation of RESs' lowly weather influences, such as geothermal source. The geothermal energy is low dependent from weather conditions for its nature, and it presents a higher capacity factor than other RESs, such as solar or wind. The total installed geothermal capacity for direct use is increased by 52% from 2015 to 2019, reaching 107,727 MW<sub>th</sub>. The increasing trend is caused by the Ground Source Heat Pumps use that do not draw the geothermal fluid from the ground. Instead, the geothermal use for direct space heating (single building and district heating system) increased by 68.0% in installed capacity, and 83.8% in annual energy use, from 2015 to 2019 [4]. However, a great potential for geothermal energy exploitation exists, but economic issues related to geothermal plant installation curb the exploitation of these technologies. Indeed, the high cost for drilling wells, and the great maintenance and purchase costs of metallic heat exchangers (HEXs) interacting with geothermal fluids, are the major cost items for geothermal plants.

The high HEXs' maintenance costs are caused by the interaction between the aggressive geothermal fluid and the heat-transfer fluid leading fouling problems [5]. This fouling issue causes the worsening of two factors in the hydronic system for heating and cooling: the increase of friction pressure losses and the worsening of thermal heat transfer coefficient. The decrease of crossing flow section also determines the reduction of plant efficiency. For these reasons, the heat exchangers of the geothermal plants require the continuous cleaning maintenance and, sometimes, the periodic replacement of traditional steel component or the employment of high fouling resistant metals, such as titanium, causing the purchase cost increase.

During the last few years, the alternative materials for HEXs are introduced to solve the fouling problem in different aggressive environments for tube plate [6], tubular immersion [6], plate [7], shell and tube [8] heat exchangers, and also economizers [9]. The advantages of plastic materials are the lower costs and weights than metallic ones; high anti-corrosion and antifouling resistances that allow the interaction with chemical aggressive fluids and good mechanical properties [10]; sustainability of manufacturing process; and the possibility of different fields of applications, such as heat recovery systems, desiccant cooling systems, electronic devices cooling, water desalination systems, and cooling evaporators [11]. Nevertheless, the polymers are characterized by low atomic density and low thermal conductivity ( $0.1 \div 0.3 \text{ W/m}\cdot\text{K}$ ); for this reason, their employments need geometric and thermodynamic optimization. Ceglia et al. [12] considered the employment of plastic material in shell and tube heat exchangers as a replacement of traditional metals one to overcome the fouling issue caused by aggressive geothermal fluid in a cogeneration system. The results showed the reduction of HEX purchase cost up to 73% by replacing titanium with high density polymers [13], and the maximum excess of heat exchange surface area was equal to 47%. The plastic HEX models optimization, aimed to match the economic advantages and the improving of heat transfer, represents a pivotal strategy to push toward the increase of geothermal source exploitation.

In this context, the thermoeconomic optimization by using exergy analysis is considered a good approach to evaluate the economic and thermodynamic advantages of a thermal system by combining the quality and the quantity of energy with its economic value. This approach is so called exergoeconomic analysis. Thus, the exergoeconomic

analysis of geothermal-based systems is spreading, demonstrating that it is useful for the identification of the thermodynamic inefficiencies in such systems. Luo et al. [14] have carried out an exergy analysis on an integrated cascade utilization system of geothermal water to identify the optimal temperature scheme. Arslan et al. [15] have used the exergoeconomic analysis to investigate a heating network for an integrated geothermal system in Turkey. To define the most performed solution for different pipelines dimension, the variation of total cost based on diameter of the pipes has been analyzed. The outcomes show that the change of the outlet temperature of geothermal fluid has a negligible effect on the optimum point. Different researchers have paid attention on exergoeconomic analysis of heat exchangers in geothermal applications to minimize the capital cost and investment cost of components by using multiple algorithms and methodologies. Jamil et al. [16] have defined an exergoeconomic optimization by considering design and operating parameters and also fiscal parameters for a shell and tube heat exchanger. The results show that the increase of mass flow rate and the baffles increased the operating cost because of an exponential growth in the pressure drops. Finally, the optimization reduced the heat transfer area by 26.4%, capital cost by 20%, and operational cost by 50%. Hajabdollahi et al. [17] have presented a study of optimization for gasket-plate and shell and tube heat exchangers. The aim of study is the minimization of the capital and operating costs by using decision variables. The results in the case of gasket-plate show an improvement of 13% in the total cost compared with shell and tube heat exchangers with the same operating conditions. In addition, the total cost in plate configuration decreases by increase of plate number. Instead, for shell and tube heat exchangers, the operating cost increases by the growth of both cold and hot side mass flow rates due to the increase of Reynolds number and consequently pressure drops. In Reference [18], an energetic and exergetic analysis on plate heat exchanger, dedicated to the heating network, based on geothermal energy has been defined. The results have showed a correlation between exergy loss rate (total or internal) and capital cost for the system. Furthermore, a correlation exists between thermodynamic (exergy-based) and economic characteristics of the overall system and its devices. Hajabdollahi et al. [19] have also performed the optimization of other types of heat exchangers including shell and tube heat exchanger, plate fin and fin tube [20], and compact heat exchanger [21].

The previous literature review stated the usefulness of exergoeconomic approach in the analysis of heat exchangers; however, the majority of these studies refer to:

- applications different from geothermal direct uses;
- metallic heat exchangers; and
- analysis in which the heat exchanger is considered as a “black box” by not considering the thermodynamic model of the component.

In this work, all the previous issues are overcome by defining the geometrical and thermodynamic model of a polymeric plate heat exchanger (PPHEX) for direct use of low-medium temperature geothermal source, to meet the space heating demand of a single building. Such an application is suitable for sites that show a geothermal interest with geothermal fluids availability in the range of about 90–120 °C. These areas cover different zones of the world; thus, in the following, Table 1, some of low-medium enthalpy geothermal site are reported. The maximum limit of the temperature geothermal fluid variation range and the corresponding references are listed, too.

Thus, the PPHEX model implemented in the MATLAB environment returns the heat exchange area, plate width, and total pressure drops of the PPHEX for a fixed heat power under various design/operating conditions (number of plates/channels and geothermal fluid inlet temperature). The results of dynamic simulation have been used as input to the exergoeconomic optimization that has the goal to minimize the exergoeconomic costs related to the thermal energy supplied to the building.

Moreover, usually, in geothermal applications, the use of shell and tube HEXs is preferred because of its faster cleaning processes by chemical or mechanical mechanisms. Nevertheless, in this application, the use of a plate heat exchanger is proposed; indeed,

the possibility to employ the polymeric material allows for investigation of various heat exchanger configurations because the plastic heat exchanger does not require cleaning during life cycle.

The study is structured as follows: In Section 2, the polymeric heat exchanger model, the exergoeconomic analysis of the numerical algorithm, and the considered case study are introduced. Finally, Section 3 reports the results and discussion, as well as the future improvement, of this work.

**Table 1.** Maximum limit of geothermal fluid temperature variation range in areas with geothermal interest.

Area	Maximum Limit of Geothermal Fluid Temperature Variation Range (°C)	References
Greece (Aristino-Alexandroupolis)	99	[22]
Thailand	100	[23]
Mexico	100	[23]
Island	110	[23]
Bulgaria	100	[23]
Hungary	108	[23]
Romania	89	[23]
Germany (north-east)	120	[24]
Turkie	240	[25]
Italy (Ferrara)	100	[23]
Italy (Phlegrean Fields)	240	[26]

## 2. Methods and Materials

In this section, the description of PPHEX modeling process is proposed, and the exergoeconomic optimization is introduced. First of all, the mathematical models are defined (see Section 2.1), and then the method used to perform the exergoeconomic analysis is presented (see Section 2.2). Then, the numerical algorithm implemented in the MATLAB environment to obtain the inputs to exergoeconomic analysis, starting from mathematical models' analysis as described (see Section 2.3). Finally, the methods described in the previous sections have been applied to a case study that is presented in Section 2.4, in which the exergoeconomic analysis introduced in Section 2.2 is detailed for the considered case study.

### 2.1. Mathematical Models

The mathematical modeling process is distinguished in the geometrical model (see subsection Section 2.1.2), heat exchange model and calculation (see Section 2.1.2), and pressure drops evaluation (see Section 2.1.3). The defined model will return the heat exchange area, plate width, number of plates, and total pressure drops of the PPHEX for a fixed heat power.

#### 2.1.1. Geometrical Model

The plate heat exchanger consists of a series of plates with corrugated flat flow passages. The hot and cold fluids flow counter-flow in alternate passages are shown Figure 1b. The geometric parameters able to define the plate heat exchanger are shown in Figure 1a,b: plate height (H), plate width (L), chevron angle ( $\beta$ ), number of channels for each flow ( $N_c$ ), wavelength of a sinusoidal surface corrugation or corrugation pitch ( $\lambda$ ), plate thickness ( $\delta$ ), and plate spacing (b).

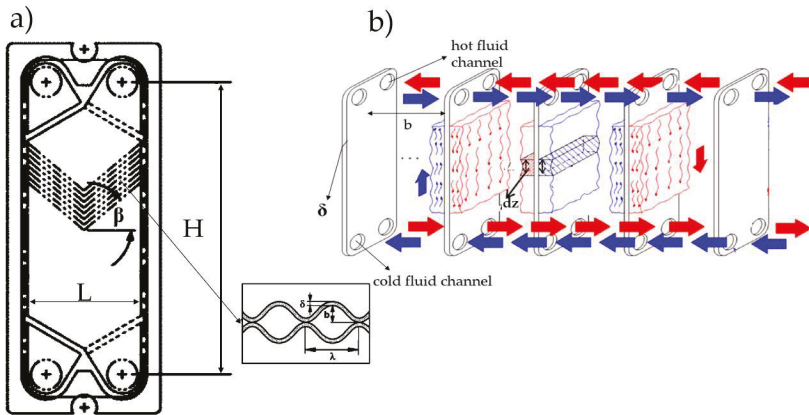


Figure 1. Geometry (a) and heat transfer process (b) of the plate heat exchanger.

In addition, hydraulic diameter ( $D$ ), corrugation parameter ( $\gamma$ ), number of plate ( $N_p$ ), enlargement factor ( $\varphi$ ), and mass flux are defined in Table 2, where  $\dot{m}$  is the mass flow rate.

Table 2. Plate heat exchanger parameters.

Parameters	Formulation
hydraulic diameter	$D = 2 \cdot b / \varphi$
corrugation parameter	$D = \pi \cdot b / \lambda$
number of plates	$N_p = 2 \cdot N_c - 1$
enlargement factor	$\varphi = (1 + \sqrt{(1 + \gamma^2)} + 4\sqrt{1 + \frac{\gamma^2}{2}})$
mass flux	$G = \dot{m} / (L \cdot N_c \cdot b)$

### 2.1.2. Heat Transfer Model and Calculation

The PPHEX model is developed by imposing the desired thermal power ( $\dot{Q}_{PPHEX}$ ) resulting from the heat transfer between the hot geothermal fluid and the cold water circulated in the building hydronic system. Equation (1) allows the calculation of thermal power  $\dot{Q}_{PPHEX}$ , and the PPHEX height is here discretized in elementary section ( $i$ ), with infinitesimal height ( $dZ$ ) as graphed in Figure 2. At the inlet section, which corresponds to  $i = 0$ , the geothermal hot fluid enters into heat exchanger, and the cold fluid exits. In this section, the outlet temperature of cold fluid is  $T_{out,c}$ , and the hot temperature of inlet fluid is  $T_{in,h}$ . The elementary thermal power in the infinitesimal height  $dZ$  ( $\delta\dot{Q}_{PPHEX,dZ(i)}$ ) is calculated according to Equation (2), by considering an adiabatic in which there is no exchange for heat between PPHEX and surroundings. In each elementary section ( $i$ ), the overall heat transfer coefficient  $U$  is evaluated by proper heat transfer correlations, as reported in the following discussion. After the calculation of  $\delta\dot{Q}_{PPHEX,dZ(i)}$ , the local temperatures associated to the elementary  $dZ$  ( $i + 1$ ) are evaluated by Equations (3) and (4) for geothermal hot fluid and cold fluid, respectively. The temperatures are corrected by also taking into account the pressure drops (see Section 2.1.3).

$$\dot{Q}_{PPHEX} = \int_0^H (U \cdot \Delta T \cdot L \cdot \varphi \cdot (2 \cdot N_c - 1)) dZ \tag{1}$$

$$\delta\dot{Q}_{PPHEX,dZ(i)} = dA \cdot U \cdot (T_{h,dZ(i)} - T_{c,dZ(i)}) \tag{2}$$

$$T_h(i + 1) = T_h(i) - \frac{\delta\dot{Q}_{PPHEX,dZ(i)}}{\dot{m}_h \cdot c_h} \tag{3}$$

$$T_c(i+1) = T_c(i) + \frac{\delta \dot{Q}_{PPHEX,dZ(i)}}{\dot{m}_c \cdot c_c} \quad (4)$$

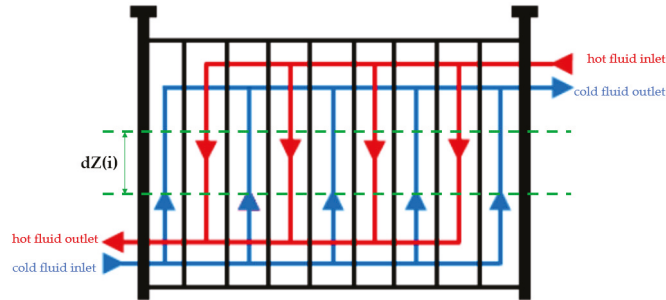


Figure 2. Plate heat exchanger height discretization.

The overall heat transfer coefficient  $U$  is calculated in Equation (5), by considering the convective thermal resistance of hot fluid ( $\alpha_h$ ) and cold fluid ( $\alpha_c$ ), the conductive thermal resistance of polymeric material ( $k_w$ ), and fouling resistance for both fluids ( $R_{f,c}$ ,  $R_{f,h}$ ) [27].

$$U = \frac{1}{\frac{1}{\alpha_h} + \frac{1}{\alpha_c} + \frac{\delta}{k_w} + R_{f,c} + R_{f,h}} \quad (5)$$

The heat transfer coefficients are both calculated by Equation (6), where the Nusselt number ( $Nu$ ) is obtained by Martin equation for liquid fluids, as reported in Equation (7) [28], where  $k$  is the fluid conductivity,  $f$  is the Fanning friction factor (Equation (8)), and  $f_0$  and  $f_1$  are calculated from Reynolds number.

$$\alpha = Nu \cdot \frac{k}{D} \quad (6)$$

$$Nu = 0.205 \cdot Pr^{\frac{1}{3}} \cdot \left( \frac{\mu_f}{\mu_w} \right)^{1/6} \cdot \left( f \cdot Re^2 \cdot \sin(2\beta) \right)^{0.314} \quad (7)$$

$$\frac{1}{\sqrt{f}} = \frac{\cos(\beta)}{\left( 0.045 \cdot \tan(\beta) + 0.09 \cdot \cos(\beta) + \frac{f_0}{\cos(\beta)} \right)^{0.5}} + \frac{1 - \cos(\beta)}{\sqrt{3.8 \cdot f_1}} \quad (8)$$

### 2.1.3. Pressure Drops Calculation

The local pressure is evaluated by integration of the pressure drop relations. Then, pressure drops are used to correct the thermodynamic properties in the energy balance (Equations (3) and (4)) by using the REFPROP library. The overall pressure drops, for both fluids, are evaluated by considering three contributions, as expressed in Equation (9) [29]. The first term ( $dp_{fric}$ ) considers the loss caused by the friction contribution in the plates, the second term ( $dp_{mon}$ ) is the momentum effect, and the last term ( $dp_{elev}$ ) considers the elevation change.

$$\frac{dp}{dZ} = \frac{dp_{fric}}{dZ} + \frac{dp_{mon}}{dZ} + \frac{dp_{elev}}{dZ} \quad (9)$$

The friction factor term can be determined by using Equation (10) [30], where  $G$  is the mass flux, and  $\rho_m$  is the density average value.

$$dp_{fric} = \frac{4 \cdot f \cdot dZ \cdot G^2}{2 \cdot D \cdot \rho_m} \quad (10)$$

The momentum pressure drops can be evaluated by using Equation (11), where  $\rho_{out}$  and  $\rho_{in}$  represent the density of fluid at outlet and inlet condition of each section area, respectively.

$$dp_{mon} = G^2 \cdot \left( \frac{1}{\rho_{out}} - \frac{1}{\rho_{in}} \right). \quad (11)$$

In this study, this contribution can be neglected because both fluids are in liquid phase during the process. The elevation term (Equation (12)) determines a positive effect on the geothermal fluid that flows downward; on the contrary, it determines a negative effect on the cold water that flows upward. In Equation (12),  $g$  is the gravitational acceleration ( $\text{m}\cdot\text{s}^{-2}$ ).

$$dp_{elev} = \pm \rho_m \cdot g \cdot dZ. \quad (12)$$

In addition, the pressure drops due to the inlet manifold is evaluated by considering Equation (13), where  $n_p$  is the number of passes in the plate heat exchanger, and  $G_{man}$  is the mass flux in the manifold.

$$\Delta p_{man} = \frac{1.5 \cdot n_p \cdot G_{man}^2}{2\rho_{in}}. \quad (13)$$

## 2.2. Exergoeconomic Analysis

The current study proposes the exergoeconomic analysis of a geothermal heating direct system for a single building by assessing the effect of two variables: the number of plates/channels for PPHEX and the inlet temperature of the geothermal fluid. The first one is an endogenous variable whose value is determined through the heat exchanger model. The inlet geothermal fluid temperature is an exogenous variable determined outside the model, and it depends on the specific application (low-medium temperature geothermal fluid). These variables are selected because they substantially influence the results of exergoeconomic analysis. This approach that analyzes the exergoeconomic optimization results referred to an energy system by varying an exogenous and an endogenous variable is widely used in scientific literature [31–33].

The exergoeconomic performance of the system has been evaluated for each combination of these parameters. The optimal operating conditions have been selected by means of an exergoeconomic optimization aimed to minimize the exergoeconomic costs associated the thermal energy supplied to the building, which represents the product of the exergoeconomic analysis. All the irreversibility of the process are calculated by using the exergy destruction rate of system ( $\dot{I}_{tot}$ ). According to the Gouy–Stodola theorem, it is be evaluated by multiplying the reference or “dead-state” temperature,  $T_0$ , by the entropy generation rate,  $\dot{S}_{gen,tot}$ , as reported in Equation (14) [34].

$$\dot{I}_{tot} = T_0 \cdot \dot{S}_{gen,tot} \quad (14)$$

The exergy destruction rate of system can be determined as the difference between the external exergy resources “required” to sustain the total process itself ( $\dot{F}_j$ ) and the exergy “product” term that constitutes the purpose of the process ( $\dot{P}$ ), as reported in Equation (15).

$$\dot{I}_{tot} = \sum_{j=1}^n \dot{F}_j - \dot{P}. \quad (15)$$

Thus, the exergoeconomic cost ( $C_{tot}$ ) to obtain the desired product ( $\dot{P}$ ) analysis is written for yearly exergetic cost (Equation (16)) by including the depreciated investment costs, expressed as the product between the purchased costs ( $Z_k$ ) and the Capital Recovery Factor (CRF) for each  $k$ -esimo component, and the operating costs, evaluated as a product between the exergetic stream ( $\dot{F}_j$ ), the related specific exergetic cost ( $c_{F,j}$ ), and the yearly

operating hours ( $\theta$ ). In Equation (16),  $nc$  is the total number of components, and the maintenance cost is neglected [31].

$$C_{tot} = \sum_{j=1}^n \dot{F}_j \cdot c_{F,j} \cdot \theta + CRF \sum_{k=1}^{nc} Z_k \quad (16)$$

CRF is defined as:

$$CRF = \frac{a(1+a)^m}{(1+a)^m - 1} \quad (17)$$

where  $a$  is the interest rate, and  $m$  is the service life of the system.

### 2.3. The Heat Exchanger Modeling and Exergoeconomic Analysis Algorithm

In this section, the numerical algorithm is defined, and the flow chart is represented in Figure 3. It is implemented in MATLAB [35] by means of a main code for exergoeconomic analysis and different functions to evaluate thermodynamic and geometrical properties by using the REFPROP software library [29]. The model returns the heat exchanger surface area ( $A_{PPHEX}$ ) needed to obtain the desired thermal power, ( $\delta\dot{Q}_{PPHEX,dZ(i)}$ ) and the calculation is carried out for each couple of endogenous and exogenous variables (the number of plates/channels for PPHEX and the hot geothermal fluid inlet temperature) in the corresponding range of variation of each variable.

The geometrical input data are width, thickness, plate spacing, chevron angle, wavelength, and others of PPHEX, while the thermodynamic input parameters are the inlet ( $T_{c,in}$ ) and outlet temperature of cold fluid ( $T_{c,out}$ ) and the hot fluid temperature variation ( $\Delta T_{h,in-out}$ ). Moreover, the conductivity of the polymer is imposed as input data.

At that first step of integration that corresponds to  $i = 1$ , the fixed parameters are assigned. The pressure drops, and the overall heat transfer coefficient  $U$  for both fluids in each  $dZ$  are calculated by using Equations (5)–(13). In this way, the elementary heat power  $\delta\dot{Q}_{PPHEX,dZ(i)}$  is achieved from Equation (2). By considering the hypothesis of an adiabatic heat exchanger through its surroundings, and by means of the Equations (3) and (4), the temperatures of both fluids in subsequent integration steps ( $i + 1$ ) are calculated. The integration stops when the desired heat power ( $\dot{Q}_{PPHEX,obj}$ ) is obtained. The output parameters are geometrical results about heat exchanger surface area ( $A_{PPHEX}$ ) and also the plate height ( $H$ ), the  $U$ , and global pressure drops. As said before, this calculation is conducted by varying  $T_{h,in}$  and  $N_c$ ; for this reason, for each output parameter, a matrix ( $\dot{X}(T_{h,in} \times N_c)$ ) is obtained. The first control is made on a limit for pressure drops in the plate, and, according to the PPHEX datasheet, this limit is fixed to 0.5 bar for each fluid flow. The heat exchanger height and area have been directly used in the exergoeconomic cost function, while the pressure drops and the temperature trend have been used as a filter to discard the impossible technical solutions. Once the unacceptable solutions are discarded, the exergoeconomic function is minimized to find the condition with minimum thermoeconomic impact for single building.

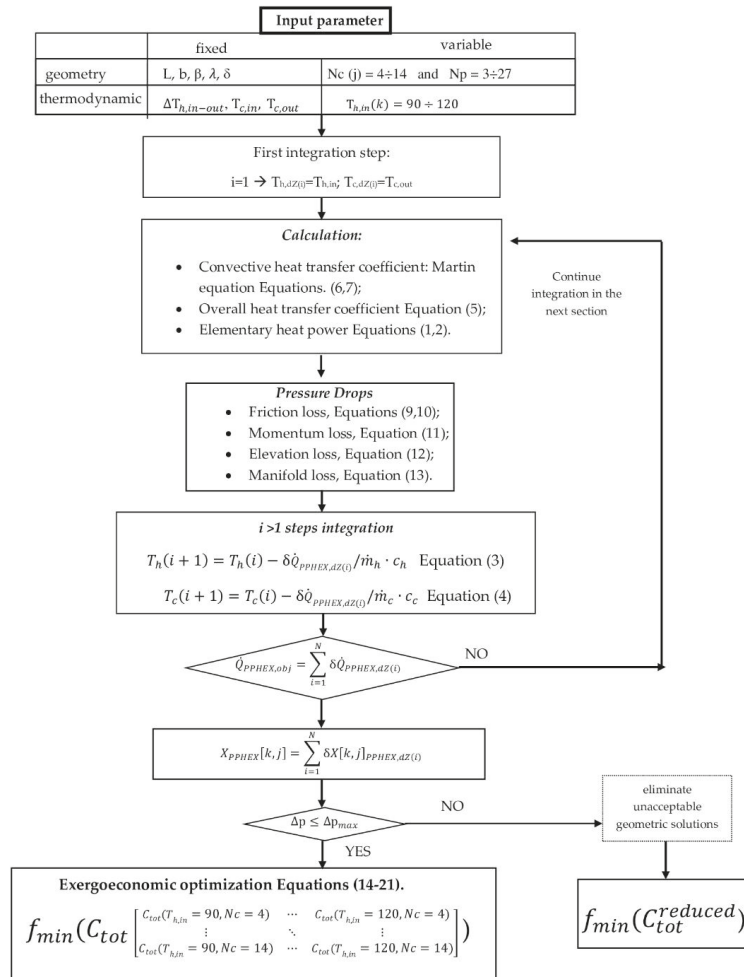


Figure 3. Algorithm flow chart.

#### 2.4. The Case Study

The methods described in the previous sections have been applied to a case study in Italy. More precisely, the Phlegrean Fields area (south of Italy) has been chosen for this application. It is an active volcano district of the Campania region characterized by high geothermal fluid temperature at shallow depth [26,36,37]. In particular, as it is possible to derive from previous analyses conducted in this area, a temperature of geothermal fluid in the range 90–120 °C has already been recorded at the depth of 86–101 m. Thus, the results of the exergoeconomic optimization are referred to this specific area, and they will be different if the same methodology is applied to a different zone with a potential interest from geothermal point of view (low-medium temperature geothermal fluid availability).

Thus, this case study takes into account the possibility to use a geothermal PPHEX of 24 kW<sub>th</sub> connected to the hydronic building heating system by means of a thermal grid. As reported in the Figure 4, the geothermal fluid is drawn from the ground by using the production well (1) and the first pump (P<sub>1</sub>), and, after, it enters in the control volume C.V.1. In C.V.1., the geothermal fluid heats the cold water, and, after, it is reinjected by using P<sub>2</sub> and injection well (2). The hot water exiting the PPHEX is sent to building circuit by means

of a circulating pump  $P_3$ . The fixed PPHEX parameters are reported in Table 3, according with datasheets [6,7,38]. The variable parameters are the inlet geothermal temperature and the number of channels for each flow (or plates).

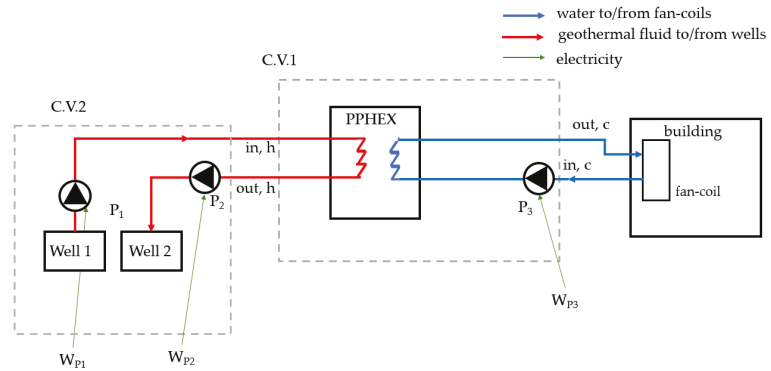


Figure 4. Geothermal heating direct process.

Table 3. Input Data.

Parameters	Symbol	Value
Inlet Temperature of geothermal hot fluid (°C)	$T_{h,in}$	90–120
Temperature difference of geothermal fluid (°C)	$\Delta T_{h,in-out}$	20
Inlet Temperature of cold water (°C)	$T_{c,in}$	45
Outlet Temperature of cold water (°C)	$T_{c,out}$	60
Thermal polymer conductivity ( $Wm^{-1} K^{-1}$ )	$k_w$	0.22
Plate spacing (mm)	$b$	2.2
Wavelength of a sinusoidal surface corrugation (mm)	$\lambda$	2
Plate thickness (mm)	$\delta$	0.4
Channels number for each flow (-)	$N_c$	4–14
Chevron angle	$\beta$	60°
Plate width (m)	$L$	0.077

The geothermal fluid is extracted from a shallow production well, indeed, according to data about geothermal fields of Phlegrean Fields area (South of Italy) [12,36,37], geothermal fluids in the temperature range of 90–120 °C at a depth varying from 86 m to 101 m. To perform the exergoeconomic analysis in the considered case study, Equations (16) and (17) have been detailed with reference to Figure 4. Referring to C.V.1, the exergy balance can be written as reported in Equation (18), where the term  $(\dot{m}_c \cdot (ex_{c,out} - ex_{c,in}))$  represents the exergy product ( $\dot{P}$ ) according to Equation (16). The exergy input ( $\dot{F}$ ) is the sum of exergy rate of geothermal fluid ( $\dot{m}_h \cdot (ex_{h,in} - ex_{h,out})$ ) and exergy electric input ( $\dot{W}_{P3}$ ). The first term can be evaluated by exergy balance on C.V.2 reported in Equation (19), where the exergy input is equal to exergy electric input ( $\dot{W}_{P1} + \dot{W}_{P2}$ ). Thus, the total exergy balance can be expressed according to Equation (20).

$$\dot{m}_h \cdot ex_{h,in} + \dot{m}_c \cdot ex_{c,in} + \dot{W}_{P3} = \dot{m}_h \cdot ex_{h,out} + \dot{m}_c \cdot ex_{c,out} + \dot{I}_{V.C.1} \quad (18)$$

$$\dot{m}_h \cdot ex_{h,out} + \dot{W}_{P1} + \dot{W}_{P2} = \dot{m}_h \cdot ex_{h,in} + \dot{I}_{V.C.1} \quad (19)$$

$$\dot{m}_c \cdot (ex_{c,out} - ex_{c,in}) = \dot{W}_{P3} + \dot{W}_{P1} + \dot{W}_{P2} - \dot{I}_{tot} \quad (20)$$

Once the exergy balance is defined, the exergoeconomic balance can be defined by using the exergoeconomic cost and the additional purchase costs (according to Equation (16)), as reported in the Equation (21).

$$C_{tot} = c_{F,el} \cdot \theta \cdot (\dot{W}_{P3} + \dot{W}_{P1} + \dot{W}_{P2}) + CRF \cdot (Z_{P1} + Z_{P2} + Z_{P3} + Z_{well,1} + Z_{well,2} + Z_{PPHEX}) \quad (21)$$

where  $C_{tot}$  is the exergoeconomic cost associated to the product  $\dot{P}$ ,  $c_{F,el}$  is the specific exergoeconomic cost of electric exergy input,  $Z_{P1}$ ,  $Z_{P2}$ ,  $Z_{P3}$  are the investment costs of pumps,  $Z_{well,1}$ ,  $Z_{well,2}$  are the wells costs, and  $Z_{PPHEX}$  is the PPHEX cost. In Table 4, the investment cost functions are listed, where  $H_{well}$  is the deep length of well ranging from 86 to 101 m in Phlegrean Fields area,  $d_{well}$  is the well diameter, and  $c_{PPHEX}$  and  $A_{PPHEX}$  are the specific cost and heat exchange surface area of PPHEX, respectively.

**Table 4.** Cost function.

Component	Investment Cost (€)	Reference
Pump	$Z_P = 107.26 \cdot \dot{W}_P^{0.7176}$	[39]
Well	$Z_{well} = 23.578 \cdot e^{0.0063 \cdot d_{well}} \cdot H_{well}$	[40]
PPHEX	$Z_{PPHEX} = c_{PPHEX} \cdot A_{PPHEX}$	[6]

The  $Z_{PPHEX}$  is obtained by market investigation, and it results in approximatively equal to  $1230 \text{ €} \cdot \text{m}^{-2}$ . However,  $\theta$  is equal to 1088 h/y, by taking into account the typical Mediterranean hot climate referred to in the South of Italy. The  $c_{el}$  is fixed equal to  $0.25 \text{ c€} \cdot \text{kWh}_{el}^{-1}$  VAT included [41].

### 3. Results and Discussion

In this section, the results of analysis are presented. In Section 3.1, the main outcomes of the mathematical modeling of heat exchanger are discussed. In Section 3.2, the results of exergoeconomic analysis are presented by including the sensitivity analysis about thermodynamic and geometrical parameters.

#### 3.1. Geometrical and Thermodynamic Results

The geometrical characteristics of PPHEX highly affect the pressure drops results. The cold fluid presents higher pressure drops due to greater mass flow rate ( $0.382 \text{ kg} \cdot \text{s}^{-1}$ ) than hot one ( $0.287 \text{ kg} \cdot \text{s}^{-1}$ ). The mass flow rate is calculated by energy balance on PPHEX, according to Equations (3) and (4). The best configuration in terms of pressure drops is verified when the geothermal fluid inlet temperature is equal to  $90 \text{ °C}$ , and the number of channels for each fluid flow is equal to 4. The results obtained by mathematical model are filtered by assuming a maximum acceptable value for  $\Delta p$  equal to 0.5 bar. In Figure 5, the pressure drops of hot and cold fluid are reported by varying  $T_{h,in}$  and Nc. If the inlet temperature of geothermal fluid is equal to its maximum ( $120 \text{ °C}$ ), the lowest acceptable Nc is 5 for hot fluid, and 7 for cold fluid. Even if  $T_{h,in}$  is equal to its lowest value ( $90 \text{ °C}$ ), the acceptable Nc increases up to 6 for hot fluid, and 9 for cold fluid. Thus, pressure drops of the cold fluid ( $\Delta p_c$ ) represent the discriminating factor to filter the results since  $\Delta p_c$  is the highest one. Thus, the lowest acceptable Nc is equal to 7.

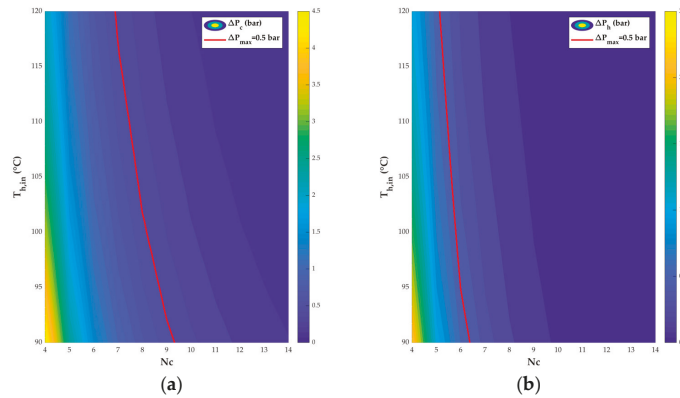


Figure 5. Pressure drops in cold (a) and hot fluid (b).

Following the methodology defined in Equations (3) and (4), the trends of temperatures in the PPHEX are represented for hot and cold fluid in 3D, in Figures 6 and 7, respectively, in the case in which the number of channels are equal to 12, and the  $T_{h,in}$  is equal to 115 °C. As a matter of fact, the heat transfer process determines the heating of cold water supplied to the building by the cooling of geothermal fluid. However, the legislation concerning the geothermal uses recommends a reinjection temperature of geothermal fluid not lower than 70 °C [42]. Thus, in order to ensure the recommended reinjection temperature, the minimum considered geothermal fluid inlet temperature is 95 °C. Figures 6 and 7 also show the flows direction. More precisely, in Figure 6, the geothermal hot fluid enters from the PPHEX in the upper side, and its temperature decreases to 20 °C, as far as the exit section ( $H = 0$  mm). In Figure 7, the cold fluid enters from the PPHEX down side, and its temperature increases from 45 to 60 °C (15 °C) as far as the exit section that corresponds to geothermal fluid entry. The temperature difference of both fluids along the height of the heat exchanger is the same because they are assimilated to liquid water in the model by using the REFPROP library. This fact is justified by the same color trend of both 3D Figures 6 and 7, even if the temperature variation range represented by the colors bars is significantly different (115–95 °C for hot fluid (Figure 6) and 60–45 °C for cooling fluid (Figure 7)).

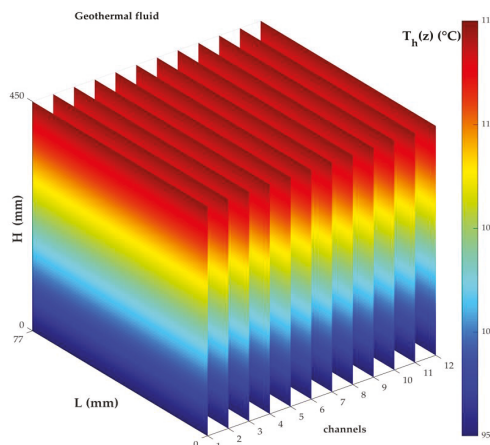
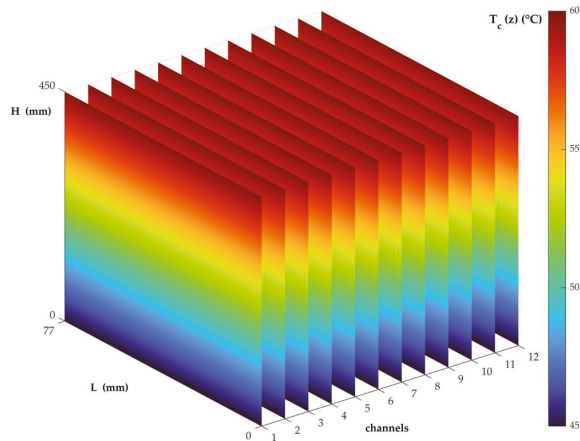
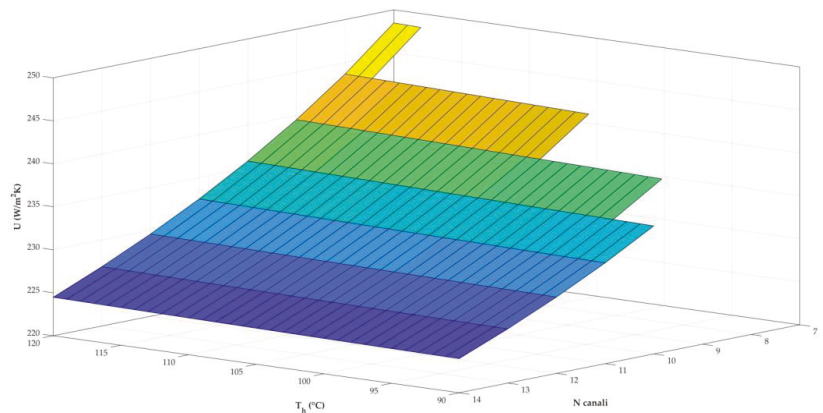


Figure 6. Temperature trend of hot geothermal fluid for  $N_c = 12$  and  $T_{h,in} = 115$  °C.



**Figure 7.** Temperature trend of cold water for  $N_c = 12$  and  $T_{h,in} = 115$  °C.

According to the methodology defined in the Equations (5)–(7), the calculation of overall heat transfer coefficient ( $U$ ) has been obtained for each combination of the two variables ( $T_{h,in}$  and  $N_c$ ) filtered by considering the restrictions on pressure drops (0.5 bar). In Figure 8, the surface plot of  $U$  is showed. The blue bar represents the condition with the lowest  $U$  value ( $225\text{--}230 \text{ W}\cdot\text{m}^{-2}\cdot\text{K}^{-1}$ ) that is verified when  $N_c$  is higher than 9.  $U$  presents the greatest value ( $248 \text{ W}\cdot\text{m}^{-2}\cdot\text{K}^{-1}$ ) when  $N_c$  is equal to 7, and  $T_{h,in}$  is equal to  $118\text{--}120$  °C. The  $T_{h,in}$  slightly influences the overall heat transfer coefficient: for a fixed value of  $N_c$ , and by varying  $T_{h,in}$  from 120 to 90 °C, the  $U$  value shows an increase lower than 1%. Differently, by fixing the temperature, and by considering a number of channels variation from 4 to 14, the  $U$  value increases up to 10%. This can be explained by taking into account the fact that the heat transfer convective coefficient ( $\alpha$ ) is strongly influenced by mass flux ( $G$ ), which assumes higher values when  $N_c$  decreases due to the reduction of the crossing flow section. However, the variation range of  $U$  is very low ( $225\text{--}248 \text{ W}\cdot\text{m}^{-2}\cdot\text{K}^{-1}$ ) because both fluids are in liquid phase, and the plate heat exchanger presents low room for improvement.



**Figure 8.** Overall heat transfer coefficient.

For filtered solutions, the heat exchange surface area of PPEHX is reported in Table 5. It presents a highest value equal to 3.91 m<sup>2</sup> when Nc = 14, and  $T_{h,in} = 90$  °C, while the lowest value is equal to 1.68 m<sup>2</sup> when Nc = 7, and  $T_{h,in} = 120$  °C. The maximum percentage variation of  $A_{PPEHX}$  is equal to 57%. So, the optimum solution, in terms of lower footprint, corresponds with best heat transfer performance.

**Table 5.** Heat exchange surface area for matching Nc- $T_{h,in}$  solution.

Polymer Plate Heat Exchange Surface Area $A_{PPEHX}$ (m <sup>2</sup> )								
T (°C)	Nc 7	8	9	10	11	12	13	14
90	-	-	-	3.73	3.78	3.83	3.87	3.91
91	-	-	-	3.60	3.66	3.69	3.74	3.78
92	-	-	-	3.47	3.53	3.58	3.62	3.65
93	-	-	3.31	3.36	3.41	3.45	3.50	3.52
94	-	-	3.21	3.25	3.31	3.33	3.38	3.41
95	-	-	3.11	3.16	3.21	3.24	3.28	3.31
96	-	-	3.01	3.07	3.10	3.15	3.19	3.20
97	-	-	2.93	2.98	3.02	3.04	3.09	3.13
98	-	-	2.84	2.88	2.92	2.98	2.99	3.05
99	-	-	2.76	2.81	2.84	2.89	2.92	2.94
100	-	-	2.70	2.74	2.78	2.80	2.85	2.86
101	-	-	2.63	2.66	2.70	2.73	2.77	2.78
102	-	2.51	2.55	2.59	2.63	2.66	2.70	2.73
103	-	2.45	2.50	2.53	2.57	2.60	2.63	2.65
104	-	2.39	2.43	2.48	2.51	2.53	2.58	2.60
105	-	2.33	2.38	2.40	2.45	2.48	2.50	2.52
106	-	2.28	2.31	2.35	2.39	2.42	2.46	2.47
107	-	2.23	2.27	2.31	2.33	2.37	2.38	2.42
108	-	2.17	2.22	2.25	2.29	2.30	2.33	2.36
109	-	2.13	2.17	2.20	2.23	2.26	2.29	2.31
110	-	2.09	2.12	2.16	2.19	2.21	2.24	2.26
111	-	2.04	2.08	2.11	2.14	2.17	2.19	2.23
112	-	2.00	2.03	2.07	2.10	2.13	2.14	2.18
113	-	1.96	2.00	2.03	2.06	2.08	2.12	2.13
114	-	1.93	1.95	2.00	2.02	2.04	2.07	2.10
115	-	1.88	1.92	1.96	1.98	2.01	2.02	2.05
116	-	1.85	1.89	1.92	1.94	1.97	1.99	2.02
117	-	1.81	1.85	1.89	1.90	1.92	1.95	1.97
118	1.74	1.78	1.82	1.85	1.88	1.90	1.92	1.94
119	1.72	1.75	1.79	1.81	1.84	1.86	1.87	1.92
120	1.68	1.72	1.75	1.77	1.80	1.83	1.85	1.86

### 3.2. Exergoeconomic Results

As mentioned above, the optimization of the two investigated parameters, the temperature of the geothermal source and number of channels, is carried out in order to find the configuration that guarantees the lower exergoeconomic cost of product,  $C_{tot}$ . First of all, the investment cost of PPEHX is represented in Figure 9. The configuration that leads to the lowest investment cost corresponds to the condition with the smallest heat exchange surface area (Nc = 7 and  $T_{h,in} = 120$  °C), in which  $Z_{PPEHX}$  amounts to 2069 €. The investment cost increase occurs when the temperature availability of geothermal fluid decreases, while it is not very influenced by Nc variation. In fact, the increasing temperature of 1 K of geothermal fluid corresponds to an investment cost average rise of 2.5% when Nc is fixed to 14. However, by considering temperatures lower than 100 °C, the investment cost is higher than 3000 €. Moreover, if the Nc is decreases up to 10, the investment cost drops below 2000 €, when the geothermal fluid temperatures are to 120 °C.

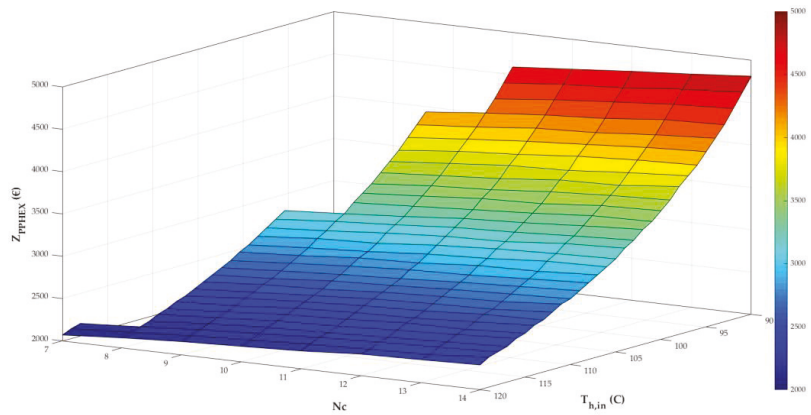


**Figure 9.** Heat exchanger investment cost.

The variation of the main exergoeconomic costs as function of  $N_c$  and  $T_{h,in}$  is illustrated in Figure 10. The exergoeconomic cost of electricity,  $C_{el}$ , calculated in first term of Equation (21), is caused by electricity consumption of pumps during heating period. It dramatically increases as the geothermal fluid temperature grows because the pressure drops, and the deep well rises, while it presents a low variation with  $N_c$ , as depicted in Figure 10a. For  $N_c$  fixed to its maximum value (14), the yearly exergetic cost of electricity is equal to  $213 \text{ €}\cdot\text{y}^{-1}$  if  $T_{h,in}$  is  $90 \text{ °C}$ , and  $245 \text{ €/y}$  if  $T_{h,in}$  amounts to  $120 \text{ °C}$ , presenting a percentage variation of 13%. By fixing  $T_{h,in}$  to  $120 \text{ °C}$ , the electricity exergoeconomic cost is equal to  $255 \text{ €}\cdot\text{y}^{-1}$  if  $N_c$  decreases to 7, showing a percentage variation of 4%. Figure 10b illustrates the yearly amortized cost of PPHEX. It reaches the highest values when the geothermal fluid temperature is lower than  $96 \text{ °C}$ ; thus, in this condition, the exergoeconomic PPHEX cost is greater than  $350 \text{ €}\cdot\text{y}^{-1}$ .  $N_c$  determines a not very relevant influence on the cost of PPHEX, too. Indeed, in each temperature condition, the exergoeconomic cost increases of 10% for  $N_c$  ranging from 7 to 14. The lowest values ( $\leq 250 \text{ €/y}$ ) can be obtained when  $T_{h,in}$  varies from 110 to  $120 \text{ °C}$ . Figure 10c shows the amortized cost of three pumps of system. According to electricity cost, the pumps investment costs need higher power capacity if the temperature increases determining higher purchase costs. Despite this, a higher influence in pumps investment cost is determined by  $N_c$  variation. Overall, this cost slightly influences the system because its maximum is  $12.6 \text{ €}\cdot\text{y}^{-1}$ , and its minimum is  $10.8 \text{ €}\cdot\text{y}^{-1}$ . Figure 10d shows the most expensive exergoeconomic parameter of geothermal plant: the well cost. As expected, this cost increases with depth and temperature increase, and it is not influenced by heat exchanger geometry. The highest value corresponds to  $455 \text{ €}\cdot\text{y}^{-1}$ , and the lowest one is  $390 \text{ €}\cdot\text{y}^{-1}$ .

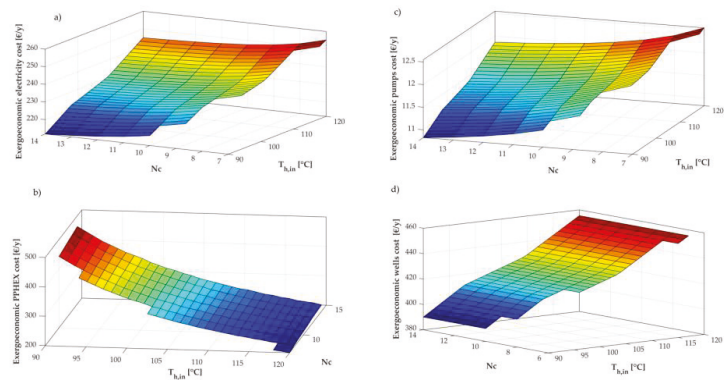


**Figure 10.** Effect of  $N_c$  and  $T_{h,in}$  on the exergoeconomic costs of electricity (a), on PPHEX purchase cost (b), on pumps purchase cost (c), and on well investment cost (d).

In Figure 11, the optimization of global exergoeconomic analysis is represented. The convenience of investment is presented by blue and light-blue solution that correspond to temperature of geothermal fluid higher than  $105\text{ }^{\circ}\text{C}$ . In these conditions, for each number of channels,  $C_{tot}$  is lower than  $950\text{ }\text{€}\cdot\text{y}^{-1}$ . Both  $T_{h,in}$  and  $N_c$  affect the total exergoeconomic costs of the product, but, for a fixed temperature, and for a changing of  $N_c$  from 7 to 14, the variation of  $C_{tot}$  is equal to 1.6%. However, by varying  $T_{h,in}$  from  $90$  to  $120\text{ }^{\circ}\text{C}$  for a fixed  $N_c$ , the variation of  $C_{tot}$  corresponds to 13%. Despite the well cost and electricity cost increase with temperature rise, the product exergoeconomic cost presents an opposite behavior with temperature. The product yearly cost is highly influenced by the exergoeconomic investment cost of PPHEX. This result is due the fact that, even if the drilling costs are usually the large portion of costs in a geothermal plant, in Phlegrean Fields, the increase of well depth to go from a geothermal fluid temperature of  $90\text{ }^{\circ}\text{C}$  to  $120\text{ }^{\circ}\text{C}$  is equal to only 15 m (from 86 m to 101 m in depth). Thus, these outcomes are strongly related to the area in which the exergoeconomic analysis is conducted. When the number of channels for each flow is equal to 10, and the temperature increases from  $90$  to  $120\text{ }^{\circ}\text{C}$ , the percentage variations of exergoeconomic yearly cost are equal to 13.8%, 16.8%, and  $-52.5\%$  for electricity pumping, well, and PPHEX investment, respectively. Finally, the product exergoeconomic cost shows a decrease of 12.8%, varying  $T_{h,in}$  from  $90$  to  $120\text{ }^{\circ}\text{C}$ . The optimum solution equal to  $922\text{ }\text{€}\cdot\text{y}^{-1}$  is found for  $N_c$  equal to 8 that corresponds to 15 plates, and  $117\text{ }^{\circ}\text{C}$  of geothermal hot inlet temperature.

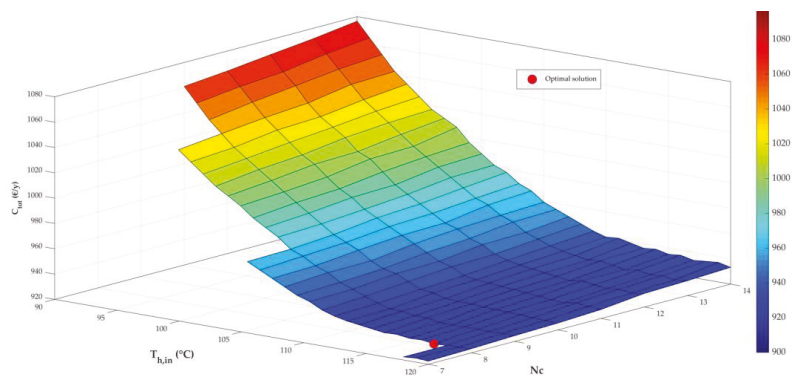


**Figure 11.** Total exergoeconomic cost minimization.

#### 4. Conclusions

This research paper presented a model and analysis of a heating system for single building operating in geothermal field from the thermodynamic and thermoeconomic viewpoints. An advanced mathematical model was used to design a plastic heat exchanger to overcome the fouling problems that affect the heat exchangers of a geothermal plant. The results of model were used as input for an exergoeconomic optimization to evaluate the thermoeconomic performance of system by varying thermodynamic and geometric parameters. Then, the general methodology was applied to a case study in which the modeled polymeric plate heat exchanger interacting with the geothermal fluid was used, to meet the space heating need of a single building located in the active volcano district of the Campania region. The results are summarized in the following:

- the overall heat exchanger coefficient presents the greatest values for high temperature of geothermal fluid (105–120 °C) and for a number of channels for each flow variable from 7 to 12;
- the required heat exchanger surface areas are low (and, consequently, the HEX purchase cost) for overall heat exchanger coefficient equal about to 240–250 W/K·m<sup>2</sup>;
- the investment cost of heat exchanger decreases when the inlet geothermal temperature increases; on the contrary, the well investment and the electricity cost increases with temperature;
- the variation of well and electricity exergoeconomic costs is lower than heat exchanger one; thus, the product exergoeconomic cost shows a trend similar to heat exchanger cost; and
- the minimum value for product is equal to 922 €·y<sup>-1</sup>, and it occurs when the geothermal hot inlet temperature is equal to 117 °C, and  $N_c$  is equal to 8, that corresponds to 15 plates.

As a general conclusion, the development of this research allows the thermodynamic improvements and potential cost reductions in a geothermal plant for direct air conditioning applications. In future works, the investigation of multi-users system will be defined by using higher variable parameters in the exergoeconomic analysis, and the validation of these results could be conducted in the framework of GEOGRID project.

**Author Contributions:** Conceptualization, A.C., F.C., E.M., M.S. and L.V.; methodology, A.C., F.C., E.M., M.S. and L.V.; software, A.C., F.C., E.M., M.S. and L.V.; validation, A.C., F.C., E.M., M.S. and L.V.; formal analysis, A.C., F.C., E.M., M.S. and L.V.; investigation, A.C., F.C., E.M., M.S. and L.V.; resources, A.C., F.C., E.M., M.S. and L.V.; data curation, A.C., F.C., E.M., M.S. and L.V.; writing—original draft preparation, A.C., F.C., E.M., M.S. and L.V.; writing—review and editing, A.C., F.C., E.M., M.S. and L.V.; visualization, A.C., F.C., E.M., M.S. and L.V.; supervision, A.C., F.C., E.M., M.S. and L.V. All authors have read and agreed to the published version of the manuscript.

**Funding:** This research received no external funding.

**Institutional Review Board Statement:** Not applicable.

**Informed Consent Statement:** Not applicable.

**Data Availability Statement:** Not applicable.

**Acknowledgments:** The authors gratefully acknowledge the partial financial support of GEOGRID project (Tecnologie e sistemi innovativi per l'utilizzo sostenibile dell'energia geotermica) CUP B43D18000230007, POR CAMPANIA FESR 2014/2020.

**Conflicts of Interest:** The authors declare no conflict of interest.

## Abbreviation

### Nomenclature

a	interest rate ( $y^{-1}$ )
A	heat exchanger surface area ( $m^2$ )
b	plate spacing (mm)
$C_{tot}$	exergoeconomic yearly product cost ( $€ \cdot y^{-1}$ )
c	specific heat ( $kJ \cdot kg^{-1} K^{-1}$ )
$c_F$	Exergoeconomic cost of exergy input ( $€ \cdot kWh^{-1}$ )
CRF	capital recovery factor ( $y^{-1}$ )
D	hydraulic diameter (m)
ex	Specific exergy ( $kJ \cdot kg^{-1}$ )
f	Fanning friction factor (-)
$\dot{F}$	required exergy (kW)
g	gravitational acceleration ( $m \cdot s^{-2}$ )
G	mass velocity ( $kg \cdot s^{-1} \cdot m^{-2}$ )
H	plate height (m)
I	destroyed exergy or irreversibility (kW)
k	thermal conductivity ( $W \cdot m^{-1} \cdot K^{-1}$ )
L	plate width (m)
$\dot{m}$	mass flow rate ( $kg \cdot s^{-1}$ )
m	service life of system (y)
$n_p$	number of passes (-)
$N_p$	number of plates (-)
$N_c$	number of channels for each flow (-)
$Nu$	Nusselt number (-)
p	pressure (bar)
$\dot{P}$	desired exergy or product (kW)
Pr	Prandtl number (-)
$\dot{Q}$	thermal power (kW)
$R_f$	fouling thermal resistance ( $m^2 \cdot K \cdot W^{-1}$ )
Re	Reynolds number (-)
$\dot{S}_{gen}$	generated entropy ( $W \cdot K^{-1}$ )
T	temperature ( $^{\circ}C$ )
U	overall heat transfer coefficient ( $W \cdot m^{-2} K^{-1}$ )
Z	investment cost (€)

### Greek Letters

$\alpha$	convective heat transfer coefficient ( $W \cdot K^{-1} \cdot m^{-2}$ )
$\beta$	chevron angle
$\varphi$	enlargement factor (-)
$\gamma$	plate corrugation aspect ratio (-)
$\delta$	plate thickness (mm)
$\mu$	viscosity (Pa·s)
$\lambda$	wavelength of a sinusoidal surface corrugation or pitch (mm)
$\rho$	density ( $kg \cdot m^{-3}$ )
$\theta$	Yearly operating hours ( $h \cdot y^{-1}$ )

### Subscripts

c	cold fluid
el	electric
elev	elevation contribution
f	fluid
fric	friction contribution
h	hot geothermal fluid
in	inlet
m	average value
man	manifold section
mon	momentum effect
OBJ	objective
out	outlet
P	pump
th	thermal
tot	total
w	wall material
0	dead state

### Acronyms

EU	European Union
HEX	Heat exchanger
PPHEX	Plastic Plate heat exchanger
RES	Renewable Energy Source

## References

1. New Rules for Greener and Smarter Buildings Will Increase Quality of Life for All Europeans. Available online: [https://ec.europa.eu/info/news/new-rules-greener-and-smarter-buildings-will-increase-quality-life-all-europeans-2019-apr-15\\_en](https://ec.europa.eu/info/news/new-rules-greener-and-smarter-buildings-will-increase-quality-life-all-europeans-2019-apr-15_en) (accessed on 19 July 2021).
2. Eurostat. Distribution of Population by Degree of Urbanisation, Dwelling Type and Income Group. 2020. Available online: [https://appsso.eurostat.ec.europa.eu/nui/show.do?dataset=ilc\\_lvho01&lang=en](https://appsso.eurostat.ec.europa.eu/nui/show.do?dataset=ilc_lvho01&lang=en) (accessed on 19 July 2021).
3. International Energy Agency. Data and Statistics. 2021. Available online: <https://www.iea.org/data-and-statistics/data-browser?country=WORLD&fuel=Electricity%20and%20heat&indicator=HeatGenByFuel> (accessed on 19 July 2021).
4. Lund, J.W.; Toth, A.N. Direct utilization of geothermal energy 2020 worldwide review. *Geothermics* **2021**, *90*, 101915. [CrossRef]
5. Tan, M.; Karabacak, R.; Acar, M. Experimental assessment the liquid/solid fluidized bed heat exchanger of thermal performance: An application. *Geothermics* **2016**, *62*, 70–78. [CrossRef]
6. CALORPLAST. Shell and Tube Heat Exchanger. Data Sheet. Available online: <https://www.calorplast-waermetechnik.de/wp-content/uploads/liquid-liquid-heat-exchanger.pdf> (accessed on 12 October 2021).
7. TMW Technologies. Plastic Plate Heat Exchanger. Data Sheet. Available online: <https://pdf.directindustry.com/pdf/tmw-technologies/plastic-heat-exchanger/168190-760122.html> (accessed on 12 October 2021).
8. ELRINGKLINGER. Shell and Tube Heat Exchanger. Data Sheet. Available online: [https://www.erlingklinger-engineered-plastics.com/fileadmin/user\\_upload/ekkt/downloads/kataloge/englisch/thermo-x\\_heat\\_exchanger.pdf](https://www.erlingklinger-engineered-plastics.com/fileadmin/user_upload/ekkt/downloads/kataloge/englisch/thermo-x_heat_exchanger.pdf) (accessed on 12 October 2021).

9. HeatMatrix Group. Polymer Economiser. Data Sheet. Available online: <https://heatmatrixgroup.com/products/economiser/> (accessed on 12 October 2021).
10. Chen, X.; Su, Y.; Reay, D.; Riffat, S. Recent research developments in polymer heat exchangers—A review. *Renew. Sustain. Energy Rev.* **2016**, *16*, 1367–1386.
11. T’Joel, C.; Park, Y.; Wang, Q.; Sommers, A.; Han, X.; Jacobi, A. A review on polymer heat exchangers for HVAC&R applications. *Int. J. Refrig.* **2009**, *32*, 763–779.
12. Ceglia, F.; Macaluso, A.; Marrasso, E.; Sasso, M.; Vanoli, L. Modelling of polymeric shell and tube heat exchangers for low-medium temperature geothermal applications. *Energies* **2020**, *13*, 2737. [[CrossRef](#)]
13. Ceglia, F.; Marrasso, E.; Roselli, C.; Sasso, M. Effect of layout and working fluid on heat transfer of polymeric shell and tube heat exchangers for small size geothermal ORC via 1-D numerical analysis. *Geothermics* **2021**, *95*, 102118. [[CrossRef](#)]
14. Luo, X.; Wang, Y.; Zhao, J.; Chen, Y.; Mo, S.; Gong, Y. Grey relational analysis of an integrated cascade utilization system of geothermal water. *Int. J. Green Energy* **2016**, *13*, 14–27. [[CrossRef](#)]
15. Arslan, O.; Kose, R. Exergoeconomic optimization of integrated geothermal system in Simav, Kutahya. *Energy Convers. Manag.* **2010**, *51*, 663–676. [[CrossRef](#)]
16. Jamil, M.A.; Goraya, T.S.; Shahzad, M.W.; Zubair, S.M. Exergoeconomic optimization of a shell-and-tube heat exchanger. *Energy Convers. Manag.* **2020**, *226*, 113462. [[CrossRef](#)]
17. Hajabdollahi, H.; Naderi, M.; Adimi, S. A comparative study on the shell and tube and gasket-plate heat exchangers: The economic viewpoint. *Appl. Therm. Eng.* **2016**, *92*, 271–282. [[CrossRef](#)]
18. Ozgener, L.; Hepbasli, A.; Dincer, I. Thermodynamic analysis of a geothermal district heating system. *Int. J. Exergy* **2005**, *2*, 231–245. [[CrossRef](#)]
19. Hajabdollahi, H.; Ahmadi, P.; Dincer, I. Thermoeconomic optimization of a shell and tube condenser using evolutionary algorithm. *Int. J. Refriger.* **2011**, *34*, 1066–1076. [[CrossRef](#)]
20. Hajabdollahi, H. Investigating the effect of non-similar fins in thermoeconomic optimization of plate fin heat exchanger. *Appl. Therm. Eng.* **2015**, *82*, 152–161. [[CrossRef](#)]
21. Hajabdollahi, H.; Tahani, M.; Fard, M.H.S. CFD modeling and multi-objective optimization of compact heat exchanger using CAN method. *Appl. Therm. Eng.* **2011**, *31*, 2597–2604. [[CrossRef](#)]
22. Gemitzi, A.; Dalampakis, P.; Falalakis, G. Detecting geothermal anomalies using Landsat 8 thermal infrared remotely sensed data. *Int. J. Appl. Earth Obs. Geoinf.* **2021**, *96*, 102283. [[CrossRef](#)]
23. Lund, J.W.; Toth, A.N. Direct utilization of geothermal energy 2020 worldwide review. In Proceedings of the World Geothermal Congress 2020+1, Reykjavik, Iceland, 27 April 2021. Available online: <https://www.geothermal-energy.org/pdf/IGAstandard/WGC/2020/01018.pdf> (accessed on 21 October 2021).
24. Hurter, S.; Schellschmidt, R. Atlas of geothermal resources in Europe. *Geothermics* **2003**, *32*, 779–787. [[CrossRef](#)]
25. Ates, H.K.; Serpen, U. Power plant selection for medium to high enthalpy geothermal resources of Turkey. *Energy* **2016**, *102*, 287–301. [[CrossRef](#)]
26. Carlino, S.; Troiano, A.; Di Giuseppe, M.G.; Tramelli, A.; Troise, C.; Somma, R.; De Natale, G. Exploitation of geothermal energy in active volcanic areas: A numerical modelling applied to high temperature Mofete geothermal field, at Campi Flegrei caldera (Southern Italy). *Renew. Energy* **2016**, *84*, 54–66. [[CrossRef](#)]
27. Çengel, Y.A. *Thermodynamics and Heat Transfer*; McGraw-Hill: New York, NY, USA, 2008; ISBN 0-390-86122-7.
28. Shah, R.K.; Seculić, D.P. *Foundamental of Heat Exchanger Design*. John Wiley & Sons, Inc.: Hoboken, NJ, USA, 2003.
29. Lemmon, E.W.; Huber, M.L.; McLinden, M.O. *Reference Fluid Thermodynamic and Transport Properties, Nist Standard Reference Database 23*; Version 9.1; Physical and Chemical Properties Division, NIST: Boulder, CO, USA, 2002.
30. Martin, H. A theoretical approach to predict the performance of chevron-type plate heat exchangers. *Chem. Eng. Process. Process. Intensif.* **1996**, *35*, 301–310. [[CrossRef](#)]
31. D’Accadia, M.D.; Fichera, A.; Sasso, M.; Vidiri, M. Determining the optimal configuration of a heat exchanger (with a two-phase refrigerant) using exergoeconomics. *Appl. Energy* **2002**, *71*, 191–203. [[CrossRef](#)]
32. Di Fraia, S.; Macaluso, A.; Massarotti, N.; Vanoli, L. Geothermal energy for wastewater and sludge treatment: An exergoeconomic analysis. *Energy Convers. Manag.* **2020**, *224*, 113180. [[CrossRef](#)]
33. D’Accadia, M.D.; Sasso, M. Exergetic cost and exergoeconomic evaluation of vapour-compression heat pumps. *Energy* **1998**, *23*, 937–942. [[CrossRef](#)]
34. Kotas, T.J. *The Exergy Method of Thermal Plant Analysis*; Butterwoths: London UK, 1995.
35. *MATLAB and Statistics Toolbox Release*; The MathWorks, Inc.: Natick, MA, USA, 2018.
36. Carlino, S.; Somma, R.; Troiano, A.; Di Giuseppe, M.G.; Troise, C.; DE Natale, G. The geothermal system of Ischia Island (southern Italy): Critical review and sustainability analysis of geothermal resource for electricity generation. *Renew. Energy* **2014**, *62*, 177–196. [[CrossRef](#)]
37. Carlino, S.; Somma, R.; Troise, C.; DE Natale, G. The geothermal exploration of Campanian volcanoes: Historical review and future development. *Renew. Sustain. Energy Rev.* **2012**, *16*, 1004–1030. [[CrossRef](#)]
38. Weinmann, S. Available online: <https://www.weinmann-schanz.de/gb/en/Heating/Solar-technology-geothermal-energy/Plate-heat-exchangers-and-accessories/Plate-heat-exchanger-ZB/Plate-heat-exchanger-P20-4x-3-4-ET-20-KW-20-plates-ZB-10-20-sid515394.html> (accessed on 19 July 2021).

39. Casasso, A.; Sethi, R.; Rivoire, M. Studio di Fattibilità Per un Impianto Geotermico a Circuito Aperto in un Complesso Residenziale (Feasibility Study For an Open Circuit Geothermal Plant in a Residential Context). Master's Thesis, Politecnico di Torino, Torino, Italy, 2018.
40. Catalogue of Operational Criteria and Constraints for Shallow Geothermal Systems in the Alpine Environment. Available online: [https://www.alpine-space.eu/projects/greta/deliverables/d3.2.1\\_catalogue-of-operational-criteria-and-constraints-update2a--2018.pdf](https://www.alpine-space.eu/projects/greta/deliverables/d3.2.1_catalogue-of-operational-criteria-and-constraints-update2a--2018.pdf) (accessed on 5 August 2021).
41. ARERA. Italian Document: Andamento del Prezzo dell'Energia Elettrica per il Consumatore Domestico Tipo in Maggior Tutela. Data of First Semester 2021. 2021. Available online: <https://www.arera.it/it/dati/eep35.htm> (accessed on 15 March 2021).
42. Franco, A.; Villani, M. Optimal design of binary cycle power plants for water-dominated, medium-temperature geothermal fields. *Geothermics* **2009**, *38*, 379–391. [[CrossRef](#)]

## Article

# 3DHIP-Calculator—A New Tool to Stochastically Assess Deep Geothermal Potential Using the Heat-In-Place Method from Voxel-Based 3D Geological Models

Guillem Piris <sup>1</sup>, Ignasi Herms <sup>2,\*</sup>, Albert Griera <sup>1</sup>, Montse Colomer <sup>2</sup>, Georgina Arnó <sup>2</sup> and Enrique Gomez-Rivas <sup>3</sup>

<sup>1</sup> Departament de Geologia, Universitat Autònoma de Barcelona (UAB), 08193 Barcelona, Spain; guillem.piris@uab.cat (G.P.); albert.griera@uab.cat (A.G.)

<sup>2</sup> Àrea de Recursos Geològics, Institut Cartogràfic i Geològic de Catalunya (ICGC), 08038 Barcelona, Spain; montse.colomer@icgc.cat (M.C.); georgina.arno@icgc.cat (G.A.)

<sup>3</sup> Departament de Mineralogia, Petrologia i Geologia Aplicada, Facultat de Ciències de la Terra, Universitat de Barcelona (UB), 08028 Barcelona, Spain; e.gomez-rivas@ub.edu

\* Correspondence: ignasi.herms@icgc.cat; Tel.: +34-620-95-92-47

**Abstract:** The assessment of the deep geothermal potential is an essential task during the early phases of any geothermal project. The well-known “Heat-In-Place” volumetric method is the most widely used technique to estimate the available stored heat and the recoverable heat fraction of deep geothermal reservoirs at the regional scale. Different commercial and open-source software packages have been used to date to estimate these parameters. However, these tools are either not freely available, can only consider the entire reservoir volume or a specific part as a single-voxel model, or are restricted to certain geographical areas. The 3DHIP-Calculator tool presented in this contribution is an open-source software designed for the assessment of the deep geothermal potential at the regional scale using the volumetric method based on a stochastic approach. The tool estimates the Heat-In-Place and recoverable thermal energy using 3D geological and 3D thermal voxel models as input data. The 3DHIP-Calculator includes an easy-to-use graphical user interface (GUI) for visualizing and exporting the results to files for further postprocessing, including GIS-based map generation. The use and functionalities of the 3DHIP-Calculator are demonstrated through a case study of the Reus-Valls sedimentary basin (NE, Spain).

**Keywords:** Heat-In-Place; recoverable heat; deep geothermal potential; mapping; MATLAB

**Citation:** Piris, G.; Herms, I.; Griera, A.; Colomer, M.; Arnó, G.; Gomez-Rivas, E. 3DHIP-Calculator—A New Tool to Stochastically Assess Deep Geothermal Potential Using the Heat-In-Place Method from Voxel-Based 3D Geological Models. *Energies* **2021**, *14*, 7338. <https://doi.org/10.3390/en14217338>

Academic Editors: Renato Somma and Daniela Blessent

Received: 11 September 2021

Accepted: 2 November 2021

Published: 4 November 2021

**Publisher’s Note:** MDPI stays neutral with regard to jurisdictional claims in published maps and institutional affiliations.



**Copyright:** © 2021 by the authors. Licensee MDPI, Basel, Switzerland. This article is an open access article distributed under the terms and conditions of the Creative Commons Attribution (CC BY) license (<https://creativecommons.org/licenses/by/4.0/>).

## 1. Introduction

Deep geothermal energy exploration and exploitation activities have vigorously grown during the last decade worldwide [1–3]. One of the key tasks during the early evaluation stages of deep geothermal plays is the assessment of the base resource in terms of the energy stored in the reservoir [4]. This quantification is an essential step to estimate the energy that can be produced from the geothermal reservoir for power generation or direct uses (district heating, greenhouses, etc.), and is key for carrying out preliminary evaluations of the project feasibility based on the required investment and the exploitation cost of the geothermal resource. However, there are uncertainties in the geological knowledge that must be considered when carrying out these preliminary assessments during the early stages of exploration of the geothermal resource. These uncertainties are mainly related to the prediction of the reservoir geometry, petrophysical properties, and temperature distribution.

The volumetric “Heat-In-Place” (HIP) method, implemented by the United States Geological Survey (USGS) [5], together with its subsequent revisions [6–10], is still the most widely used evaluation technique for the estimation of the available stored heat and the recoverable heat fraction (Hrec) of deep geothermal reservoirs [11–16]. This method considers the volume of the reservoir (surface and thickness), the petrophysical properties

(e.g., rock type, porosity, specific heat capacity, etc.), fluid properties (e.g., fluid density, etc.), as well as the reservoir and reinjection (or reference) temperatures. Due to the potential influence of these parameters and their uncertainty, Nathenson [17] considered the need to follow a stochastic approach through Monte Carlo simulations [18]. This approach systematically varies the parameters considered over a defined range of values by using probability distribution functions (PDF) (e.g., triangular, normal, lognormal, etc.) [8,19,20].

Traditionally, common commercial software designed for risk and decision analysis purposes, such as @Risk [21] and Crystal Ball [22], have been used for geothermal resource assessment. They apply the volumetric method using Monte Carlo simulations (i.e., stochastic calculations implementing PDFs for the variables). Both tools run as Microsoft Excel add-ins, and calculations are normally applied at the scale of the entire reservoir or to a specific part of it, where the selected volume is conceptually treated as a single voxel [23–26]. In terms of open-source software, Pocasangre et al. [27] have more recently developed the ‘GPPeval’ application (Geothermal Power Potential assessment), a Python-based stochastic library for the assessment of the geothermal power potential using the volumetric method in a liquid-dominated reservoir. A handicap of these applications is that the analyzed domain must be treated as a lumped parameter model, i.e., with a homogeneous distribution of parameters in the whole volume considered. However, local variabilities are expected in reservoirs, mainly due to the variation of the petrophysical properties, temperature distribution, and reservoir geometry (thickness, depth, etc.). For this reason, approaches based on GIS (Geographic Information System) coupled with 3D subsurface models are promising, because they explicitly allow the application of the volumetric method using 3D voxel models as inputs. Several authors have used 3D geological models to calculate the volume of a reservoir to subsequently apply the HIP volumetric method in a deterministic way by assigning values to parameters of each unit to estimate, quantify, and map a first estimation of the geothermal reserve [28,29].

A more sophisticated approach is that applied by the VIGORThermoGIS code [12], an implementation of the ThermoGIS TNO code [30–32]. This tool was implemented specifically to assess prospective areas for geothermal development in the Netherlands and in southern Italy during the VIGOR Project [12]. The codes and the methodology implemented in these two tools can be considered nowadays as a reference for the scientific community working on the evaluation of resources at the regional scale. These tools demonstrated the use of methods that couple 3D subsurface data with GIS tools to stochastically assess the deep geothermal potential. Nevertheless, their implementation was limited to their case study areas and specific datasets. Therefore, there is still a need for a standard and freely available tool for the whole geothermal community in order to be able to estimate the HIP using Monte Carlo simulations, and in which any 3D geological and 3D thermal models can be utilized to assess case studies.

A gap is identified between what the geoscience community working in geothermal energy would need (including geological surveys, universities, research institutes, or consulting companies) and what is currently offered by free commercial or open-source software packages to assess deep geothermal potential at the regional scale in three-dimensions and by stochastically using the volumetric method. To close this gap, a novel and free software called the ‘3DHIP-Calculator’ is presented here. This tool allows for estimating the geothermal potential of a reservoir using the volumetric Heat-In-Place (HIP) method, originally implemented by the United States Geological Survey (USGS) [5], combined with a Monte Carlo simulation approach [17] and using 3D geological and 3D thermal models based on a voxel format as inputs.

The 3DHIP-Calculator application has many competitive advantages. Firstly, the source code and the installation files are accessible for all users and developers from open-source repositories such as GitHub. Secondly, as the tool allows importing 3D models that integrate previously generated geological, petrophysical, and thermal data, it considers the whole geological heterogeneity of the reservoir to estimate the geothermal potential using the HIP method. Finally, the results can be exported in ASCII format for their

subsequent post-processing in other environments, such as GIS software packages. This allows generating maps of the assessed deep geothermal potential at the regional scale, and to use 3D visualization tools and statistical packages, such as R [33], for further evaluations. All these advantages open a wide range of possibilities, including the construction of GIS-based maps or to conduct feasibility studies of the deep geothermal potential through risk analysis approaches.

This contribution presents the structure, capabilities, and use of the 3DHIP-Calculator and its graphical user interface (GUI). Moreover, the method is demonstrated through a case study of the Reus-Valls Basin (RVB) [34]. The RVB is part of the Neogene extensional basins of the Catalan Coastal Ranges (NE of the Iberian Peninsula, Spain), which, according to previous studies [35–37], has a high potential for the development of deep geothermal energy for direct heat or power generation. However, the lack of enough subsurface information (from deep appraisal wells) results in a relatively large uncertainty for the assessment of its geothermal potential. The RVB case is a useful example of deep geothermal potential assessment at the regional scale, where the 3DHIP-Calculator can offer a first estimate of the spatial distribution of the deep geothermal resource based on the existing geological knowledge and its associated uncertainty.

## 2. Materials and Methods

### 2.1. Mathematical Background of the HIP Method

The 3DHIP-Calculator is based on the HIP approach, which allows estimating the geothermal resource and the recoverable fraction of a subsurface reservoir [5,10–12]. The HIP (kJ) is calculated according to Equation (1):

$$\text{HIP} = V \cdot [\varnothing \cdot \rho_F \cdot C_F + (1 - \varnothing) \cdot \rho_R \cdot C_R] \cdot (Tr - Ti) \quad (1)$$

where  $V$  is the voxel volume ( $\text{m}^3$ ),  $\varnothing$  is the rock porosity (parts per unit),  $\rho$  is the rock density ( $\text{kg}/\text{m}^3$ ),  $C$  is the specific heat capacity ( $\text{kJ}/\text{kg} \cdot ^\circ\text{C}$ ), and the  $F$  and  $R$  sub-indexes account for the fluid and host rock, respectively.  $Tr$  is the reservoir temperature ( $^\circ\text{C}$ ) and  $Ti$  refers to either the re-injection, reference, or abandonment temperature ( $^\circ\text{C}$ ). Therefore,  $Ti$  can refer to the threshold of economic or technological viable temperature, the ambient temperature (i.e., the annual mean surface temperature value), or a temperature value defined according to other criteria [11]. Equation (1) is solved within the 3DHIP-Calculator for each voxel in the model that satisfies the condition that  $(Tr - Ti) \geq 5^\circ\text{C}$ . Otherwise, the HIP for that voxel is not evaluated and is set to zero. The HIP is expressed in kJ.

Then, the obtained HIP value is used to calculate the recoverable heat (Hrec) following Equation (2), which accounts for the producible thermal power during a given plant or project lifetime ( $Tlive$ ):

$$\text{Hrec} = \frac{\text{HIP} \cdot C_e \cdot R}{Tlive \cdot Pf} \quad (2)$$

where the HIP resulting from Equation (1) is scaled by a recovery factor ( $R$ , in parts per unit) to represent the part of the heat that can be extracted. This first estimation of the recovery factor ( $R$ ) requires special attention because it depends on many factors, including the hydrogeological characteristics of the reservoir and the current drilling technology. Some authors suggest using  $R$  values between 0.02 and 0.2 [38] or close to 0.01 [12] for studies where there is no previous information. A recovery factor for a geothermal doublet (with a production borehole and an injection borehole) was defined at 0.33 according to the Atlas of Geothermal Resources in Europe [16,39], based on Muffler and Cataldi [5] and Lavigne [40]. Williams et al. [6,7,41] proposed a range of  $R$  values according to the geothermal reservoir type: a range from 0.08 to 0.2 for fracture-dominated reservoirs, 0.01 for Enhanced Geothermal Systems [42], and from 0.1 to 0.25 for sediment-hosted reservoirs with a maximum value of 0.5 [3]. Additionally, a conversion efficiency factor ( $C_e$ , in parts per unit) is used to incorporate the effect of the efficiency of the heat exchange from the geothermal fluid to a secondary fluid in a thermal plant.  $C_e$  can vary as a function of

geothermal exploitation (e.g., heat or electricity production). Finally, since most of the direct heat applications of geothermal energy (such as district heating, greenhouse heating, etc.) do not operate continuously throughout the year, a plant factor ( $P_f$ , in parts per unit) is included. This factor considers the fraction of the total time in which the geothermal plant is in operation. Thus, Hrec is expressed in kW.

### 2.2. Mathematical Background of the Monte Carlo Method

The Monte Carlo method, i.e., a multiple probability simulation, is a mathematical solution widely used to estimate the possible outcomes of an uncertain event. Unlike a normal forecasting model, Monte Carlo simulations predict a set of outcomes based on an estimated range of values versus a deterministic or fixed input value. This method is used in the 3DHIP-Calculator to probabilistically evaluate the uncertainty associated with the input parameters and the corresponding geothermal potential results [18]. The first step is to link a probability distribution function (PDF) to each parameter, to infer the unknown quantities of the samples, and to take into account the range and pattern of variation of the different parameters [43]. Thus, Equations (1) and (2) are applied using a stochastic approach, instead of a deterministic one, so that their input values are not fixed parameters yielding a unique result. The calculations based on these two equations are repeated as many times as desired ( $N$ , number of simulations), producing a large number of likely outcomes, using random values extracted from probability distribution functions assigned to the parameters and predefined depending on the pattern variation. The application allows selecting normal or triangular PDFs for the input parameters of Equations (1) and (2). The mean and standard deviation are used to define normal distributions, while the lower, most probable, and upper values are for triangular distributions. The required input data for the calculations are 3D geological models (3DGM), 3D thermal models (3DTM), and random values within the selected PDF for each parameter. The values of the variables defined in a deterministic way (i.e., without assigning PDFs) are considered as fixed. Accordingly, the application calculates as many different HIP and Hrec values as the number of simulations defined by the user for each voxel of the model. The results of the calculations are also expressed as PDFs.

### 2.3. Program Description

The 3DHIP-Calculator (Figure 1) was developed using MATLAB® (v. R2019b) [44] based on the MATLAB App Designer, and then compiled for Windows as a standalone application. The installation files, as well as the user manual and examples, can be freely downloaded from the “Deep geothermal energy” web page of the Institut Cartogràfic i Geològic de Catalunya (ICGC) (under the Creative Commons license Attribution 4.0 International, CC BY 4.0). The source code can also be downloaded from <https://github.com/OpenICGC/3DHIP-Calculator> (accessed on 15 October 2021).

An easy-to-use graphical user interface (GUI) was implemented and organized in six main steps, as shown in the workflow of Figure 2. The first part comprises the pre-processing step, that includes the selection of input parameters (step 1 in Figure 2). In this step, the input 3D geological and 3D thermal models (referred to as 3DGM and 3DTM, respectively) are converted to a matrix, where each row corresponds to one voxel in the 3D model and the columns are the petrophysical/reservoir parameters. Using depth ranges and geological units, the target volume of the whole model is defined. The parameters that are not included as initial data in the 3D models are defined using PDFs (2, Figure 2).

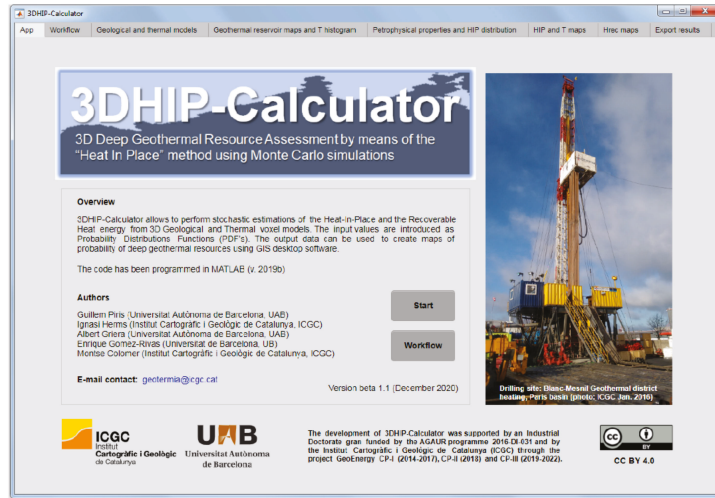


Figure 1. Screenshot of the main GUI window. The 3DHIP-Calculator is organized in eight tabs.

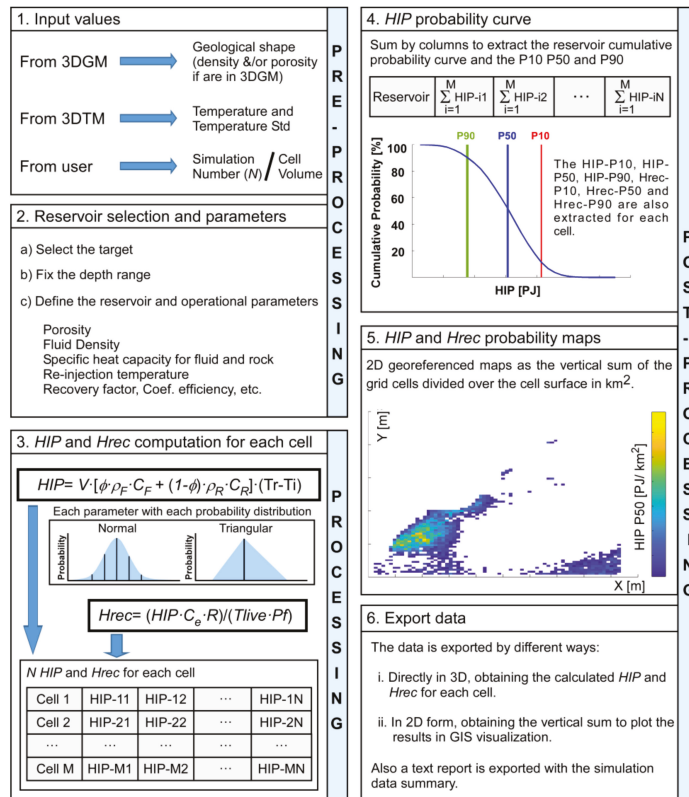


Figure 2. 3DHIP-Calculator workflow. It is divided into six main steps: (1) input values, (2) reservoir selection and parameters, (3) HIP and Hrec computation, (4) HIP probability curve, (5) HIP and Hrec probability maps, and (6) export data (modified from Herms et al., 2021 [34]).

During the processing step, the HIP and Hrec calculations are carried out using Equations (1) and (2), and performed as many times ( $N$ ) as desired (3, Figure 2). The full results from the  $N$  simulations are stored for each voxel of the model and include the entire uncertainty obtained from the Monte Carlo method. Then, the results are statistically compiled to obtain a cumulative probability distribution (CDF) for each voxel, from which the representative probability values are extracted. The voxels corresponding to the target volume are also summed and compiled statistically to obtain the probability results for the entire target reservoir (4, Figure 2). Finally, the post-processing allows visualizing the probability results (4 and 5, Figure 2) and exporting the original data and the stochastic results to ASCII files (6, Figure 2).

### 2.3.1. Pre-Processing: Input Data

An essential step to run the application is to choose and upload the imported 3DGM and 3DTM. The application allows for loading data using ASCII text files, delimited by tabulators, spaces, or commas. A 3DTM is not always required, and alternatively, an approach based on a linear geothermal gradient according to depth can be used, if a 3DTM is not available. When this option is chosen, the temperature of each voxel is calculated according to Equation (3):

$$Tz = T_0 + \Delta T \times Dz \quad (3)$$

where  $Tz$  is the estimated temperature at depth  $z$ ,  $T_0$  is the mean annual surface temperature,  $\Delta T$  is the measured thermal regional gradient in  $C/km$ , and  $Dz$  is the depth  $z$  of the target according to the preliminary 3D model. This approach assumes a conductive steady-state regime and is indicated for geothermal plays in passive tectonic settings where no asthenospheric anomalies occur [45].

The 3DGM and 3DTM files should follow certain rules in terms of data organization (e.g., Figure 3). Particularly, they need to include at least one line of column headers before listing the data. The file is organized in a way that each column contains a variable, and each line corresponds to a voxel. The columns normally correspond to (in this order): voxel coordinates ( $X$ ,  $Y$ , and  $Z$ , usually corresponding to its centroid) in UTM or geographic coordinates in decimal degrees, and a numerical identifier to differentiate the geological units (e.g., lithology, formation, reservoir, target, etc.). Additionally, the 3DGM can contain petrophysical parameters such as density (in  $g/cm^3$ ) and porosity (parts per unit) that can vary for each voxel. The 3DTM should include the voxel coordinates ( $X$ ,  $Y$ , and  $Z$ ), the temperature (in  $^{\circ}C$ ), and the temperature standard deviation (in  $^{\circ}C$ ) for each voxel. The temperature standard deviation is an optional parameter that can be set to zero if it is unknown. Furthermore, the voxel position and resolution (in  $X$ ,  $Y$ , and  $Z$ ) of the geological and thermal models must be identical and match each other.

<b>A</b>	1	X, Y, Z, Lithology, Density
	2	317027.9125, 4540905.475, -6967.857143, 1, 2.90372729
	3	317721.7375, 4540905.475, -6967.857143, 1, 2.99401951
	4	318415.5625, 4540905.475, -6967.857143, 1, 2.68000007
	5	319109.3875, 4540905.475, -6967.857143, 1, 2.75085641
<b>B</b>	1	X, Y, Z, Mean_Lithology, Mean_Temperature, Stddev_Temperature
	2	317027.9125, 4540905.475, -6967.857143, 1, 180.15632, 1.52323
	3	317721.7375, 4540905.475, -6967.857143, 1, 180.26542, 1.36252
	4	318415.5625, 4540905.475, -6967.857143, 1, 180.65485, 2.01631
	5	319109.3875, 4540905.475, -6967.857143, 1, 180.90902, 1.86546

**Figure 3.** Internal structure of the data files of the voxel-based geological (A) and thermal (B) models that the 3DHIP-Calculator needs to be imported.

These input files for the voxel-based 3DGM and 3DTM can be generated using common commercial geological modeling software, such as GeoModeller3D (©BRGM, Intrepid-Geophysics) or SKUA-GOCAD<sup>®</sup> (Paradigm), or GemPy, an open-source 3D geological model based on Python [46], among many other packages able to export 3D models in this format. The files for the testing case presented in this paper were generated using GeoModeller3D (v4.0.8).

### 2.3.2. Post-Processing: Output Data

The outputs from the stochastic simulations are utilized to:

- Generate a CDF for each voxel, from which a probability 10% (P10) (very low confidence of the estimation and high values), P50, and P90 (high confidence of the estimation and low values) are extracted. Furthermore, the mean and standard deviation are also calculated.
- Generate a CDF for the entire investigated target (e.g., geological unit, reservoir, etc.) summing the voxel values, and the P10, P50, and P90 are calculated. This approach is only used for the HIP calculation and not for the Hrec one.
- Generate 2D maps using the relationship between the vertical sum of the values calculated in each voxel with respect to the area occupied by the voxel (in km<sup>2</sup>). The P10, P50, and P90 of HIP and Hrec are then estimated.
- The application allows exporting two ASCII files with all results for further post-processing and generates an automatic report that summarizes the input data and the main results.

One of these files is the 3D model with all the voxels of the selected target. Each output register for each voxel contains the initial data (*X*, *Y*, *Z*, and geology and thermal properties) plus the HIP (PJ) and Hrec (kW) calculations. The HIP and Hrec are expressed in terms of P10, P50, P90, mean, and standard deviation. This file can be exported again to 3D geological modeling software for subsequent post-processing, or to other environments, such as GIS suites (e.g., the results of this study are presented in maps using the free and open-source QGIS 3.16.1 ‘Hannover’ version), 3D visualization tools, or statistical packages such as R [33]. The second file is the 2D model with the vertical summation of the HIP (PJ) and Hrec (kW) values of each voxel and their coordinates (in this case only *X* and *Y*), which can also be used for further geospatial analysis in GIS for mapping. The values of HIP and Hrec are not divided by the voxel area, and they are expressed as they have been calculated, i.e., in P10, P50, and P90. Finally, the last file contains a brief report in text format that includes the data and parameters used for the simulation, as well as the main results obtained.

### 2.3.3. Modeling Scenarios Depending on Data Availability

The software can be used for different situations and contexts, depending on the availability of data. The optimal scenario is when both a 3DGM containing the distribution of petrophysical parameters (e.g., density, porosity) and a 3DTM with the same voxel structure that includes the temperature distribution with depth are available. An intermediate case would be when only a 3DGM is available and the temperature information of the study region is estimated using the mean geothermal gradient. In that case, the 3DHIP-Calculator can be run using a linear geothermal gradient instead of a thermal model. The worst scenario would be when the reservoir volume and temperature are roughly known, and the rest of the parameters need to be inferred. The 3DHIP-Calculator can also be used in these cases, although the uncertainty of the variables and resulting PDFs increase.

## 3. Example Case Study—The Reus-Valls Basin (NE, Spain)

This section demonstrates the use and capabilities of the 3DHIP-Calculator assessing the geothermal potential of the Reus-Valls Basin (RVB) based on the geological and thermal models presented by Herms et al. [34]. The Triassic and Jurassic units were selected as potential targets. As the main goal is to show the capabilities of the tool, the stratigraphic complexity of Triassic and Jurassic units was simplified in the model used for this analysis. The three scenarios described in the previous section are considered here to calculate the geothermal potential of the RVB. A fourth scenario that also includes the calculation of the recoverable heat is also considered here.

### 3.1. Geological Setting

The RVB is part of a set of SW–NE oriented extensional basins of the Catalan Coastal Ranges (Figure 4), which were formed during the Neogene rifting related to the opening of the Western Mediterranean and the Valencia Trough. The basin has a half-graben geometry strongly tilted towards its NW margin, where it is limited by the Camp Fault, which controls the basin depocenters [47]. This is an extensional NE-trending and SE-dipping basement fault [48] that was active from the early Miocene to the Quaternary. The fault separates the Prades-Llaberia and Miramar ranges (where the Mesozoic cover and the Paleozoic basement rocks crop out) and the Neogene sedimentary infill of the basin. These Neogene sediments reach a maximum thickness of about 2000 m near La Selva del Camp and Montbrió del Camp towns [47]. The Neogene sediments unconformably overlay the Mesozoic and the Paleozoic basement. Paleogene deposits are not preserved within the RVB, but such sediments lie unconformably on top of the Mesozoic succession in the Ebro Basin, NW of the study area.

There is no evidence of hydrothermal activity in the RVB except for the western limit of the basin, where there is a shallow hydrothermal aquifer controlled by W edge faults of the basin (called the ‘Camp Fault’) in the surroundings of the town of Montbrió del Camp. The hydrothermal aquifer shows an upward groundwater thermal flow of deep origin and a temperature of 81 °C at a 52 m depth. This fault-controlled hydrothermal aquifer is used nowadays by a thermal spa located within the town, exploiting its hot groundwaters.

Moreover, there is no evidence of magmatic activity, and it can be assumed that the main heat transport mechanism for the entire sedimentary basin at the regional scale is conduction. This is controlled by the thermal conductivity distribution of the lithologies that fill the basin and by the radiogenic heat production from the underlying granites. Therefore, the system can be classified as a conduction-dominated geothermal play in an intracratonic basin for the Mesozoic aquifers, which corresponds to a CD-1 of the catalog of geothermal play types based on geologic controls defined by Moeck [45,49] and CD-3 for the crystalline basement rocks.

### 3.2. The Potential Hot Deep Sedimentary Aquifers

The main deep aquifers acting as targets in the test case are in the Jurassic and Triassic limestones and sandstones. Currently, their deep geothermal energy potential is still untapped. It is well-known that these aquifers are geothermal reservoirs that have been exploited for a long time in other places of central and western Europe, such as the Malm limestones of the Molasse Basin in Germany [51], the Dogger limestones of the Paris Basin [52], and the Buntsandstein sandstones in northern Germany [53] and the Upper Rhine Graben [54].

The Jurassic sequence of the RVB is defined by a basal layer of brecciated dolostones followed by a carbonate interval constituted by limestones and sandy limestones with widespread dolomitization and karstification. In the old Reus-1 well (Figure 4), which was drilled for oil/gas exploration [55,56], these materials correspond to a 261 m thick unit of partially karstified dolostones, with an estimated porosity ranging between 11% and 21% and an average value of 16%, according to available data measured in the same facies of nearby offshore fields [56]. This unit was considered a possible reservoir target for an underground gas storage project in the 90’s due to its hydraulic properties.

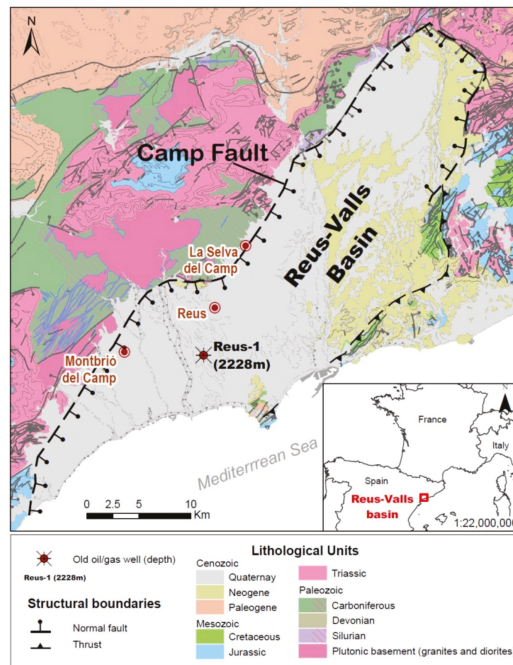


**Figure 4.** Geological map with the delimitation of the Reus-Valls Basin (modified from [50]). Source of EU map: © EuroGeographics for the administrative boundaries, European Commission, Eurostat/GISCO.

The Middle Triassic corresponds to the Muschelkalk facies. These are defined from bottom to top by a basal interval of limestones and dolostones (Lower Muschelkalk), an intermediate interval of continental red fine sandstones, mudstones, and gypsum layers, and finally, an interlayered interval of limestones-dolostones and siltstone layers (Upper Muschelkalk). The total thickness of the unit is irregular in all the Catalan Coastal Ranges, and is about 359 m in the Reus-1 well. The basal dolostone (Lower Muschelkalk) is about 81 m thick in this well [55,56]. The main characteristics for inferring the reservoir porosity are the karstification of carbonates and the intense fracturing related to the Alpine exhumation and Neogene extension periods. Thus, the available data measured in nearby areas show values of primary porosity ranging between 7% and 12% (Ebro-1 and Fraga wells) [57], which can be considerably increased by secondary porosity. Finally, Buntsandstein facies (Lower Triassic) are composed of red detrital sediments formed by heteromeric conglomerates and fine sandstones, grading to mudstones at the top. The sedimentary sequence is constituted (from bottom to top) by a few meters of basal breccia, conglomerates, red sandstones, and a unit of interlayered siltstones with carbonate and evaporitic levels (Röt facies). Accordingly, the potential reservoir horizons that must be considered (in terms of host rock and fracture porosity) are the conglomerates and especially the sandstones of the lowest part of the sequence, with a total thickness range between 60 and 130 m in the Tarragona region [58]. The basal conglomerate has an irregular surface distribution and its porosity can be altered by its siltstone portion [59]. Moreover, the fluvial sandstones may have high porosity, as suggested by data from oil exploration wells (Ebro-1 and Ebro-2) in a nearby area, with average values of porosity ranging from 5.5% to 12.1%, with maximum values of 18% [57]. Attending to the range of measured porosities in the formations considered, a triangular distribution is consistent with the actual porosity pattern and is selected to be used for the reported examples (Table 1).

**Table 1.** Petrophysical and operational parameters used for the HIP and Hrec calculations in example 2 (Low and Upp correspond to the minimum and maximum temperature values assigned to the triangular distribution with lowest frequencies; Max—the value with the highest frequency; PDF—probability distribution function; SD—standard deviation).

	Property	Units	PDFs	Values
<b>Petrophysical</b>	Porosity	-	Triangular	Low: 0.07, Max: 0.12, Upp: 0.18
	Fluid Density	kg/m <sup>3</sup>	Normal	Mean: 1020, SD: 5
	Fluid specific heat capacity	kJ/kg·°C	Normal	Mean: 4.8, SD: 0.1
	Rock density	kg/m <sup>3</sup>	Triangular	Low: 2450, Max: 2500, Upp: 2600
	Rock specific heat capacity	kJ/kg·°C	Normal	Mean: 0.9, SD: 0.01
<b>Operational</b>	Recovery factor	-	Triangular	Min: 0.08, Max: 0.12, Upp: 0.15
	Reinjection temperature	°C	-	30
	Conversion efficiency	-	-	0.85
	Plant factor	-	-	0.95
	Mean plant lifetime	years	-	30

The 3DGM used for the RVB was built using the GeoModeller3D software (v4.0.8) after several iterative steps including additional geological and geophysical data [34]. First, a reference model was generated using a Digital Terrain Model 15 × 15 [60], the geological map 1:50,000 of the area [61], data from the surface-based 3D regional geological model of Catalunya [62], unpublished geological cross-sections, information from deep oil/gas borehole (Reus-1 well; BTH depth −2228 m and Z: +74.26 m a.s.l.), interpreted horizons from 2D seismic profiles, as well as complementary information from the borehole database of Catalonia [63]. To refine this model, a full gravity/magnetic litho-constrained stochastic geophysical inversion approach was carried out using a Bayesian inference scheme implemented in the geologic modeling package of GeoModeller3D based on Markov Chain Monte Carlo simulations [64,65]. The gravity and magnetic raw data used in the inversion process were obtained from the geophysical database of Catalonia [66]. The 3D inversion modeling was applied to fit the most probable 3DGM using a stochastic approach [34]. The resulted 3DGM honors all the available geological constraints (well data, density values, stratigraphic order, and surface geology), and the gravity and magnetic data.

The 3DTM was also prepared using GeoModeller3D, applying a forward modeling approach using the quasi-stochastic methodology called *Parameter Sweep*—an algorithm for heat resource uncertainty studies in steady-state. In this approach, we assumed that the main heat transport mechanism in the basin is thermal conduction. Dirichlet boundary conditions were assigned at the top and bottom of the model, with a pre-fixed temperature of 15 °C corresponding to the mean annual surface temperature on top, and 176 °C at a 7 km depth. The bottom temperature boundary condition of the model was set from a generalized 3D lithospheric scale steady-state conductive heat transfer model for the whole territory of Catalonia (NE, Spain), previously built with the software LitMod\_3D, and assuming local isostasy [67]. This model considered three layers: two layers model the crust with constant values of radiogenic heat production and thermal conductivity, and a third layer models the upper mantle without radiogenic heat production and constant thermal conductivity. The LitMod\_3D approach considers, among others, the effect of gravity, geoid, surface heat flow, and petrological and seismic data [68]. Several temperature layers were obtained from this model at the base of the crust and at 15, 7, and 3 km depths, with a corresponding temperature of 176 °C at a 7 km depth, which are currently published on the ICGC website [35].

Assuming an average ambient air temperature of 15 °C and a ground temperature of 176 °C at a 7 km depth, the resulting average thermal gradient is estimated at 23 °C/km considering the whole thickness of the model. However, if the calculation focuses on specific depths, the thermal gradient distribution can vary slightly with respect to this value due to the heterogeneous vertical distribution of thermal properties across the different lithologies. For example, the contrast between the lower thermal conductivity distribution in Neogene and Mesozoic sediments compared to the Paleozoic basement

induces a local gradient of 28.3 °C/km, from the surface to the top of the Jurassic reservoir in the Reus-1 well. The petrophysical parameters, i.e., the mean value of thermal conductivity, the heat production rate, and their corresponding standard deviation, for each lithology were obtained from previous works and the literature [34]. As stated above, the 3DHIP-Calculator can be used in different contexts according to the available data and assumptions. To introduce the different options, different scenarios of data availability were considered.

### 3.2.1. Example 1: Using a Single-Voxel 1D Geological Model

The first case considered here corresponds to the worst-case scenario, where a voxel-based 3DGM is not available. In this case, we assume an idealized reservoir defined only by a single voxel, prepared in a simple way. We impose a fixed value for the reservoir whole volume and the parameters are defined according to the PDF. This approach can be useful to obtain a first-order estimation of the HIP when the geometry and temperature of the target reservoir and the model must be idealized as a single-voxel reservoir. This case is equivalent to those considered in the literature when using commercial applications such as @Risk (Palisade) or Crystal Ball (Oracle) [23–25], and by the ‘GPPeval’ Python-based stochastic library [27]. These software packages cannot consider the distributed 3D geometry of the reservoirs and therefore must assume the reservoir as a single volume.

Since the geological and thermal models are simplified to a single voxel, it is necessary to determine the total target reservoir volume in the calculations. The petrophysical and operational properties are introduced to indicate the corresponding triangular or normal distribution functions (Table 1). The results generated by the 3DHIP-Calculator tool are limited to the HIP histogram and the CDFs with the corresponding P10, P50, and P90 for the entire target (such as shown in Figure 5b for example 2).

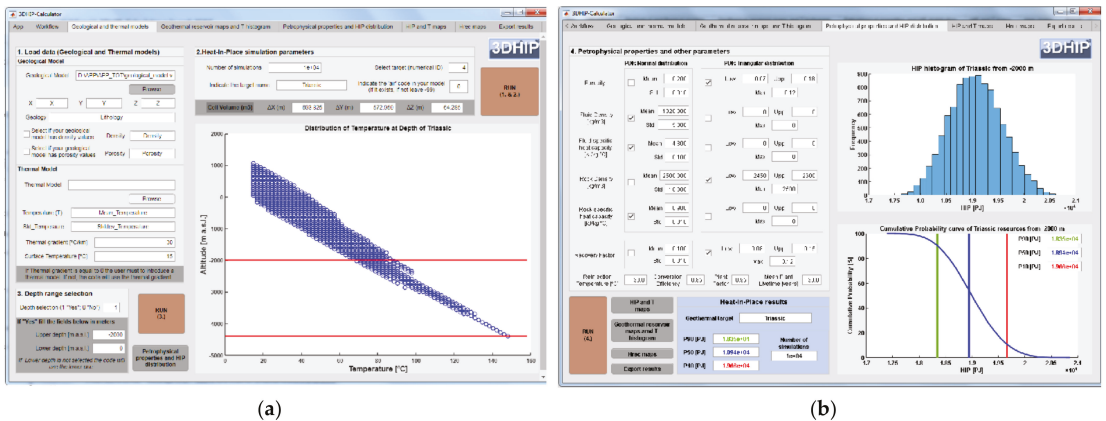


**Figure 5.** (a) Depth–temperature distribution for the Triassic unit using a linear geothermal gradient (example 2). Each blue circle corresponds to a temperature value of each of the voxels that discretize the Triassic unit. The red lines indicate the fixed depth range for the HIP and Hrec calculations. (b) Petrophysical and operational properties, and the corresponding PDFs used for this example. On the right-side: the HIP histogram and its CDF (blue curve) with the P10 (red line), P50 (blue line), and P90 (green line) for the entire targeted reservoir.

### 3.2.2. Example 2: Using a 3DGM but Not a 3DTM

The second scenario assumes a 3DGM that contains only information of the lithology class of each voxel, but not of its petrophysical parameters (such as rock density, porosity, and thermal properties) or specific temperature data from a calibrated 3D thermal model to estimate the temperature distribution in all the voxels of the model. To address the thermal context in this scenario, a regional gradient is assumed using Equation (3). In this example, a regional geothermal gradient of 30 °C/km and a mean annual surface temperature of

15 °C are assumed. Thus, the depth–temperature profile directly results from Equation (3) (Figure 5a).

After uploading the 3DGM and providing an input value for the geothermal gradient (30 °C/km), a total of  $N = 10,000$  realizations were carried out. This number of simulations is accepted by different authors as high enough for Monte Carlo evaluations [4,19,27,43]. For this example, we considered the Triassic unit as the geothermal target reservoir.

The selected depth range of the Triassic reservoir is indicated by two red lines in Figure 5. We selected the lower limit as the bottom of the model, while the upper depth corresponds to  $-2000$  m a.s.l. The upper depth range was chosen as the limit where the reservoir temperature is  $>60$  °C, a standard lower cut-off temperature for district heating stations [69]. The summary of petrophysical and operational properties, and their corresponding PDFs, are displayed in Table 1 and Figure 5b.

The values of the different parameters have been defined according to the available data, as well as from the scientific literature. The range of porosity values for the Buntsandstein and Muschelkalk units assumes a triangular PDF with porosity values of 7%, 12%, and 18% for the lowest, most probable, and highest values, respectively. Other parameters were obtained from the general literature, including the fluid density [70], fluid specific heat capacity [71], rock density [72], and rock specific heat capacity [73]. Considering the large uncertainty of the recovery factor ( $R$ ), we used a triangular PDF with a lower value of 0.08, a most probable value of 0.12, and an upper value of 0.15, according to a conservative setting.

The results of the HIP and Hrec parameters can be displayed as histograms of their frequency and/or CDFs with P10, P50, and P90 values for the target reservoir (Figure 5b). Alternatively, the resulting HIP and Hrec values (P10, P50, and P90) can also be recalculated and displayed in 2D maps as the vertical summation of the calculated values assigned to each voxel divided by the voxel area in  $\text{km}^2$  (see Figure 6 for an example of HIP). In these maps, the voxels with a zero value were left without color. Finally, the results can be exported to GIS software packages for post-processing (e.g., QGIS), as shown in Figure 7, where an isoline map of the HIP\_P90 is plotted to highlight the probability results.

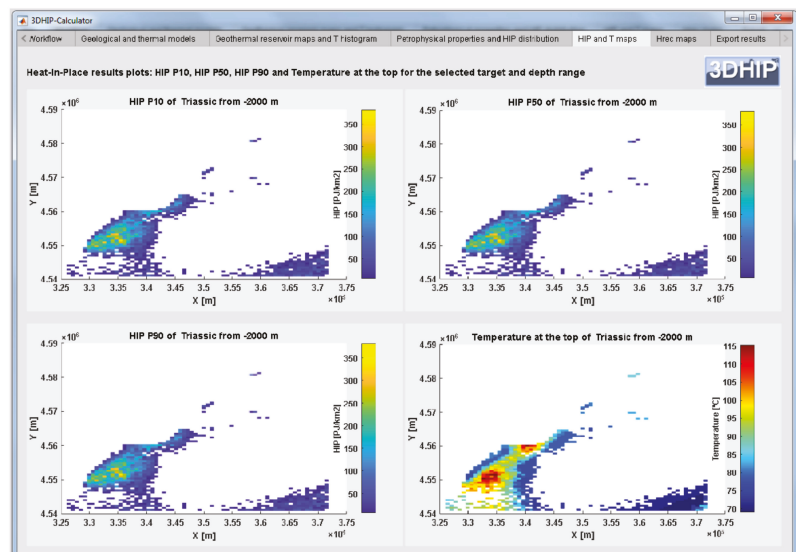


**Figure 6.** 2D maps of the HIP results of the P10, P50, and P90, and the temperature distribution at the top of the Triassic units below the pre-fixed depth range. For the HIP parameters, the values were calculated as an integration over the depth range and normalized by the voxel area. Units are in  $\text{PJ}/\text{km}^2$  and °C, respectively.

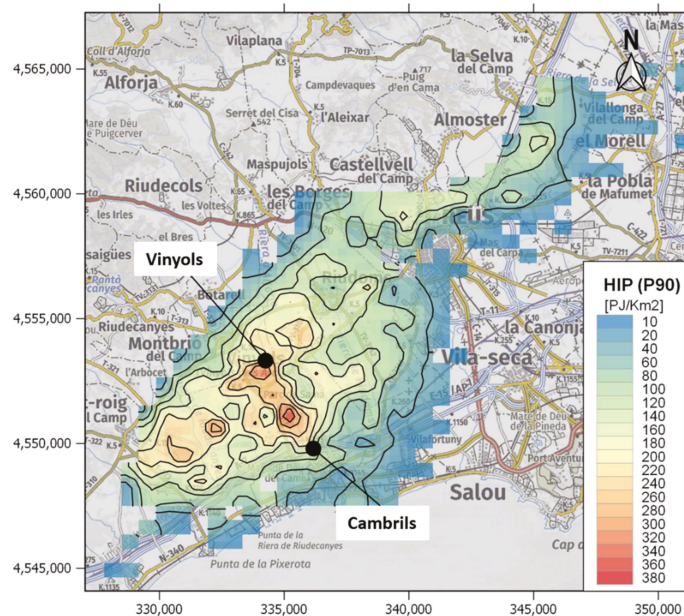


**Figure 7.** The HIP with P90 for the Triassic unit (example 2). The map was plotted with constant contour lines (20 PJ/Km<sup>2</sup>) following the described second example (i.e., with a 3DGM but not a 3DTM).

The maximum geothermal potential in the study area (approximately 320–340 PJ/km<sup>2</sup>) is concentrated near the Vinyols town (Figure 7). This region coincides with the zone where the RVB is deeper and Triassic attains its higher thickness at the regional scale. This spatial distribution of the results shows not only an estimation of the geothermal potential but also reveals where the prospective zones for geothermal energy production are located within the RVB. This demonstrates the importance of using 3D georeferenced data as inputs, containing the spatial geological information in three dimensions.

### 3.2.3. Example 3: Using Both a 3DGM and a 3DTM

The third scenario corresponds to a case in which a 3DGM, which includes petrophysical data (e.g., density), and a 3DTM, with the temperature and its standard deviation for each voxel, are available. The number of simulations and the reservoir target are the same as those of the previous example. Figure 8 shows a graph of the temperature distribution against depth for all the voxels corresponding to the target reservoir. As the temperature distribution in depth is the result of a 3DTM, the temperature dispersion is lower than that of the previous example and less affected by topography. The reservoir top, base, vertical thickness, and temperature distribution are shown in Figure 9 for the selected target and depth range. A summary of the parameters and PDFs used in this scenario and the resulting HIP frequency and CDFs are displayed in Figure 10.

The HIP and Hrec results are displayed in a georeferenced map (Figure 11) to provide a background of geographical context, and this allows for further analysis. The highest values (260–300 PJ/km<sup>2</sup>) were observed southwest of the basin, concentrated around the town of Vinyols. However, in this scenario, the estimation of HIP values was sensibly lower than those of the previous example. This is because the 3DTM mean gradient is lower than that of the previous scenario.

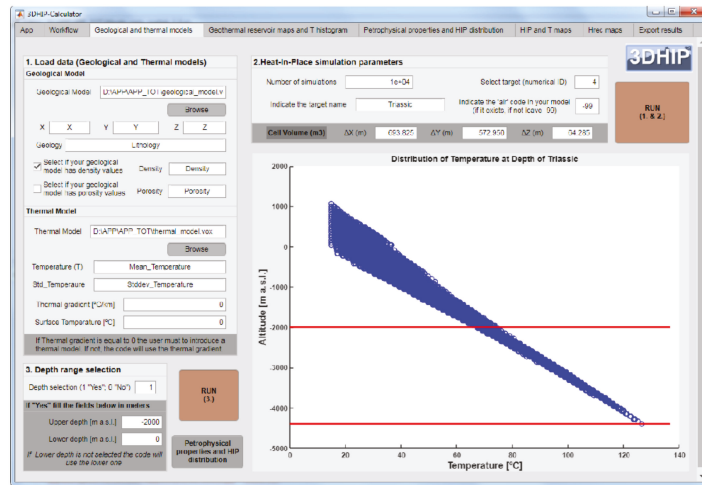


**Figure 8.** Altitude with respect to the temperature distribution for the selected target in example 3 (Triassic unit). Each blue circle corresponds to a voxel temperature value within the target reservoir. The red lines indicate the depth range fixed for performing calculations.

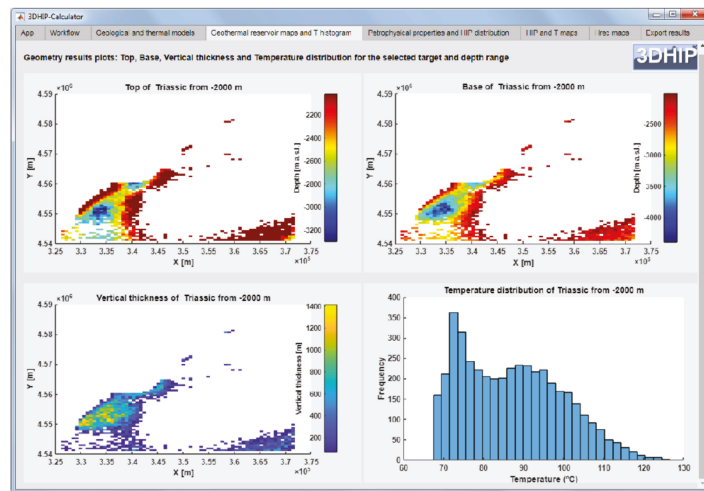


**Figure 9.** 2D distribution map of the top, base, and vertical thickness of the Triassic unit. Maximum depth and thickness are observed SW of the basin. The temperature distribution for the Triassic unit is shown in the bottom right diagram.

### 3.2.4. Example 4: The Use of the Recoverable Heat (Hrec) Values

The last scenario corresponds to a case in which the recoverable heat (Hrec) is also estimated. The results provide a first estimation of the percentage of the urban thermal demand that could be covered with the thermal energy recovered from a hypothetical geothermal doublet, where production and injection wells are typically separated from 1 to 2 km [72]. The Jurassic unit was considered as the target reservoir and the well locations were assumed to be next to the old Reus-1 oil well, where the Jurassic thickness is about 250 to 300 m from 1430 to 1700 m depth [54,55]. The example uses the same data assumption as that in example 3 (3DGM, which includes petrophysical data (e.g., density), and a

3DTM, with the temperature and its standard deviation for each voxel). For this case, the formation temperature oscillates between 55 and 65 °C and the rock porosity follows a normal distribution with a mean of 16% and a standard deviation of 5% [55]. Table 1 shows the other values used for the calculation.

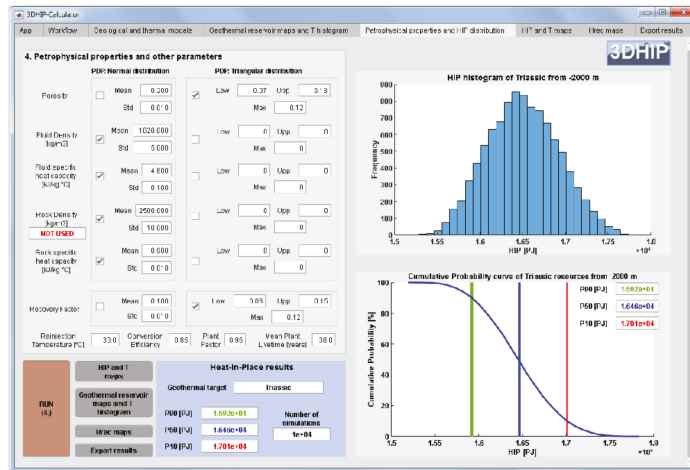


Figure 10. Summary of the petrophysical and operational parameters and PDFs used in example 3. For this example, the 3D geological model includes a rock density value for each voxel, and for this reason, it was not stochastically simulated using a pre-scribed PDF. On the right: the HIP histogram and the HIP CDF's results for the entire target reservoir (P10, P50, and P90).

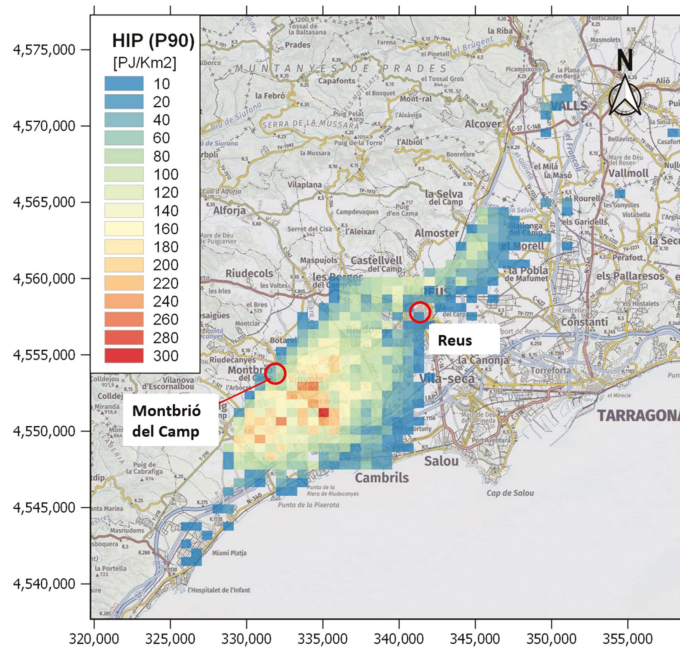
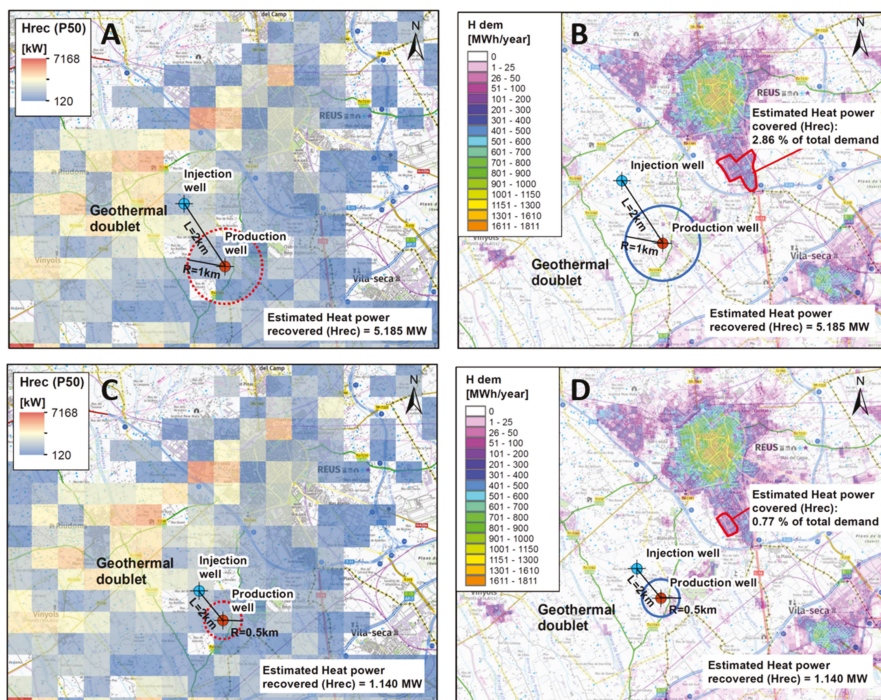


Figure 11. 2D georeferenced map showing the HIP results obtained using example 3. The resulting HIP (P90) values are divided by the voxel area to express the results in PJ/km<sup>2</sup>. Only on-shore values are displayed.

Here, we compared the obtained Hrec with respect to the urban heat demand of the city of Reus (Figure 12). We compared the sum of the obtained Hrec for the different probabilities, Hrec\_P10, Hrec\_P50, and Hrec\_90, under the influence radius of the hypothetical production deep well. Considering that the influence radius of the exploitation area in the reservoir has a value of half of the spacing between the injection and extraction wells (e.g., of up to 0.5 to 1 km), we obtained that the Hrec can range from 927 kW (P90 with 0.5 km of influence in the injection well) to 6.1 MW (P10 with 1 km of influence in the injection well). The heat demand density information was gathered from the Hotmaps EU project (<https://www.hotmaps-project.eu> (accessed on 15 October 2021)). The total heat energy demand obtained for the city of Reus was 391.05 GWh/year. Considering as a hypothesis that this demand concentrates during the colder part of the year (6 months) and with heaters working 12 h per day (2160 h/year), we can estimate the demand of thermal heat power capacity. In this case, the Hrec results suggested that a geothermal production well of a doublet in the Jurassic reservoir in this location could cover a range of 0.51% to 3.38% of the total heat demand of this city (Figure 12 and Table 2).



**Figure 12.** Two geothermal doublet scenarios comparing the Hrec\_P50 (A–C) with the heat demand of the city of Reus (B–D): the red polygon shows the covered area of the Reus total demand. (A,B) The injection and production wells are separated by 2 km and the radius of influence into the reservoir is considered to be 1 km. (C,D) The injection and production wells are separated by 1 km and the well influence radius into the reservoir is 0.5 km.

**Table 2.** Estimated probable heat recovery capacity as a function of the influence radius for a hypothetical geothermal doublet well in the Jurassic reservoir close to the Reus-1 well.

Hrec—Recoverable Heat vs. Estimated R—Radius of Influence	Hrec P10 (kWt)	Hrec P50 (kWt)	Hrec P90 (kWt)
R = 0.5 km	1337	1140	927
R = 1 km	6127	5185	4211

The Hrec results also suggest that the geothermal potential is much higher in the northwest of the Reus-1 well. This can be explained due to the fact that to the NW, the Jurassic formation lies deeper, up to 2000 m, and thus its temperature, following the 3DTM, oscillates between 70 and 80 °C. However, we considered a location close to the Reus-1 oil well to use its data.

#### 4. Discussion and Conclusions

This paper describes a novel and freely available tool named the 3DHIP-Calculator, which is used to assess the deep geothermal energy potential of hot aquifers. The tool allows applying the HIP method to calculate the HIP and the Hrec of a target reservoir following a Monte Carlo stochastic approach, and using 3D geological and 3D thermal models as inputs. The HIP method [5] is widely known and used in geothermal energy studies. The tool can be used to generate probability maps, which are of particular importance during the preliminary assessment of geothermal resources, mainly at the regional scale. In this work, the operation and workflow of the 3DHIP-Calculator tool have been presented. Its use has been demonstrated through an example of an area identified with deep geothermal potential in Mesozoic aquifers located in the NE of the Iberian Peninsula (Reus-Valls Basin), and from considering four different conceptual scenarios based on the available data.

The 3DHIP-Calculator covers the need to have a standard and freely available tool for the whole geothermal community with which users can estimate the HIP using Monte Carlo simulations and where they can use their 3D models to assess their case studies. In this regard, the 3DHIP-Calculator is the only free tool that allows to carry out estimations of the geothermal potential assessment at the same time, either considering a homogeneous distribution of parameters (i.e., lumped parameter models) in the whole reservoir or including spatial variability of petrophysical properties through the considered reservoir (e.g., density and porosity). Moreover, the 3DHIP-Calculator is not regionally constrained and can be used to perform geothermal potential assessment exercises independently from where their data is. Additionally, the 3DHIP-Calculator simulations are not limited to a specific case study and the initial input data can change and incorporate data as these are refined or obtained through the reservoir characterization. The link between the 3DGM and 3DTM (examples 2 and 3), and the corresponding 3D geothermal potential assessment model (3DGPAM), represents an important step forward with respect to scenarios such as that of example 1, where the reservoir is represented as a single voxel and the geothermal potential results are limited to a single CDF with values of P10, P50, and P90 for the entire target reservoir, and where the option to include more data as the reservoir knowledge increases is truncated.

The results of the 3DGPAM can also again be exported back into 3D geological modeling software to carry out further steps of geothermal exploration of a specific project, or simply exported in 3D visualization software to plot the obtained results (e.g., the open-source, multi-platform data analysis and visualization application, such as ParaView).

The 3DHIP-Calculator is designed to assess and map geothermal resources at the regional scale. It bridges the gap between the first phases of field exploration and geological 3D modeling, and the necessary phase of quantification of the geothermal heat available in deep hot reservoirs, maintaining the uncertainty of the data. Therefore, it should be considered a complementary tool to the well-known open-source software DoubletCalc 2D [74], which allows calculating the hydraulic performance around geothermal doublets

(producing well and injector) over time, and that is also based on stochastic simulations (Monte Carlo). Indeed, this analysis corresponds to a more advanced and detailed phase in the development of geothermal projects, considering, for example, that it is required for many grant applications related to specific geothermal projects in the Netherlands. The 3DHIP-Calculator is not designed to calculate the hydraulic performance of a doublet or to directly calculate the flow, temperature, and therefore the potential energy recovered from them, as other already available tools do for these purposes. However, it is able to make a first estimation from a hypothetical geothermal doublet, as shown in example 4.

The results obtained in the test case of the Reus-Valls Basin (NE, Spain) demonstrate how the 3DHIP-Calculator can satisfactorily evaluate and map the deep geothermal potential of reservoirs in a distributed manner from 3D models. In the presented test case study, the results reveal the existence of a high geothermal potential located between the villages of Vinyols and Cambrils (e.g., Figure 7). Although the exploration phase is in a preliminary stage, the results obtained considering the 3D modeling and the stochastic approach will allow progress in the decision-making process for the design of new exploratory campaigns, and thus increase the precision of the predictions. This modeling workflow has improved the estimates from previous studies based exclusively on a deterministic and a basin-wide aggregate approach [36,37,75].

The examples presented here demonstrate how geoscientists and engineers can use the 3DHIP-Calculator to easily evaluate the geothermal potential from their 3D geological models in a repeatable and systematic manner following a stochastic approach. The tool will help investors and research organizations determine the suitability of continuing to advance with new investments in pre-feasibility studies of future deep geothermal projects.

**Author Contributions:** Conceptualization, G.P.; Methodology, G.P., I.H. and A.G.; Software, G.P., I.H., A.G., M.C. and E.G.-R.; Resources, M.C. and G.A.; Writing—Original draft preparation, G.P.; Writing—Review and editing, I.H., A.G. and E.G.-R.; Visualization, M.C. and G.A.; Supervision, I.H., A.G. and E.G.-R. All authors have read and agreed to the published version of the manuscript.

**Funding:** G.P. was supported by Agència de Gestió d’Ajuts Universitaris i de Recerca (AGAUR) for Industry Doctorate Research 2016-DI-031 grant and by Institut Cartogràfic i Geològic de Catalunya (ICGC) through the MoU06092016ICGC-UAB and by the MoU11112019ICGC-UAB. E.G.-R. acknowledges the support of the Ramón y Cajal fellowship funded by the Spanish Ministry of Science, Innovation and Universities (RYC2018-026335-I and PID2020-118999GB-I00).

**Institutional Review Board Statement:** Not applicable.

**Informed Consent Statement:** Not applicable.

**Data Availability Statement:** The source code can be download from the following GitHub repository: <https://github.com/OpenICGC/3DHIP-Calculator> (accessed on 15 October 2021) mail for contact: [geotermia@icgc.cat](mailto:geotermia@icgc.cat). The installation files, as well as the user manual in PDF format and some examples for testing the tool, can also be freely downloaded from the Deep geothermal energy web page of the Institut Cartogràfic i Geològic de Catalunya (ICGC) (under the Creative Commons license Attribution 4.0 International, CC BY 4.0).

**Acknowledgments:** The 3DHIP-Calculator software was developed during a PhD grant of the Industrial Doctorate programme sponsored by the AGAUR (Agència de Gestió d’Ajuts Universitaris i de Recerca) of the Government of Catalonia (reference number 2016-DI-031), and funded and maintained by the Institut Cartogràfic i Geològic de Catalunya (ICGC) under the project GeoEnergy of the CP-I (2014–2017), CP-II (2018), and CP-III (2019–2022). E.G.-R. acknowledges the Spanish Ministry of Science, Innovation and Universities for the “Ramón y Cajal” fellowship RYC2018-026335-I and research project PID2020-118999GB-I00. We thank the anonymous reviewers for their constructive comments and suggestions which led to a substantial improvement of the paper as well as all the researchers that has collaborated in this research.

**Conflicts of Interest:** The authors declare no conflict of interest.

## References

- Bertani, R. Geothermal Power Generation in the World 2010–2015 Update Report. In Proceedings of the World Geothermal Congress 2015, Melbourne, Australia, 19–25 April 2015; pp. 19–25.
- Sigfússon, B.; Uihlein, A. *2015 JRC Geothermal Energy Status Report*; EUR 27623 EN; Joint Research Center: Petten, The Netherlands, 2015; p. 59. [\[CrossRef\]](#)
- Van Wees, J.-D.; Boxem, T.; Angelino, L.; Dumas, P. *A Prospective Study on the Geothermal Potential in the EU. GEOLEC Project*; EC: Utrecht, The Netherlands, 2013; p. 97.
- Agemar, T.; Weber, J.; Moeck, I. Assessment and Public Reporting of Geothermal Resources in Germany: Review and Outlook. *Energies* **2018**, *11*, 332. [\[CrossRef\]](#)
- Muffler, P.; Cataldi, R. Methods for Regional Assessment of Geothermal Resources. *Geothermics* **1978**, *7*, 53–89. [\[CrossRef\]](#)
- Williams, C.F. Updated Methods for Estimating Recovery Factors for Geothermal Resources. In Proceedings of the Thirty-Second Workshop on Proceedings, Geothermal Reservoir Engineering, Stanford University, Stanford, CA, USA, 22 January 2007; p. 7.
- Williams, C.F.; Reed, M.J.; Mariner, R.H. *A Review of Methods Applied by the U.S. Geological Survey in the Assessment of Identified Geothermal Resources*; U.S. Geological Survey: Reston, VA, USA, 2008; p. 30.
- Garg, S.K.; Combs, J. Appropriate Use of USGS Volumetric “Heat in Place” Method and Monte Carlo Calculations. In Proceedings of the Thirty-Fourth Workshop on Geothermal Reservoir Engineering, Stanford University, Stanford, CA, USA, 1 February 2010; p. 7.
- Garg, S.K.; Combs, J. A Reexamination of USGS Volumetric “Heat in Place” Method. In Proceedings of the Thirty-Sixth Workshop on Geothermal Reservoir Engineering, Stanford University, Stanford, CA, USA, 31 February 2011; p. 5.
- Garg, S.K.; Combs, J. A Reformulation of USGS Volumetric “Heat in Place” Resource Estimation Method. *Geothermics* **2015**, *55*, 150–158. [\[CrossRef\]](#)
- Limberger, J.; Boxem, T.; Pluymaekers, M.; Bruhn, D.; Manzella, A.; Calcagno, P.; Beekman, F.; Cloetingh, S.; van Wees, J.-D. Geothermal Energy in Deep Aquifers: A Global Assessment of the Resource Base for Direct Heat Utilization. *Renew. Sustain. Energy Rev.* **2018**, *82*, 961–975. [\[CrossRef\]](#)
- Trumpy, E.; Botteghi, S.; Caiozzi, F.; Donato, A.; Gola, G.; Montanari, D.; Pluymaekers, M.P.D.; Santilano, A.; van Wees, J.D.; Manzella, A. Geothermal Potential Assessment for a Low Carbon Strategy: A New Systematic Approach Applied in Southern Italy. *Energy* **2016**, *103*, 167–181. [\[CrossRef\]](#)
- Miranda, M.M.; Raymond, J.; Dezayes, C. Uncertainty and Risk Evaluation of Deep Geothermal Energy Source for Heat Production and Electricity Generation in Remote Northern Regions. *Energies* **2020**, *13*, 4221. [\[CrossRef\]](#)
- Arango-Galván, C.; Prol-Ledesma, R.M.; Torres-Vera, M.A. Geothermal Prospects in the Baja California Peninsula. *Geothermics* **2015**, *55*, 39–57. [\[CrossRef\]](#)
- Pol-Ledesma, R.-M.; Carrillo-de la Cruz, J.-L.; Torres-Vera, M.-A.; Membrillo-Abad, A.-S.; Espinoza-Ojeda, O.-M. Heat Flow Map and Geothermal Resources in Mexico / Mapa de Flujo de Calor y Recursos Geotérmicos de México. *Terra Digit.* **2018**. [\[CrossRef\]](#)
- Hurter, S.; Schellschmidt, R. Atlas of Geothermal Resources in Europe. *Geothermics* **2003**, *32*, 779–787. [\[CrossRef\]](#)
- Nathenson, M. *Methodology of Determining the Uncertainty in the Accessible Geothermal Resource Base of Identified Hydrothermal Convect-Tion Systems*; Open-File Report; U.S. Geological Survey: Menlo Park, CA, USA, 1978; p. 51.
- Rubinstein, R.Y.; Kroese, D.P. *Simulation and the Monte Carlo Method*, 3rd ed.; Wiley Series in Probability and Statistics; Wiley: Hoboken, NJ, USA, 2017; ISBN 978-1-118-63220-8.
- Shah, M.; Vaidya, D.; Sircar, A. Using Monte Carlo Simulation to Estimate Geothermal Resource in Dholera Geothermal Field, Gujarat, India. *Multiscale Multidiscip. Model. Exp. Des.* **2018**, *1*, 83–95. [\[CrossRef\]](#)
- Trota, A.; Ferreira, P.; Gomes, L.; Cabral, J.; Kallberg, P. Power Production Estimates from Geothermal Resources by Means of Small-Size Compact Climeon Heat Power Converters: Case Studies from Portugal (Sete Cidades, Azores and Longroiva Spa, Mainland). *Energies* **2019**, *12*, 2838. [\[CrossRef\]](#)
- Palisade Corporation. *@Risk for Excel*; Palisade Corporation: Ithaca, NY, USA, 2014.
- Oracle. *Oracle Crystal Ball Spreadsheet Functions for Use in Microsoft Excel Models*; Oracle: Austin, TX, USA, 2014.
- Arkan, S.; Parlaktuna, M. Resource Assessment of Balçova Geothermal Field. In Proceedings of the World Geothermal Congress 2005, Antalya, Turkey, 24–29 April 2005.
- Yang, F.; Liu, S.; Liu, J.; Pang, Z.; Zhou, D. Combined Monte Carlo Simulation and Geological Modeling for Geothermal Resource Assessment: A Case Study of the Xiongqian Geothermal Field, China. In Proceedings of the World Geothermal Congress 2015, Melbourne, Australia, 19–25 April 2015; pp. 19–25.
- Halcon, R.M.; Kaya, E.; Penarroyo, F. Resource Assessment Review of the Daklan Geothermal Prospect, Benguet, Philippines. In Proceedings of the World Geothermal Congress 2015, Melbourne, Australia, 19–25 April 2015; pp. 19–25.
- Barkaoui, A.-E.; Zarhloule, Y.; Varbanov, P.S.; Klemes, J.J. Geothermal Power Potential Assessment in North Eastern Morocco. *Chem. Eng. Trans.* **2017**, *61*, 1627–1632. [\[CrossRef\]](#)
- Pocasangre, C.; Fujimitsu, Y. Geothermics A Python-Based Stochastic Library for Assessing Geothermal Power Potential Using the Volumetric Method in a Liquid-Dominated Reservoir. *Geothermics* **2018**, *76*, 164–176. [\[CrossRef\]](#)
- Zhu, Z.; Lei, X.; Xu, N.; Shao, D.; Jiang, X.; Wu, X. Integration of 3D Geological Modeling and Geothermal Field Analysis for the Evaluation of Geothermal Reserves in the Northwest of Beijing Plain, China. *Water* **2020**, *12*, 638. [\[CrossRef\]](#)

29. Calcagno, P.; Baujard, C.; Dagallier, A.; Guillou-Frottier, L.; Genter, A. Three-Dimensional Estimation of Geothermal Potential from Geological Field Data: The Limagne Geothermal Reservoir Case Study (France). In Proceedings of the Geothermal Resources Council GRC Annual Meeting, Reno, NV, USA, 4–7 October 2009; p. 326.
30. Van Wees, J.-D.; Juez-Larre, J.; Bonte, D.; Mijnlief, H.; Kronimus, A.; Gesse, S.; Obdam, A.; Verweij, H. ThermoGIS: An Integrated Web-Based Information System for Geothermal Exploration and Governmental Decision Support for Mature Oil and Gas Basins. In Proceedings of the World Geothermal Congress 2010, Bali, Indonesia, 25 April 2010; p. 7.
31. Kramers, L.; van Wees, J.-D.; Pluymaekers, M.P.D.; Kronimus, A.; Boxem, T. Direct Heat Resource Assessment and Subsurface Information Systems for Geothermal Aquifers; the Dutch Perspective. *Neth. J. Geosci.* **2012**, *91*, 637–649. [[CrossRef](#)]
32. Vrijlandt, M.A.W.; Struijk, E.L.M.; Brunner, L.G.; Veldkamp, J.G.; Witmans, N.; Maljers, D.; van Wees, J.D. ThermoGIS Update: A Renewed View on Geothermal Potential in the Netherlands. In Proceedings of the European Geothermal Congress 2019, The Hague, The Netherlands, 11 June 2019; p. 10.
33. R Core Team. *R: A Language and Environment for Statistical Computing*; R Foundation for Statistical Computing: Vienna, Austria, 2013.
34. Herms, I.; Piris, G.; Colomer, M.; Peigney, C.; Grier, A.; Ledo, J. 3D Numerical Modelling Combined with a Stochastic Approach in a MATLAB-Based Tool to Assess Deep Geothermal Potential in Catalonia: The Case Test Study of the Reus-Valls Basin. In Proceedings of the World Geothermal Congress 2020 + 1, Reykjavik, Iceland, 24–27 October 2021; p. 9.
35. ICGC. Geothermal Atlas of Catalonia: Geoindex-Deep-Geothermal. 2020. Available online: <https://www.icgc.cat/en/Public-Administration-and-Enterprises/Tools/Geoindex-viewers/Geoindex-Deep-geothermal-energy> (accessed on 15 October 2021).
36. Colmenar-Santos, A.; Folch-Calvo, M.; Rosales-Asensio, E.; Borge-Diez, D. The Geothermal Potential in Spain. *Renew. Sustain. Energy Rev.* **2016**, *56*, 865–886. [[CrossRef](#)]
37. Arrizabalaga, I.; De Gregorio, M.; De Santiago, C.; Pérez, P. Geothermal Energy Use, Country Update for Spain. In Proceedings of the European Geothermal Congress 2019, The Hague, The Netherlands, 11 June 2019; p. 9.
38. Beardsmore, G.R.; Rybach, L.; Blackwell, D.; Baron, C. A Protocol for Estimating and Mapping Global EGS Potential. *Geotherm. Resour. Counc. Trans.* **2010**, *34*, 301–312.
39. Hurter, S.; Haenel, R. *Atlas of Geothermal Resources in Europe*; Official Publications of the European Communities, European Commission: Luxembourg, 2002.
40. Lavigne, J. Les Ressources Géothermiques Françaises-Possibilités de Mise En Valeur. *Ann. Mines* **1977**, 57–72.
41. Williams, C.F. Development of Revised Techniques for Assessing Geothermal Resources. In Proceedings of the Twenty-Ninth Workshop on Geothermal Reservoir Engineering, Stanford University, Stanford, CA, USA, 26 January 2004; p. 5.
42. Lund, J.W.; Boyd, T.L. Direct Utilization of Geothermal Energy 2015 Worldwide Review. *Geothermics* **2016**, *60*, 66–93. [[CrossRef](#)]
43. Wang, Y.; Wang, L.; Bai, Y.; Wang, Z.; Hu, J.; Hu, D.; Wang, Y.; Hu, S. Assessment of Geothermal Resources in the North Jianguo Basin, East China, Using Monte Carlo Simulation. *Energies* **2021**, *14*, 259. [[CrossRef](#)]
44. MathWorks. *MATLAB*; The MathWorks, Inc.: Natick, MA, USA, 2019.
45. Moeck, I.; Beardsmore, G.R. A New ‘Geothermal Play Type’ Catalog: Streamlining Exploration Decision Making. In Proceedings of the Thirty-Ninth Workshop on Geothermal Reservoir Engineering, Stanford University, Stanford, CA, USA, 24 February 2014; p. 8.
46. De la Varga, M.; Schaaf, A.; Wellmann, F. GemPy 1.0: Open-Source Stochastic Geological Modeling and Inversion. *Geosci. Model Dev.* **2019**, *12*, 1–32. [[CrossRef](#)]
47. Massana, E. L’activitat Neotectònica a Les Cadenes Costaneres Catalanes. Ph.D. Thesis, University of Barcelona, Barcelona, Spain, 1995.
48. Cabrera, L.; Calvet, F. Onshore Neogene record in NE Spain: Vallès–Penedès and El Camp half-grabens (NW Mediterranean). In *Tertiary Basins of Spain*; Friend, P.F., Dabrio, C.J., Eds.; Cambridge University Press: Cambridge, UK, 1996; pp. 97–105, ISBN 978-0-521-46171-9.
49. Moeck, I.S. Catalog of Geothermal Play Types Based on Geologic Controls. *Renew. Sustain. Energy Rev.* **2014**, *37*, 867–882. [[CrossRef](#)]
50. ICGC. Base Geològica 1:50,000 de Catalunya. Available online: <https://www.icgc.cat/en/Public-Administration-and-Enterprises/Downloads/Geological-and-geochematic-cartography/Geological-cartography/Geological-map-1-50-000> (accessed on 1 January 2021).
51. Moeck, I.S.; Dussel, M.; Weber, J.; Schintgen, T.; Wolfgramm, M. Geothermal Play Typing in Germany, Case Study Molasse Basin: A Modern Concept to Categorise Geothermal Resources Related to Crustal Permeability. *Neth. J. Geosci.* **2019**, *98*, e14. [[CrossRef](#)]
52. Lopez, S.; Hamm, V.; Le Brun, M.; Schaper, L.; Boissier, F.; Cotiche, C.; Giuglaris, E. 40 Years of Dogger Aquifer Management in Ile-de-France, Paris Basin, France. *Geothermics* **2010**, *39*, 339–356. [[CrossRef](#)]
53. Blöcher, G.; Reinsch, T.; Hennings, J.; Milsch, H.; Regenspur, S.; Kummerow, J.; Francke, H.; Kranz, S.; Saadat, A.; Zimmermann, G.; et al. Hydraulic History and Current State of the Deep Geothermal Reservoir Groß Schönebeck. *Geothermics* **2016**, *63*, 27–43. [[CrossRef](#)]
54. Haffen, S.; Géraud, Y.; Diraison, M.; Dezayes, C.; Siffert, D.; Garcia, M. Temperature Gradient Anomalies in the Buntsandstein Sandstone Reservoir, Upper Rhine Graben, Sultz, France. In Proceedings of the Tu D203 09—76th EAGE Conference & Exhibition 2014, Amsterdam, The Netherlands, 16 June 2014.

55. Zapatero, M.A.; Reyes, J.L.; Martínez, R.; Suárez, I.; Arenillas, A.; Perucha, M.A. *Estudio Preliminar de las Formaciones Favorables para el Almacenamiento Subterráneo de CO<sub>2</sub> en España*; Instituto Geológico y Minero de España (IGME): Madrid, Spain, 2009; p. 135.
56. AURENSA. *Proyecto de Almacenamientos Subterráneos de Gas. Reus*; Auxiliar de Recursos y Energía, S.A.: Madrid, Spain, 1996; p. 65.
57. Campos, R.; Recreo, F.; Perucha, M.A. *AGP de CO<sub>2</sub>: Selección de Formaciones Favorables en la Cuenca del Ebro*; Informes Técnicos Ciemat; CIEMAT: Madrid, España, 2007; p. 124.
58. Marzo, M. *El Bundstandstein de los Catalánides: Estratigrafía y Procesos Sedimentarios*. Ph.D. Thesis, Universitat de Barcelona, Barcelona, Spain, 1980.
59. Zapatero, M.A.; Suárez, I.; Arenillas, A.; Marina, M.; Catalina, R.; Martínez-Orío, R. *Proyecto Europeo GeoCapacity. Assessing European Capacity for Geological Storage of Carbon Dioxide*; Instituto Geológico y Minero de España (IGME): Madrid, España, 2009; p. 162.
60. ICGC. Model d'Elevacions Del Terreny de Catalunya 15 × 15 Metres (MET-15) v2.0. 2018. Available online: <https://www.icgc.cat/Descarregues/Elevacions/Model-d-elevacions-del-terreny-de-15x15-m> (accessed on 11 January 2021).
61. ICGC. Mapa Geològic Comarcal de Catalunya. Full Del Baix Camp. 2006. Available online: <https://www.icgc.cat/en/Public-Administration-and-Enterprises/Downloads/Geological-and-geothematic-cartography/Geological-cartography/Geological-map-1-50-000> (accessed on 11 January 2021).
62. ICGC. Model 3D Geològic de Catalunya. 2013. Available online: <https://www.icgc.cat/ca/Administracio-i-empresa/Descarregues/Cartografia-geologica-i-geotematica/Cartografia-geologica/Model-geologic-3D-de-Catalunya> (accessed on 15 January 2020).
63. ICGC. Base de Dades de Sondejors de Catalunya (BDSoc). 2015. Available online: <https://www.icgc.cat/ca/Administracio-i-empresa/Eines/Visualitzadors-Geoindex/Geoindex-Prospeccions-geotecniques> (accessed on 15 January 2020).
64. Scott, S.W.; Covell, C.; Júlíusson, E.; Valfells, Á.; Newson, J.; Hrafnkelsson, B.; Pálsson, H.; Gudjónsdóttir, M. A Probabilistic Geologic Model of the Krafla Geothermal System Constrained by Gravimetric Data. *Geotherm. Energy* **2019**, *7*, 29. [CrossRef]
65. Scott, S.; Covell, C.; Júlíusson, E.; Valfells, Á.; Newson, J.; Hrafnkelsson, B.; Pálsson, H.; Gudjónsdóttir, M. A Probabilistic Geologic Model of the Krafla Geothermal System Based on Bayesian Inversion of Gravimetric Data. In Proceedings of the World Geothermal Congress 2020 + 1, Reykjavik, Iceland, 24–27 October 2021; p. 13.
66. ICGC. Base de Dades Geofísica de Catalunya. 2013. Available online: <https://www.icgc.cat/Administracio-i-empresa/Serveis/Geofisica-aplicada/Geoindex-Tecniques-geofisiques> (accessed on 15 January 2020).
67. Fulla, J.; Afonso, J.C.; Connolly, J.A.D.; Fernández, M.; García-Castellanos, D.; Zeyen, H. LitMod3D: An Interactive 3-D Software to Model the Thermal, Compositional, Density, Seismological, and Rheological Structure of the Lithosphere and Sublithospheric Upper Mantle: LITMOD3D-3-D Interactive code to model lithosphere. *Geochem. Geophys. Geosyst.* **2009**, *10*. [CrossRef]
68. Carballo, A.; Fernández, M.; Jiménez-Munt, I. Corte Litosférico al Este de La Península Ibérica y Sus Márgenes. Modelización de Las Propiedades Físicas Del Manto Superior. *Física Tierra* **2011**, *23*, 131–147. [CrossRef]
69. Agemar, T.; Weber, J.; Schulz, R. Deep Geothermal Energy Production in Germany. *Energies* **2014**, *7*, 4397–4416. [CrossRef]
70. Oldenburg, C.M.; Rinaldi, A.P. Buoyancy Effects on Upward Brine Displacement Caused by CO<sub>2</sub> Injection. *Transp. Porous Media* **2011**, *87*, 525–540. [CrossRef]
71. Lukosevicius, V. *Thermal Energy Production from Low Temperature Geothermal Brine—Technological Aspects and Energy Efficiency*; ONU Geothermal Training Programme; Orkustofnum—National Energy Authority: Grensasvegur, Reykjavik, Iceland, 1993; p. 42.
72. Ayala, C. Basement Characterisation and Cover Deformation of the Linking Zone (NE Spain) from 2.5D and 3D Geological and Geophysical Modelling. In Proceedings of the 8th EUREGEO, Barcelona, Spain, 15–17 June 2015; p. 23.
73. Willems, C.J.L.; Nick, H.M. Towards Optimisation of Geothermal Heat Recovery: An Example from the West Netherlands Basin. *Appl. Energy* **2019**, *247*, 582–593. [CrossRef]
74. Veldkamp, J.G.; Pluymaekers, M.P.D.; van Wees, J.-D. *DoubletCalc 2D (v1.0) Manual*; TNO 2015 R10216; TNO: Utrecht, The Netherlands, 2015.
75. Arrizabalaga, I.; De Gregorio, M.; De Santiago, C.; García de la Noceda, C.; Pérez, P.; Urchueguía, J.F. Country Update for the Spanish Geothermal Sector. In Proceedings of the World Geothermal Congress 2020 + 1, Reykjavik, Iceland, 24–27 October 2021.



MDPI  
St. Alban-Anlage 66  
4052 Basel  
Switzerland  
Tel. +41 61 683 77 34  
Fax +41 61 302 89 18  
[www.mdpi.com](http://www.mdpi.com)

*Energies* Editorial Office  
E-mail: [energies@mdpi.com](mailto:energies@mdpi.com)  
[www.mdpi.com/journal/energies](http://www.mdpi.com/journal/energies)





MDPI  
St. Alban-Anlage 66  
4052 Basel  
Switzerland

Tel: +41 61 683 77 34

[www.mdpi.com](http://www.mdpi.com)



ISBN 978-3-0365-5244-6